Vrijezuiger-expander met een variabele ingebouwde volumeverhouding
en met een geïntegreerde lineaire alternator

Free Piston Expander with a Variable Built-In Volume Ratio
and with an Integrated Linear Alternator

Sergei Gusev

Promotoren: prof. dr. ir. M. De Paepe, dr. D. Ziviani
Proefschrift ingediend tot het behalen van de graad van
Doctor in de ingenieurswetenschappen: werktuigkunde-elektrotechniek

UNIVERSITEIT
GENT

Vakgroep Mechanica van Stroming, Warmte en Verbranding
Voorzitter: prof. dr. ir. P. De Baets
Faculteit Ingenieurswetenschappen en Architectuur
Academiejaar 2018 - 2019

ISBN 978-94-6355-211-0
NUR 978, 961
Wettelijk depot: D/2019/10.500/19

Members of the Examination Board

Voting members:

Chair:	Prof. Hendrik Van Landeghem
Faculty reading committee:	Prof. Dieter Fauconnier (EA08) Prof. Eckhard A. Groll (Purdue University, West Lafayette, USA) Dr. ir. Steven Lecompte (EA03) Prof. Vincent Lemort (Université de Liège) Prof. Kurt Stockman (EA08), secretary
Other members:	Prof. Sebastian Verhelst (EA03)

Members ineligible to vote:

Supervisors:	Prof. Michel De Paepe (EA03) Dr. Davide Ziviani (Purdue University, West Lafayette, USA)

Universiteit Gent
Faculteit Ingenieurswetenschappen en Architectuur
Vakgroep Mechanica van Stroming, Warmte en Verbranding

Promotoren: Prof. dr. ir. Michel De Paepe
Dr. Davide Ziviani

Universiteit Gent
Faculteit Ingenieurswetenschappen en Architectuur

Vakgroep Mechanica van Stroming, Warmte en Verbranding
Sint-Pietersnieuwstraat 41, B-9000 Gent, België

Tel.: +32-9-264.32.88
Fax.: +32-9-264.35.75

Proefschrift tot het behalen van de graad van
Doctor in de ingenieurswetenschappen:
werktuigkunde - elektrotechniek
Academiejaar 2018-2019

Acknowledgements

I would like to show my gratitude to my supervisor Prof. Michel De Paepe for all the provided support. In 2008, as a result of his recommendation I got an opportunity to participate in a series of projects on organic Rankine cycle run by Bruno Vanslambroek. To whom I am also thankful for the experience I obtained during these last ten years. It is this work that brought me to the idea which forms the basis of this thesis.

Due to these projects I met several PhD candidates who inspired me to start my own research, especially, Davide Ziviani who became my co-supervisor after his defense. More than four years of common work made us more than colleagues, it made us friends. His positive mindset and support helped me to overcome various issues during this period. His deep knowledge of thermal processes is unrivaled, especially in grilling and cooking.

Andrés Hernández provided me with the needed background information of model predictive control which was very valuable input that helped me to understand the working principle of various advanced control techniques. This experience was very useful for the development of the current setup's algorithm. Furthermore, thanks to him I discovered the wonders of Colombia and it has stayed with me ever since.

I would like to mention Jeroen De Maeyer and his colleagues, in particular Kris Bonnarens for a great support provided during the patent application. Jeroen believed in my story and at a certain point could explain the working principle and the advantages thereof to external parties better than I could. His questions helped me to form the backbone of my research and the multiple simulations I performed on his request became a significant part of the current study.

I want to thank Prof. Martijn van den Broek who convinced me to become a PhD student at my age. It was under his supervision that I wrote my first paper and presented it in 2014 at the conference in Purdue University organized by Prof. Eckhard A. Groll. I believe, this conference triggered my further research on the topic.

Without Prof. Kurt Stockman and his group, that specializes in automation and general electrical machines, I could not have realized this project. Prof. Stijn Derammelaere provided me with the first input for the project. Being a thermodynamicus myself, I really appreciated this input. Jasper De Viaene helped in the

preliminary sizing up of the test setup and in contacting the hardware suppliers. Many thanks to Pieter Defreyne for the reliable electrical equipment he built. Special thanks to Heinz Vervaeke for his great theoretical and practical assistance during the commissioning and experimental campaign. My understanding of linear machines' behavior is the result of his efforts.

I cannot overstate the value of Prof. Jan Vierendeels's support and suggestions. Because of him, a very important part of the model was developed in a very efficient way. It is a great loss that he is no longer with us.

Also I want to thank José Vangheluwe for his active guidance in the design, manufacturing coordination of the components for the test setup and his very valuable suggestions in general. Without him and his morning coffee this setup would not be as shiny.

Besides my colleagues, I would like to thank people who helped me and my family to set our first steps in Belgium: Prof. Etienne Vermeersch, Prof. Michel Vanhoorne, Carla Ronkes and Jaqueline De Scheppere. This story would be impossible without them.

My family deserves my special gratitude. For years they were mostly seeing me sit in front of my laptop instead of living a normal life. My daughter Anastasia became familiar with thermodynamics by reading my texts, my son Jegor and my wife Lyubov missed me during this period but provided the necessary emotional support. My parents from both sides and my friends have always encouraged me in my ambitions. I am grateful to all of you.

Ghent, February 2019
Sergei Gusev

Table of Contents

List of Figures

List of Tables

Nomenclature

Acronyms

ABC	Air Bottoming Cycle
BVR	Built-in Volume Ratio
CDS	Cold Drawn Seamless
CV	Control Volume
CVT	Continuously Variable Transmission
DAQ	Data Acquisition
DPF	Diesel Particulate Filter
EDM	Electrical Discharge Machining
EGR	Exhaust Gas Recirculation
EPDM	Ethylene Propylene Diene Monomer
ERTRAC	European Road Transport Research Advisory Council
ETC	Electric Turbo Compound
EV	Electric Vehicle
FPLA	Free Piston Linear Alternator
HA	Halbach Array
HDV	Heavy Duty Vehicle
I/O	Input/Output
ICE	Internal Combustion Engine
IEC	International Electrotechnical Commission
IHX	Internal Heat Exchanger
IPC	Industrial Personal Computer

LDP	Left Dead Point
LDV	Light Duty Vehicle
LMA	Linear Motor/alternator
MPC	Model Predictive Control
MTC	Mechanical Turbo Compound
ORC	Organic Rankine Cycle
PMSM	Permanent Magnet Synchronous Motor
PTFE	PolyTetraFluoroEthylene
RDP	Right Dead Point
RMS	Root Mean Square
SRC	Steam Rankine Cycle
TEG	Thermo-Electric Generators
TLC	Thrilateral Cycle
VET	Variable Event and Timing
VVL	Variable Valve Lift
VVT	Variable Valve Timing

Greek Symbols

β	Coefficient of thermal expansion	1/K
β	Opening angle	rad
η	Efficiency, rate	–
γ	Ratio of the specific heats	–
κ	Thermal conductivity	$W/(m \cdot K)$
$\mathcal{T}$	Torque	$N \cdot m$
μ	Dynamic viscosity	$Pa \cdot s$
ν	Kinematic viscosity	m^2/s
Φ	Filling factor	–
ρ	Density	kg/m^3

ρ	Electrical resistivity	$\Omega \cdot$ m
σ	Electrical conductivity	S/m
φ	Angle of rotation	rad
e	Angular acceleration	rad/s^2

Roman Symbols

$\dot{m}$	Mass flow	kg/s
$\dot{Q}$	Heat transfer rate	kW
a	Intersection length	m
b	Intersection width	m
c_p	Specific heat at constant pressure	J/(kg $\cdot$ K)
c_V	Specific heat at constant volume	J/(kg $\cdot$ K)
D	Diameter	m
F	Force	N
f	Frequency	Hz
f	Friction coefficient	–
Fa	Fanno parameter	–
Gr	Grashof number	–
h	Heat transfer coefficient	–
h	Specific enthalpy	J/kg
I	Current	A
I	Moment of inertia	kg $\cdot$ m^2
K	Motor constant	N^2/W
k	Thermal conductivity	W $\cdot$ K/m
L	Length	m
M	Mach number	–
m	Mass	kg
n	Amount	–

Nu	Nusselt nuber	–
P	Power	W
p	Pressure	Pa
Pr	Prandtl number	–
R	Resistance	Ω
r	Ratio	–
Re	Reynolds number	–
S	Area	m^2
S	Seebeck coefficient	–
s	Specific entropy	J/(kg · K)
t	Time	s
V	Volume	m^3
v	Velocity	m/s
x	Linear coordinate	m
y	Tangential coordinate	m
ZT	Figure of merit	–

Subscripts

ν	Viscous
τ	Tangential
a	Available
acc	Acceleration
act	Actual
adm	Admitted
alt	Alternator
avg	Average
bv	Built-in volume
c	Coulomb

$cond$	Condenser
$corr$	Corrected
$crit$	Critical
cte	Constant
Cu	Copper
$cycle$	Cycle
cyl	Cylinder
d	Displacement
dec	Deceleration
dis	Discharge
e	External
$elec$	Electronics
em	Electromagnetic
$evap$	Evaporator
exp	Expander
fr	Friction
H	Hydraulic
hi	Higher
in	Inner
$iron$	Iron
is	Isentropic
$left$	Left
lo	Lower
$long$	Long
$loss$	Losses
$lump$	Lumped
max	Maximal

$mean$	Mean
$mech$	Mechanical
min	Minimal
mp	Most probable
N	Normal
nom	Nominal
o	Offset
$open$	Opening
opt	Optimal
out	Outer
$over$	Over
$port$	Port
$power$	Power
ps	Piston
$pump$	Pump
r	Required
$right$	Right
rot	Rotor
S	Stribeck
s	Isentropic
sen	Sensor
$short$	Short
$size$	Size
$slot$	Slot
str	Stroke
su	Supply
$surf$	Surface

$theor$	Theoretical
top	Top
$tran$	Transducer
tri	Triangularity
und	Under
vol	Volumetric
wh	Waste heat

Nederlandse samenvatting

De voortdurend groeiende wereldwijde economie vereist elk jaar een steeds grotere hoeveelheid energie. Tijdens de vorige eeuw werd dit probleem grotendeels aangepakt door intensieve exploitatie van grondstoffen. De inspanningen om de efficiëntie van thermische machines te verbeteren, werden voornamelijk gestimuleerd door economische overwegingen. In de laatste decennia echter, naarmate het bewustzijn toenam voor de gevaren van een onomkeerbare klimaatverandering als gevolg van CO_2-emissies, hebben technologieën die gericht zijn op het verminderen van emissies een nieuwe impuls gekregen. Deze technologiën waren in het verleden bekend maar niet economisch haalbaar.

Thermische reststromen zijn typisch gas- en vloeistofstromen bij temperaturen die nutteloos zijn voor een industrieel proces. Daarom worden ze beschouwd als restwarmte en gedissipeerd naar de omgeving. De organische Rankine cyclus (ORC) biedt de mogelijkheid om laagwaardige thermische energie door middel van Elektriciteitsproductie te valoriseren. De grootste uitdaging voor ingenieurs is om een systeem te ontwikkelen dat reageert op een sterk fluctuerende restwarmtestroom en toch een maximaal vermogen behoudt.

Dit doctoraat richt zich op kleinschalige ORC's die worden gebruikt als secundaire cycli voor interne verbrandingsmotoren (ICE) van vrachtwagens. Naast de juiste keuze van een werkingsfluidum en de cyclusarchitectuur, is het ontwerp van de expander de sleutel tot succes. Omdat de rijomstandigheden voortdurend veranderen, zal het motorvermogen niet constant zijn. De werkdrukken en de massadebiet van een dergelijke ORC-machine zullen snel en in een breed bereik veranderen als gevolg van fluctuerende restwarmtebronparameters, die de controller van een ORC moet volgen. De expander moet onder deze omstandigheden efficiënt kunnen werken om de thermodynamische prestaties van het systeem te maximaliseren. Dit kan gerealiseerd worden door het aanpassen van de frequentie en de ingebouwde volumeverhouding (BVR) van de expander aan de vereiste expansieverhouding van de werkmedium.

De keuze voor een volumetrische machine wordt ingegeven door relatief hoge expansieverhoudingen die worden verwacht voor deze toepassingen. Verder kan de BVR van een zuiger-expander eenvoudig worden ingesteld door middel van kleptiming. Deze aanpak wordt al tientallen jaren gebruikt voor ICE's. In de meeste gevallen worden schotelkleppen gebruikt, maar er is een alternatief dat men een schuifklep noemt. Omdat een schotelklep ruimte nodig heeft om in de werkkamer te bewegen, is zeker dood volume onvermijdelijk. Een schuifklep is vrij van dit conceptueel nadeel, hierdoor kan het dode volume aanzienlijk verminderd worden

en kan de volumetrische efficiëntie toenemen, vooral bij hoge volumeverhoudingen.

Er is nog een feature dat gebruikt wordt om het definitieve ontwerp van de expander te vereenvoudigen. Een directe verbinding van de zuiger met een lineaire motor/alternator (LMA) elimineert de noodzaak van een krukmechanisme dat typisch wordt gebruikt om de lineaire beweging in rotatie te transformeren. Verder, aangezien de zuiger een cilindrische vorm heeft, kan deze rond zijn as roteren, wat de optie biedt om een extra vrijheidsgraad te gebruiken voor de werking van de kleppen, vergelijkbaar met de manier waarop deze wordt gerealiseerd in schuivenmotoren.

Door de bovengenoemde technieken te combineren, is een ontwerp voor een nieuwe expansiemachine ontwikkeld en gepatenteerd. Er is slechts één bewegend onderdeel in deze machine, namelijk de zuiger zelf. De kleppen die de inlaattiming definiëren, zijn geïntegreerd in de zuiger en de behuizing. De lineaire alternator wordt ook gebruikt als een servomotor om de kleppen te bedienen. Magneten zijn bevestigd aan de binnenwand van de hulszuiger die werkt als een rotor en translator, de statorwikkelingen zijn ingebed in de behuizing en vormen samen met de zuiger twee werkkamers.

Om de testopstelling te dimensioneren, werd een mechanistisch model ontwikkeld. Dit model omvat alle krachten die op de zuiger werken en zijn beweging bepalen. De meeste aandacht werd besteed aan de gaskracht. De drukverandering in de werkkamer wordt bepaald door verschillende factoren, zoals het profiel van de zuigerbeweging, warmteoverdracht en lekkagestromen. Dit laatste wordt in detail bestudeerd. De lekpaden worden geïdentificeerd en gemodelleerd. De massadebieten kunnen berekend worden als een functie van de padlengte en het drukverschil. Een robuuste berekeningsmethode die geen iteraties vereist en die dus een vaste rekentijd heeft, werd ontwikkeld. Dit is cruciaal voor realtime regeling van de zuigerbeweging.

Het model wordt gevalideerd door middel van een testopstelling. De lineaire beweging en de rotatie werden gescheiden om de studie van beide te vereenvoudigen. Standaard industriële hardware en software werd gebruikt om de motoren te bouwen en te besturen. De eerste experimenten hielpen de meest significante problemen te onthullen, zoals wrijvingsschade van de zuiger als gevolg van onvoldoende uitlijnings- en positioneringsfouten veroorzaakt door een onvermogen van de standaard controller om het vereiste bewegingsprofiel te realiseren. Het mechanische ontwerp werd aangepast en de volgende fase van de experimentele campagne was gericht op motion control en de synchronisatie van de rotatie van de zuiger met de translatie omdat deze essentieel is voor de timing van de inlaat.

Er is gekozen voor een model predictive control, in plaats van een standaard PID om de positionering van de zuiger te verbeteren. Wrijvings- en kleefkracht werden experimenteel geïdentificeerd en opgenomen in het model. Aangezien alle op de zuiger inwerkende krachten zijn gedefinieerd, kan een feedforward kracht die door de LMA moet worden geleverd om de zuiger aan te zetten om de gewenste beveingsprofiele te volgen, in real time berekend worden. De correctie van onvermijdelijke fouten wordt gerealiseerd door een controller die de positieterug-

koppeling gebruikt en een beperkte extra kracht produceert.

Ook werd een onderzoek uitgevoerd naar het optimale bewegingsprofiel binnen het maximale LMA-efficiëntie bereik. Hoewel experimentele gegevens en methoden voor de efficiëntie van rotatiemachines algemeen beschikbaar zijn, is er een gebrek aan die voor lineaire machines. De grootste moeilijkheid is dat een lineaire motor slechts een constante snelheid kan bereiken gedurende een zeer korte tijdsperiode, wat soms onvoldoende is om de metingen uit te voeren. De voorgestelde methode voor het inschatten van de LMA-efficiëntie maakt het mogelijk het meest efficiënte bereik van de zuigersnelheid te identificeren in functie van de belasting.

Naast de doeltoepassing van de ORC zijn er ook andere opties mogelijk. Het voorgestelde apparaat kan fungeren als een expander of een compressor van een warmtepomp (HP). De bedieningsmodus kan on the fly veranderd worden door de draairichting te wijzigen. Daarom kan deze machine gebruikt worden in hybride HP/ORC-installaties. Een circulatiepomp kan in de expander geïntegreerd worden, maar de invloed van de warmtewisseling tussen de pomp en de expander en de invloed hiervan op de efficiëntie van de cyclus en een cavitatieprobleem moeten worden bestudeerd.

Ten slotte, zijn de volgende mogelijke stappen in de ontwikkeling van het voorgestelde concept geformuleerd. Een realistisch prototype met een geïntegreerde LMA kan worden gebouwd op basis van de lessen die tijdens deze studie zijn getrokken. De haalbaarheid van een geïntegreerd ontwerp is bewezen. De vorm van de in- en uitlaatpoorten moet worden geoptimaliseerd om de smoorverliezen en lekkages tot een minimum te beperken en de volumetrische efficiëntie te verbeteren. De bekomen resultaten laten zien dat het voorgestelde concept in de toekomst zal kunnen concurreren met bestaande systemen en in de praktijk kan worden toegepast.

English summary

The continuously growing economy worldwide requires an increasingly large amount of energy each year. During the last century, this problem has been tackled mostly by intensive exploitation of natural resources. The effort to improve the efficiency of thermal machines was stimulated primarily by economic considerations. However, as awareness of the dangers of irreversible climate change due to thermal and CO_2 emissions has increased, technologies focused on the reduction of those emissions, well known but economically unfeasible in the past, have gotten a new boost in the last decades.

Thermal emissions are typically gas and liquid flows at temperatures useless for the process at hand. Therefore, they are considered waste heat and often discharged to the environment. The organic Rankine cycle (ORC) technology provides a possibility of low grade thermal energy valorization by means of electricity production. The main challenge for engineers is to develop a system reacting to an unsteady waste heat flow and maintaining a maximum of power output.

This study is focused on small-scale ORCs used as bottoming cycle for internal combustion engines (ICE) of trucks. Beside the right choice of a working fluid and the cycle architecture, the design of the expansion device is the key to success. As road conditions continuously change, the engine power will not be constant. The working pressures and the mass flow rate of such an ORC machine will change quickly and in a wide range due to fluctuating waste heat source parameters, which the ORC controller needs to follow. The expander must be able to operate efficiently under these conditions maximizing the thermodynamic performance of the system. This can be done by adjusting the working frequency of the expander and by matching its built-in volume ratio (BVR) with the required expansion ratio of the working fluid.

The choice of a reciprocating machine is dictated by relatively high expansion ratios expected for target applications. Furthermore, the BVR of a piston expander can be easily adjusted by means of valve timing. This approach has been used for ICEs for decades. In most cases, poppet valves are used, however there is an alternative called a sleeve valve. Since a popped valve needs space to move inside the working chamber, some dead volume is unavoidable. A sleeve valve is free of this conceptual drawback, so the dead volume can be significantly reduced and the volumetric efficiency increased, especially at high volume ratios.

One more feature is used to simplify the final design of the expander. A direct connection of the piston to a linear motor/alternator (LMA) eliminates the need for a crank mechanism which is typically used to transform the linear motion into

rotation. Furthermore, since the piston has a cylindrical shape, it can rotate around its axis, which gives the option to use an additional degree of freedom for the valves' operation similar to the way it is realized in sleeve valve engines.

By combining the aforementioned techniques, a design for a novel expansion machine has been developed and patented. There is only one moving part in this machine, namely the piston itself. The valves defining the intake timing are integrated into the piston and the housing. The linear alternator is also used as a servo motor to operate the valves. The magnets are attached to the inner wall of the sleeve piston acting as a rotor and translator, the stator coils are embedded into the housing and together with the piston form two working chambers.

In order to size the test setup, a mechanistic model was developed. This model includes all forces acting on the piston and defining its motion. Most attention was payed to the gas force. The pressure change in the working chamber is defined by various factors such as the piston movement profile, heat transfer and leakage flows. The latter is studied in detail. The leakage paths are identified and modeled. The mass flow rate can be calculated as a function of the path length and the pressure difference. A robust computation method requiring no iterations, and which is therefore time-certain, was developed. The time-certainty is crucial for real-time control of the piston motion.

The model is validated by means of an experimental test setup. The linear motion and the rotation were separated in order to simplify the study of both. Standard industrial hardware and software was used to build and to control the motors. The first experiments helped reveal the most significant problems such as frictional damage of the piston due to insufficient alignment and positioning errors caused by an inability of the standard controller to realize the required motion profile. The mechanical design was adjusted and the next phase of the experimental campaign was focused on motion control and the synchronization of the piston rotation with the translation since it is critical for the intake timing.

A model predictive control approach was chosen instead of a standard PID to improve the piston positioning. Frictional and cogging forces were identified experimentally and included into the model. Since all forces acting on the piston are defined, a feed forward force which must be provided by the LMA to impel the piston to follow the desired trajectory can be calculated in real time. The correction of unavoidable errors is realized by a controller using the position feedback and producing a limited additional force.

Also, a study on the optimal motion profile within the maximum LMA efficiency range was performed. While experimental data and methods on rotational machines efficiency are widely available, there is a lack of those for linear ones. The major difficulty is that a linear motor can only reach a steady speed for a very short period of time, sometimes insufficient to perform the measurements. The proposed method of estimation of LMA efficiency allows to identify the most efficient range of the piston speed in function of the load.

Beside the target applications, other options are possible. The proposed device can act as either an expander or a compressor of a heat pump (HP). The operation mode can be changed on the fly by altering the rotation direction. Therefore, this

machine can be used in hybrid HP/ORC installations. A circulation pump can be integrated into the expander, however the influence of the heat exchange between the pump and the expander and its influence on the cycle efficiency as well as a cavitation problem must be studied.

Finally, the next possible steps in the development of the proposed concept are formulated. A realistic prototype with an integrated LMA can be built based on the lessons learned during this study. The feasibility of an integrated design is proven. The shape of the in- and outlet ports needs to be optimized in order to minimize the throttling losses and leakages and to improve the volumetric efficiency. The obtained results show that the proposed concept will in the future be able to compete with existing systems and be implemented in practice.

1
Introduction

In this chapter, the organic Rankine cycle (ORC) technology is analyzed as a possible solution to increase the efficiency of an internal combustion engine (ICE). The growing amount of truck sales in Europe urges the necessity of lowering the fuel consumption and strengthening emissions requirements in order to prevent heavy air pollution in the EU. An ORC as a bottoming cycle to the ICE is a viable solution. A smaller power ICE in combination with an ORC unit based on a similar technology can provide the same power with a lower emission level and smaller fuel consumption. By taking into account a strongly variable waste heat flow of an ICE, a variable volume ratio expander is needed in order to gain maximum work from the expansion process. Valve mechanisms providing a possibility to optimize the expansion ratio are analyzed.

1.1 Background

The European transport sector is mostly represented by vehicles which are driven by combustion engines consuming oil derivatives such as gasoline and diesel fuel. The fact that Europe has to import up to 84 % of oil [1] urges a shift from petrochemical fuels toward carbon-free or CO_2-neutral ones. The aim of the Commission's Transport 2050 Strategy is to break EU transport's dependency on oil. The strategy implies among other things the greenhouse gas emissions reduction as low as 60 % by 2050 [2]. The irreversible shift to a low CO_2 emission mobility requires an introduction of less-energy consuming cars on the market next to an alternative fuel infrastructure.

On the other hand, the economics demands more transportation facilities and stimulates the growth of vehicles production. The worldwide amount of trucks sales in 2014 was about 2.4 million and 3.4 million per year is expected by 2024 which means the average annual growth of more than 3 % in the global truck market, mostly in the US and the EU and especially in East Europe: 10 % [3]. As Figure 1.1(a) illustrates, 462.000 trucks would be sold in EU, wherein 62 % new vehicles as is depicted in Figure 1.1(b). Assuming all new trucks would be electric, about 115–172 GW of additional generating capacity would be needed each year. This is quite challenging, taking into account the current total of the installed electricity capacity: 1030 GW in 2015, wherein 441 GW is generated from fossil fuels [4].

Disregarding the promotion of electric traction, electric vehicles (EV) are far from overtaking the ones with ICE. The total amount of registered on-road vehicles in the world broke through a psychological mark of one billion in 2010 and is now estimated around 1.4 billions [5]. A historical milestone of one million registered EV was reached in 2015 which is less than 0.1 % of the total amount. This tiny niche is expected to be extended up to 150 millions of EV by 2040. However, the total amount of on-road vehicles will also increase up to 2 billions, so the fraction of EV will remain very small. Moreover, the implementation of electric traction is mostly focused on light duty vehicles (LDV) with a relatively low fuel consumption, so the gain in terms of oil substitution and CO_2 emissions will be even less remarkable. Also, those analysis do not include off-road vehicles and long-haul ships where the implementation of electric power is more difficult since a high power density and autonomous operation for a long period is required.

Electric traction remains in a pre-mature stage not only because of the necessity of additional electricity generation for new electric vehicles but also because of a significantly longer recharging time in respect to a conventional refueling time. So ICE adjusted to new carbon-free or CO_2-neutral fuels will most likely dominate in the sector of heavy duty vehicles (HDV) in the short and mid-term prospective.

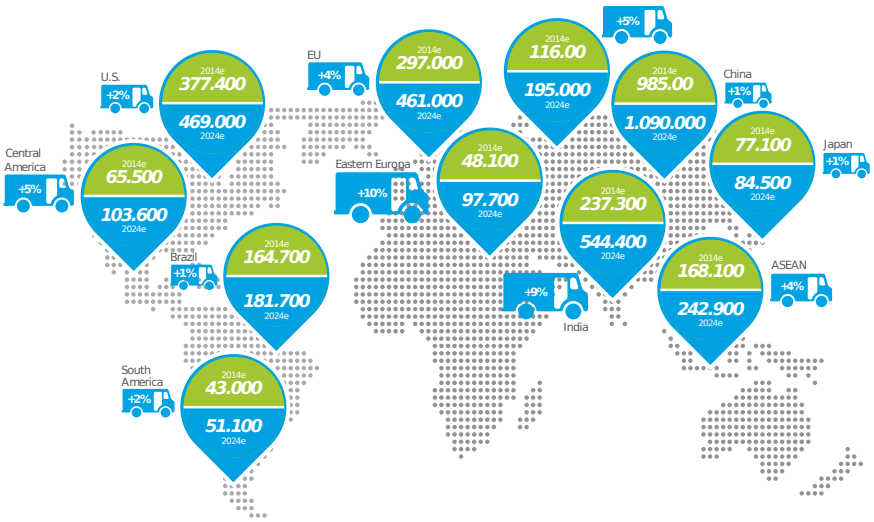

(a) Segments expected to show the strongest increase in sales volume.

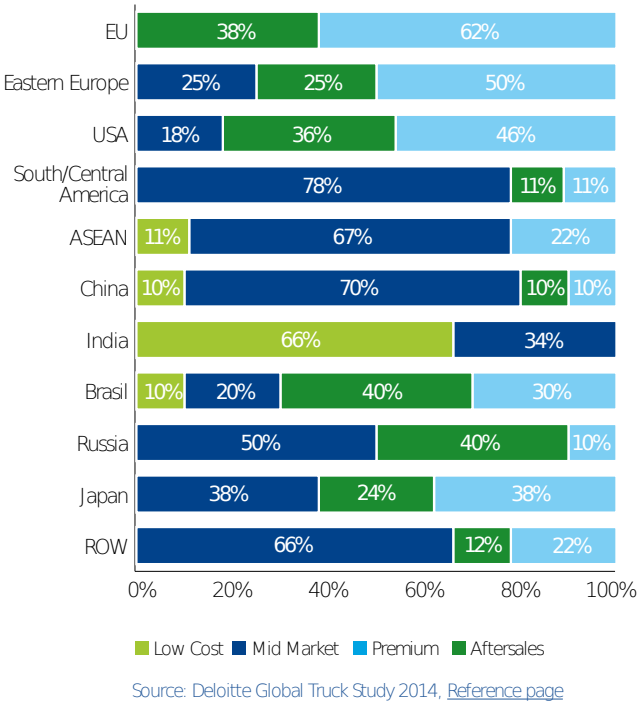

(b) Expected increase in sales volume per region.

Figure 1.1: World truck market overview. Source: [3].

1.2 Potential improvements on engine efficiency

Continuously increasing requirements for the internal combustion engines efficiency and CO_2 emissions stimulate the improvement not only of engines as such but also of technologies for heat recovery from the exhaust gases, providing a possibility to increase the overall engine efficiency.

This can be done in different ways: (i) by using residual energy of the exhaust gas in form of pressure by expanding the gas through an additional turbine; (ii) by using the thermal energy of the gas transforming it into electricity by means of thermo-electric generators (TEG) (iii) by employing thermal machines such as ORCs to convert the thermal energy into mechanical or electrical power. These technologies can also be combined providing a maximum gain for the waste heat recovery. As shown in Figure 1.1(b), the sales increase in Europe and USA is expected in a segment of advanced and featured trucks. This represents a great opportunity for heat recovery technologies to be considered as an option.

1.2.1 Turbo compound

Exhaust gases leave a combustion chamber at a certain pressure, typically, 1.5–2.5 bar, which means there is still recoverable energy left. This energy is in most cases used to drive a turbo charger. However, even after that, the pressure is still higher than the ambient. If the gas is further expanded through an additional turbine or a volumetric machine, the obtained mechanical power can be coupled to the engine crankshaft. By using the mechanical turbo compound (MTC) technology, up to 5 % of the fuel energy can be saved or up to 10 % of the engine peak power output increase achieved [6].

One of the limiting factors in implementation of this technology is that the outlet pressure of the turbocharger must be higher than the pressure losses through the exhaust which consist of a diesel particulate filter (DPF), a muffler etc. causing a certain pressure drop. However, this requirement cannot always be met, especially at part load. If a turbo compound is not bypassed in this case, the turbo charger's efficiency will drop leading to a lower total efficiency of the power train [7, 8].

Another issue of this technology is the quite different turbine and the crank shaft rotational speeds: 70,000 rpm and more for a turbine and around 2,000 rpm for the crankshaft. In order to couple a turbo compound to the crankshaft, a gearbox is required as depicted in Figure 1.2 on the left side. Furthermore, a turbine typically operates in a narrow high-efficiency region of rotational speeds while the engine speed can widely fluctuate under variable load or road conditions. A continuously variable transmission (CVT) can be implemented in order to provide the necessary flexibility for the optimization of the whole power train but it has a lower mechanical efficiency and a higher complexity than a gearbox [9].

In order to avoid the complexity of the coupling to the engine, an electric turbo

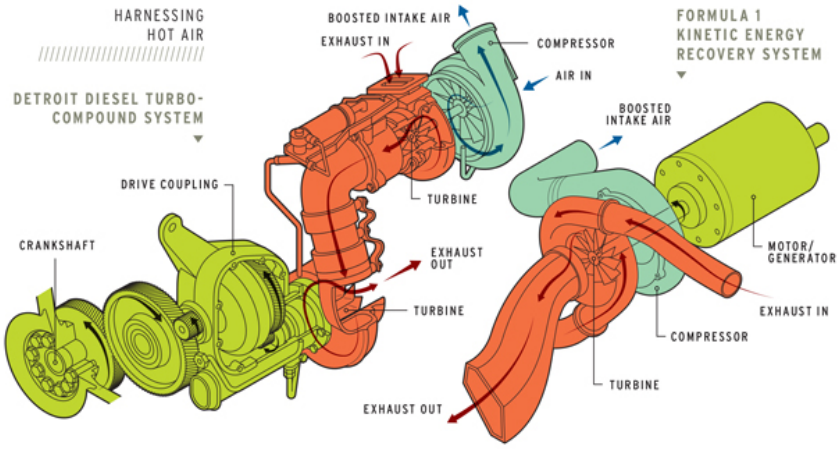

Figure 1.2: Mechanical end electric turbo compound.
Source: `http://blog.caranddriver.com`.

compound (ETC) can be used. In ETC, the turbine drives an electric generator as is shown on the right side in Figure 1.2. The produced electricity can be used for an auxiliary equipment or integrated with an hybrid engine. Several models of ICE with ETC are available [10, 11]. The results presented by the authors confirm a significant improvement of the engine's global efficiency in terms of a lower fuel consumption and CO_2 emissions. The same approach is recommended for the heavy duty diesel engines optimization.

1.2.2 Thermoelectric generators

The working principle of a thermoelectric generator (TEG) is based on the Seebeck effect: the electricity production across the junction of two different metals if one side of the junction is exposed to the heat and another one is cooled [12]. Metals can be substituted by *n*- and *p*- type semi-conducting materials connected in series and staked between two thermally conductive plates, which are, in turn, attached to the heat source and the heat sink as is shown in Figure 1.3. The higher the temperature difference between these plates, the more electricity can be generated [13].

The thermoelectric efficiency of a TEG is defined by the dimensionless figure of merit which is depicted in Figure 1.4 for several thermoelectric materials:

$$ZT = \frac{S^2 \sigma T}{\kappa}, \tag{1.1}$$

where S is the Seebeck coefficient, σ is the electrical conductivity, T is the abso-

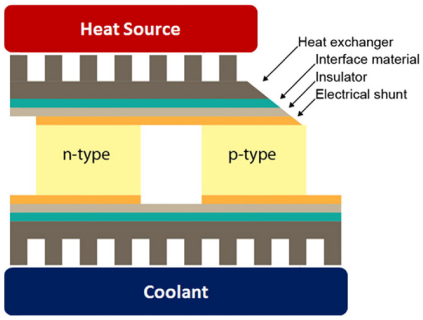

Figure 1.3: Thermoelectric generator schematics. Source: [13].

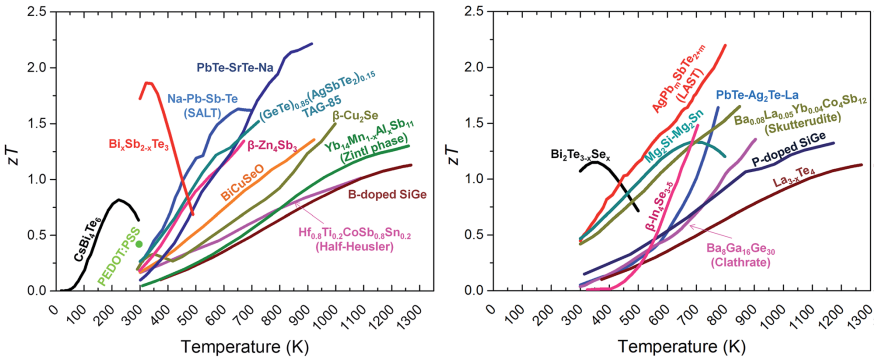

(a) p-type materials (b) n-type materials

Figure 1.4: Figure of merit for the best thermoelectric materials. Source: [16].

lute temperature, and κ is the total thermal conductivity. The relationship between the figure of merit and the energy conversion efficiency is explained in [14] and is simulated by [15].

The experiments on the TEG efficiency improvement and manufacturing costs reduction are still ongoing. The major efforts are made in development of new materials, increasing the density of semi-conductor elements per unit and matching the heat source cooling profile with the appropriate TEG materials [17]. Also a properly integrated TEG implemented as a stand-alone unit can save the total costs of the system [18, 19].

TEGs have been used from the second part of the twentieth century on, mostly in space applications for flights to distant planets when photo-voltaic technology can not provide enough power. Remote terrestrial applications are also known, for example as radio beacons, sensing and radar stations and unmanned lighthouses. The main advantage of TEG is the absence of any moving parts which makes these

Waste heat source	**Typical temperature** °C	**Available power** kW
Tail pipe	312	51.2
Exhaust gas recirculation (EGR)	454	15.9
Hot air after the compressor of a turbocharger	95	15
Jacket coolant and lubricating oil	90	89.5

Table 1.1: Available waste heat flows of a heavy-duty long haul truck at a cruise point. Source: [28].

devices extremely robust and sustainable. However, for a relatively efficient operation of TEGs, high temperatures are required: 800–1000 °C which is typically provided by a radioactive material. Even under these conditions the system's efficiency does not exceed 10 % (15 % is expected in the near future) and specific power of about 8 W/kg, as reported by [20]. The temperature of the exhaust gas is typically lower, especially at a low engine load. This makes the implementation of TEG economically unattractive in a short time prospective.

1.2.3 Bottoming cycles

It is well-known that any thermodynamic power cycle can potentially be used as a bottoming cycle of an ICE or a gas-turbine given the fact that the temperature difference between the heat source and the heat sink is sufficient to provide a noticeable power output in order to justify the expenses of an additional power unit. steam Rankine cycle (SRC), Stirling and Brayton or air bottoming cycle (ABC) cycles [21–24], Maisotsenko combustion turbine cycle (MCTC) are analyzed and compared by [25] and used [26]. Among others, ORC is a frequently considered candidate [27]. However, the sizing of an ORC for a truck engine is not a trivial task because of difficulties in defining a design point at fluctuating exhaust gas temperature and the mass flow rate. The waste heat flows which can be identified are listed in Table 1.1.

The last two options can hardly be considered as viable because of their low temperature. Moreover, if the exhaust heat is valorized by ORC, the condenser heat must be rejected at nearly the same temperature level. This issue requires a special attention in the case of ORC deep integration into a truck engine [29].

There are multiple publications about possibilities of cascading the waste heat input, for instance, by using the jacket heat for working fluid preheating and the exhaust gas for evaporation [30, 31]. This is actually a substitution of a regenerator by a preheater which is, from thermodynamical point of view, at least equivalent.

Sensible heat dissipation to the ambient means the use of gas-to-gas heat exchanger instead of a more compact liquid-to-gas conventional radiator. The jacket heat in this case is not dissipated in a classic way directly to the ambient but through the ORC cycle which requires an additional amount of working fluid to be pumped within the cycle. In addition, the insertion of a preheater or a regenerator before the evaporator prevents the exhaust gas to be cooled down to the engine jacket temperature, which means lower energy utilization.

This idea is similar to a jacket waste heat recovery by means of a SRC from large marine diesel engines. The main difference is that in SRC steam is not superheated after expansion, so there is no sensible heat to recover and preheating does make sense.

While the sector of commercial trucks still remains a difficult niche for the ORC, small tug boats and long haul ships provide more space and flexibility for ORC integration. From the practical point of view, the use of the same machinery technologies for the ICE and the ORC sounds logic, for example by dedicating one of the cylinders for ORC [32]. However, in this case, the loss of an ORC working fluid and its contamination by combustion products through the common carter is unavoidable so this technology still needs some serious improvements.

If implemented on an ICE, the organic Rankine cycle could recover thermal energy from the exhaust gases, which amounts to about 35 % of the energy provided by the fuel. This estimation is based on the assumption that the exhaust gas is cooled down to the ambient temperature. Considering a typical net efficiency of at least 23 % for the ORC under the given conditions, the fuel consumption of an ICE at maximum load can be reduced by 8–10 %. Even higher results are reported and listed in a comprehensive overview of the ORC technology for heavy duty diesel engines [33]. However, lowering too much the gas temperature can lead to acid condensation formation if sulphur-containing fuels are used.

The expected fuel consumption benefits for heavy duty (HD) and light duty (LD) vehicles by means of waste heat recovery technologies are studied by the European Road Transport Research Advisory Council (ERTRAC) and summarized in Table 1.2 [34]. The ORC shows the best potential among the technologies mentioned above so, as such the current study is focused on this and similar technologies.

1.3 Expander as ORC key component

Large scale ORC plants with nominal power higher than 500 kW use turbine technology to expand the working medium. A turbine is smaller in size than a volumetric machine of the same power, the maintenance is cheaper and the reliability is higher. A generator is typically directly connected to the grid since a large turbine can be designed for a matching rotational speed. The lower the shaft power,

Technology	LD benefit, %	HD benefit, %
Organic Rankine Cycle	3–5	4–6
Thermoelectric Generators	2–4	1–2.5
Turbocompounding	1–3	1–3

Table 1.2: Expected ICE fuel consumption benefits for light duty (LD) and heavy duty (HD) vehicles. Source: [34].

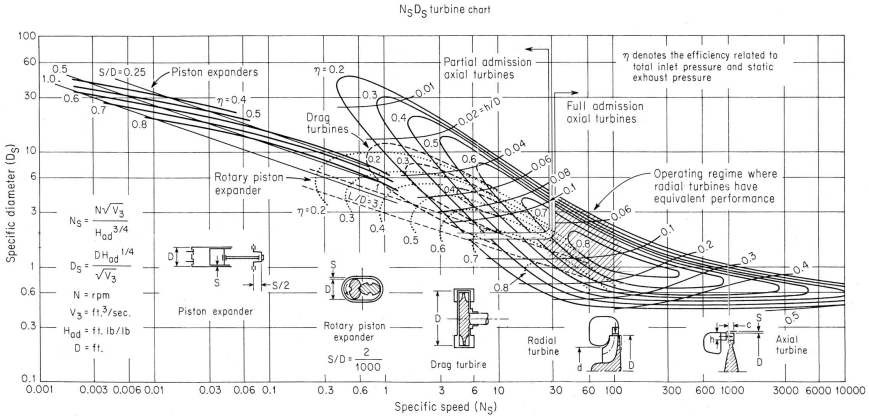

Figure 1.5: Expander specific speed and specific diameter diagram. Source: [35].

the higher the rotational speed of the turbine must be, this relationship is depicted in Figure 1.5. At a certain power level, the efficiency of a slow speed turbine becomes unacceptably low and the manufacturer needs to make a choice: either to use a gearbox or a regenerative inverter to decouple the turbine rotational speed from the grid. Both solutions have disadvantages preventing them from a wider use in medium-scale power plants, namely additional investments and higher losses. Power electronics for such a high power level are rather expensive.

1.3.1 Volumetric expanders

Expansion devices used in small- and medium scale ORC installations are typically reversed compressors or derived from combustion engines. The use of off-the-shelf components has the advantage of a lower investments and operational costs since such machines only need minimum adjustments in order to be used in ORC installations. Furthermore, the maintenance can be performed using the same routines and spare parts. Turbine technology is still present in the range of 50–500 kW (Turboden, Tri-O-Gen, Calnetix) but below 50 kW, the use of volu-

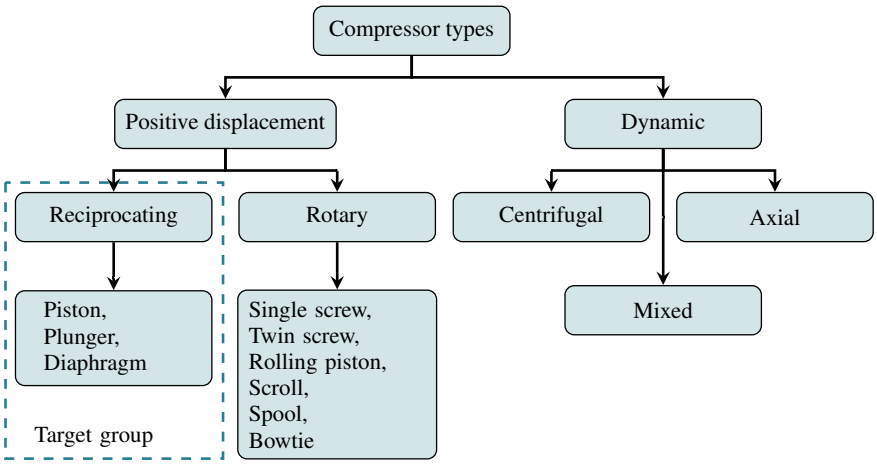

Figure 1.6: Compressors which can be used as expanders.

metric machines becomes more interesting. First of all, this is the range typical for refrigeration — a very mature niche where the technologies have been constantly improved for several decades. So, it is no wonder that the first small-scale ORC installations have been built using adjusted scroll compressors with a removed check valve in order to reverse the flow.

Single- and twin screw expanders originate from compressed air production. Compressors, from which these expanders are derived, do not need thorough adjustments, only shaft and housing seals can be eventually changed for a better compatibility with a working fluid. A general overview of compressor technologies useful for ORC applications is schematically shown in Figure 1.6. Additionally, a comprehensive review of working fluids and methods for the expander selection for the use in ORC installations can be found in [36].

1.3.2 Free-piston technology

The current study is focused on reciprocating machines because of its ability to handle high and widely variable pressures. As a further development, the free-piston technology was proposed several decades ago. The use of a linear alternator directly connected to a piston eliminates the crankshaft mechanism and results in a compact lightweight engine suitable for hybrid cars. Also, there are no limitations such as volume in function of the crankshaft angle, which allows to optimize the expansion profile for maximum power output. A very valuable input is yielded by researchers from the automotive sector. Various companies have put a lot of effort into developing free-piston combustion engines [37–40].

In order to quantify potential benefits of using the free-piston technology, Jia

et al. [41] performed a theoretical comparison of frictional losses in free-piston and crankshaft engines with comparable indicated power. The authors assumed the losses of the valve train systems equal and simulated only the gain of using a free-piston system, which is indicated to be about 5.5 % or nearly half of the reference.

1.4 Built-in volume ratio

Since refrigeration or air compressors are well known energy consumers in the industry, many efforts have been made to improve their energy efficiency. This experience is also valuable for expanders derived from these compressors. Ideally, after the compression or the expansion process, the pressure in the working chamber must be equal to the pressure in the discharge line. If this is not the case, the pressure equalization at the discharge reduces the overall system efficiency.

With other words, the ratio of the supply and discharge volume flows of the machine must be matched with these of the system. The term âĂIJvolume ratioâĂİ can be defined as follows: the ratio of the volume of gas trapped at the beginning of the compression or expansion process to the volume of gas remaining in this closed chamber when it is connected to the discharge line.

Scroll and screw compressors are devices with a fixed geometry, and therefore with a fixed built-in volume ratio (BVR). Screw compressors, designed to operate under variable conditions, are equipped with a slide valve at the high pressure side [42]. This valve advances or retards the release of the compressed fluid allowing the pressure in the working chamber to equalize with the system pressure at the discharge line. When such a compressor is used in expander mode, the same valve controls the volume of the admitted working fluid, matching the built-in volume ratio with the system one. The same approach can be used for scroll machines [43].

Piston compressors, by their nature have a variable BVR. The discharge valve is actuated by the pressure difference. When the pressure in the working chamber exceeds the pressure in the discharge line, the valve opens releasing the compressed fluid. When such a compressor needs to be used as an expander, the discharge valve must be replaced by an externally actuated one since the pressure difference works against the valve in this case. This technology is implemented in ICEs, where poppet valves are mostly used.

1.4.1 Poppet valves

The main advantage of reciprocating expanders in comparison with other types of volumetric machines is the possibility to control the intake process within a very wide range, allowing the admission of the desired amount of fluid into the working chamber. The right management of the intake process of a reciprocating

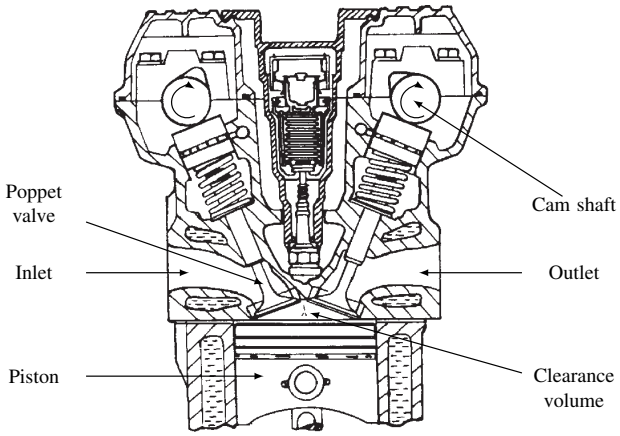

Figure 1.7: Typical arrangement of poppet valves. Source: [44].

machine is of great importance: in combustion engines, it defines the efficiency and emissions, in expanders — the volume ratio. Typical poppet valve design is shown in Figure 1.7.

Poppet valves are commonly actuated by a camshaft which is driven by the crankshaft through a chain, gears or a belt. Cam profiles define the valve movement during the engine operation. When a slight adjustment of the timing is needed, the cam sprocket can be rotated in the desired direction and then fastened. Although such adjustment is possible only during the engine maintenance, it would be useful if it could be realized dynamically in response to a variable load. In order to address this issue, several automotive companies introduced their variable valve lift (VVL) and variable valve timing (VVT) systems. The VVL extends or shortens the opening time, the VVT advances or retards it. As a further development, a variable event and timing (VET) technology was introduced providing a better flexibility in the expansion ratio.

An overview of the available camshaft based technologies including their classification and comparison can be found in [45]. The main drawbacks of the mentioned systems are the complexity and reduced reliability.

As an alternative solution, camless electrically actuated valves depicted in Figure 1.8, can be mentioned. Despite the fact this type of actuation provides quasi unlimited control on the inlet valve timing, the power consumption still remains the major issue preventing this technique to be widely implemented.

A valve train is one of significant sources of losses. Depending on the engine size and operation mode, the losses vary from 7 % to 15 % [46–48]. If a cam-actuation system is replaced, about 10 % of improvement in fuel economy can be achieved as reported by [49]. Authors also state that the control of the valves lift can bring 10 % more.

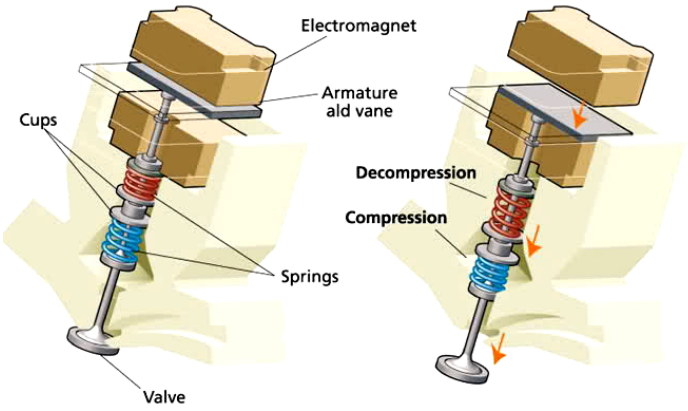

Figure 1.8: Electromagnetically actuated valves. Source: `www.valeo.com`.

1.4.2 The history of rotary and sleeve valves

The first attempt to replace a poppet valve with another system consisting of two surfaces with overlapping openings forming a gas passage has been taken in 1906 by Charles Y. Knight. He intended to reduce the noise produced by combustion engines at that time. The first working prototype was introduced in 1906 at the Chicago Auto Show, although it was not very successful.

Equipped with patented double-sleeve valves, driven by a separate crankshaft this system replaced a classic poppet valve train which made it possible to reduce the number of parts and to achieve a smooth and silent engine operation. Additionally, the maintenance interval was significantly extended since the sleeve valves did not suffer from problems typical for poppet valves at that time, such as carbonization, detuning and the so called "valve float" — valve lag at the closing phase at a high engine speed.

Later on, his engine, improved by Daimler engineers and called "Silent Knight" was introduced in Britain in 1909 and was in production until the mid 1930's. Regardless of the obvious advantages, there were also certain drawbacks: a relatively high oil consumption and hindered heat transfer through double-wall valves which, in addition to being casted iron, were fairly massive. The full story about the design and experiments on this engine can be found in [50].

Further development of the sleeve valve technology revealed the Burt-McCollum concept. A much simpler design and the improved manufacturing technologies brought Argyll (car manufacturing company) big success. Later, Harry Ricardo improved the valve actuation mechanism. The port shape is the result of extensive research and experiments aimed to obtain a maximum port area with a minimal sleeve travel as shown in Figure 1.9.

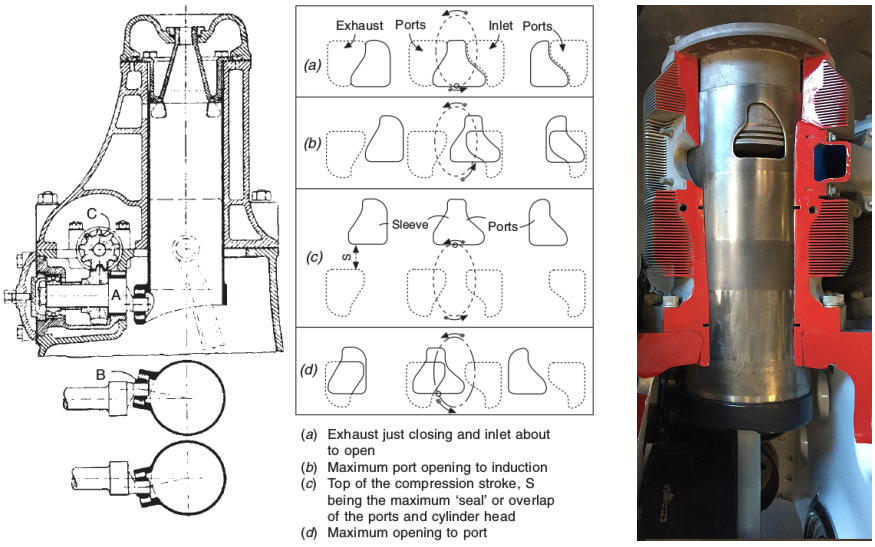

(a) Ricardo actuation mechanism. (b) Valve cut view.

Figure 1.9: Ricardo actuation mechanism for Burt-McCullum sleeve valve. Sources: [44], `www.meilleureimage.eu`.

Sleeve valve engines were also widely used in aviation: The Bristol Hercules 14-cylinder engine shown in Figure 1.9(b) was the first one designed in 1939 by Sir Roy Fedden and produced by the Bristol Engine Company which was installed on several types of aircrafts, mainly military ones during the Second World War and later on cargo aircrafts [51]. A comprehensive overview of the rotary valve technology can be found in [52].

When the problems of the first generation poppet valves were mainly solved, and piston engines in aviation were replaced by jet turbines, the sleeve valve design was abandoned for several decades. However, a certain interest in this technology is still present. Turner et al. [53] performed reverse engineering of a Bristol Centaurus engine cylinder set and simulated the motion in Siemens NX™[1] software in order to better understand sleeve valve timing concept. The authors compared the obtained model with an equivalent engine equipped with poppet valves and plotted the angle-area diagram for both. The maximum available area for the sleeve valve was found to be around 16 % larger for the exhaust and about 44 % larger for the intake valve in respect to the poppet ones. Furthermore, the air flow is not obstructed by the valve head as in the case of poppet design. Additionally, the closing and the opening of the sleeve valve is reported to be faster. As a result, a

[1] Siemens NX™ is a registered trademarks of Siemens Product Lifecycle Management Software Inc.

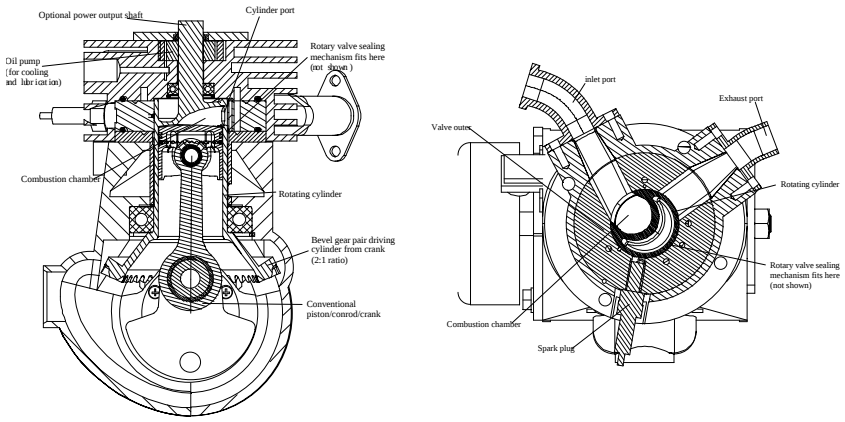

(a) Overall cross section (b) Cross section through valve area

Figure 1.10: Axial rotary valve design. Source: [54].

higher mass flow rate and lower throttling losses can be expected. Since the authors analyzed a solely reproduced design, the aforementioned characteristics can be further improved by means of modern simulation and design technologies.

1.4.3 Modern rotary and sleeve valve engines

The idea to find an alternative for a poppet valve remains actual as it would provide a smooth and noiseless operation, would reduce the amount of parts which potentially increase the reliability of the engine and reduce the costs.

A modern version of a rotary cylinder valve engine uses axial rotation for the port timing [54]. This engine looks very similar to the Aspin one but here the entire cylinder rotates about the axis of the piston driven by the crankshaft through a gear transmission as it can be seen in Figure 1.10. Regarding the position of the valve there are two major types:

- Rotary valve is coaxial with the piston (Figure 1.10).
- Rotary valve is placed transversal (Figure 1.11).

The use of rotary valves instead of poppet ones has been described by [55–57]. Peak torque of a rotary system is reported to be 40–50 % lower than of the poppet one [58]. This means a higher mechanical efficiency of the rotary system. Also, the rotary valve porting system allows 23–30 % higher peak volumetric flow rate due to a smoother path of the working fluid entering and leaving the cylinder.

The same improvements can be applied to piston compressors since the technologies and their design are similar to the ones used in ICEs. The discharge plate

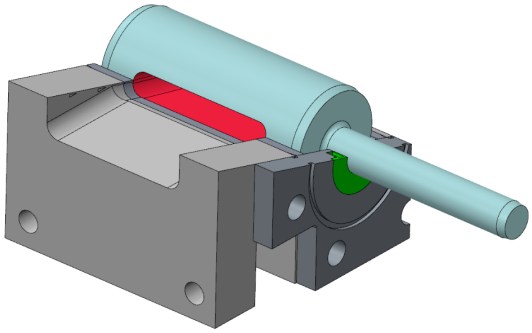

Figure 1.11: Transversal cylindrical rotary valve. Source: [55].

typically used in piston compressors is actuated by the pressure difference between the in-cylinder pressure and the discharge line. The associated over-compression varies from 1 to 2 bar as reported by [59, 60]. These losses are especially significant at low discharge pressures. By using a rotary valve, the discharge port can be opened when the in-cylinder pressure equalizes with the discharge one. In this way, the over-compression losses can be minimized. The same argumentation is applicable to the intake port.

Other interesting types of non-poppet engine valves are shown and discussed in [61]. A comprehensive overview of slide, rotary and piston valves and their comparison with poppet valves implemented in ICEs can be found in [62]. An overview with a description of the working principle of valves which can be implemented in compressors and expanders is provided by [63]. The comparison of the most current valve types is provided in Table 1.3 based on the study of [64].

1.4.4 ORC and rotary valves

Rotary valves can be implemented easier in ORC expanders than in the ICE because there is no oil burning problem, since typical temperatures of ORC expanders are not higher than the practical limit of lubricant oils. Also, no combustion product settling can be expected. At this point, the operation of an expander is comparable with the one of an air compressor. Because of relatively low temperatures, the same oil types can be used. Alternatively, high temperature non-reactive, non-flammable, and long-lasting fluorinated synthetic oils, such as Krytox®[2], can be considered.

[2] Krytox® is a registered trademark of E.I. du Pont de Nemours and Company.

	Poppet valve	**Rotary valve**
Advantages	• The leakage flow is quasi zero when closed. • The flow rate is high due to a large surface area when opened. • No sticking. • The response time is fast and predictable.	• Smooth and quasi noiseless operation due to a continuous steady motion. • Fewer amount of moving parts, potentially reducing manufacturing and maintenance costs and increasing the reliability. • High volumetric efficiency due to wide and straight gas passage and the absence of dead volume. • Reduced engine height, allowing a higher power density. • Ball or flat disk valve can be easily sealed by a single round ring. • Sleeve valves can be sealed by segmented spring-backed seals.
Disadvantages	• The valve opens against the pressure difference, so considerable force is needed. This is especially problematic for electromagnetically actuated valves. • If a variable timing is implemented, an individual actuator is needed for each valve or an additional mechanism must be installed which significantly increases the complexity and the total cost. • Noisy operation due to a reciprocating motion. • Advanced manufacturing techniques result in high costs.	• Relatively high oil consumption and oil burning problem if implemented in internal combustion engines. • A trade-off between friction and leakage flow is needed.

Table 1.3: Comparison of poppet and rotary valves.

1.5 Objectives of the work

In ORC applications, it is common practice to size and optimize the expander for a certain design point corresponding to a given heat source inlet temperature, which defines the evaporation pressure. This approach causes an exergy loss at higher temperatures and a lower cycle efficiency at lower temperatures. In general, the expander operates at a non-optimal pressure ratio most of the time resulting in over- or underexpansion [65]. The expanders' BVR should be adjusted in order to obtain an optimal expansion ratio anytime so that the cylinder pressure is equalized with the condenser pressure at the end of the expansion process.

If an expander with a variable BVR is implemented, the ORC installation can react to the variations in the heat source by increasing or decreasing the pump speed to adjust the evaporation pressure to achieve maximum power output. Typical waste heat source temperatures and flow rates can be obtained, for example, from driving cycles of long-haul truck applications: flat, rolling hill and hilly driving cycles [66]. The same approach can be used for the sizing of an ORC installation applied to a harbor ship or a locomotive engine. These data give an idea of the variation of the evaporation temperature and the pressure of a working fluid. Based on this knowledge, an optimal working fluid can be chosen as is described in Section C.1.

There are several publications about mechanisms realizing the variable BVR by means of the inlet port timing [67]. This type of expander can be recommended as the most optimal one for high and variable pressure ratio ORC machines. A rotary valve is considered as a suitable device to perform this action [56–58].

Combining the technologies mentioned in Section 1.3, a novel concept of a variable-BVR free-piston expander/compressor with an integrated linear alternator is formulated and patented [68].

In order to size and estimate the main characteristics of the expander, a hybrid gray box model is developed according the algorithm proposed in [69]. The simulation program is written in Python[3]. All necessary thermodynamic properties are retrieved from the CoolProp library [70].

The main objective of the current study is to develop models and methods for the design of a variable BVR expander. In order to achieve this goal, the following sub-objectives must be accomplished:

- Since most advanced high temperature cycles require a high expansion ratio, a suitable expander needs to be designed which can provide both the required volume ratio and a solution to dynamically adjust it.
- Considering the expansion ratio is mainly dependent on the inlet timing, the best mechanism realizing this principle must be compared and selected.

[3] `https://anaconda.org`

- Models describing the piston movement and the major losses must be developed for sizing and control purposes.
- An experimental setup must be designed and built in order to validate the developed models.
- The most efficient cycle architecture and the required range of the expansion ratio must be defined.
- An appropriate working fluid providing the possibility to utilize as much exergy available from the heat source, taking into account its fluctuating character, must be selected.
- The gained power output must be quantified in order to proof the feasibility of the proposed technology.
- General optimization criteria and future plans must be formulated.

1.6 Outline

In order to accomplish the aforementioned objectives, this work is organized as follows:

Chapter 1 is a general introduction with some historical overview, explaining the background of the work and the main milestones.

Chapter 2 introduces the preliminary design of the invented free-piston expander and the model, implying the friction, pressure and electromagnetic forces, is developed in order to size the expander and to improve its efficiency. The flows through the piston/cylinder and through the ports are analyzed and the optimization criteria are provided.

Chapter 3 describes the test setup and the data acquisition system. The evolution of the design process is provided, the most critical aspects are highlighted. Two generations of the expander are introduced.

Chapter 4 provides the experimental campaign description and the results obtained. The model is validated using the experimental data.

Chapter 5 contains simulation of the expander operation in a real application. The advantages of the free piston concept are provided. Several optimization criteria are summarized.

Chapter 6 summarizes the obtained results, its analysis and conclusions.

Appendix A frames the publications in conferences and journals, which are relevant to this thesis.

Appendix B holds a technical information about the main and important components of the test setup.

Appendix C represents a description of the ORC working principle and typical cycle architectures.

References

[1] *EU energy in figures. Statistical pocketbook 2016*.

[2] European Commission. *Roadmap to a Single European Transport Area – Towards a competitive and resource efficient transport system*.

[3] Christopher Nürk and Michael A. Maier. *Truck Market 2024 Sustainable Growth in Global Markets*. Technical report, Deloitte Consulting GmbH, 2014.

[4] European Network of Transmission System Operators for Electricity. *Electricity in Europe 2015 – Synthetic overview of electric system consumption, generation and exchanges in the ENTSO-E Area*.

[5] Statista – The portal for statistics. *Number of passenger cars and commercial vehicles in use worldwide from 2006 to 2015*.

[6] Rongchao Zhao, Weilin Zhuge, Yangjun Zhang, Yong Yin, Yanting Zhao, and Zhen Chen. *Parametric study of a turbocompound diesel engine based on an analytical model*. Energy, 115:435 – 445, 2016.

[7] Levente-Botond Kocsis, Dan Moldovanu, and Doru-Laurean Băldean. *The Influence of Exhaust Backpressure Upon the Turbocharger's Boost Pressure*, pages 367–374. Springer International Publishing, Cham, 2016.

[8] Rongchao Zhao, Weilin Zhuge, Yangjun Zhang, Mingyang Yang, Ricardo Martinez-Botas, and Yong Yin. *Study of two-stage turbine characteristic and its influence on turbo-compound engine performance*. Energy Conversion and Management, 95:414–423, 2015.

[9] B. Bonsen. *Efficiency optimization of the push-belt CVT by variator slip control*. PhD thesis, TUE : Department of Mechanical Engineering, 2006.

[10] Ivan Arsie, Andrea Cricchio, Cesare Pianese, Vincenzo Ricciardi, and Matteo De Cesare. *Evaluation of CO_2 reduction in SI engines with Electric Turbo-Compound by dynamic powertrain modelling*. IFAC-PapersOnLine, 48(15):93–100, 2015.

[11] Jacopo Dellachà, Lorenzo Damiani, Matteo Repetto, and Alessandro Pini Prato. *Dynamic Model for the Energetic Optimization of Turbocompound Hybrid Powertrains*. Energy Procedia, 45:1047–1056, 2014. ATI 2013 - 68th Conference of the Italian Thermal Machines Engineering Association.

[12] Francis J. DiSalvo. *Thermoelectric Cooling and Power Generation*. Science, 285(5428):703–706, 1999.

[13] Saniya LeBlanc. *Thermoelectric generators: Linking material properties and systems engineering for waste heat recovery applications*. Sustainable Materials and Technologies, 1-2:26–35, 2014.

[14] Hee Seok Kim, Weishu Liu, Gang Chen, Ching-Wu Chu, and Zhifeng Ren. *Relationship between thermoelectric figure of merit and energy conversion efficiency*. Proceedings of the National Academy of Sciences, 112(27):8205–8210, 2015.

[15] C. L. Hapenciuc, T. Borca-Tasciuc, and I. N. Mihailescu. *The relationship between the thermoelectric generator efficiency and the device engineering figure of merit Zd,eng. The maximum efficiency ðİIJijmax*. AIP Advances, 7(4):045007, 2017.

[16] M. Rull-Bravo, A. Moure, J. F. Fernández, and M. Martín-González. *Skutterudites as thermoelectric materials: revisited*. RSC Advances, 5(52):41653–41667, 2015.

[17] Andrea Montecucco, Jonathan Siviter, and Andrew R. Knox. *The effect of temperature mismatch on thermoelectric generators electrically connected in series and parallel*. Applied Energy, 123:47–54, 2014.

[18] Dimitri Tatarinov, Daniel Wallig, and Georg Bastian. *Optimized Characterization of Thermoelectric Generators for Automotive Application*. Journal of Electronic Materials, 41(6):1706–1712, 2012.

[19] Y.D. Deng, W. Fan, K. Ling, and C.Q. Su. *A 42-V Electrical and Hybrid Driving System Based on a Vehicular Waste-Heat Thermoelectric Generator*. Journal of Electronic Materials, 41(6):1698–1705, 2012.

[20] J.-P. Fleurial, T. Caillat, B.J. Nesmith, R.C. Ewell, D.F. Woerner, and G.C. Carr. *Thermoelectrics: from space power systems to terrestrial waste heat recovery applications*, 2011.

[21] Mikhail Korobitsyn. *Industrial applications of the air bottoming cycle*. Energy Conversion and Management, 43(9-12):1311–1322, 2002.

[22] M. Ghazikhani, M. Passandideh-Fard, and M. Mousavi. *Two new high-performance cycles for gas turbine with air bottoming*. Energy, 36(1):294–304, 2011.

[23] Fouad Khaldi. *Air Bottoming Cycle for Hybrid Solar-Gas Power Plants*. In World Renewable Energy Congress - Sweden, volume 14, pages 3813–3820, 8-13 May 2011.

[24] Raphaë Sandoz, James Spelling, Björn Laumert, and Torsten Fransson. *Air-Based Bottoming-Cycles for Water-Free Hybrid Solar Gas-Turbine Power Plants*. Journal of Engineering for Gas Turbines and Power, 135(10):101701–101701–10, Sep 2013.

[25] Andreas Poullikkas. *An overview of current and future sustainable gas turbine technologies*. Renewable and Sustainable Energy Reviews, 9(5):409–443, 2005.

[26] *Waste Heat Recovery System (WHRS) for Reduction of Fuel Consumption, Emissions and EEDI*, 2015.

[27] Iacopo Vaja and Agostino Gambarotta. *Internal Combustion Engine (ICE) bottoming with Organic Rankine Cycles (ORCs)*. Energy, 35(2):1084–1093, 2010. ECOS 2008, 21st International Conference, on Efficiency, Cost, Optimization, Simulation and Environmental Impact of Energy Systems.

[28] Vincent Grelet. *Rankine cycle based waste heat recovery system applied to heavy duty vehicles : topological optimization and model based control*. PhD thesis, Université de Lyon, 2016. ThÃĺse de doctorat dirigÃľe par Dufour, PascalNadri, Madiha et Lemort, Vincent Automatique Lyon 2016.

[29] Nicolas Stanzel, Thomas Streule, Markus Preißinger, and Dieter Brüggemann. *Comparison of Cooling System Designs for an Exhaust Heat Recovery System Using an Organic Rankine Cycle on a Heavy Duty Truck*. Energies, 9(11), 2016.

[30] Jiacheng Ma, Liuchen Liu, Tong Zhu, and Tao Zhang. *Cascade utilization of exhaust gas and jacket water waste heat from an Internal Combustion Engine by a single loop Organic Rankine Cycle system*. Applied Thermal Engineering, 107:218–226, 2016.

[31] Gequn Shu, Xuan Wang, and Hua Tian. *Theoretical analysis and comparison of rankine cycle and different organic rankine cycles as waste heat recovery system for a large gaseous fuel internal combustion engine*. Applied Thermal Engineering, 108:525–537, 2016.

[32] Ulrik Larsen, Jorrit Wronski, Jesper Graa Andreasen, Francesco Baldi, and Leonardo Pierobon. *Expansion of organic Rankine cycle working fluid in a cylinder of a low-speed two-stroke ship engine*. Energy, 119:1212–1220, 2017.

[33] Simone Lion, Constantine N. Michos, Ioannis Vlaskos, Cedric Rouaud, and Rodolfo Taccani. *A review of waste heat recovery and Organic Rankine Cycles (ORC) in on-off highway vehicle Heavy Duty Diesel Engine applications*. Renewable and Sustainable Energy Reviews, 79:691–708, 2017.

[34] ERTRAC Working Group: Energy and Environment. *Future Light and Heavy Duty ICE Powertrain Technologies*, 2016.

[35] O. E. Baljé. *A Study on Design Criteria and Matching of Turbomachines: Part A Similarity Relations and Design Criteria of Turbines*. Journal of Engineering for Power, 84(1):83, 1962.

[36] Junjiang Bao and Li Zhao. *A review of working fluid and expander selections for organic Rankine cycle*. Renewable and Sustainable Energy Reviews, 24:325–342, 2013.

[37] T. A. Johnson, M. T. Leick, and R.W. Moses. *Experimental Evaluation of the Free Piston Engine – Linear Alternator (FPLA)*. Technical report, Energy Innovation Sandia National Laboratories, 2015.

[38] C. Ferrari and H. E. Friedrich. *Development of a Free-Piston Linear Generator for use in an Extended-Range Electric Vehicle*. EVS26 International Battery, Hybrid and Fuel Cell Electric Vehicle Symposium, 2012.

[39] Hidemasa Kosaka, Tomoyuki Akita, Kazunari Moriya, Shigeaki Goto, Yoshihiro Hotta, Takaji Umeno, and Kiyomi Nakakita. *Development of Free Piston Engine Linear Generator System Part 1 - Investigation of Fundamental Characteristics*. In SAE Technical Paper. SAE International, 04 2014.

[40] Shigeaki Goto, Kaznunari Moriya, Hidemasa Kosaka, Tomoyuki Akita, Yoshihiro Hotta, Takaji Umeno, and Kiyomi Nakakita. *Development of Free Piston Engine Linear Generator System Part 2 - Investigation of Control System for Generator*. In SAE Technical Paper. SAE International, 04 2014.

[41] Boru Jia, Rikard Mikalsen, Andrew Smallbone, and Anthony Paul Roskilly. *A study and comparison of frictional losses in free-piston engine and crankshaft engines*. Applied Thermal Engineering, 140:217 – 224, 2018.

[42] ASHRAE. *2012 ASHRAE Handbook – HVAC Systems and Equipment*, chapter 38. ASHRAE, 2012.

[43] Emerson. *Variable Volume Ratio Scroll Compressor*. Patent WO2015187816, 2015.

[44] T.K. Garrett, K. Newton, and W. Steeds. *Chapter 5 - Sleeve-valve and special engines*. In T.K. Garrett, K. Newton, and W. Steeds, editors, Motor Vehicle (13), pages 177–185. Butterworth-Heinemann, Oxford, 13 edition, 2000.

[45] Seinosuke Hara, Seiji Suga, Satoru Watanabe, and Makoto Nakamura. *Variable Valve Actuation Systems for Environmentally Friendly Engines*. In Hitachi Review, volume 58, 2009.

[46] Allen Comfort. *An Introduction to Heavy-Duty Diesel Engine Frictional Losses And Lubricant Properties Affecting Fuel Economy - Part I*. In SAE Technical Paper. SAE International, 10 2003.

[47] Andrew D. Ball. *A tribological study of the design and performance of automotive cams*. PhD thesis, University of Leeds, 1988.

[48] Christopher Joseph James. *Analysis of parasitic losses in heavy duty diesel engines*. Master's thesis, Massachusetts Institute of Technology, 2012.

[49] W. S. Chang, T. A. Parlikar, M. D. Seeman, D. J. Perreault, J. G. Kassakian, and T. A. Keim. *A new electromagnetic valve actuator*. In Power Electronics in Transportation, 2002, pages 109–118, Oct 2002.

[50] Ray T. Bohacz. *Silent Knight. How sleeve-valve engines work*. Hemmings Classic Car, 2010.

[51] S.R. Adams. *The centenary patent – Single-sleeve valve engines*. World Patent Information, 32(4):320–325, 2010.

[52] M.C.I. Hunter. *Rotary Valve Engines*. Anchor Press, Limited, Tiptree, Essex, 1946.

[53] James W.G. Turner and James P. Lewis Monsma. *An Investigation Into the Port Timing of a Burt-McCollum Sleeve Valve and Its Interaction with a Simple Variable Compression Ratio Mechanism*. In SAE Technical Paper. SAE International, 09 2017.

[54] Keith Lawes. *The Rotating Cylinder Valve 4-Stroke Engine. A Practical Alternative*. Technical report, RCV Engines Limited, Wimborne, United Kingdom, 2002.

[55] Jorrit Wronski. *Design and Modelling of Small Scale Low Temperature Power Cycles*. PhD thesis, Technical University of Denmark, 2015.

[56] T. Wallis. *The Bishop Rotary Valve*. Auto Technology, Special Motorsports Technology, pages 2–5, 2007.

[57] A.D. Thomas, A.B. Wallis, and G.D. Horrocks. *Internal combustion engine with rotary valve*, 2009.

[58] R. Palmisano and H. D. Ng. *Design Analysis and Comparison Between Standard and Rotary Porting Systems for IC Engine*. International Journal of Automotive Technology, 13(2):175–191, 2012.

[59] Kun Liang, Richard Stone, Gareth Davies, Mike Dadd, and Paul Bailey. *Modelling and measurement of a moving magnet linear compressor performance*. Energy, 66:487 – 495, 2014.

[60] Jaroslav Šustek. *Analysis of pressure losses through valve plate in compressor with CO_2*. AIP Conference Proceedings, 1768(1):020036, 2016.

[61] Philip H. Smith. *Valve mechanisms for high-speed engines: Their design and development*. Robert Bentley Inc., 1971.

[62] Eugene P. Batzell. *Slide, Rotary and Piston Valves Versus Poppet Valves for Gas Engine Service*. Transactions (Society of Automobile Engineers), 5:261–305, 1910.

[63] Talent Nyawo. *Design of a rotary valve for pressurised steam*. Master's thesis, KTH, Machine Design (Dept.), 2016.

[64] Robert J. Raymond. *Comparison of Sleeve and Poppet-Valve Aircraft Piston Engines*. Aircraft Engine Historical Society, 2005.

[65] Yadong Zhu, Liang Jiang, Victor Jin, and Lijun Yu. *Impact of built-in and actual expansion ratio difference of expander on ORC system performance*. Applied Thermal Engineering, 71(1):548–558, 2014.

[66] D. Luong. *Modeling, Estimation, and Control of Waste Heat Recovery Systems.* PhD thesis, UCLA, 2013.

[67] J. Wronski, M. J. Skovrup, B. Elmegaard, H. N. Rislå, and F. Haglind. *Design and Modelling of a Novel Compact Power Cycle for Low Temperature Heat Sources*. In The 25th International Conference on Efficiency, Cost, Optimization, Simulation and Environmental Impact of Energy Systems., 2012.

[68] S. Gusev. *Free piston device*, December 15 2016. WO2016198554A1 Patent App. PCT/EP2016/063223.

[69] Yulia Glavatskaya, Pierre Podevin, Vincent Lemort, Osoko Shonda, and Georges Descombes. *Reciprocating Expander for an Exhaust Heat Recovery Rankine Cycle for a Passenger Car Application*. Energies, 5(6):1751, 2012.

[70] Ian H. Bell, Jorrit Wronski, Sylvain Quoilin, and Vincent Lemort. *Pure and pseudo-pure fluid thermophysical property evaluation and the open-source thermophysical property library CoolProp*. Industrial & Engineering Chemistry Research, 53(6):2498–2508, 2014.

2

Modeling and Design of a Novel Variable Volume Ratio Expander

In this chapter, the first approach to the preliminary design of the proposed concept expander is described. The goal is to prove the feasibility of a novel patented technology, which involves the integration of the intake and the discharge valves into the piston-cylinder assembly. The advantage of the proposed design is the simplicity of the mechanical design which features only one moving part: the piston. Furthermore, with respect to the conventional reciprocating machines, the proposed design eliminates the use of the crank mechanism and associated losses as well and integrates the valve control with the piston control system. The dynamic equation of motion is derived for the system, the leakage flows and friction forces are analyzed and included in a deterministic model. The intake flow can be maximized by the optimization of the port shape and the piston linear and rotative motion profile.

2.1 Expander description

The invented device [1] is a double-acting reciprocal machine which can operate as an expander or a compressor. The integrated motor/alternator has two degrees of freedom, namely, translation and rotation. The piston linear motion is used to expand or to compress the working medium. The major difference with classic reciprocating machines is how the piston is driven. A typically used crankshaft mechanism is replaced by a linear motor/alternator (LMA). This linear device can either accelerate the piston while it compresses the working fluid, using the electric energy from the power source, or recover the mechanical work from the expansion process, transform it into electricity and return it back to the power source.

By means of the rotation, the intake and discharge ports are actuated, therefore the same electrical machine also acts as a servo-motor. The idea to combine both types of motion in one unit was first realized in the world of pick-and-place actuators. This approach gives a possibility to reduce the weight and size of a multiple degrees of freedom system, which can be made cylindrical [2–4], spherical [5] or planar [6]. The chapter study is mainly focused on thermodynamic and fluid mechanic processes assuming that the technologies needed to design and to manufacture the electrical components are available.

2.1.1 Working principle

The expander conceptual drawing is shown in Figure 2.1. The housing has a cylindrical shape with two stator assemblies attached to both flanges. The assemblies consist of laminated iron cores with windings and supporting rods. The stator provides a helical magnetic field to the piston dictating its motion profile. Permanent magnets are fixed to the inner wall of the piston and this assembly acts as a rotor/-translator. All cavities in the stator assemblies and between magnets are filled with an epoxy compound in order to minimize the dead volume and to protect and seal the windings. The right side of the expander is shown without compound in order to demonstrate the internal structure. The stator coils and magnets are shown for completeness; the number of poles, the magnets amount and its distribution may differ in the final design.

The piston is manufactured and placed inside the housing with a free running fit and can slide and rotate simultaneously with limited friction [7]. The exact value of the clearance is the object of optimization and it will be described later in this chapter. In order to prevent uncontrolled contact of the piston with the cylinder walls, guide rings can be placed close to the piston flanges, in the same way it is realized in ICEs. The dry molybdenum disulfide lubricant applied to the piston fills excessive cavities and is removed from areas with closely contacting surfaces. This redistribution allows a very close fit of the piston inside the cylinder without any direct contact.

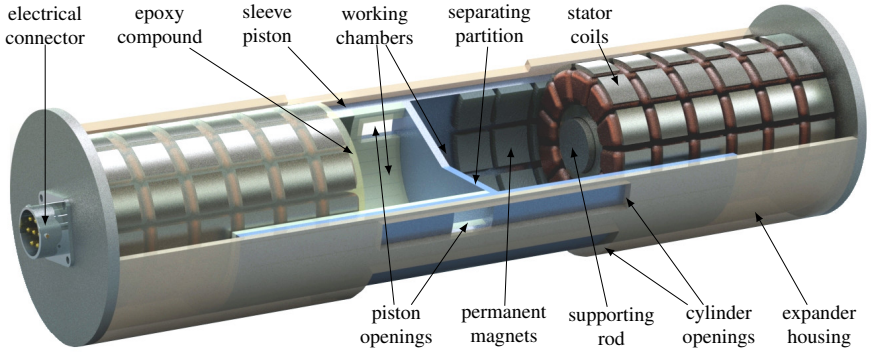

Figure 2.1: Expander cutaway view.

The working chambers are formed by two assemblies: the housing with two stator coils, and a sleeve piston with a separating partition in the middle. The working chambers operate alternately: while the working medium expands in one chamber, the volume of the other chamber decreases and the working fluid discharges. The piston reciprocates under the altering pressure difference. The energy is transferred to the stator resulting in the electricity production.

Both the housing and the piston are provided with two sets of axisymmetrical wall openings which are connected to the high and the low pressure manifolds. By the piston rotation, the expander valves can be opened or closed: the openings in the sleeve piston can be alternately aligned with the high or the low pressure openings in the housing, so the working fluid can be admitted, expanded in the working chamber and thereafter discharged into the low pressure port. The openings in the piston are located near the central partition with a shift of one set of $90°$ in respect to the other one. This allows to connect one working chamber to the high pressure port while the other chamber is connected to the low pressure port. The low pressure port is made wider in order to close the inlet keeping the outlet open.

The explanation of the in- and outlet ports operation principle is depicted in Figure 2.2:

a) The smaller opening in the housing acts as an intake port. The left chamber is connected to the high pressure line, the piston moves from left to right, the volume of the working chamber increases, the working medium enters the working chamber. The piston rotates simultaneously from the bottom to the top gradually closing the port. In the right chamber, previously expanded working fluid is discharged towards the low pressure line through the wider opening in the housing.

b) The openings in the left working chamber are oriented against the housing wall, the port is closed, the intake process is finished. In the left working

chamber, the expansion starts, the discharge process in the right working chamber continues.

c) The discharge port of the right working chamber is about to close, the discharge process is almost finished. The expansion process in the left working chamber also ends.

d) After the piston reaches its extreme right position, it starts to move back to the left. The intake process starts in the right working chamber, the expanded working fluid in the left working chamber flows towards the low pressure line.

This concept provides also a possibility to vary the inlet timing by adjusting the rotational speed relatively to the piston translation. The control of the expander built-in volume ratio depicted on Figure 2.2(b). For illustration purpose, the stators are simplified and the housing is shown semi-transparent. The piston is shown slightly after the translation from left to right has been started. The inlet port is almost closed, so the intake process is about to finish. The BVR can be expressed as:

$$r_{bv} = \frac{V_{max}}{V_{adm}} = \frac{L_{str}}{x_{adm}}\,, \tag{2.1}$$

where V_{adm} is the working chamber volume at he moment when the inlet port is closed and the admitted working medium is isolated and starts to expand, V_{max} is the working chamber volume when the expansion finishes.

2.1.2 Two degree of freedom motor/alternator

A linear motor can be considered as an unrolled permanent magnet synchronous motor (PMSM), where the rotor consisting of permanent magnets becomes a flat magnet assembly, which is called the secondary section, and the primary section consisting of flattened stator coils. A sequential commutation of the coils results in a linear movement of the primary section relatively to the secondary one or vice versa. The load is connected to the moving section while the stationary one is fastened to a chassis. Typically, a linear guiding system is used in order to guarantee the alignment and the right clearance between the sections. An encoder is used for the position feedback. Linear motors are characterized by a very high speed and resolution, such as around one micron at 3 m/s which, in combination with a very good repeatability, provides an excellent positioning precision. Speeds up to 6 m/s are also possible with a reduced precision, which is, however, still sufficient for most applications. Since there is no mechanical transmission, there is also no backlash or wear and the stiffness is also not an issue. There are three main types of linear motors shown in Figure 2.3:

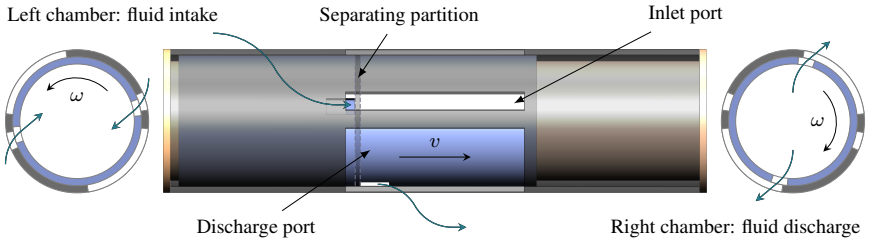

(a) Intake process finishes.

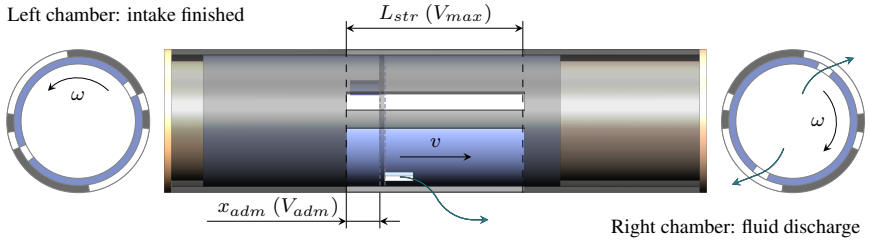

(b) Expansion process started.

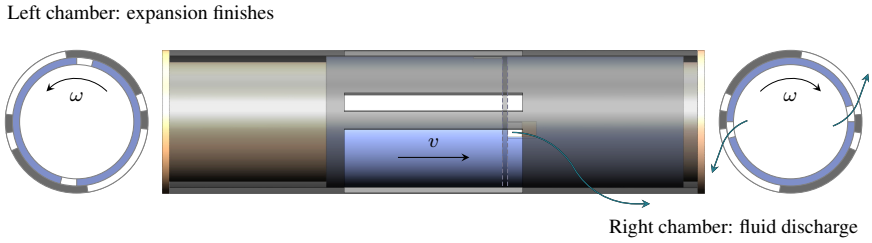

(c) Discharge process finishes.

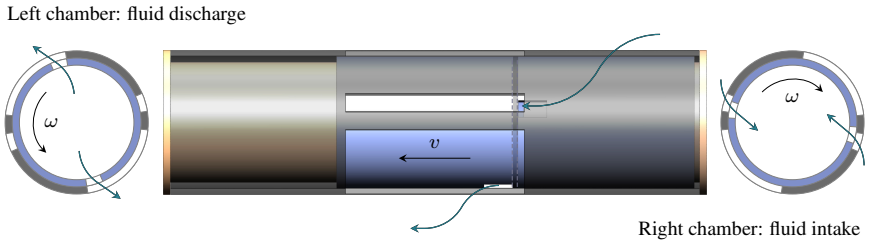

(d) Piston reversed.

Figure 2.2: Different operating modes of the valves. Cross-sectional views of the left and right working chambers are shown in the vicinity of the piston openings from the left and from the right respectively.

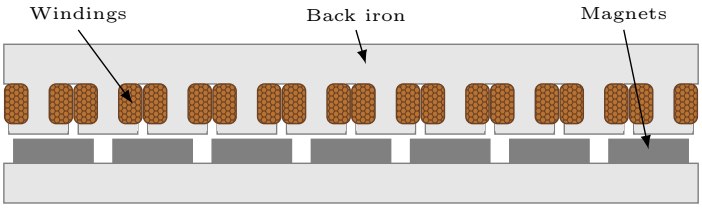

(a) Iron core linear motor.

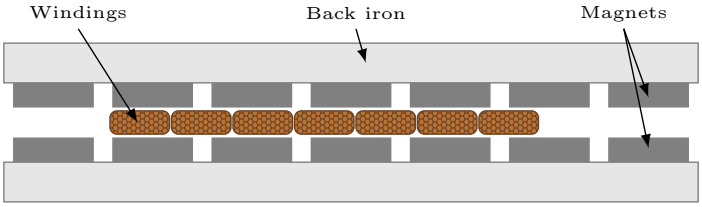

(b) Ironless linear motor.

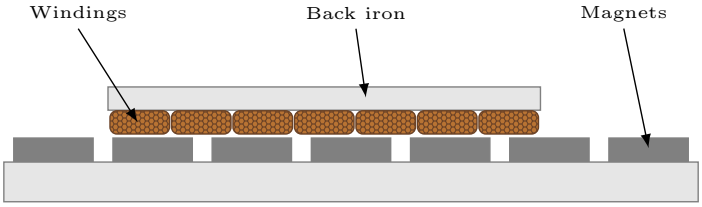

(c) Slotless linear motor.

Figure 2.3: Common synchronous linear motor types.

	Iron Core	**Air Core**	**Slotless**
Attractive force	Highest	None	Moderate
Cogging	Highest	None	Moderate
Force density	Highest	Moderate	Good
Heat dissipation	Best	Worst	Good
Cost	Low	High	Lowest

Table 2.1: Linear alternator main parameters.

a) The iron core motor. The primary section consists of a laminated steel core with a shape of teeth with the windings wound around it. Permanent magnets are attached to a common steel plate as shown in Figure 2.3(a). This type of linear motors has a maximal force density which is important for compact devices. However, there are two major drawbacks as well: a very high attractive force between the core and the magnets and a cogging produced by the attraction force switching from one tooth/magnet couple to another during the motion. The first problem causes an increased friction in the linear guiding system, the second one manifests in a non-uniform motion speed.

b) The air-core or iron-less motor, shown in Figure 2.3(b) does not suffer from these disadvantages since it has no steel core. The coils of the primary section are typically attached to an aluminum frame acting as a support and as a heat sink. The cavities are filled with an epoxy compound. This allows for a lightweight moving part design which is desirable for high dynamic applications. However, the force density is much lower than for the iron core type. Also, the heat dissipation is affected due to the epoxy low thermal conductivity. Furthermore, the mechanical strength of an epoxy/aluminum assembly is much lower than for the iron core design. One more drawback is the necessity to use a double amount of expensive magnets.

c) The slotless motor depicted in Figure 2.3(c) is a mixture of both an iron core and ironless types. It combines the advantages and disadvantages of both types so the main characteristics are somewhere in between. For example, the attractive force and cogging are lower than for the iron core design. The force density is also lower but higher than for the ironless one.

All mentioned above is summarized in Table 2.1

The choice between the iron core and the ironless design is dictated by a particular application. Where a smooth and fast movement is needed and the required forces are not high, an ironless design is more preferable since the primary section is a moving part of the motor. The main drawback is a lower efficiency in compar-

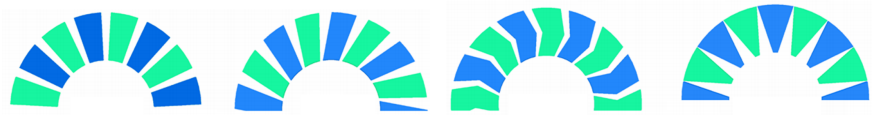

Figure 2.4: Permanent magnets placing, from left to right: straight, skewed, dual skewed, triangular skewed. Adapted from: [9].

ison with the iron core design. For power generation, the efficiency is of a great importance. The proposed design comprises a secondary section which is moving and the coils are located in the stator. Therefore, the choice of the iron core stator is obvious: less amount of magnets in the moving part for the same power can be realized resulting in a lower weight and a higher frequency.

However, iron core motors are characterized by significant cogging forces since the magnetic field is not continuous. The attraction force between stator core poles and the magnets is dependent on the distance between them, which changes as the slider moves. This variation in the attraction between the primary and the secondary section results in velocity ripples and affects the positioning. A partial solution, which is typically implemented, is a skewed placing of magnets or an adjustment of its shape as it is reported in [8, 9].

One more technology, which can be used to improve the characteristics of a free-piston linear alternator (FPLA) is a Halbach Array (HA) first realized by Klaus Halbach in 1980 [10]. The working principle and design strategy is comprehensively explained by [11]. The magnets in HA are placed in a row and are oriented in a way as is shown in Figure 2.5. The magnetic field of each magnet is rotated by 90° relatively to the adjacent magnets resulting in a maximization of the magnitude of a common magnetic flux density on one side and almost complete elimination on the other side. This arrangement significantly increases the efficiency of a magnetic circuit. The advantage of such a magnetic assembly is that only one side becomes the working one, so no back iron or a second set of coils are needed in order to obtain the same force from the same amount of the magnet alloy as it is proclaimed by [12]. This property is very attractive for the current application, therefore, the piston does not need to act as a back iron and can be made light weight, even of a composite material. For this particular application, a two dimensional Halbach cylinder can be formed of multiple stacked one dimensional cylinders.

The known disadvantages of the HA technique are its relatively complex assembly procedure, caused by the magnet retention, and a faster demagnetization at high temperatures compared to a regular magnet placement. The first problem is reported to be solved by [13]. The impact of demagnetization on the efficiency of a Halbach cylinder as well as some sizing considerations are explained in [14]. The choice of a magnetic alloy for applications, where high temperatures are expected,

Alloy	**units**	**Ferrite**	**NdFeB**	**SmCo**	**AlNiCo**
Grade		GSFD-44	GSN-25BH	GSS-30	GSA-9B
Remanence, Br	mT	390	1000	1120	1080
Normal coercivity, Hc	kA/m	271	750	828	120
Max. energy product, BH	kJ/m^3	36	190	247	80
Max. operating temperature	°C	225	230	350	550
Density	kg/m^3	5000	7400	8400	7300

Table 2.2: Properties of common high-temperature magnetic alloys. Source: [16].

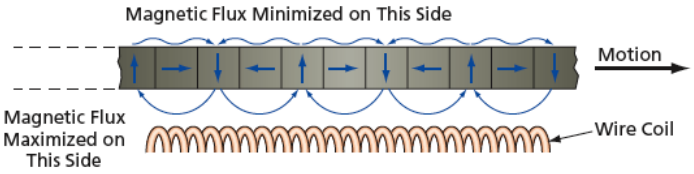

Figure 2.5: Schematic view of Halbach array. Source: `www.techbriefs.com`.

is explained by [15]. Also the temperature influence on the most common magnet types and the method for evaluation of the loss of magnetization is described. Table 2.2 provides a summary of the parameters of magnets with highest operating temperature. The remanence, Br, is a magnetic flux density which remains in the magnet after magnetization. The normal coercivity, Hc, is the field strength required to compensate the magnetic induction of an alloy. The maximum energy product, BH, is the energy density. The density of these four alloys is provided to give an idea about the total mass of the magnetic assembly. According to this data, samarium-cobalt permanent magnets appear to be the best candidate since they combine a high-temperature tolerance with a high magnetic strength. AlNiCo magnets may be used if temperatures above 350 °C are expected [16]. Such high temperatures are very unlikely for ORC applications but for FPLA-based combustion engines they can be potentially interesting. Regardless the aforementioned issues, HA technique is widely used in production of magnetic bearings, high efficiency generators and can be also useful for the proposed expander.

Not only can magnets be damaged if exposed to a temperature of 220–250 °C but also the windings [18]. Materials used for high-temperature electrical insulation are typically ceramics, fluoropolymers or polyetheretherketone (PEEK). Ceramic and fluoropolymer insulation can not withstand mechanical stress during the winding process, therefore sharp bending angles must be avoided [19]. PEEK flows when at high temperatures and therefore must be reinforced. Sihvo et al. [20]

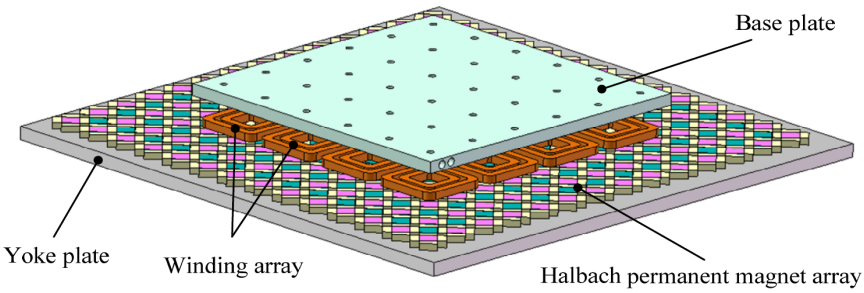

Figure 2.6: Planar actuator with a two-dimensional magnetic array. Source: [17].

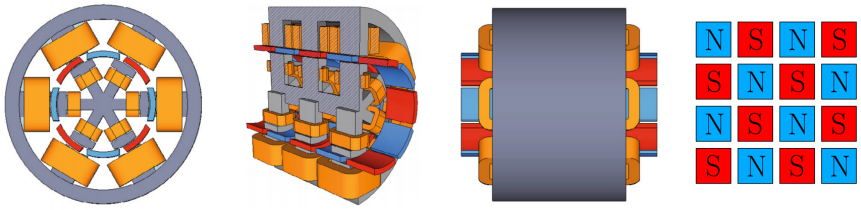

Figure 2.7: Rotary-linear actuator with a chessboard permanent magnet array. Source: [3].

compared several insulation materials, e.g. Kapton® and Mylar®[1] and provided the results of the insulation exposure to a high-temperature steam and pressurized water. The use of an inorganic polymer matrix and fiberglass reinforcement ensures the reliable operation of motors at temperatures up to 300 °C used for down-hole pumps as reported in [21].

By arranging the stator coils and the magnets in a chessboard pattern, as is shown in Figure 2.6, a two-dimensional movement of the secondary section can be realized. The working principle of such an actuator has been patented by [22] and a linear-rotary actuator based on this principle has been patented by Anorad Corporation [23]. This type of actuator has been modeled and a prototype has been build by [3] as depicted in Figure 2.7. The iron core is shown in gray, the windings are orange. The magnets are arranged in the way that the south (red) and north poles (blue) alter. This arrangements allows the magnets to be attracted to the core poles in linear and in circumferential direction simultaneously.

[1] Kapton® and Mylar® are registered trademarks of E.I. du Pont de Nemours and Company

2.2 The dynamic equation of motion

The motion of the piston in FPLA-based machines must be controlled with a high accuracy in order to achieve a maximum efficiency, which is defined by an optimal speed profile. Furthermore, the linear and rotary motion must be synchronized since BVR is dependent on the piston position relatively to the inlet port at the end of the intake process. The positioning accuracy of both the piston rotation and translation is therefore crucial for the expander's volumetric efficiency.

The second reason why the linear positioning is important is the need to stop and to reverse the piston right at the dead points. On the one hand, the impact of the piston to the housing is avoided and, on the other hand, the stroke length is maximized. This functionality is realized by the alternator controller. The use of a classic PID-controller is not the most efficient solution for high-dynamic applications, where both, a fast positioning and inadmissibility of overshoots is required.

For time-constrained applications with multiple inputs, a model predictive control (MPC) approach is used in most cases. As follows from the name, this technique predicts the behavior of the system based on an accurately designed model and subsequently optimizes the control signal accordingly. It is also possible to optimize the process on-line by adjusting the model. The theory of MPC is explained and illustrated by multiple examples in MATLAB® and Simulink®[2] [24].

The design of an MPC controller starts from the system identification. This means that all forces and torques acting on the piston during its linear motion and the rotation must be identified analytically or empirically. A comprehensive knowledge about the system gives a possibility to design a learning motion controller with an excellent performance as demonstrated in [25]. The authors developed a control algorithm using a model-based feedback combined with a learning feed-forward component. The algorithm is based on a limited second-order model, but already shows the ability to reduce the positioning error by a factor 25 in comparison with a classic PID-controller.

The forces and which can be identified in the current system are: position-dependent, such as the gas force and the cogging force, velocity-dependent such as frictional force and acceleration-dependent inertia force. The electromagnetic force, provided by the alternator acts together or against these forces and it can be calculated in a real time by using the system model.

The torques have the same origin, hence its identification principle is the same. The designed framework provides synchronized thrust force and torque signal to the alternator power electronics ensuring the right inlet port timing and the piston velocity profile.

[2] www.mathworks.com

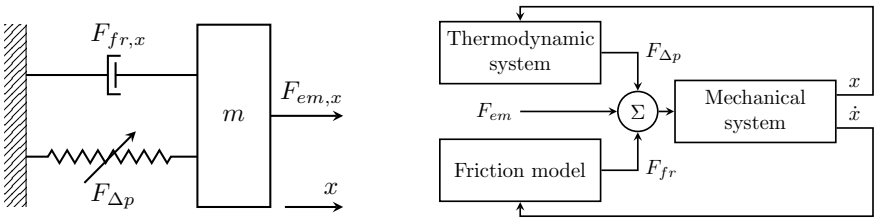

(a) Mechanical model (b) Motion model

Figure 2.8: Linear motion model.

2.2.1 Linear motion

The piston translation dynamics are governed by Newton's second law of motion which predicts the piston behavior under several forces acting on it. A similar approach is used by [26] for design of a FPLA ignition engine. The balance of the forces can be written as follows:

$$F_{p,\,cyl} - F_{p,\,dis} - F_{fr} - F_{em} = \sum_{i=1}^{n} m_{ps,\,i} \frac{d^2x}{dt^2}\,, \tag{2.2}$$

where $F_{p,\,cyl}$ and $F_{p,\,dis}$ are the gas forces induced on the piston central element by the pressures in the expanding and in the discharging working chamber respectively. In further calculations the net force, $F_{\Delta p_{cyl}}$, is used. F_{fr} is the frictional force in axial direction, F_{em} is the electromagnetic thrust force generated by the linear alternator and $m_{p,\,i}$ is the sum of all the moving masses as it is schematically depicted in Figure 2.8.

2.2.1.1 Gas force

The pressure change during the expansion process results in a gas force varying in time, $F_{\Delta p}$, which is applied to the piston central element with a certain surface area:

$$F_{\Delta p}(t) = \frac{\pi D^2}{4}(p_{cyl}(t) - p_{dis}) \tag{2.3}$$

2.2.1.2 Frictional force

The frictional force has a complex behavior. A good prediction of its variation under changing conditions remains a challenging task for control engineers. Numerous advanced friction models, i.e. the Dahl model and the LuGre model, have been developed by combining and adjusting basic models such as a viscous friction model, the Coulomb model and the Stribeck model. The most used friction

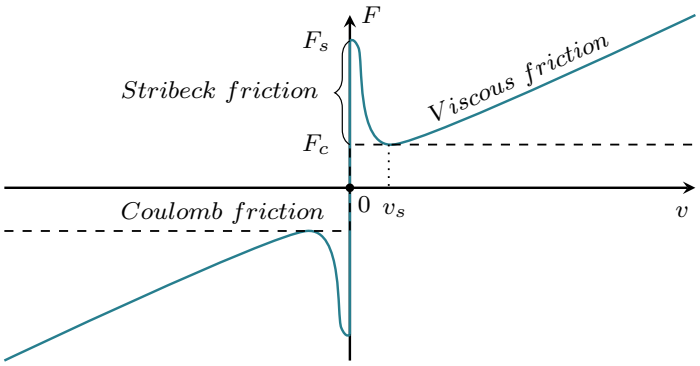

Figure 2.9: LuGre friction model.

models are summarized in [27]. The reason why a combination of different models is necessary, is that the relationship between the velocity of a sliding part and the induced frictional force is strongly non-linear, especially in the range of very low speeds. A superposition of the aforementioned models is show in Figure 2.9. This figure illustrates the transition from one frictional model to another. The piston speed is obtained from the mechanical model and further used in the friction model.

- Stiction. If the sliding part is not moving, a certain external force F_e is needed to overcome the static friction and to start the motion. This force is called the breakaway force.

- Coulomb friction model assumes the friction F_c is independent of the sliding velocity v and the contacting surface, proportional to the load F_N via Coulomb friction coefficient f_c, and opposed to the velocity, which is expressed with the signum function:

$$F_c = f_c F_N sgn(v)\,. \tag{2.4}$$

- Viscous friction F_ν is an additional component which is in practice always present since there is always a fluid layer between sliding surfaces. This makes the friction force almost linearly dependent on the velocity through the viscous friction coefficient f_ν:

$$F_\nu = f_\nu v\,. \tag{2.5}$$

- The Stribeck friction model describes the transition from the stiction to the Coulomb friction model. It corresponds to the negatively slope of the friction curve. The velocity v_s is the limit for the Stribeck model.

Summarizing the above mentioned cases, the system of equation describing the friction force behavior can be obtained:

$$F = \begin{cases} F(v), & \text{if } v \neq 0\,, \\ F_e, & \text{if } v = 0 \text{ and } |F_e| < F_s\,, \\ F_s sgn(F_e) & \text{otherwise;} \end{cases} \tag{2.6}$$

where F_s is the minimum force to overcome stiction. According to [28], the function $F(v)$ can be written as:

$$F(v) = F_c + (F_s - F_c)e^{-|v/v_s|^{\zeta_s}} + f_\nu v\,, \tag{2.7}$$

where v_s is the Stribeck velocity and ζ_s is an empirical coefficient which is equal to 2.

A more accurate dynamic friction model developed by Canudas De Wit and Olsson is the LuGre (Lund-Grenoble) model [29–31]. This model includes all mentioned sub-regimes and provides a smooth transition from one to another. This method is especially valuable when the velocity changes direction. The interaction between two surfaces is modeled with elastic bristles replacing irregular microscopic asperities. The friction force F can be expressed as follows:

$$\begin{cases} F = \sigma_0 z + \sigma_1 \dot{z} + \sigma_2 v\,, \\ \dot{z} = v - |v|z/g(v)\,, \\ \sigma_0 g(v) = F_c + (F_s - F_c)e^{-|v/v_s|^{\zeta_s}} \end{cases} \tag{2.8}$$

where $g(v)$ is the function describing the average bristles deflection at various velocities, σ_0 is the contact stiffness, σ_1 is the damping coefficient and σ_2 is the viscous friction parameter.

A numerical method for determining of the parameters for Dahl and LuGre dynamic models based on simulations has been proposed by [32]. However, the easiest way to obtain the coefficients used in the LuGre model is to process the experimental data. For the first guess, the friction force F_{fr} is estimated using a correlation obtained by [33] for pneumatic cylinders. The results are simplified and assumed pressure-independent since the expansion of a thick-wall sleeve piston within the considered pressure range is negligible. Further, it can be verified and adjusted using experimental data.

The influence of the Stribeck-effect at near-zero velocities can be neglected as the piston velocity is a vector along which the friction force acts and it is never zero due to the piston rotation as shown in Figure 2.10. Even when the piston changes direction of its axial movement and the axial velocity drops to zero, the helical velocity becomes equal to the tangential one which is almost constant and remains not lower than 0.63 m/s for the current setup. This effect is described in [34] and is used to reduce the stick-slip friction at small velocity changes and to improve

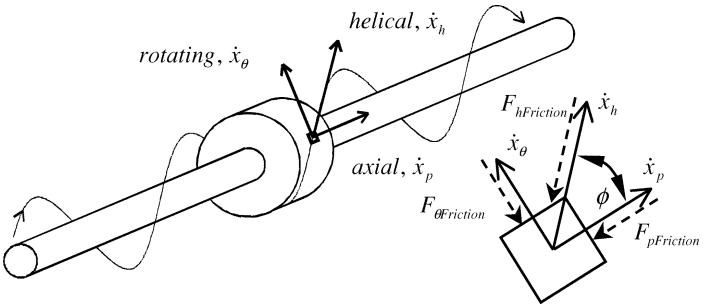

Figure 2.10: Vector form of the piston velocity. Source: [34].

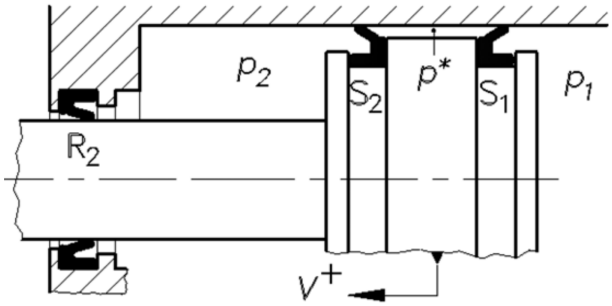

Figure 2.11: Compression pneumatic seal. Source: [35].

the positioning accuracy in hydraulic systems. It was experimentally proven that at high helical velocities (>0.5 m/s), the friction force can be assumed to be a linear function of the translation speed of the piston. Some non-linearity is still observable in the range of the axial speed of $\pm$0.005 m/s which can be neglected so that the equation for the friction force can be simplified as follows:

$$F_{fr}(t) = F_c + f_\nu v(t) sgn(v)\,, \tag{2.9}$$

where $sgn()$ is a function extracting the sign of the piston velocity. The heat produced by the friction is included into the thermodynamic model which will be explained in Section 2.3.

Compression pneumatic seal rings are designed in order to use the pressure in the cylinder to push the seal towards the piston wall or the rod improving the gap tightness as depicted in Figure 2.11. This solution, however, causes a higher friction at higher pressures. This leads to excessive heat production and increases the seal wear at high velocities, which are typical for linear expanders or engines. This type of seals is used in the test setup to seal the piston rod only.

For sealing the clearance between the piston and the cylinder wall, solid carbon, bronze or glass impregnated fluoroplastic sealing rings, attached around the

Figure 2.12: Gapless PTFE seal rings. Source: [36].

piston, can be used as is shown on Figure 2.12. The common materials are Polytetrafluoroethylene (PTFE), also known as Teflon®, and Viton® which can withstand high temperatures[3]. The maximum operating temperature for PTFE is about 260 °C, for Viton about 200 °C. The use of seal rings located close to the piston flanges can help to center it inside the housing.

2.2.1.3 Electromagnetic force

The electromagnetic force, F_{em}, which is created by the alternator, is applied to the piston through the magnet assembly. Depending on the piston position, it can accelerate or decelerate the piston. The electric energy is accumulated in form of the piston linear motion during the acceleration phase. The alternator operates as a motor until the piston velocity reaches its maximum. The kinetic energy is then returned back to the grid when the piston decelerates. The alternator generates electrical energy operating in a brake mode. The electromagnetic force profile for the given piston motion profile is dependent on the other forces arising in the system such as the pressure and the frictional forces. These forces together define the piston speed change in function of time. When the piston reaches the end of the stroke, it needs to be stopped and reversed. At this point, the net energy provided by the alternator becomes equal to the expansion energy subtracting the energy dissipated due to the friction, as it is formulated by [37]. The equation describing this transformation can be expressed as follows:

$$F_{em}(t) = \frac{\pi D_{ps}^2}{4} \Delta p_{cyl}(t) - f_\nu \left(\frac{dx}{dt} \right) - \sum_{i=1}^{n} m_{ps,\,i} \frac{d^2x}{dt^2} \,, \tag{2.10}$$

where D_{ps} is the piston diameter, Δp_{cyl} is the pressure difference across the piston central element. Equation 2.10 is used to provide the value of the electromagnetic force to the linear alternator drive. The piston position feedback is realized by means of a position sensor.

[3] Both Teflon® and Viton® brand names are owned by Chemours Company

2.2.1.4 Cogging and reluctance forces

As aforementioned, a linear alternator consists of several coil/magnet pairs spread out along the primary sections and the slider. The cogging force is a result of the interaction of the magnets with the core poles, resulting in thrust ripples at constant force acting on the secondary section. There are several analytically based models of the cogging force reported in literature, i.e. [38–41]. However, the complexity of these models makes it less attractive for control applications than experimental mapping. Since the cogging force is related to the magnetic pitch of the motor, it can be mapped as a function of the piston displacement. The second source of magnetic disturbances is the winding self-inductance, which varies with the current flowing through it. These forces are defined by the alternator geometry and they are also position-dependent. However, its distribution can be slightly irregular due to assembly imperfection. Both forces cause an unwanted force ripple. The best way to include this ripple into the model is to measure it directly since these forces are mainly the function of the piston displacement and therefore it can be mapped in the way it is done by [42].

2.2.1.5 Gas force

The expansion or compression of the working fluid in the working chambers defines the pressure change which induces the gas force applied to the piston central element. The determination of the pressure profile as a function of time and the piston position is further explained in Section 2.3.

2.2.2 Rotation

The rotational motion of the piston is dictated by the same laws as the translation, which can be rewritten using the angular coordinates and torques instead of forces. The torque balance at the motor shaft is expressed by the general equation of torque as follows:

$$\mathcal{T}_{em} = \mathcal{T}_j + \mathcal{T}_{fr}\,, \tag{2.11}$$

where $\mathcal{T}_{el}$ is the electromagnetic torque, $\mathcal{T}_j$ is the inertia torque and $\mathcal{T}_{fr}$ is the friction torque.

2.2.2.1 Inertia torque

The inertia torque is defined by the total moment of inertia of the rotation train, which is equal to the sum of moments of inertia of all rotating components such as the servo motor, the piston and the shafts:

$$\mathcal{T}_j = \sum_{i=1}^{n} I_i e\,, \tag{2.12}$$

where I_i is the moment of inertia of each rotating part and e is the angular acceleration, which is the same for all parts since they rotate around the same axis. The moments of inertia can be calculated by using the main dimensions of the components, which have cylindrical shapes, so the formula for the moment of inertia of a hollow cylinder can be used:

$$I = \frac{1}{8} m (D_{out}^2 + D_{in}^2) \,, \tag{2.13}$$

where m is the mass of a rotating part, D_{out} is the outer diameter, D_{in} is the inner diameter which is equal to zero for parts without cavities such as the piston shaft and the central element as well as the rotor of the servo motor.

2.2.2.2 Frictional torque

The frictional torque can be calculated by using the same correlation as in Section 2.2.1.2 adjusted for the rotary motion as proposed by [33]. The tangential speed of the piston, v_τ, must be used instead of the linear one. Taking into account that the rotation never stops, the equation for the frictional torque can be simplified as follows:

$$\mathcal{T}_{fr}(t) = f_\nu v_\tau(t) \frac{D_{ps}}{2} = f_\nu \omega(t) \frac{D_{ps}^2}{4} \,, \tag{2.14}$$

where ω is the rotation velocity and D_{ps} is the piston diameter. Since the direction of the rotation does not change, the sign of the frictional torque remains the same.

2.2.2.3 Electromagnetic torque

The combination of Equation 2.11, 2.13 and 2.14 yields the electromagnetic torque, which can be expressed as:

$$\mathcal{T}_{em}(t) = \frac{\mathrm{d}^2\varphi}{\mathrm{d}t^2} \frac{1}{8} \sum_{i=1}^{n} m_i \left(D_{i,out}^2 + D_{i,in}^2\right) + f_v \left(\frac{\mathrm{d}\varphi}{\mathrm{d}t}\right) \frac{D_{ps}^2}{4} \,, \tag{2.15}$$

where the subscript i is related to the rotating parts of the piston assembly. The obtained value is used for the servo motor control.

2.2.2.4 Gas torque

There is no influence of the forces induced on the piston by the gas pressures acting in tangential directions since the openings are symmetrically located resulting in the sum of the torques being equal to zero.

2.3 Thermodynamic model

For the description of the processes taking place in volumetric machines during their operation, multiple thermodynamic compressor models are available in literature, i.e. [43–46]. Mostly, these models are used for compressor parametric studies, performance assessment or a design optimization. Such models provide a very good accuracy of the pressure and temperature estimation, however, a relatively high complexity of such models makes them unsuitable for control applications. Typically, the calculation process involves multiple iterations and can not always converge. This is not an issue at the design stage but the model meant for real time predictive control needs to be simplified in order to reduce the computation time and to guarantee a robust operation. This model uses the piston geometry and position as input and calculates the working fluid thermodynamic parameters by means of CoolProp library. This library implements equations of state and transport properties of pure and pseudo-pure fluids and provides it to the kinematic model. The goal of this study is to develop a robust and computation efficient algorithm dictating the piston motion.

2.3.1 Control volume method

In order to describe the energy flows in the considered system, a control volume (CV) method is used. The control volume shown in Figure 2.13 consists of two sub-volumes: one volume, CV_1, is formed by the inner wall of the sleeve piston, its separating partition and the transversal wall of the stator coil. The other one, CV_2, is an annulus between the housing, the stator and the piston flange. The piston diameter D_{ps} and the displacement x defines the total volume:

$$\frac{\mathrm{d}V}{\mathrm{d}t} = \frac{\pi D_p^2}{4}\frac{\mathrm{d}x}{\mathrm{d}t}\,. \tag{2.16}$$

Two clearances numbered in Figure 2.13 must be distinguished:

1. The working chamber is sealed between the piston outer wall and the cylinder. This clearance must be kept as small as possible. From the literature, the maximum of the volumetric efficiency of the machines with comparable dimensions, was found for the gap size in range of 5–10 µm [47], Sher [48] suggests the gap size to be around 20 µm. With a smaller gap size, the friction losses become dominant, while a larger gap leads to a drastic increase of the leakage flow rate and decrease of the volumetric efficiency. This clearance also influences the leakage flow rate bypassing the expander from the inlet to the outlet port in circumferential direction. More detailed overview of the leakage paths is provided in Section 2.5 and is illustrated in Figure 2.25.

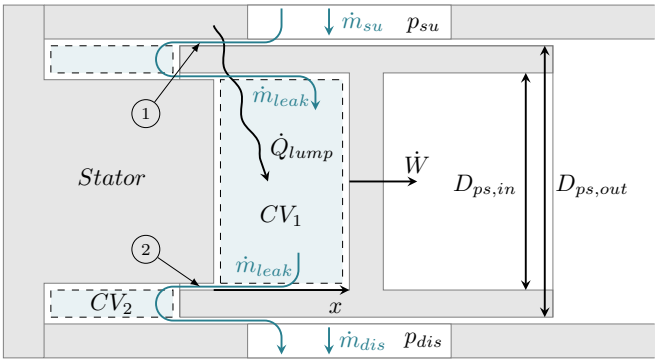

Figure 2.13: Control volume.

2. The clearance between the piston's inner wall with magnets attached and the stator is mainly defined by the FPLA design. The influence of the air gap size and eccentricity on the efficiency and the dynamics of a permanent magnet machines can be found in literature [49, 50]. The larger air gap thickness between the stator and rotor of the motor results in a high eddy current loss. Furthermore, for the current design, the temperature of the stator is expected to be higher than this of the rotor. This can lead to a decrease of the air gap size at high temperatures because of different thermal expansion of these parts. Typically, the gap size varies from fractions to several millimeters. The optimization of this parameter is out of the scope of the current study.

The expander is proposed to be used at relatively high temperatures. If an appropriate lubricant can not be found, the only way to minimize the leakage flow rate is to make the clearance (1) as small as possible.

At the beginning of the piston stroke, during the intake process, the piston speed is increasing from zero, so the pressure drop across the channel (2) is minimal. Even if the pressure drop becomes significant at low values of the clearance and the pressure in CV_2 differs from one in CV_1 remarkably, the surface of the piston flange is much smaller than the surface of the central partition. Therefore, the influence of the pressure drop on the piston dynamics can be neglected. At this point, the priority of the modeling is to provide a fast computable estimation of the gas force even with a limited accuracy. The error is then compensated by the second stage of the cascaded controller.

The wall thickness of the piston is dictated by the maximum working pressure and the size of the magnets attached to the inner surface. For the current study, the total wall thickness is assumed to be equal to 5 mm and the clearance between the motor stator and the surface of the magnets is 0.5 mm.

The main disadvantage of a larger clearance is a larger dead volume which limits the maximum expansion ratio. Therefore, a careful optimization of the clearance size is required both for the desired FPLA dynamics and the volumetric efficiency of the expander. For the piston diameter of 80 mm end the stroke length of 300 mm, the dead volume will be equal to 2.2 %.

2.3.2 Overall energy balance

The conservation of energy of an open control volume in the general form can be written as:

$$\frac{\mathrm{d}E_{CV}}{\mathrm{d}t} = \dot{Q}_{CV} + \dot{W}_{CV} + \sum_i (\dot{m}e)_i \,, \tag{2.17}$$

where $\dot{Q}_{CV}$ is the heat transfer rate of the working fluid in the control volume with its boundaries, $\dot{W}_{CV}$ is the indicated work done by the control volume (expander) or done on the control volume (compressor), $\dot{m}$ are the mass flow rates to and from the control volume and $(\dot{m}e)_i$ is the energy rate associated with each flow stream entering or leaving the CV which are:

- $\dot{m}_{su}$ – the mass flow rate during the intake;
- $\dot{m}_{dis}$ – the mass flow rate during the discharge;
- $\dot{m}_{leak,i}$ – the i-th leakage mass flow rate.

The change in specific potential energy and specific kinetic energy are neglected because of the geometry of the machine considered and due to the fact that the gas has low-density and the velocities at in- and outlet ports are comparable, respectively. The Equation 2.17 gives the change of the internal energy of the working fluid inside the CV:

$$\frac{\mathrm{d}U_{CV}}{\mathrm{d}t} = \dot{Q}_{CV} + \dot{W}_{CV} + \sum_i (\dot{m}h)_i \,, \tag{2.18}$$

where h is the specific enthalpy of each flow.

The working fluid entering the expander is cooled down since the expander wall temperature is typically between the in- and the outlet temperature of the working medium. The mass and the thermal conductivity of the piston and the housing is much larger than the one of the admitted working fluid, therefore the spatial gradients of the wall temperature can be neglected. Both chambers work alternately, therefore in steady state the wall temperature can be assumed constant in time.

By taking into account a compact design and the fact that the alternator is embedded into the same housing, all expander components including the alternator, form a lumped mass with a uniform temperature T_{lump} , which is shaded in

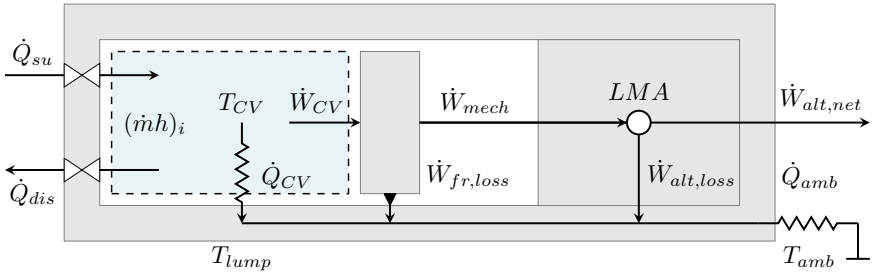

Figure 2.14: Expander single-lump energy balance schematics.

gray in Figure 2.14. The temperature of the lumped mass varies less than ± 1°R (or around ± 0.56 K), as shown by the experimental study conducted by Adair et al. [51]. Hence, a single-lumped model is implemented.

The major heat sources flows into or from CV are associated with:

- $\dot{Q}_{su}$ – admitted working fluid.
- $\dot{Q}_{dis}$ – working fluid leaving the expander.
- $\dot{Q}_{amb}$ – heat flow to the ambient through the expander walls.
- $\dot{W}_{fr,loss}$ – friction losses.
- $\dot{W}_{alt,loss}$ – alternator losses.

The work associated with the control volume $\dot{W}_{CV}$, being reduced by the friction and alternator losses, $\dot{W}_{fr,loss}$ and $\dot{W}_{alt,loss}$ respectively, results in the net work delivered by the LMA, $\dot{W}_{alt,net}$ as follows:

$$\dot{W}_{alt,net} = \dot{W}_{CV} - \dot{W}_{alt,loss} - \dot{W}_{fr,loss}\,, \tag{2.19}$$

The mentioned losses are being transformed into heat and this heat is injected into the lumped mass. Under steady state conditions, the energy balance of the lumped mass can be written as follows:

$$\dot{Q}_{CV} + \dot{W}_{fr,loss} + \dot{W}_{alt,loss} - \dot{Q}_{amb} = 0\,, \tag{2.20}$$

where $\dot{Q}_{CV}$ and $\dot{Q}_{amb}$ are the functions of the lumped mass temperature, T_{lump}.

2.3.2.1 Heat transfer between fluid and lumped mass

The heat transfer between the working fluid and the lumped mass is described by Newton's law of cooling:

$$\dot{Q}_{CV}(t) = h(t) \cdot A_{CV}(t) \cdot (T_{CV}(t) - T_{lump})\,. \tag{2.21}$$

where $\dot{Q}_{CV}$ is the heat flux from or to the working medium, A_{CV} is the expander surface participating in a heat exchange, T_{CV} is the gas temperature inside the working chamber and T_{lump} is the lumped temperature. The heat transfer mechanism inside the working chamber is assumed to be dominated by a forced convection. There are several correlations, available in literature, for calculation of in-cylinder convective heat transfer coefficient h, for example, the Eichelberg correlation [52], the Woschni correlation [53] and the Hohenberg correlation [54]. These correlations, applied to a high stroke/diameter ratio reciprocating Ericsson engine, have been compared by [55]. Authors analyzed the impact of the in-cylinder heat transfer on the engine parameters. Despite the fact that the temperatures of the working fluid in the engine components were clearly affected, the fluid mass flow rate and the net power output did not change significantly.

Disconzi et al. [56] performed a numerical analysis of in-cylinder heat transfer for a reciprocating compressor operating with different fluids. Authors compared the obtained results with several most used correlations. The Woschni correlation was found to be best matching with simulation results, especially at high pressures when the impact of the gas force estimation is the most important. Therefore it was decided to use the Woschni correlation with some adjustments in the current model.

In his research, Woschni used non-SI units, such as $kcal/\left(m^2h^{\circ}\mathrm{C}\right)$ for the heat transfer coefficient h and kp/cm^2 for the cylinder pressure, so the correlation is rewritten in order to be used with SI-units:

$$h(t) = 0.012997 D_{cyl}^{-0.2} p_{cyl}(t)^{0.8} \left(C_1 \cdot \bar{v}_{ps}\right)^{0.8} T_{lump}(t)^{-0.53}, \tag{2.22}$$

where $\bar{v}$ is the average piston velocity, p_{cyl} is the cylinder pressure in pascal. The constant C_1 is equal to 6.18 taking into account a higher flow turbulence during the scavenging period of an ICE. The flow pattern of intake phase of the expander is similar, so the same value can be used. When the expansion takes place, C_1 becomes equal to 2.28 since the turbulence is lower at that moment. These coefficients are affected by the geometry of a particular machine and therefore might be adjusted. Furthermore, the working fluid properties may affect the heat transfer significantly. Experiments performed by [57] with a combustion engine fed by hydrogen, revealed a significant estimation error of the results obtained from the model calibrated for methane. Therefore, this correlation must be re-calibrated for each specific operating conditions. Woschni developed his correlation for fossil-fueled engines and he used several simplifications, explained in [58], which are only valid for air. If a working fluid with a high molecular weight is used, the aforementioned simplified Woschni correlation should be replaced by a more general one including the gas properties as suggested by the authors.

In contrast with an ICE, the heat flux direction in an expander is not constant. The temperature of the admitted working fluid is higher than the lumped temper-

ature, so the working medium is cooled down both due to expansion and the heat exchange with the lumped mass. After the equalization of these temperatures, the direction of the heat flux alters. In order to solve the energy balance of the current setup, the lumped temperature must be found. For the first iteration, this temperature can be assumed as the average between the in- and outlet gas temperatures:

$$T_{lump} = \frac{T_{su} + T_{dis}}{2} \,. \tag{2.23}$$

In a real expander, surface temperatures of different parts can be different. For instance, the integrated alternator temperature can be higher than the piston one hence the coils dissipate heat inside the working chambers while the piston and the housing walls absorb the heat from the working fluid being cooled to the ambient. Therefore, the correlation can be applied to each surface separately or the lumped temperature can be averaged from several temperature sensors, providing the necessary input for the model. This can help avoiding an iterative solving scheme and reducing the computation time.

2.3.2.2 Heat transfer to the ambient

The heat transfer mechanism from the housing to the ambient is strongly dependent on the surrounding equipment. For instance, if the expander is placed close to the engine exhaust manifold, the impact of radiative heat transfer can become significant. If there is an air circulation due to the operation of the radiator fan, the forced heat transfer mechanism must be considered. For a test setup, a free convection heat transfer model can be used. Generally, in contrast with compressors which are normally cooled in order to achieve maximum performance, heat losses from expanders are undesired.

If an expander is not insulated, the free convective heat transfer to the ambient can be calculated using an appropriate correlation for the Nusselt number, Nu, substituted into a general equation for the heat transfer coefficient:

$$h = \frac{k}{L} Nu \,, \tag{2.24}$$

where k is the thermal conductivity and L is the characteristic length. Several cases of heat transfer from horizontal cylinders are listed in [59]. A similar geometry as in this work, namely 20.5 mm $\leq D \leq$ 89 mm and $34 \leq L/D \leq 147$, where L is the length of the cylinder and D is its diameter, was studied by Wamsler. The Nusselt number for this case can be written as:

$$Nu = 0.480 (GrPr)^{0.25} \,, \tag{2.25}$$

for $3 \times 10^4 \leq GrPr \leq 3.5 \times 10^6$, where Gr is the Grashof number which express the ratio of the buoyancy to viscous force acting on a fluid and Pr is the

Prandtl number, which is defined as the ratio of momentum diffusivity to thermal diffusivity and it can be expressed as:

$$Pr = \frac{\mu c_p}{k}\,, \tag{2.26}$$

where μ is the dynamic viscosity, c_p is the specific heat capacity. The value of Grashof number can be calculated for horizontal pipes as:

$$Gr = \frac{g\beta\left(T_{lump} - T_{amb}\right)D^3}{\nu^2}\,, \tag{2.27}$$

and for horizontal plates as follows:

$$Gr = \frac{g\beta\left(T_{lump} - T_{amb}\right)L^3}{\nu^2}\,, \tag{2.28}$$

where g is the gravitational constant, β is the coefficient of thermal expansion, T_{lump} is the lumped temperature, T_{amb} is the ambient temperature, L is the characteristic length, D is the diameter of a cylindrical part, ν is the kinematic viscosity.

The heat transfer from the expander flanges and possible flat surfaces can be described by the correlation provided by [60].

$$Nu = \left(0.825 + \frac{0.387\left(GrPr\right)^{1/6}}{\left(1 + \left(\frac{0.492}{Pr}\right)^{9/16}\right)^{8/27}}\right)^2 \tag{2.29}$$

In order to reduce the heat transfer of the expander with the ambient, aerogel insulation can be applied, which parameters are quite suitable for this application: the thermal conductivity: 0.016 W/(m · K), temperature range: from –200°C to +650 °C. The overall heat transfer coefficient UA_{amb} for reciprocating machines, reported in the literature, ranges from 2.5 W/K [61] to 6.38 W/K [62, 63].

2.3.2.3 Frictional losses

The only source of the friction heat is the interface between the piston and the cylinder. The mechanical power needed to compensate the friction losses can be calculated as follows:

$$\dot{W}_{fr}(t) = F_{fr}(t)\frac{\mathrm{d}x}{\mathrm{d}t}\,, \tag{2.30}$$

where, F_{fr} is the friction force explained in Section 2.2.1.2 and x is the piston position. The friction losses from the rotation can be calculated in the same way. This work is transformed into heat and can be substituted into Equation 2.19.

Temperature, K	293	300	350	400	500
Specific resistivity, $10^{-8}\Omega \cdot$ m	1.678	1.725	2.063	2.402	3.090

Table 2.3: Annealed copper electric resistivity. Source: [67].

2.3.2.4 Alternator losses

The following losses occurring in an alternator [64]:

- Copper loss: ohmic heating of the field winding. The heat produced by the current in the winding is expressed as follows:

$$P_{Cu} = nI^2R = nI^2\frac{4\rho L}{\pi D^2}\,, \tag{2.31}$$

where n is the number of phases, I is the current in one of the phases and R is the winding resistance, which is, in turn, the function of the wire length L, the wire cross-section area defined by the diameter D, and the material specific resistivity ρ. Typically, the value of $1.7241 \times 10^{-8}\ \Omega \cdot$ m is used as a reference at 20 °C according to the International Annealed Copper Standard (IACS) established in 1914 [65]. However, modern commercially available pure copper wires may have the conductivity up to 103 % IACS since manufacturing technologies allows to remove the impurities much better than at that time. The resistivity change as a function of temperature is linearly approximated as:

$$\rho = \rho_{ref}(1 + \alpha(T - T_{ref}))\,, \tag{2.32}$$

where α is the temperature coefficient of resistivity. For copper at 20 °C it is equal to 3.93×10^{-3} Ω/°C.The accuracy of the approximation is acceptable for engineering purposes in a limited range of the temperature variations [66]. Alternatively, experimental data can be used [67]. The values of the electric resistivity of annealed copper for the target temperature range are provided in Table 2.3.

- Iron loss: caused by eddy current and hysteresis losses in the core iron. The core is made of electromagnetic steel and therefore conducts the electric current, inducted by the alternating magnetic field, which causes ohmic losses. In order to reduce this effect, the core is assembled from multiple plates insulated from each other by a laminating coating. The total core losses can be expressed as follows:

$$P_{iron} = K_hB^2f + K_c(Bf)^2 + Ke(Bf)^{3/2}\,, \tag{2.33}$$

where K_h , K_c , and K_e are the coefficients of hysteresis loss, classical eddy current loss, and excess eddy current loss which can be found in specifications of the manufacturers or in other literature. B is the peak flux density. Equation 2.33 is valid only for sinusoidal excitation field. However, linear alternators or motors are controlled by inverters, the source of harmonics. Furthermore, the movement in linear applications is typically unsteady. Therefore, a more accurate model of core losses, explained in [68] must be used.

- Power electronics loss, P_{elec}. These are represented by switching losses and semiconductor conduction losses. Since for the current design, the condenser temperature is expected to be about 80 °C, the power electronics can be cooled by the condensed working fluid. In this case, this heat input must be also taken into account.

The total heat rate from the LMA to the working fluid is:

$$\dot{W}_{alt,loss} = P_{Cu} + P_{iron} + P_{elec}\,. \tag{2.34}$$

As reported by [69], the overall efficiency of a linear motor is very low under low speed and load conditions due to the domination of copper losses over the energy production. This is the case during the acceleration of the piston. The use of magnetic springs can assist the piston to accelerate faster and will reduce the use of power electronics during this period.

2.3.3 Analysis of the pressure-volume diagram

Another way to express the work delivered by the system is the use of pV-diagram (Figure 2.16). The work is the area under the expansion curve which can be written as:

$$\dot{W}_{alt} = \Delta p_{cyl} \frac{\mathrm{d}V}{\mathrm{d}t} = \Delta p_{cyl} \frac{\pi D^2}{4} \frac{\mathrm{d}x}{\mathrm{d}t}\,, \tag{2.35}$$

where Δp_{cyl} is the pressure difference across the central element and $\frac{\mathrm{d}x}{\mathrm{d}t}$ is the piston velocity shown in Figure 2.17. This profile is obtained in Section 2.2 and it is defined by the moving mass and the acting forces. When the piston starts to move from its left dead point (LDP) to its right dead point (RDP), it is accelerated by the gas force and the electromagnetic force until the maximum speed is reached. Then the piston is decelerated by the electromagnetic force so the kinetic energy is transformed into electricity. In contrast with a classic crankshaft mechanism, this profile can be flexibly adjusted. The only limitation is the alternator velocity/force characteristics. An example of the realization of such a control algorithm is depicted in Figure 2.15.

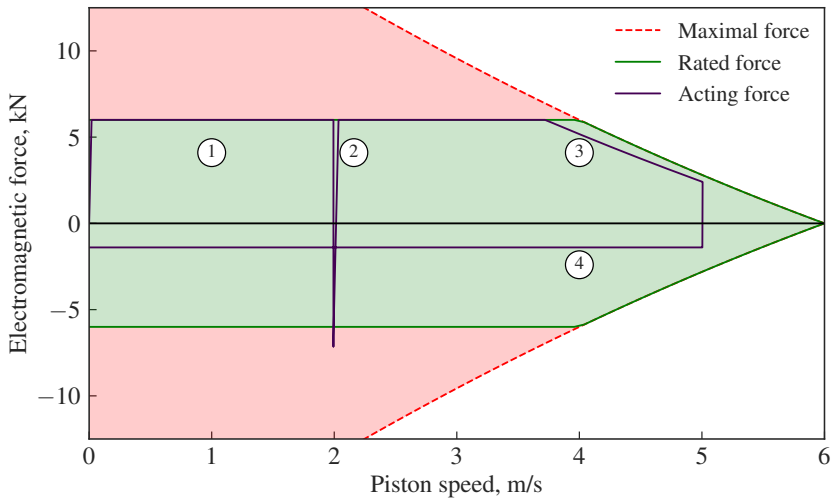

Figure 2.15: Applied electromagnetic force in function of the piston speed.

1. The piston is accelerated by LMA since there is no sufficient pressure difference over the piston to initialize the movement. When the inlet port is open, the pressure in the working chamber rises and at a certain moment reaches the supply pressure. The piston accelerates under two forces: the gas force and the electromagnetic force.

2. At the end of the intake process, the thrust force is adjusted in order to keep the piston speed constant and to provide additional time for the intake process. At this moment, the piston rotation is synchronized with the linear movement in order to set the desired volume ratio.

3. Depending on the LMA characteristics, the electromagnetic force is adjusted in order to keep the piston motion controlled around the maximum allowed speed.

4. The maximum piston speed is reached. From now on, the piston must be decelerated and stopped at the end of the stroke, the electromagnetic force reverses, the energy recovered from the piston inertia is transformed into electricity. During this phase, the expansion process continues. The required electromagnetic force is calculated as described in Section 2.2.

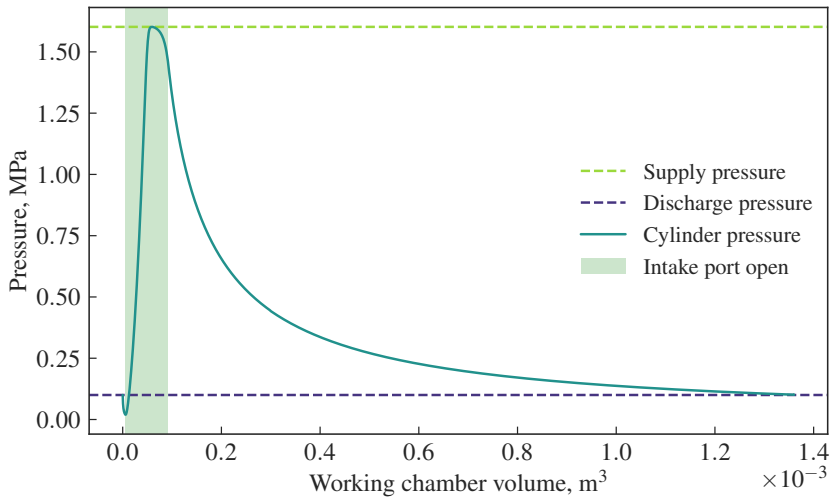

Figure 2.16: pV-diagram of the expansion process.

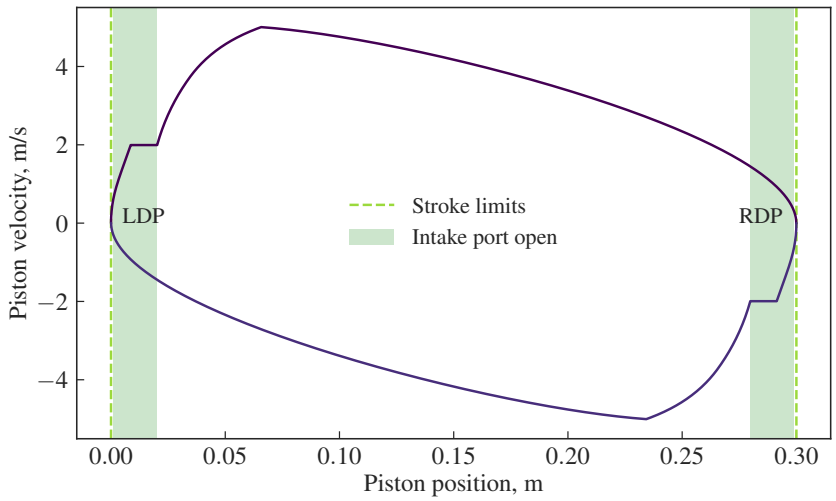

Figure 2.17: Simulated piston speed.

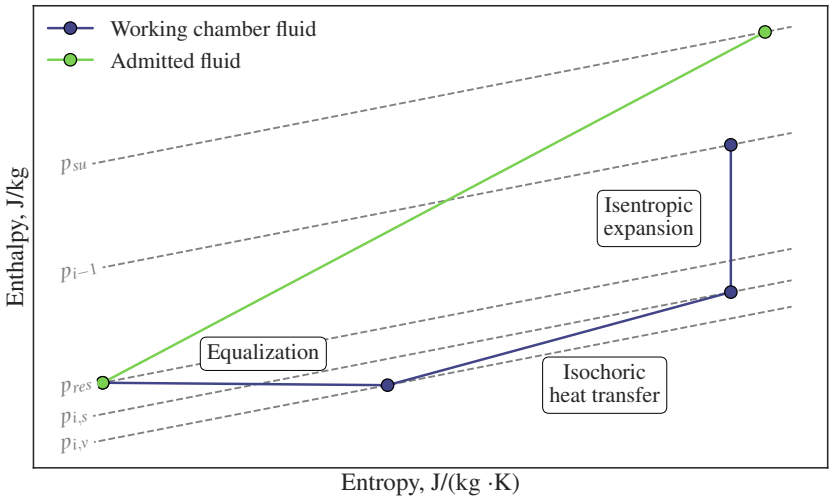

Figure 2.18: Schematic illustration of the intake process.

2.4 Overall mass balance

In order to use Equation 2.3.3 and Equation 2.10, the cylinder pressure p_{cyl} needs to be calculated. While the piston reciprocates and rotates simultaneously, three phases of the pressure change occur consequentially during one complete working cycle of the expander: intake, closed expansion and discharge.

2.4.1 Intake process

The intake process is modeled as a sequence of elementary thermodynamic processes within a small time step as shown in Figure 2.18:

1. The working fluid in the working chamber undergoes isentropic expansion from pressure p_{i-1}, obtained in the previous time step, to $p_{i,s}$. The pressure in the working chamber remains lower than p_{su}.

2. Isochoric heat transfer from the working fluid to the lumped mass takes phase. The working fluid cools down, the pressure decreases from $p_{i,s}$ until p_v.

3. Driven by the pressure difference across the inlet port, the working fluid from the supply line enters the working chamber.

4. Equalization. The admitted fluid is being mixed with the working fluid in the working chamber. The resulting cylinder pressure p_{res} will be used in

the next time step.

2.4.1.1 Isentropic expansion

At the beginning of the piston travel from one dead point to another, the pressure in the expanding working chamber is equal to the discharge pressure. Therefore, the piston movement must be started by means of the LMA until the intake phase begins and the pressure difference over the piston induces the gas force. The mechanical model provides the piston displacement for a given small time step. The relationship between the volume ratio and the change of other thermodynamic parameters of the working fluid undergoing isentropic expansion can be calculated by means of CoolProp [86] as follows:

$$\begin{cases} \rho_{i,s} & = \rho_{i-1} \dfrac{V_{i-1}}{V_i} \,, \\ p_{i,s} & = f\left(\rho_{i,s}, s_{i-1}\right) \,, \\ T_{i,s} & = f\left(\rho_{i,s}, s_{i-1}\right) \,. \end{cases} \tag{2.36}$$

where the index $i-1$ means the conditions before and the index i — after the expansion process, p is the pressure, T is the temperature, and ρ is the mass density of the working fluid.

2.4.1.2 Heat transfer

The heat transfer process between the lumped mass and the working fluid is previously explained in Section 2.3.2. The temperature and pressure of the working fluid changes isochoric due to the heat flux from or to the lumped mass:

$$\begin{cases} T_{i,V} & = T_{i,s} - \dfrac{\dot{Q}_{i,cyl} \Delta t}{m_{i,cyl} c_V} \,, \\ p_{i,V} & = p_{i,s} \dfrac{T_{i,V}}{T_{i,s}} \,. \end{cases} \tag{2.37}$$

where $m_{i,cyl}$ is the mass of the working fluid inside the working chamber at time step i, c_V is the specific heat capacity at constant volume. The heat flux from the working fluid to the lumped mass is considered to be positive.

2.4.1.3 Throttling through the opening

When the openings in the piston walls are being aligned as shown in Figure 2.19, the working fluid enters the expanding chamber driven by the pressure difference between the supply pressure, p_{su}, and the pressure inside the working chamber, $p_{cyl} = p_{i,s}$, calculated in the previous step. The pressure difference equalizes as

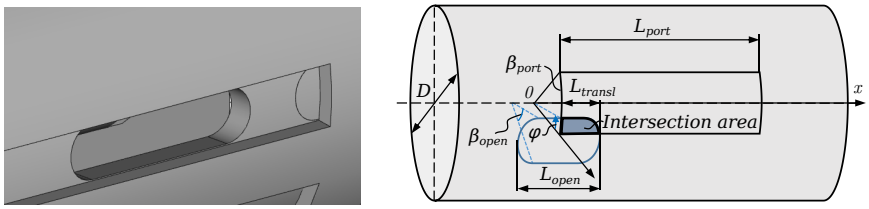

(a) Intake area (b) Intersection geometry

Figure 2.19: Port intersection area.

the working fluid enters the working chamber. The pressure ratio across the port defines the flow type. The flow is choked and the mass flow rate is independent on the pressure downstream if the pressure ratio is lower than the critical one, which can be calculated as follows:

$$\frac{p_{cyl}}{p_{su}} = \left(\frac{2}{\gamma+1}\right)^{\frac{2}{\gamma-1}} . \tag{2.38}$$

In this case, the mass flow rate through the inlet port is calculated by using an isentropic compressible flow model and it is expressed by:

$$\dot{m}_{adm}(t) = C_d S_{area}(t) \sqrt{\frac{2\gamma}{(\gamma+1)} p_{su}\rho_{su} \left(\frac{2}{\gamma+1}\right)^{\frac{2}{\gamma-1}}} , \tag{2.39}$$

where C_d is the discharge coefficient and S_{area} is the inlet port area. As the pressure difference equalizes, the pressure ratio becomes higher than the critical one. For this flow type, Equation 2.40 is applied:

$$\dot{m}_{adm}(t) = C_d S_{area}(t) \sqrt{\frac{2\gamma}{\gamma-1} p_{su}\rho_{su} \left[\left(\frac{p_{cyl}(t)}{p_{su}}\right)^{\frac{2}{\gamma}} - \left(\frac{p_{cyl}(t)}{p_{su}}\right)^{\frac{\gamma+1}{\gamma}}\right]} . \tag{2.40}$$

In general, the mass flow rate through the inlet port, $\dot{m}_{adm}$, is a function of the inlet pressure p_{su}, the cylinder pressure, p_{cyl}, and the inlet port area, S, which is expressed as a conjunction of the port area and the opening area in function of time:

$$S_{area}(t) = (S_{port} \wedge S_{open}) n_{port} , \tag{2.41}$$

where n_{port} is the number of inlet ports. As it can be seen, the rotation and the translation of the piston define the area of the expander inlet port since it is formed by the overlap of the opening in the cylinder wall and the opening in the piston

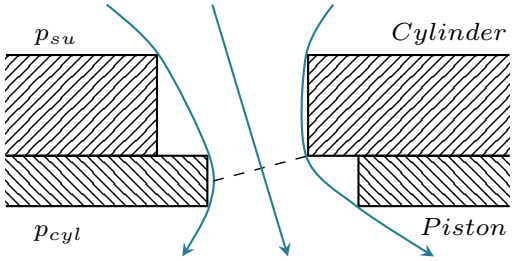

Figure 2.20: Flow through the inlet port.

wall. Both might require an optimization and therefore are defined as arbitrary n-vertex polygons with coordinates:

$$\begin{cases} Port & = ([x_j],\ [y_j]),\ j = 1, ..., n_{port}) \,, \\ Opening & = ([x_k],\ [y_k]),\ k = 1, ..., n_{open}) \,, \end{cases} \tag{2.42}$$

where the Cartesian coordinate y is related to the cylindrical one β as follows: $y = \beta D_{ps}/2$, where D_{ps} is the piston outer diameter. The set of coordinates of the conjunction of two polygons can be obtained by using Vatti's clipping algorithm [70], which is included in the Pyclipper package[4]. The area of the resulting polygon is calculated by means of so called Gauss' shoelace formula also known as Surveyor's area formula [71], which is expressed as follows:

$$S_{area} = \frac{1}{2}(x_1y_2 - x_2y_1 + x_2y_3 - x_3y_2 + ... + x_{n-1}y_n - x_ny_{n-1} + x_ny_1 - x_1y_n) \tag{2.43}$$

The discharge coefficient C_d is the ratio of the actual and ideal mass flow and it depends on multiple factors, whereof the most significant are:

- pressure ratio across the opening,
- opening aspect ratio,
- opening geometry.

The discharge coefficient is higher at higher pressure ratios, as reported by [72, 73]. This fact was explained by Ward-Smith [74] by widening the area of the vena contracta which leads to a greater proportion of the flow field occupied by the through-flow while the separated flow area decreases. Applied to the current geometry, this phenomenon can be illustrated with Figure 2.20.

In order to obtain a correlation for a given pressure ratio, the upper plot in Figure 2.22 is extended as an asymptotic function. The value of C_d tends to unity at extremely high pressure ratios[5]. Assuming the discharge coefficient equal to

[4] https://pypi.python.org/pypi/pyclipper

[5] The author uses reciprocated notation of the pressure ratio in respect to the definition above.

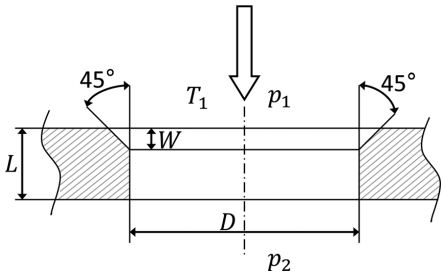

Figure 2.21: Orifice investigated in [73].

1 at infinitesimal pressure ratio, this curve has a horizontal asymptote of 1. The function fitting the plot can be written as follows:

$$C_d = 1 - 0.418 p_2/p_1 \,. \tag{2.44}$$

The length-to-diameter ratio L/D is also found influencing the discharge coefficient as it can be seen in Figure 2.22. The C_d value strongly decreases at L/D ratios below 0.75, which is the case of the middle part of the intake process in the current setup and therefore must be taken into account. For the current design, L is the sum of the piston and the cylinder wall thicknesses, which is equal to 15 mm. The diameter D can be substituted by the port hydraulic diameter D_H, which is for rectangular shape:

$$D_H = \frac{2ab}{a+b} \,, \tag{2.45}$$

where a and b are the port dimensions which are equal to:

$$a = max(x_{area}) - min(x_{area}) \,, \tag{2.46a}$$

$$b = max(y_{area}) - min(y_{area}) \,. \tag{2.46b}$$

The use of chamfered orifices, shown in Figure 2.21, gives the possibility to increase the discharge coefficient by 22–33 % depending on the chamfer angle. The angle of 25–30 °C is recommended in the above mentioned literature. There are no chamfers made in the port openings of the prototype, so this factor is neglected. However, it might be useful to make these in the advanced prototype.

Some experimental data for the discharge coefficient of non-circular orifices is also available in the literature. Novák and Koza [75] performed measurements of C_d for triangular, square and narrow slot orifices by measuring the flow rate of gas escaping to the ambient from a pressurized tank. The authors figured out that the C_d value of triangular orifices (T1.1 and T2.1) and narrow slots (S1 and S2) is typically higher than of circular ones (1_1, 1_3, 1_4 and 1_6) as shown in

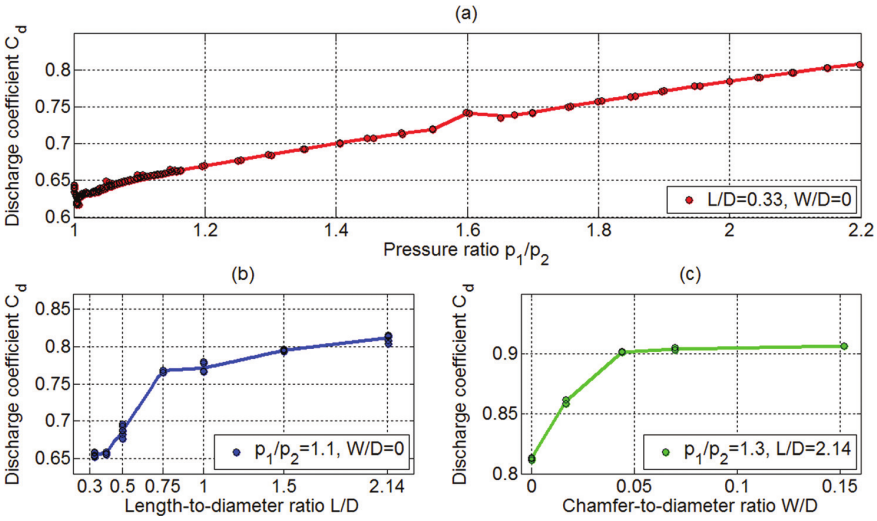

Figure 2.22: Factors influencing the discharge coefficient [73].

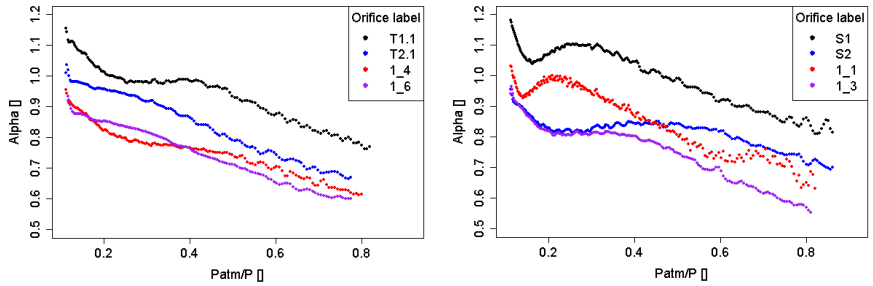

(a) Triangular vs. circular orifices.

(b) Narrow slots vs. circular orifices.

Figure 2.23: Discharge coefficient comparison of circular and non-circular orifices [75].

Figure 2.23, and this difference is larger for smaller orifices (T1.1 and S1), while the difference between circular and rectangular orifices is not significant.

As in many other publications, the discharge coefficient increases almost linearly if the pressure upstream the flow increases. This increase continues until the pressure ratio becomes critical, then it flattens. Here, a unexpected rise of C_d (α in the paper) above 1.0 is shown which can indicate an incorrectness of the theoretical model used by the authors. The discharge coefficient may not exceed 1.0 for the chocked flow. For further calculations, this region on the plots is neglected.

During the intake process in the current setup, the opening transforms from nearly triangular shape through a quasi rectangular one to a narrow slot at the end

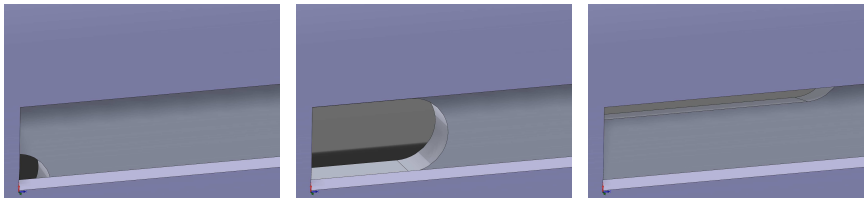

(a) Triangular inlet. (b) Rectangular inlet. (c) Narrow inlet.

Figure 2.24: Inlet opening transformation.

of the intake as shown in Figure 2.24. Summarizing the described experimental results, a custom correlation can be obtained:

$$C_d = f\left(\frac{p_{su}}{p_{cyl}}, \frac{L}{D}, \frac{W}{D}, shape\right) \tag{2.47}$$

For computational purposes, the factor $shape$ is formulated for the opening with the length a and the width b. The improvement of the discharge coefficient is expressed as a reduction of the difference between the ideal case $C_d = 1$ and the actual one:

- The shape is triangular if the surface area is equal to $\frac{ab}{2}$. So the impact of the triangularity on C_d can be expressed as

$$k_{tri} = \left(2 - \frac{2 \cdot S_{act}}{ab}\right) \cdot 10\% = 0.02\left(1 - \frac{S_{act}}{ab}\right), \tag{2.48}$$

  where the factor 0.1 or 10 % is the improvement for larger orifices and S_{act} is the actual intersection surface area. When the opening is quasi rectangular, $S_{act} \rightarrow ab$, the effect becomes zero.

- The improvement of the discharge coefficient is assumed 20 % for a smaller orifice and 10% for a larger one. Knowing the dimensions of both orifices, the size correction factor can be expressed as:

$$k_{size} = 0.1\left(1 + 0.2448 \cdot S^{0.991}\right). \tag{2.49}$$

- The shape is assumed as a narrow slot if $a \gg b$. For computational purposes the correction coefficient can be approximated as follows:

$$k_{slot} = 1 - e^{\left(1 - \frac{a}{b}\right)} \tag{2.50}$$

The total improvement of the discharge coefficient C_d can be expressed as a sum of all mentioned factors, however, the resulting coefficient may not exceed the unity. Therefore, the resulting form of Equation 2.47 can be written as follows:

$$C_{d,\,corr} = 1 - (1 - C_d)\,(1 - k_{size} - k_{tri} - k_{slot})\ . \tag{2.51}$$

The obtained value is further substituted into Equation 2.39 and Equation 2.40. When the maximum possible mass flow rate is obtained, it is multiplied by the time step in order to calculate the mass of the working fluid which theoretically can enter the working chamber. This value is further compared with the mass of the working fluid which is needed to cancel the pressure difference across the port opening. The smallest value is then used in the calculations.

The second way for the working fluid to enter or to leave the working chamber is one through a clearance between the piston and the cylinder walls. The method for the leakage mass flow rate calculation is explained in Section 2.5. The leakage mass flow rate can be both positive and negative depending on the pressure gradient. Both, the intake and the leakage mass flow rates are summarized and are used for the next step.

2.4.1.4 Equalization

After a certain amount of the working fluid is admitted to the working chamber through the intake port and some fluid has escaped or entered the working chamber through the piston clearance, the temperature of the resulting mass of the fluid equalizes. The resulting enthalpy of the working fluid at a time step i, $h_{i,res}$, can be calculated as follows:

$$h_{i,res} = \frac{m_{i,s}h_{i,s} + m_{i,adm}h_{i,adm} + m_{i,leak}h_{i,leak}}{m_{i,s} + m_{i,adm} + m_{i,leak}}\,, \tag{2.52}$$

where the subscript s means the state of the working fluid after isentropic expansion, adm is the state of the admitted fluid, $h_{i,adm}$ is calculated at p_{su} and $leak$ is the state of the working fluid entering the working chamber through the piston clearance. This process is isochoric, therefore, the state change of the working fluid can be written as follows:

$$\begin{cases} T_{i,res} &= f(h_{i,res}, \rho_{i,res})\,, \\ p_{i,res} &= f(h_{i,res}, \rho_{i,res})\,, \end{cases} \tag{2.53}$$

where $\rho_{i,res} = (m_{i,s} + m_{i,adm} + m_{i,leak})\,/V_i$.

2.4.2 Expansion

When the port area becomes equal to zero and the intake process finishes, the expansion process starts seamless. The leakage flow remains the only source of

the change in the mass of the working fluid inside the chamber. This process is simulated in the same way as the intake process.

2.4.3 Discharge

The discharge process is simulated using the same correlations with the high and the low pressures sides altered and the larger cylinder wall opening for the calculation of the port area. The highest pressure is then p_{cyl} and p_{dis} is the lowest one.

2.5 Leakage flow model

Leakages in reciprocating machines are the major source of losses beside friction and throttling losses during the intake and discharge. The working fluid bypasses the expander through the leakage paths which results in a reduction of the produced useful work. This issue, applied to compressors, is very well covered in literature [76, 77]. Most of the available models are developed for reciprocating machines with compression rings and a simpler geometry. In a classic piston compressor, only an axial leakage flow across the piston from the high pressure side to a lower pressure side is present.

For the current design, an advanced leakage flow model is required due to the piston shape and an additional circumferential leakage flow from a high pressure port to a lower pressure one. A literature study gives some clues for a model development. For instance, Lohn [78] analyzed two models of non-compressible and compressible flow between two plates, developed by Ferrara [79] and Zuk [80] respectively. Both models were compared with CFD simulations for a stationary and a moving piston. The best results were obtained for a compressible flow model, however, a correction regarding the piston speed must be applied. This deviation of maximum 30 % has almost a linear dependency on the piston speed. The tested range covers the expected speeds of the current design.

Some advanced models considering cavities and pockets in the cylinder are also available [81]. The pressure distribution along the piston is shown in Figure 2.25(b). The depth of the pockets made in a moving piston is larger than the clearance which results in the absence of a pressure drop across the pocket. The authors proposed a solution for similar problems arising in pneumatic applications where a precision positioning is required and high temperatures are possible. The latter limits the choice of lubricants which not only reduce the frictional force but also improve the sealing. In the current design, a worst case scenario is considered. The use of oils in the expander is avoided because of the target application: exhaust gas heat recovery. Taking into account the aforementioned, a simplified quasi two dimensional flow model is developed.

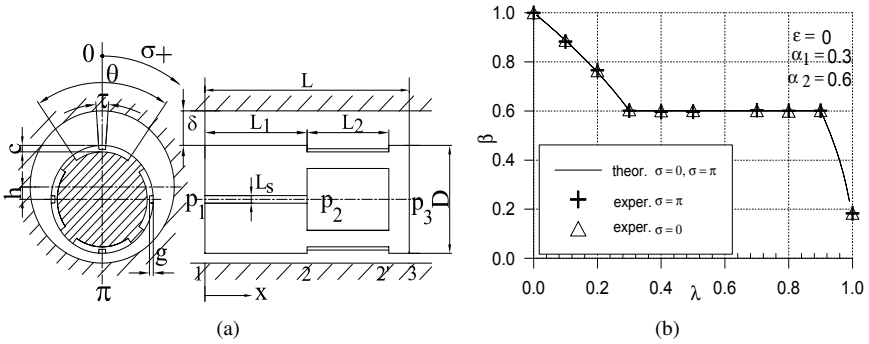

Figure 2.25: Slot type piston geometry (a) and the axial pressure distribution (b). Source: [82].

The space along the piston can be divided in three zones with different pressures and two transition zones with a certain pressure gradient as depicted in Figure 2.25. The location of the pressure in the expanding chamber p_{cyl} is similar to p_1 and the pressure in the discharging chamber p_{dis}, indicated as p_3. The pressure in the vicinity of the in- and the outlet ports, shown as p_2, is higher than p_{su} and lower than p_{dis} and must be defined separately by solving the equation in a circumferential direction. Similar to the axial direction, there are two inlet zones with the pressure p_{su}, two discharge zones with the pressure p_{dis} and four transition zones with different length as shown in Figure 2.26(a). The leakage flow paths in axial direction are shown in Figure 2.26(b). Based on this scheme, the following leakage paths can be identified:

1. inlet port (p_{su}) $\rightarrow$ outlet port (p_{dis});
2. expanding chamber (p_{dis}) $\rightarrow$ discharging chamber (p_{dis});
3. expanding chamber (p_{dis}) $\rightarrow$ outlet port (p_{dis});
4. inlet port (p_{su}) $\rightarrow$ expanding chamber (p_{cyl});
5. inlet port (p_{su}) $\rightarrow$ discharging chamber (p_{dis}).

These flows can be further simplified to the following two major flows:

- Circumferential flow from the inlet to the outlet ports: this flow is constant since the in- and outlet pressures do not change much during one piston stroke. The pressure distribution over this zone can be calculated first, assuming only a circumferential flow there.
- Axial flow between the port area and the working chambers: this flow alters its direction and magnitude accordingly to the pressure gradient.

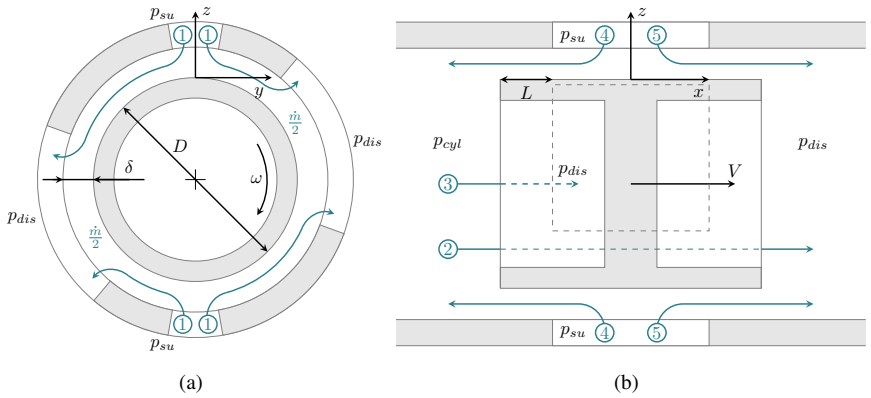

Figure 2.26: Circumferential (a) and axial (b) gas flow paths through the clearances.

Each flow path is further simulated as one-dimensional flow through a narrow channel between the piston and the cylinder walls. The flow is pressure-driven since it occurs due to a pressure gradient between two zones with different pressures. The following assumptions are taken:

- The influence of the piston speed on the mass flow rate is neglected at this point.
- There is no heat transfer between the working fluid and the expander walls inside the channel.
- Only the flow from or to the expanding chamber is important for control purposes since it affects the pressure inside the chamber and therefore the force acting on the piston.
- The flow from the in- to the outlet port bypasses the expander and therefore affects the machine volumetric efficiency. This flow is assumed to be only dependent on the pressure up- and downstream (p_{su} and p_{dis}).
- Due to this flow, there is a circumferential zone with a certain pressure gradient. The mean pressure over the cylinder perimeter is the back pressure for the flow from the expanding chamber.
- The flow from the circumferential zone to the discharging chamber does not affect the piston movement.

The flow through a narrow channel is illustrated in Figure 2.27. At the inlet of the channel, the flow accelerates isentropically along a virtual converging diffuser (0–1). The volume before the inlet of the channel is much larger than the

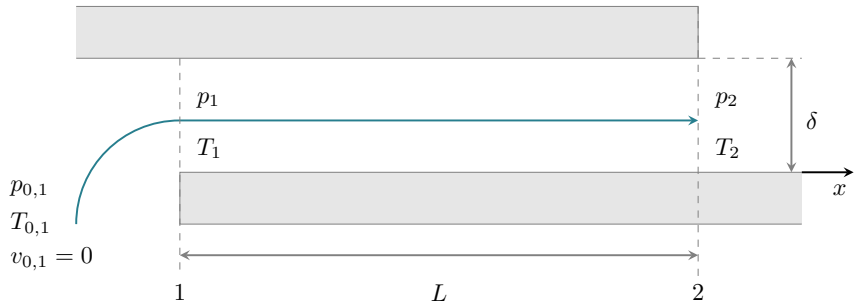

Figure 2.27: Flow through a piston / cylinder clearance.

channel volume. Therefore the gas velocity v_{01} can be assumed to be zero and therefore the pressure and the temperature of this volume are stagnation pressure and temperature $p_{0,1}$ and $T_{0,1}$ respectively. In a real application, these parameters are typically directly measured.

After entering the channel with the length L (1–2), the flow passes between the piston and the cylinder walls separated by an uniform clearance δ. The pressure drop is caused by friction. This type of flow is known as Fanno flow. At the outlet of the channel, the flow is either choked and therefore only dependent on the pressure upstream, or it is non-choked and the outlet pressure is equal to the pressure in the receiving volume, p_2. The solutions for the aforementioned problems can be found in literature, i.e. in [83] or [84]. By combining the sets of equations for both cases, the common unknown values can be found.

First, the set of equation for an isetropic flow can be expressed as functions of the Mach number as follows:

$$\begin{cases} p_1 = \dfrac{p_{0,1}}{(2 + (1-\gamma)M_1^2)^{\frac{\gamma-1}{\gamma}}}, \\ T_1 = \dfrac{T_{0,1}}{\frac{\gamma-1}{2}M_1^2 + 1}, \end{cases} \tag{2.54}$$

where M_1 is the Mach number at the inlet of the channel. However, this value is unknown, so one more equation is needed.

The Mach number for any point inside the channel can be found from the Fanno parameter Fa, which is defined by the channel geometry and the wall roughness. The relationship between the Mach number and the Fanno parame-

ter for given channel parameters is therefore:

$$Fa(M) = \frac{f}{D_H}(x^* - x) = \frac{1}{\gamma}\left(\frac{1-M^2}{M^2}\right) + \left(\frac{\gamma+1}{2\gamma}\right)\ln\left(\frac{(\gamma+1)M^2}{2+(\gamma-1)M^2}\right), \tag{2.55}$$

where f is the Darcy friction factor, D_H is the channel hydraulic diameter, x^* is the coordinate with $M = 1$ and x is the coordinate of interest. The hydraulic diameter D_H of an annulus can be calculated as follows:

$$D_H = \frac{4S}{P} = \frac{\pi((D+\delta)^2 - D^2)}{\pi((D+\delta)+D)} = D_{cyl} - D_{ps} = \delta\,, \tag{2.56}$$

where S - is the cross-sectional area, P is the wetted perimeter and δ is the piston/cylinder clearance.

Equation 2.55 is further rewritten for the in- and the outlet of the channel as follows:

$$\begin{cases} Fa(M_1) &= \dfrac{f}{\delta}(x^* - x_1)\,, \\ \\ Fa(M_2) &= \dfrac{f}{\delta}(x^* - x_2) = \dfrac{f}{\delta}(x^* - x_1 + L)\,, \end{cases} \tag{2.57}$$

Since $(x^* - x_2) = (x^* - x_1 + L)$, The system of equations 2.57 can be simplified assuming that the friction factor f and the ratio of the specific heats γ are constant along the whole channel length. The result is then expressed as:

$$Fa(M_2) = Fa(M_1) - \frac{fL}{\delta}\,, \tag{2.58}$$

The ratio of the pressure at an arbitrary coordinate in the channel and the critical one is given by the equation:

$$\frac{p}{p^*} = \frac{1}{M}\sqrt{\frac{1+\gamma}{2+(\gamma-1)\,M^2}}\,, \tag{2.59}$$

The ratio of static pressures across the channel can be obtained as follows:

$$\frac{p_2}{p_1} = \frac{p_2}{p^*}\frac{p^*}{p_1} = \frac{M_1}{M_2}\sqrt{\frac{2+(\gamma-1)\,M_1^2}{2+(\gamma-1)\,M_2^2}}\,. \tag{2.60}$$

If there is no pressure difference and, therefore, no flow, this ratio becomes equal to unity and it tends to zero at very high inlet pressures. The pressure $p_1$needs to be expressed in a different way since it is difficult to measure. Instead, $p_{0,1}$ can be used. By combining Equation 2.54 and Equation 2.60, the ratio of pressures before and after the leakage path can be written as follows:

$$\frac{p_2}{p_{0,1}} = \frac{M_1}{M_2}\sqrt{\frac{2+(\gamma-1)\,M_1^2}{2+(\gamma-1)\,M_2^2}}\,\left(2+(1-\gamma)M_1^2\right)^{\dfrac{1-\gamma}{\gamma}}\,. \tag{2.61}$$

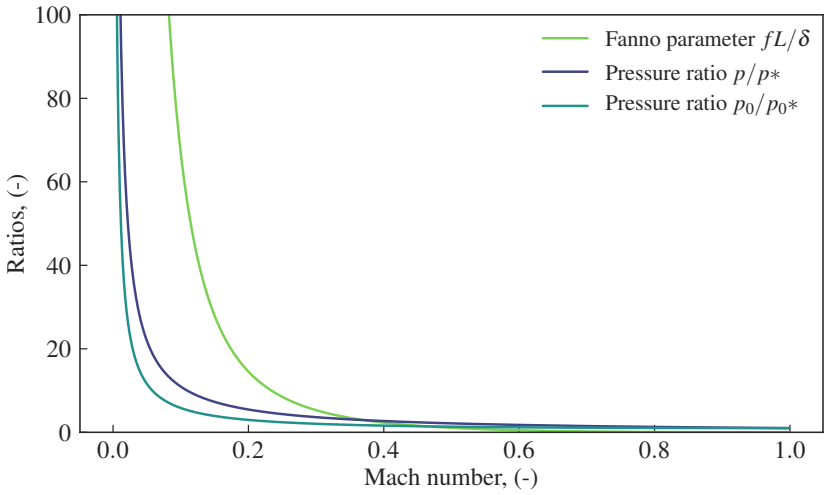

Figure 2.28: Ratios in function of Mach number.

The system of equations (Equation 2.58 and 2.61) is sufficient to calculate the unknown values of M_1, M_2 but can only be solved iteratively. The solver *nsolve* from *SymPy* package[6] was employed. However, the first trial revealed two major problems: a significantly low calculation speed caused by multiple iterations and uncertain convergence.

For very large Fanno parameter values fL/δ, corresponding with very small Mach numbers and vice versa, the solver produced unreliable results and frequently failed. As is illustrated in Figure 2.28, the plots of these regions are either too steep or too flat, which makes the iteration uncertain. Other equations involving Mach numbers at no flow conditions will produce "division by zero" numerical problem, so this range needs to be "patched" by using interpolation. Moreover, starting from a certain value of the pressure ratio close to unity, the solution for M_1, M_2 never converges to zero, obviously, for the same reason. The convergence is also strongly dependent on guess values, which were found different for low and high Mach numbers.

The aforementioned issues make the use of the solver unsuitable in a high dynamic control system. A simplified simulation method is needed in order to obtain a robust algorithm. Alternatively, a set of lookup tables can be created in advance and the result can be obtained by interpolating the values in these tables. Another way is to construct an asymptotic function based on some point calculated in a "safe" range of pressure ratios and the function extrema.

[6] `http://docs.sympy.org/latest/modules/solvers/solvers.html`

	Direct solver use	**Fitting with a power function**	**Array interpolation**
Computation time, µs	11,198.2	108.6	17.1
Deviation, %	0.0	4.6	0.0

Table 2.4: Comparison of computation time and deviation for different algorithms.

All methods were compared with an exact solution by measuring the deviation of the results and the computation time. An array with the size of 30 elements was created. This size corresponds with the displacement of 10 mm. For the reference, an exact solution was calculated in reversed direction: a pressure ratio was obtained for the given M_1 and M_2. The results are presented in Table 2.4. The absolute values of the computation time are less important by reason of its dependence on a particular computer's performance, but the comparison shows clearly that the most appropriate method is the array interpolation. This method is further used as the fastest and the most accurate one.

In order to calculate the Mach numbers in a real time, some preparations are needed. First, two arrays of pressure ratios in function of Mach numbers and the piston position are created.

The range of possible fL/δ values is defined as a function of the piston position and is split into regular steps with a sufficient resolution. The friction factor and the piston clearance are assumed constant.

The outlet Mach number M_2 is varied from 1 to an infinitesimal small value with the same resolution as fL/δ. For each value of fL/δ and M_2, a corresponding value of the Mach number at the outlet of the channel, M_1, is calculated by solving Equation 2.58 with *nsolve*. For each pair of Mach numbers, the pressure ratio $p_2/p_{0,1}$ is calculated by using Equation 2.61.

The obtained values of fL/δ, M_1, M_2 and $p_2/p_{0,1}$ are stored in form of arrays and later, during the real time simulations, are used as a lookup table. The relevant combinations of M_1 and M_2 are depicted in Figure 2.29 as functions of the pressure ratio, $p_2/p_{0,1}$, and the piston position. The optimal resolution providing the best accuracy and computation speed ratio can be obtained experimentally.

The lookup procedure for real time simulation works as follows: the piston position gives the length of the leakage path, L, the pressure ratio across the leakage path is measured directly. Both values are used as input for the interpolation routine returning the Mach numbers. This procedure is illustrated on the hand of Figure 2.30. The values of 0.255 for the pressure ratio, $p_2/p_{0,1}$, and 65 for fL/δ are chosen arbitrary. The indexes of four adjacent points $M_{hi,\,left}$, $M_{hi,\,right}$, $M_{lo,\,left}$ and $M_{lo,\,right}$ are determined by using a bisection method explained

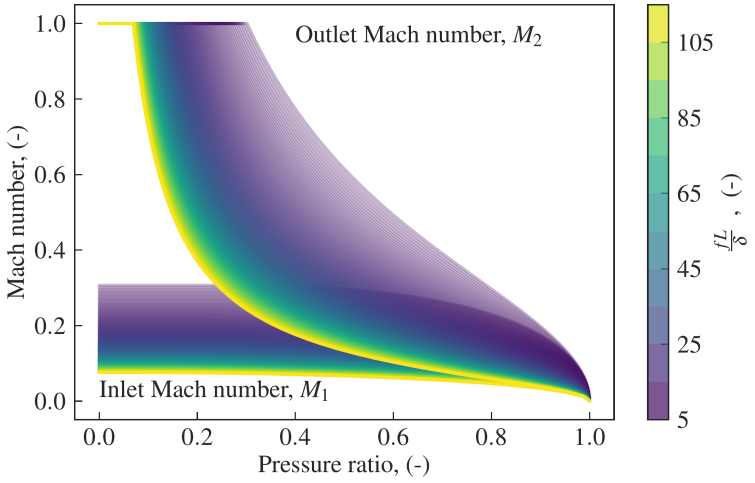

Figure 2.29: Lookup table of Mach numbers for fL/δ from 4 to 120.

in [85] p. 48, which is available in *bisect* module of Python[7]. Further, the values of M_{hi} and M_{lo} located at two closest isolines of fL/δ are calculated by means of linear interpolation as follows:

$$\begin{cases} M_{hi} = M_{hi,\,left} - (M_{hi,\,left} - M_{hi,\,right})\dfrac{(r - r_{hi,\,left})}{(r_{hi,\,right} - r_{hi,\,left})}\,, \\ \\ M_{lo} = M_{lo,\,left} - (M_{lo,\,left} - M_{lo,\,right})\dfrac{(r - r_{lo,\,left})}{(r_{lo,\,right} - r_{lo,\,left})}\,. \end{cases} \tag{2.62}$$

The resulting Mach number is obtained by interpolating the values of M_{hi} and M_{lo} over the fL/D span. This procedure is performed twice: for M_1 and for M_2.

$$M = M_{lo} + (M_{hi} - M_{lo})\frac{(f/L\delta - f/L\delta_{lo})}{(f/L\delta_{hi} - f/L\delta_{lo})}\,. \tag{2.63}$$

The Darcy friction factor, f, which was assumed constant so far, is in fact a function of the wall roughness and the Reynolds number. The latter can be calculated as follows:

$$Re = \frac{\rho v D_H}{\mu} = \frac{v D_H}{\nu} = \frac{v\delta}{\nu}\,, \tag{2.64}$$

where ρ is the fluid volumetric mass density, v is the fluid velocity, μ is the dynamic

[7] https://docs.python.org/2/library/bisect.html

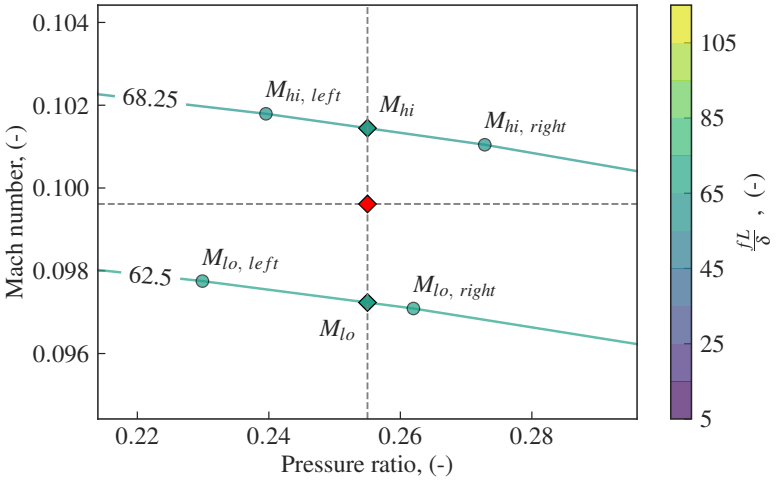

Figure 2.30: Mach number calculation using sequential linear interpolation method.

viscosity and ν is the kinematic viscosity of the fluid. The fluid properties can be obtained from CoolProp library[8] [86] integrated into a control software.

The analysis of possible pressure and temperature levels within the considered operation regimes, and the corresponding fluid properties, shows that the Reynolds number may vary in the range from 140 to 3600 which means a cyclic transition between laminar and turbulent flow through a critical region. Determination of the boundary values for this region is not a trivial task. Several publications are available with comparisons of theoretical models and experiments [87, 88]. Also, [89] reported the results of simulations of the friction factor and Reynolds simulations for transitional regime.

Technically, the flow in an axial direction can be defined as a viscous compressible flow through an annulus, however, since the clearance is much smaller than the piston diameter, the flow can be assumed as a two-dimensional flow between two plates where one of them is moving. This type of flow, called Couette flow, is viscosity driven, assuming there is no slip between the plate and the fluid, so that the fluid layer contacting the upper plate has the same velocity as the plate. Analogously, the velocity of the fluid in contact with the bottom plate is assumed to be zero as it can be seen in Figure 2.31(a). Assuming the velocity gradient proportional to the distance between the plates δ, and the velocity of the bottom plate

[8] http://www.coolprop.org/

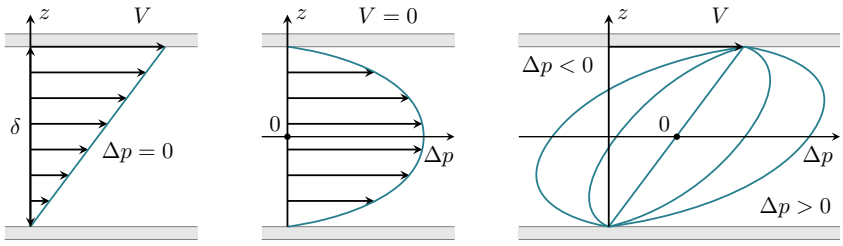

(a) Couette Flow (b) Poiseuille Flow (c) General Flow

Figure 2.31: Gas flow between two plates.

Flow type	Re expression	Eigenvalue analysis, Re_c	Experiments, Re_c	K_{max} at Re_c (from experiments), $\equiv K_c$
Pipe Poiseuille	$Re = \rho UD / \mu$	Stable for all Re	2000	385
Plane Poiseuille	$Re = \rho UL / \mu$	7696	1350	389
	$Re = \rho u_0 l / \mu$	5772	1012	389
Plane Couette	$Re = \rho Ul / \mu$	Stable for all Re	370	370

Table 2.5: Comparison of the critical Reynolds number for the canonical flows. Source: [91].

equal to zero:

$$\begin{cases} u_{(z=0)} = 0 \\ u_{(z=\delta)} = V \,, \end{cases} \tag{2.65}$$

so the average velocity is:

$$V_{avg} = \frac{V_{top}}{2} \,, \tag{2.66}$$

where V_{top} is the velocity of the top plate.

The second component of the flow through the piston clearance is the pressure driven, or Poiseuille Flow, as shown in Figure 2.31(b). The resulting velocity profile, which is shown in Figure 2.31(c) is dependent on the magnitude and the direction of these two basis types of flow profiles [90]. For the circumferential flow from the inlet to the outlet port, the translation of the piston can be neglected. This case is described in [91] as a flow between two rotating cylinders. Similarly, the rotation can be excluded from calculations of the flow between the working chambers and the port area. Therefore, both flows can be handled separately as one-dimensional ones.

Concluding this discussion, the flow is assumed to be transitional in the range of Reynolds number from 370 to 1350.

The friction factor for the laminar flow can be expressed as follows:

$$f_{lam} = \frac{96}{Re} = \frac{96\nu}{v\delta}\,. \tag{2.67}$$

The Colebrook-White equation was developed for the prediction of the friction coefficient for a fully developed turbulent flow in pipes and it is expressed as:

$$f_{tur} = \frac{1}{\left(-2log\left(\frac{\varepsilon}{3.7D_H} + \frac{2.51}{Re\sqrt{f_{tur}}}\right)\right)^2}\,, \tag{2.68}$$

where ε is the surface absolute roughness. This value for finished surfaces typically ranges between 0.1 µm and 1.6 µm depending on the finishing technology [92]. In this particular case, the surface is honed, so the value of 0.8 µm is used, no measurements of the actual roughness have been performed.

This correlation can be applied to the flow in annuli or between two parallel plates with small adjustments. Experiments conducted by Lawn [93] demonstrated that the friction factor for annuli is 5–8.5 % higher than for pipes. This correction factor can be integrated into Equation 2.68. Another approximation of the Colebrook-White equation is proposed by Brkić [94]. This correlation is less accurate but can be solved without iterations.

Equation 2.68 must be solved iteratively since there is no way to obtain an analytical solution. In order to fill the gap between the laminar and the turbulent flow, a piecewise formula is used:

$$f = \begin{cases} f_{lam}, & \text{if } Re < 370\,, \\ f_{tur}, & \text{if } Re > 1350\,, \\ \dfrac{(f_{tur} - f_{lam})}{1350 - 370}(Re - 370) + f_{lam}, & \text{if } 370 > Re > 1350\,. \end{cases} \tag{2.69}$$

Knowing the Mach number at the channel entrance, M_1, the working fluid density ρ_1 and the channel cross section area S, the mass flow rate can be calculated:

$$\dot{m}_{leak}(t) = \rho_1(t) \cdot v_1(t) \cdot S_{leak} = p_1(t) M_1(t) \sqrt{\frac{\gamma}{RT_1(t)}} S_{leak}\,. \tag{2.70}$$

Assuming the flow escaping from or entering the working chamber with a constant volume as isentropic process, the following relationships are valid:

$$\begin{cases} \dfrac{p_2}{p_1} = \left(\dfrac{\rho_2}{\rho_1}\right)^{\gamma} = \left(1 + \dfrac{\dot{m}_{leak}(t)\Delta t}{m_{cyl}}\right)^{\gamma}\,, \\ \dfrac{T_2}{T_1} = \left(\dfrac{\rho_2}{\rho_1}\right)^{(\gamma-1)} = \left(1 + \dfrac{\dot{m}_{leak}(t)\Delta t}{m_{cyl}}\right)^{\gamma-1}\,, \end{cases} \tag{2.71}$$

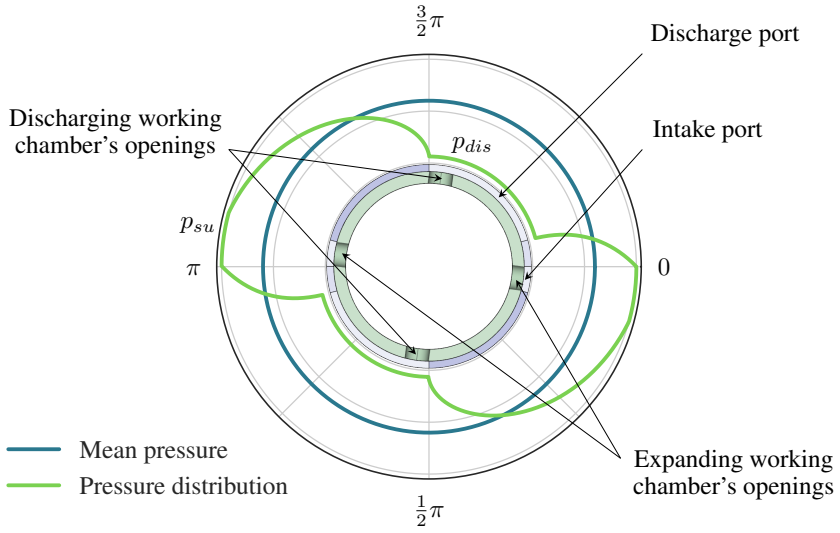

Figure 2.32: Pressure distribution in radial direction in the ports area.

where indexes 1 and 2 indicate the states before and after the density change due to the leak flow. A more general approach, taking the heat exchange with the cylinder walls and the ambient is proposed by [95] and might be useful for certain cases.

2.5.1 Leakage across the ports area

For the ports area in the current design, the circumferential mass flow rate from the inlet port to the outlet port can be calculated by using Equation 2.70, which is rewritten, taking into account a double set of the inlet and the outlet ports, as follows:

$$\dot{m}_{leak}(t) = p_{su}(t)\sqrt{\frac{\gamma}{RT_{su}(t)}}(M_{1,short}(t) + M_{1,long}(t))L_{port}\delta\,, \qquad (2.72)$$

where $M_{1,short}$ and $M_{1,long}$ are the inlet Mach numbers for the leakage flow through the shortest (counter-clockwise) and the longest (clockwise) paths respectively as it can be seen in Figure 2.32.

By calculating the pressure drop for several coordinates along the leakage path, the pressure distribution and the mean pressure can be obtained. Assuming that p_{su} and p_{dis} do not change during one piston reciprocation, the mean pressure p_{mean} is considered constant. This value will be further used to calculate the axial leakage flow rate.

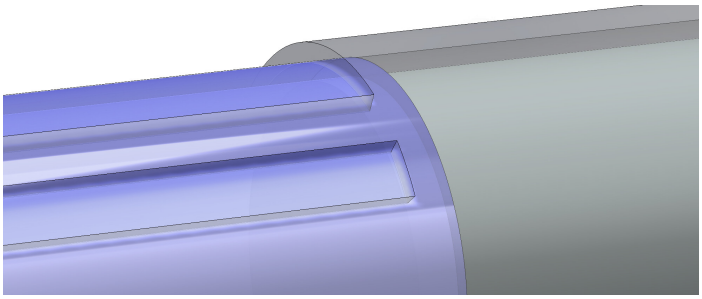

Figure 2.33: Piston-ports overlap in extreme left position.

2.5.2 Leakage in axial direction

When the piston starts to move, the inlet port opens and the pressure in the expanding working chamber equalizes with the supply pressure. At this moment, since the mean pressure in the vicinity of the ports has the value between the supply and the discharge pressure, the leakage flow is directed from the expanding working chamber to the ports and it is considered negative as depicted in Figure 2.35. After the inlet port is closed, the piston travels further to the right expanding the working fluid. When the pressure inside the working chamber equalizes with the port mean pressure, the leakage flow reverses, so some additional amount of gas takes part in the expansion process. At the same time, the leakage flow from the ports towards the discharging chamber decreases with the piston travel but remains constant in its direction. At extreme positions when the expansion process is finished, the leakage mass flow rate towards the expanding chamber is maximal. The major defining factor here is the flow path length which is equal to the overlap between the ports and the piston edges (15 mm in the current design) which is shown in Figure 2.33.

Similar to the circumferential leakage flow, the axial flow can be calculated using the same equations. The surface area of the axial leakage channel can be expressed as follows:

$$S_{leak} = \frac{\pi}{4}\left(D_{cyl}^2 - D_{ps}^2\right) . \tag{2.73}$$

The channel length varies according to the piston displacement x, namely, the channel length between the expanding chamber and the port area decreases: $L_{str} - x$ and the channel length between the discharging chamber and the port area increases.

Summarizing everything mentioned above, the leakage flow rate becomes a sum of the flow from the inlet port and the flow from the expanding chamber. The channel area for each case is a product of the perimeter and the average piston clearance size. By reducing the clearance size, the leakage flow rate can be minimized.

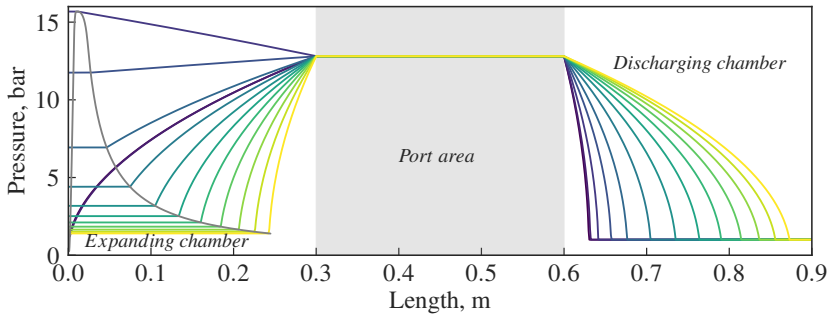

(a)

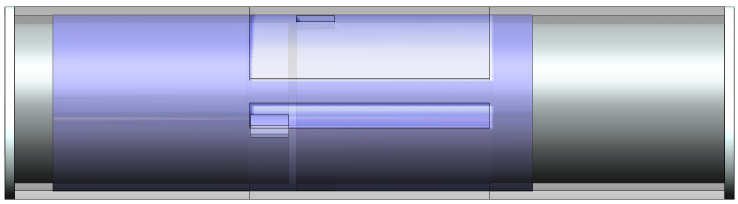

(b)

Figure 2.34: Axial pressure distribution (a) in current design setup (b).

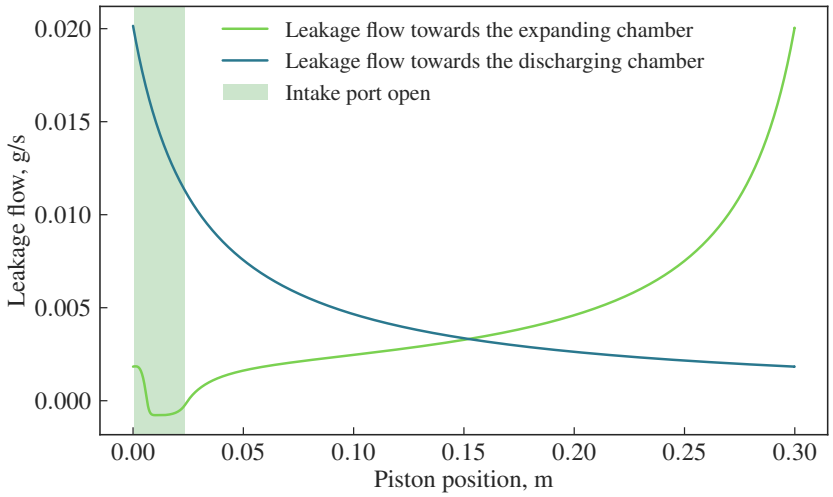

Figure 2.35: Leakage mass flow rates.

2.6 Concluding remarks

In order to achieve an optimal operation of the expander, which means the right port timing as function of the inlet and outlet pressures, the two dimensional trajectory of the piston in respect to the housing must be defined. This can be done in advance for several typical pressure values by using separate simulations as was proposed in [96].

In the next step, the obtained set of linear and angular coordinates in function of time must be transformed into the thrust force and the rotation torque which are further used as setpoints for the LMA controller. The piston speed is the first derivative of the piston position. It is used to calculate the frictional force. The acceleration, being the second derivative, together with the value of the moving mass yields the piston inertia force and torque.

During the next step, the obtained values of the thrust force and torque are compared with the maximum allowed ones and the trajectory is eventually adjusted if the limit is exceeded.

The next goal is to reach the maximum linear piston speed as fast as possible in order to increase the overall cycle frequency and, therefore, the maximum volume flow rate. When the desired speed is reached, the piston must be decelerated and reversed. The value of the electromagnetic force, which must be applied to the moving mass is obtained iteratively.

The obtained set of setpoints is used in the control procedure depicted in Figure 2.36. Every time step, the deviation from the expected values is measured and the correction is applied to Equation 2.10 and 2.15. As aforementioned, the piston trajectory is modeled in the way to stop and reverse its motion as close as possible to the dead points. At the end of the stroke, a separate collision avoidance routine can be engaged if the piston speed remains too high. Both, the fully controlled piston motion and the safety routine ensure a safe expander operation without bounce devices.

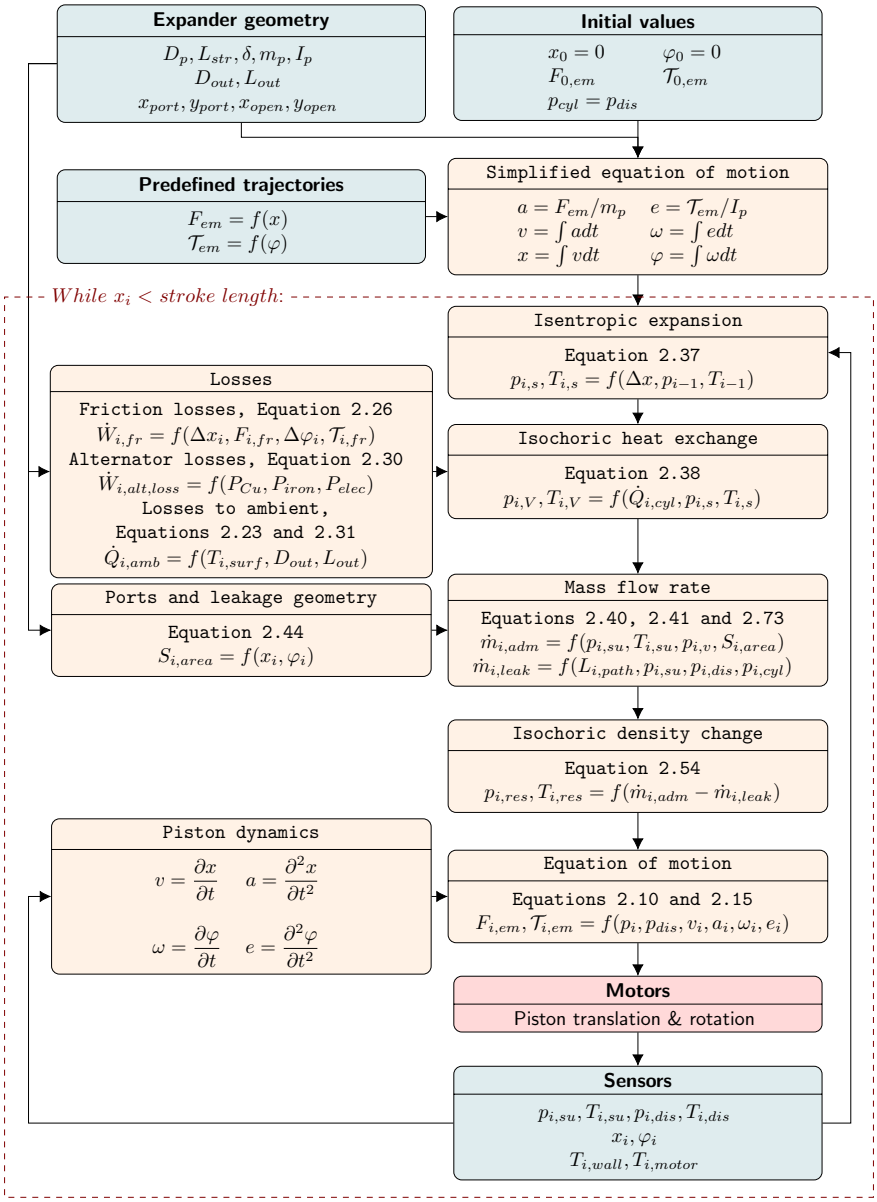

Figure 2.36: Piston movement during the experiments.

References

[1] Sergei Gusev, Davide Ziviani, Jasper De Viaene, Stijn Derammelaere, and Martijn van den Broek. *Modelling and preliminary design of a variable-BVR rotary valve expander with an integrated linear generator*. In 23rd International Compressor Engineering Conference, page 10, 2016.

[2] T. Onuki, W. J. Jeon, and M. Tanabiki. *Induction motor with helical motion by phase control*. IEEE Transactions on Magnetics, 33(5):4218–4220, Sep 1997.

[3] G. Krebs, A. Tounzi, B. Pauwels, D. Willemot, and F. Piriou. *Modeling of A Linear and Rotary Permanent Magnet Actuator*. IEEE Transactions on Magnetics, 44(11):4357–4360, Nov 2008.

[4] Ebrahim Amiri and Ernest Mendrela. *Induction Motors with Rotor Helical Motion*. In Prof. Rui Esteves Araújo, editor, Induction Motors - Modelling and Control, chapter 10. InTech, Rijeka, 2012.

[5] Weihai Chen, Liang Zhang, Liang Yan, and Jingmeng Liu. *Design and control of a three degree-of-freedom permanent magnet spherical actuator*. Sensors and Actuators A: Physical, 180:75–86, 2012.

[6] J.M.M. Rovers, M. Stöck, J.W. Jansen, C.M.M. van Lierop, E.A. Lomonova, and Y. Perriard. *Real-time 3D thermal modeling of a magnetically levitated planar actuator*. Mechatronics, 23(2):240–246, 2013. Special Issue on Linear Drives.

[7] Joseph Shigley. *Standard Handbook of Machine Design, 3rd Edition*. McGraw-Hill Education, jul 2004.

[8] Chengcheng Liu, Jiawei Lu, Youhua Wang, Gang Lei, Jianguo Zhu, and Youguang Guo. *Techniques for Reduction of the Cogging Torque in Claw Pole Machines with SMC Cores*. Energies, 10(10), 2017.

[9] Joya C. Kappatou, Georgios D. Zalokostas, and Dimitrios A. Spyratos. *Design Optimization of Axial Flux Permanent Magnet (AFPM) Synchronous Machine Using 3D FEM Analysis*. Journal of Electromagnetic Analysis and Applications, 8(11), 2016.

[10] K. Halbach. *Design of permanent multipole magnets with oriented rare earth cobalt material*. Nuclear Instruments and Methods, 169(1):1–10, 1980.

[11] L. Yan, L. Zhang, J. Peng, L. Zhang, and Z. Jiao. *Electromagnetic Linear Machines with Dual Halbach Array: Design and Analysis*. Springer Singapore, 2016.

[12] Helena A. Khazdozian, Ravi L. Hadimani, and David C. Jiles. *Development of rare earth free permanent magnet generator using Halbach cylinder rotor design*. Renewable Energy, 112:84–92, 2017.

[13] C.K. Chandrana, J.A. Neal, D. Platts, B. Morgan, and P. Nath. *Automatic alignment of multiple magnets into Halbach cylinders*. Journal of Magnetism and Magnetic Materials, 381:396–400, 2015.

[14] R. Bjørk, A. Smith, and C.R.H. Bahl. *The efficiency and the demagnetization field of a general Halbach cylinder*. Journal of Magnetism and Magnetic Materials, 384:128–132, 2015.

[15] C. Debruyne, M. Polikarpova, S. Derammelaere, P. Sergeant, J. Pyrhönen, J. J. M. Desmet, and L. Vandevelde. *Evaluation of the Efficiency of Line-Start Permanent-Magnet Machines as a Function of the Operating Temperature*. IEEE Transactions on Industrial Electronics, 61(8):4443–4454, Aug 2014.

[16] *Permanent Magnets*. Goudsmit Magnetics.

[17] Baoquan Kou, Feng Xing, Chaoning Zhang, Lu Zhang, Yiheng Zhou, and Tiecheng Wang. *Improved ADRC for a Maglev Planar Motor with a Concentric Winding Structure*. Applied Sciences, 6(12), 2016.

[18] Leon Ben Waldner, Kelvin Wonitoy, Wayne Klaczek, and Shauna G. Noonan. *SPE-160317-MS*, chapter Thermal Performance Testing of a High Temperature ESP Motor for SAGD Applications, page 9. Society of Petroleum Engineers, San Antonio, Texas, USA, 2012.

[19] D. Cozonac, S. Babicz, S. Ait-Amar-Djennad, G. Velu, A. Cavalini, and P. Wang. *Study on ceramic insulation wires for motor windings at high-temperature*. In 2014 IEEE Conference on Electrical Insulation and Dielectric Phenomena (CEIDP), pages 172–175, Oct 2014.

[20] V. Sihvo, J. Nerg, and J. Pyrhönen. *Design and Testing of a Steam-Resistant Insulation System for the Stator of a Low-Voltage Turbo-Generator Taking Thermal Aspects into Account*. WSEAS Transactions On Power Systems, 2008.

[21] Inc. Composite Technology Development. *High-Temperature Motor Windings for Downhole Pumps Used in Geothermal Energy Production*. Technical report, Composite Technology Development, Inc., 2010.

[22] Teruo Asakawa. *Two-dimensional positioning device*. US Patent 4626749A, 1982.

[23] Anwar Chitayat. *Rotary-linear actuator*. US Patent 6215206B1, 2001.

[24] Liuping Wang. *Model Predictive Control System Design and Implementation Using MATLAB® (Advances in Industrial Control)*. Springer, 2009.

[25] Gerco Otten, Theo J. A. De Vries, Adrian M. Rankers, and Erik W. Gaal. *Linear Motor Motion Control Using a Learning Feedforward Controller*. IEEE/ASME Transactions on Mechatronics, 2:179–187, 1997.

[26] R. Mikalsen and A.P. Roskilly. *The design and simulation of a two-stroke free-piston compression ignition engine for electrical power generation*. Applied Thermal Engineering, 28(5-6):589–600, 2008.

[27] Y.F. Wang, D.H. Wang, and T.Y. Chai. *Modeling and control compensation of nonlinear friction using adaptive fuzzy systems*. Mechanical Systems and Signal Processing, 23(8):2445–2457, 2009.

[28] Brian Armstrong-Hélouvry, Pierre Dupont, and Carlos Canudas De Wit. *A survey of models, analysis tools and compensation methods for the control of machines with friction*. Automatica, 30(7):1083–1138, 1994.

[29] C. Canudas de Wit, H. Olsson, K. J. Astrom, and P. Lischinsky. *A new model for control of systems with friction*. IEEE Transactions on Automatic Control, 40(3):419–425, Mar 1995.

[30] Henrik Olsson. *Control Systems with Friction*. PhD thesis, Linköping University, 1996.

[31] Karl Johan Åström and Carlos Canudas de Wit. *Revisiting the LuGre friction model*. IEEE Control Systems Magazine, 28(6):101–114, December 2008.

[32] T. Piatkowski. *Dahl and LuGre dynamic friction models – The analysis of selected properties*. Mechanism and Machine Theory, 73:91–100, 2014.

[33] Xuan Bo Tran and Hideki Yanada. *Dynamic Friction Behaviors of Pneumatic Cylinders*. Intelligent Control and Automation, 4(2), 2013.

[34] W. S. Owen and E. A. Croft. *The reduction of stick-slip friction in hydraulic actuators*. IEEE/ASME Transactions on Mechatronics, 8(3):362–371, Sept 2003.

[35] Luigi Mazza and Guido Belforte. *Analytical/Experimental Study of the Contribution of Individual Seals to Friction Force in Pneumatic Actuators*. Journal of Tribology, 139(2):022202–022202–10, August 2016.

[36] T. A. Johnson, M. T. Leick, and R.W. Moses. *Experimental Evaluation of the Free Piston Engine – Linear Alternator (FPLA)*. Technical report, Energy Innovation Sandia National Laboratories, 2015.

[37] D. Petrichenko, A. Tatarnikov, and I. Papkin. *Approach to Electromagnetic Control of the Extreme Positions of a Piston in a Free Piston Generator*. Modern Applied Science, 9(1):119–128, 2015.

[38] P. J. Hor, Z. Q. Zhu, D. Howe, and J. Rees-Jones. *Minimization of cogging force in a linear permanent magnet motor*. IEEE Transactions on Magnetics, 34(5):3544–3547, Sep 1998.

[39] Alija Cosic and Sadarangani Chandur. *Cogging torque calculations for a novel concept of a Transverse Flux Linear Free-Piston Generator*, 2007.

[40] I.I. Abdalla, A.E.Z.B. Zainal, N.A. Ramlan, Firmansyah, A.R.A. Aziz, and M.R. Heikal. *Cogging force investigation of a free piston permanent magnet linear generator*. IOP Conference Series: Materials Science and Engineering, 257(1):012055, 2017.

[41] Gabriele Gilardi, Kei Szeto, Steve Huard, and Edward J. Park. *Finite element analysis of the cogging force in the linear synchronous motor array for the Thirty Meter Telescope*. Mechatronics, 21(1):116–124, 2011.

[42] Hai-Hua Mu, Yun-Fei Zhou, Xin Wen, and Yan-Hong Zhou. *Calibration and compensation of cogging effect in a permanent magnet linear motor*. Mechatronics, 19(4):577–585, 2009. Robotics and Factory of the Future, New Trends and Challenges in Mechatronics.

[43] V. E. Shcherba, V. V. Shalai, E. A. Pavlyuchenko, and V. S. Vinichenko. *Mathematical Modeling of the Workflows of a Reciprocating Compressor with Intensive Cooling of the Cylindrical Piston Group*. Chemical and Petroleum Engineering, 51(3):260–267, Jul 2015.

[44] Dennis Roskosch, Valerius Venzik, and Burak Atakan. *Thermodynamic model for reciprocating compressors with the focus on fluid dependent efficiencies*. International Journal of Refrigeration, 84:104–116, 2017.

[45] Thiago Dutra and Cesar J. Deschamps. *A simulation approach for hermetic reciprocating compressors including electrical motor modeling*. International Journal of Refrigeration, 59:168–181, 2015.

[46] A. Pont, J. López, J. Rigola, and C.D. Pérez-Segarra. *Numerical dynamic analysis of reciprocating compressor mechanism. Parametric studies for optimization purposes*. Tribology International, 105:1–14, 2017.

[47] Craig Bradshaw, Eckhard A. Grol, and Suresh Garimella. *A Sensitivity Analysis of a Miniature-Scale Linear Compressor for Electronics Cooling using a Comprehensive Model*. International Compressor Engineering Conference, 2012.

[48] I. Sher, D. Levinzon-Sher, and E. Sher. *Miniaturization limitations of HCCI internal combustion engines*. Applied Thermal Engineering, 29(2-3):400–411, 2009.

[49] Xu Hu, Yong Li, and Li Luo. *The Influence of Air Gap Thickness between the Stator and Rotor on Nuclear Main Pump*. Energy Procedia, 142:259 – 264, 2017. Proceedings of the 9th International Conference on Applied Energy.

[50] M. Don 'at. *Investigation of the influence of air gap thickness and eccentricity on the noise of the rotating electrical machine*. Applied and Computational Mechanic, 7:123 – 136, 2013.

[51] R. P. Adair, E. B. Qvale, , and J. T. Pearson. *Instantaneous Heat Transfer to the Cylinder Wall in Reciprocating Compressors*. In International Compressor Engineering Conference., 1972.

[52] G. Eichelberg. *Some new investigations on old combustion engine problems*. Engineering, 148:463–446 et 547–560, 1939.

[53] G. Woschni. *A Universally Applicable Equation for the Instantaneous Heat Transfer Coefficient in the Internal Combustion Engine*. In SAE Technical Paper. SAE International, 02 1967.

[54] G.F. Hohenberg. *Advanced approaches for heat transfer calculations.* SAE Special Publications, SP-449:61–79, 1979.

[55] A. Fula, P. Stouffs, and F. Sierra. *In-Cylinder Heat Transfer in an Ericsson Engine Prototype*. Renewable Energy and Power Quality Journal, ISSN 2172-038 X, 2013.

[56] Fernanda P. Disconzi, Cesar J. Deschamps, and Evandro L. L. Pereira. *Development of an In-Cylinder Heat Transfer Correlation for Reciprocating Compressors*. In International Compressor Engineering Conference at Purdue, 2012.

[57] Joachim Demuynck, Sebastian Verhelst, Michel De Paepe, Henk Huisseune, and Roger Sierens. *Evaluation of Heat Transfer Models With Measurements in a Hydrogen-Fuelled Spark Ignition Engine*. In Proceedings of the 14th International Heat Transfer Conference, pages 87–95, 2010.

[58] J. Demuynck, M. De Paepe, H. Huisseune, R. Sierens, J. Vancoillie, and S. Verhelst. *On the applicability of empirical heat transfer models for hydrogen combustion engines*. International Journal of Hydrogen Energy, 36(1):975–984, 2011.

[59] Sandra K. S. Boetcher. *Natural Convection Heat Transfer From Horizontal Cylinders*, pages 3–22. Springer International Publishing, Cham, 2014.

[60] Stuart W. Churchill and Humbert H.S. Chu. *Correlating equations for laminar and turbulent free convection from a vertical plate*. International Journal of Heat and Mass Transfer, 18(11):1323–1329, 1975.

[61] Yulia Glavatskaya, Pierre Podevin, Vincent Lemort, Osoko Shonda, and Georges Descombes. *Reciprocating Expander for an Exhaust Heat Recovery Rankine Cycle for a Passenger Car Application*. Energies, 5(6):1751, 2012.

[62] V Lemort, S Declaye, and S Quoilin. *Experimental characterization of a hermetic scroll expander for use in a micro-scale Rankine cycle*. Proceedings of the Institution of Mechanical Engineers, Part A: Journal of Power and Energy, 226(1):126–136, 2012.

[63] V. Lemort, S. Quoilin, and J. Lebrun. *Numerical Simulation of a Scroll Expander for Use in a Rankine Cycle*. In Proceedings of the International Compressor Engineering Conference at Purdue 2008., 2008.

[64] Co Huynh, Liping Zheng, and Dipjyoti Acharya. *Losses in High Speed Permanent Magnet Machines Used in Microturbine Applications*. Journal of Engineering for Gas Turbines and Power, 131(2):022301–022301–6, Dec 2008.

[65] *US National Bureau of Standards, Circular No. 31, Copper Wire Tables*, 1914.

[66] H. Kaya. *Dependence of electrical resistivity on temperature and composition of Al-Cu alloys*. Materials Research Innovations, 16(3):224–229, 2012.

[67] R. A. Matula. *Electrical resistivity of copper, gold, palladium, and silver*. Journal of Physical and Chemical Reference Data, 8(4):1147–1298, 1979.

[68] W. Roshen. *Iron Loss Model for Permanent-Magnet Synchronous Motors*. IEEE Transactions on Magnetics, 43(8):3428–3434, Aug 2007.

[69] F. Poltschak. *A high efficient linear motor for compressor applications*. In 2014 International Symposium on Power Electronics, Electrical Drives, Automation and Motion, pages 1356–1361, 18-20 June 2014.

[70] Bala R. Vatti. *A Generic Solution to Polygon Clipping*. Commun. ACM, 35(7):56–63, July 1992.

[71] Bart Braden. *The Surveyor's Area Formula*. The College Mathematics Journal, 17(4):326–337, 1986.

[72] E. E. Callaghan and D. T. Bowden. *Investigation of flow coefficient of circular, square, and elliptical orifices at high pressure ratios*. Technical report, National Advisory Committee for Aeronautics, Lewis Flight Propulsion Laboratory, Cleveland, Ohio, September 1949.

[73] C. Binder, M. Kinell, and E. Utriainen. *Experimental Study on Pressure Losses in Circular Orifices for the Application in Internal Cooling Systems*. ASME. J. Turbomach., 137(3):031005–1–031005–10, March 2014.

[74] A. J. Ward-Smith. *Critical flowmetering: The characteristics of cylindrical nozzles with sharp upstream edges*. International Journal of Heat and Fluid Flow, 1(3):123–132, 1979.

[75] O. Novák and V. Koza. *Measuring a Discharge Coefficient of an Orifice for an Unsteady Compressible Flow*. Fuels, 5(1):21–25, 2013.

[76] Ian H. Bell, Eckhard A. Groll, James E. Braun, and W. Travis Horton. *A computationally efficient hybrid leakage model for positive displacement compressors and expanders*. International Journal of Refrigeration, 36(7):1965 – 1973, 2013. New Developments in Compressor Technology.

[77] B Yang, D Ziviani, and E A Groll. *Comprehensive model of a hermetic reciprocating compressor*. IOP Conference Series: Materials Science and Engineering, 232(1):012007, 2017.

[78] Sérgio Koerich Lohn and Evandro Luiz Lange Pereira. *Numerical Investigation of the Gas Leakage through the Piston-Cylinder Clearance of Reciprocating Compressors*. International Compressor Engineering Conference, 2014. Paper 2295.

[79] R.T. S. Ferreira and D. E. B. Lilie. *Evaluation of the Leakage Through the Clearance Between Piston and Cylinder in Hermetic Compressors*. International Compressor Engineering Conference, 1984. Paper 424.

[80] J. Zuk and P. J. Smith. *Computer program for viscous, isothermal compressible flow across a sealing dam with small tilt angle*. Technical report, NASA, D-5373, Washington, D.C., USA, 1969.

[81] G. Belforte, T. Raparelli, L. Mazza, and A. Trivella. *Analysis, Design, and Comparison of Different Types of Pistons for Sealless Pneumatic Cylinders and Valves*. Tribology Transactions, 48(3):377–388, 2005.

[82] G. Belforte, T. Raparelli, L. Mazza, and A. Trivella. *Study of Slot-Controlled Pistons on Air Bearings for Pneumatic Actuators*. In World Tribology Congress, 2001.

[83] H. Daneshyar and W.A. Woods. *One-Dimensional Compressional Flow*, pages 38–82. Elsevier Science, 2016.

[84] J.D. Anderson. *Modern Compressible Flow: With Historical Perspective*, pages 85–91, 154–167. McGraw-Hill series in aeronautical and aerospace engineering. McGraw-Hill, 1990.

[85] R.L. Burden and J.D. Faires. *Numerical Analysis*, page 48. Cengage Learning, 9^{th} edition, 2010.

[86] Ian H. Bell, Jorrit Wronski, Sylvain Quoilin, and Vincent Lemort. *Pure and pseudo-pure fluid thermophysical property evaluation and the open-source thermophysical property library CoolProp*. Industrial & Engineering Chemistry Research, 53(6):2498–2508, 2014.

[87] H.S. Dou, B.C. Khoo, and H.M. Tsai. *Determining the Critical Condition for Turbulent Transition in a Full-Developed Annulus Flow*. Journal of Petrolum Science and Engineering, 71, 2010.

[88] K. T. Trinh. *On The Critical Reynolds Number For Transition From Laminar To Turbulent Flow*. ArXiv e-prints, July 2010.

[89] Takahiro Ishida and Takahiro Tsukahara. *Friction factor of annular Poiseuille flow in a transitional regime*. Advances in Mechanical Engineering, 9(1):1687814016683358, 2017.

[90] I.G. Currie and I.G. Currie. *Fundamental Mechanics of Fluids, Third Edition*. Taylor & Francis, 2002.

[91] Hua-Shu Dou, Boo Cheong Khoo, and Khoon Seng Yeo. *Instability of Taylor-Couette flow between concentric rotating cylinders*. International Journal of Thermal Sciences, 47(11):1422–1435, 2008.

[92] Mikell P. Groover. *Fundamentals of modern manufacturing: materials, processes and systems, 4th ed.*, page 95. John Wiley & Sons, Inc., 2010. ISBN 978-0470-467002.

[93] C. J. Lawn and C. J. Elliott. *Fully Developed Turbulent Flow through Concentric Annuli*. Journal of Mechanical Engineering Science, 14(3):195–204, 1972.

[94] Dejan Brkić. *A note on explicit approximations to Colebrook's friction factor in rough pipes under highly turbulent cases*. International Journal of Heat and Mass Transfer, 93:513–515, 2016.

[95] Thomas Bourgeois, Fouad Ammouri, Mathilde Weber, and Christophe Knapik. *Evaluating the temperature inside a tank during a filling with highly-pressurized gas*. International Journal of Hydrogen Energy, 40(35):11748–11755, 2015.

[96] Sergei Gusev, Andres Hernandez, Davide Ziviani, and Martijn van den Broek. *Modeling of a Variable-BVR Rotary Valve Free Piston Expander/-Compressor*. In Latin American conference on Automatic Control, pages 42–48, Medellin, Colombia, 2016.

3
Experimental Test Setup

In this chapter, the test setup is described. The piston movement, as a combination of a reciprocation and a rotation, is realized by a separate linear and a rotative machine. This approach provides a possibility to develop a control algorithm for the translation and rotation independently. As in the conceptual design, the intake and the discharge process is realized by means of the piston itself. The gas supply system is equipped with an automatically adjustable flow regulator and provides the possibility to adjust the pressure and the temperature of the working fluid entering the expander. The data acquisition system is integrated into the control system based on an industrial computer.

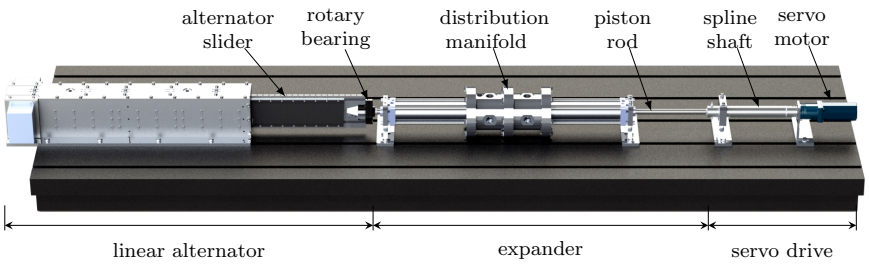

Figure 3.1: Main components of the experimental setup.

3.1 General overview.

The expander integrated design, proposed in Section 2.1, implies too many unknown techniques and, therefore, it was not feasible to develop a working prototype within the available time and budget without some simplifications. A trade-off solution found was to separate the linear movement and the rotation by placing a linear alternator and a servo motor outside of the expander. Both machines are connected to the piston rod of the expander through the couplings which separate the linear and the rotative motion. It was decided to use standard components where possible in order to simplify the preliminary design. In general, the experimental setup is designed according to a modular principle for easy access to any component. The general view of the setup without gas supply system is shown in Figure 3.1. The linear alternator is connected to the piston rod by means of a rotary bearing wherein the piston rod can rotate, so only the translation can be transmitted to the piston. The rotation of the piston is realized by a servo motor through a spline coupling to disconnect the rotation from the translation. The in- and outlet port assembly is attached externally to the cylinder.

3.2 Linear alternator.

The linear alternator sizing is performed using the approach described in Section 2.2. The maximum of static force obtained in Equation 3.8 defines the maximum electromagnetic force which must be provided by the linear alternator in order to maintain a controlled piston motion at any moment.

3.2.1 Design considerations

The main issue was to find an appropriate stand-alone linear alternator since such devices are still rare on the market. Machines producing electricity by conversion of a linear motion are not always "purely" linear, as shown in Figure 3.2(a), but

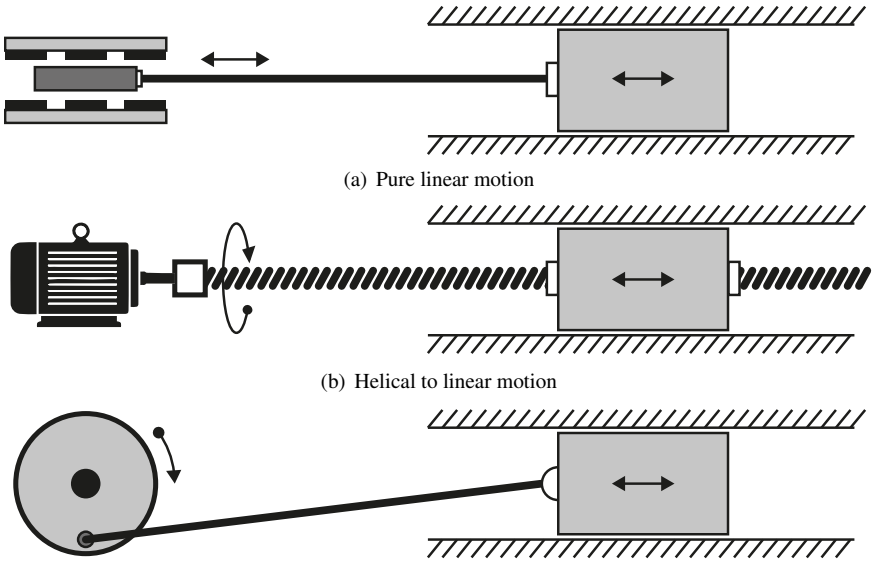

(a) Pure linear motion

(b) Helical to linear motion

(c) Crankshaft, rack/pinion or swash plate to linear motion

Figure 3.2: Possible realizations of the linear motion.

rotating ones with a transmission which transforms the linear motion into rotation. Such a transmission can be realized in several ways:

- Helical interface: Figure 3.2(b).
- Crankshaft mechanism.
- Rack and pinion.
- Swash plate or guiding groves.

The last three options are schematically depicted in Figure 3.2(c) as they have similar geometrical characteristics.

The main goal of the current design is to avoid any mechanical transmission if possible and to convert the piston linear motion directly into electricity in order to approach the functionality of an integrated prototype. The logical choice was to use standard components of industrial linear motion systems and to design a distinct chassis. Since the main parameters of the designed installation are interdependent, some preliminary assumptions have been made. The rated power is chosen around 10 kW — the same as of the other ORC installations in the lab. This opens up a possibility to compare the results of the experiments in the future.

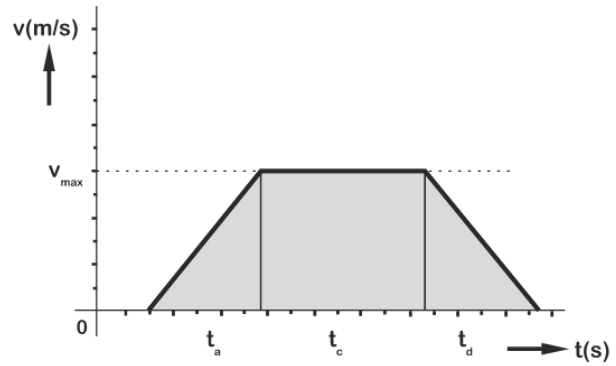

Figure 3.3: Simplified piston velocity profile. Source: `www.beckhoff.com`.

3.2.2 Alternator sizing

For the linear motor/alternator (LMA) sizing, a simplified trajectory is considered: acceleration until the maximal speed, a constant speed part and deceleration until the piston stops. The system is assumed to be frictionless, also no gas force is taken into account at this point. The resulting trajectory is shown in Figure 3.3

The time needed to accelerate the piston is:

$$t_{acc} = \frac{v_{max}}{a_{ps}} = \frac{m_{ps} v_{max}}{F_{acc}} \,, \tag{3.1}$$

where v_{max} is the maximum piston speed, a_{ps} is the piston acceleration, F_{acc} is the acceleration force and m_{ps} is the mass of the piston.

The distance which the piston covers during this phase is:

$$x_{acc} = \frac{a_{ps} t^2}{2} = \frac{m_{ps} v_{max}^2}{2 F_{acc}} \,. \tag{3.2}$$

The deceleration part of the trajectory can be calculated in the similar way.

During the constant velocity phase, the absolute value of the electromagnetic force is minimal and only compensates the frictional losses and the cogging. The length of this part is:

$$x_{cte} = v_{max} t_{cte} \,. \tag{3.3}$$

In a real application, this part needs to be kept as short as possible since there is no energy recovery from the expansion. Furthermore, the frictional force will brake the piston, transforming the useful energy into heat. If the part with a constant speed can be avoided, the motor will operate continuously accelerating and decelerating the piston, so trajectory can be simplified and the equation for the sizing of the LMA can be written as follows:

$$m_{max} = \frac{L_{str} F_{em}}{v_{max}^2} \,, \tag{3.4}$$

where m_{max} is the sum of the masses of all moving parts, L_{str} is the stroke length, F_{em} is the electromagnetic force applied by the considered LMA and v_{max} is the maximum motion speed which can be realized by the LMA. For the sizing, a nominal force, $F_{em,nom}$, is used. In order to avoid the motor overheating, the value of the nominal force may not be exceeded by the root mean square (RMS) of the force produced or recovered by the motor, which is:

$$F_{rms} = \sqrt{\frac{\sum_{i=1}^{n} \left(F_i^2 t_i\right)}{\sum_{i=1}^{n} t_i}}\,, \tag{3.5}$$

where F_i is an instant force value acting during the time step t_i. The maximum static force which LMA must provide is dependent on the expander sizing explained in Section 3.4.

After the motor is chosen, one can apply simplified profiles of gas and frictional forces. During the simulations, a motor speed/force diagram shown in Figure 2.15 is built based on the manufacturer's data, which are provided in Appendix B.1. This diagram is used to define the maximum possible speed/force combinations.

The power dissipated by the motor during its operation is equal to:

$$Q_{dis} = 1.3\frac{F_{rms}^2}{K_{25}}\,, \tag{3.6}$$

where K_{25} is the motor constant at 25 °C. If the motor operates close to its limit during a long time, its temperature can rise significantly. Therefore, the motor constant must be adjusted as follows:

$$K_{act} = \frac{S_{25}}{1 + 0.004(T_{act} - 25)}\,, \tag{3.7}$$

where T_{act} is the actual motor temperature which can be measured by means of the integrated temperature sensor. If the motor is integrated into the housing of the expander, the dissipated power must be included into the model described in Chapter 2. In this case, the power electronics could be cooled by the working fluid. In this way, the motor/inverter losses can be partially recovered.

3.2.3 Practical realization

The cross section schematic view of the designed alternator is shown in Figure 3.5(a). Two iron core primary sections are installed inside the housing facing each other with the moving magnetic section in between. The magnetic section is assembled from standard magnetic blocks which are attached back-to-back to a

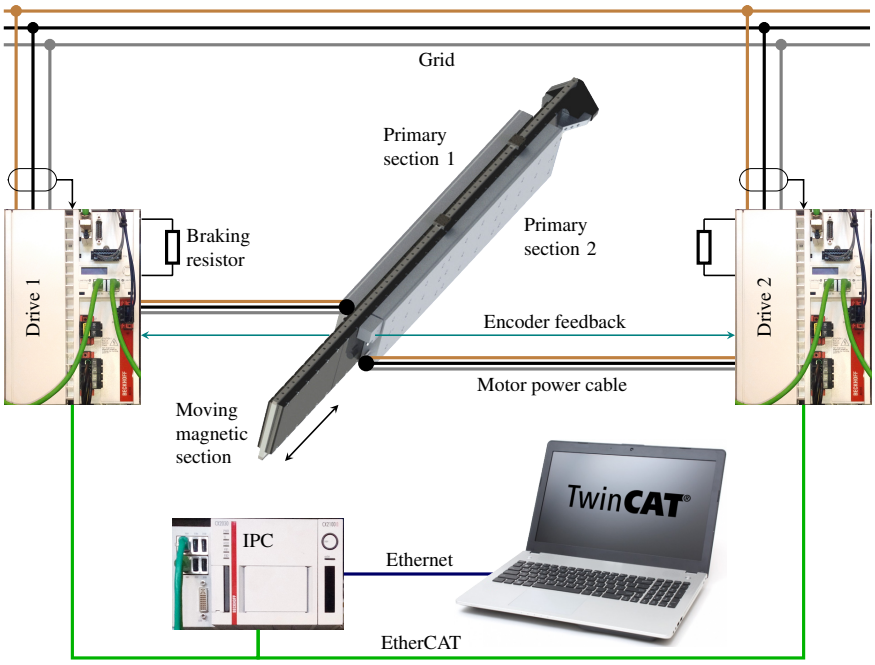

Figure 3.4: Test setup configuration, the linear motor is shown without the housing.

common frame with two guiding rails. This assembly is supported by linear bearings and it can move in an axial direction. In order to decouple the slider from the piston rotation, a rotary bearing is installed on the side connected to the piston shaft. The side view of both the primary and the secondary section without the housing is depicted in Figure 3.5(b). One magnetic plate is removed to visualize the slider structure. The magnetic plate serves as a back iron for permanent magnets glued to it. The magnets are covered with an epoxy compound protective layer. A part of this layer is removed in the drawing for illustration purposes.

The feedback of a linear position is provided by two incremental magnetic encoders. Each motor is connected to its own drive and it can operate independently as depicted in figure 3.4. The main advantages of twin-coil configuration are:

- electromagnetic attraction forces acting against each other are equalized, so the linear guiding system is unloaded and the friction losses are significantly reduced;
- the forces of both motors are joined within the same assembly length.

The assembled alternator is presented in Figure 3.5(c). The resulting linear alternator parameters are summarized in Table 3.2, the detailed information about the main components can be found in Appendix B.1.

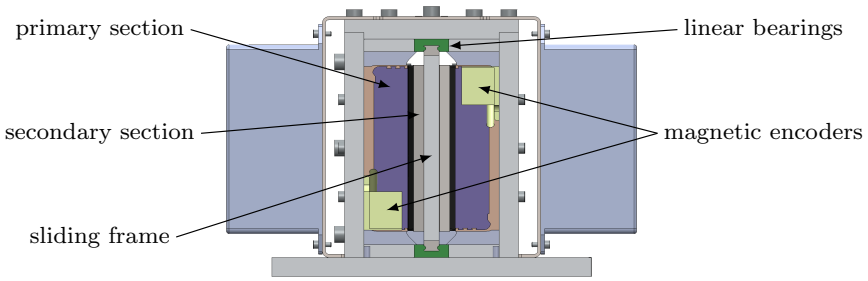

(a) Cross-section view of the linear alternator.

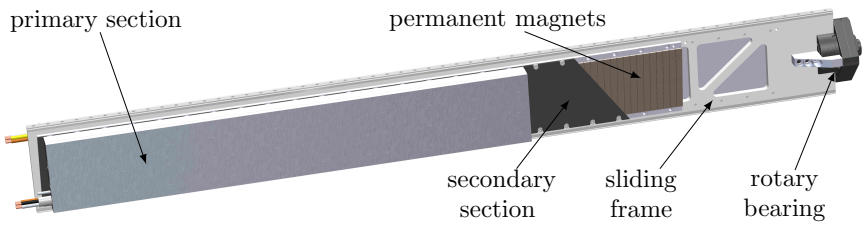

(b) Alternator shown without housing.

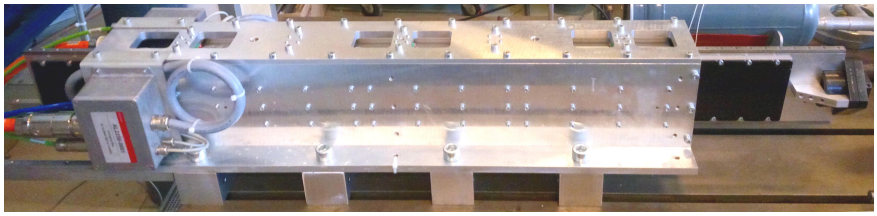

(c) Assembled linear alternator.

Figure 3.5: Linear alternator design.

Peak static force, kN	**Maximum force at nominal speed,** kN	**Maximum speed,** m/s	**Maximum speed at nominal force,** m/s	**Moving mass,** kg	**Stroke length,** m
13.5	6.0	6.0	4.5	32.0	0.34

Table 3.1: Main parameters of the twin-coil linear alternator.

Working medium -	**Inlet pressure,** bar	**Inlet temperature,** °C	**Swept volume per cycle,** m^3	**Rated power,** kW
Nitrogen	< 16	15 - 90	3.47×10^{-3}	10.0

Table 3.2: Setup main parameters.

Rated torque, N m	**Peak torque,** N m	**Rated speed,** rad/s	**Rotor moment of inertia,** $kg \cdot m^2$	**Torque constant,** N m/A	**Voltage constant,** V/(rad/s)	**Gear-box ratio,** –
2.3	11.66	314.16	8.42×10^{-5}	1.39	0.955	7

Table 3.3: Servo motor main parameters.

3.3 Port timing

The timing of the ports is controlled by means of a permanent magnet servo motor. Figure 3.6(a) represents such a motor with a gearbox reducing the rotation speed by a factor of seven. A gearbox is installed since the expected piston rotational speed is much lower than most servo motors provide. Additionally, the use of a gearbox increases the available torque, which allows using a smaller motor for the same required torque. The motor is coupled to the piston rod through a splined coupling and is placed on the opposite side in respect to the linear generator. The cut view of the coupling is shown in Figure 3.6(b). A straight sided 6-splined shaft [1] is attached to the piston rod by means of a thread and is fixed with a hard steel pen to prevent unscrewing. Six parallel teeth made on the shaft are mated with the groves of the corresponding hub, so the shaft can freely slide inside the hub while the angular position changes by means of the servo motor and the torque is transmitted to the piston rod. The hub is inserted into a hollow shaft and welded around. The hub assembly is supported by means of a rotary bearing and the gear box shaft which are aligned with each other.

The motor rotates the piston with an average frequency of half to that one of the translation since there are two opposite inlets and two outlet ports in each working chamber. The sizing of the components is described in Section 2.2.2. The servo motor characteristics are summarized in Table 3.1, the motor and the gear box specifications can be found in Appendix B.2.

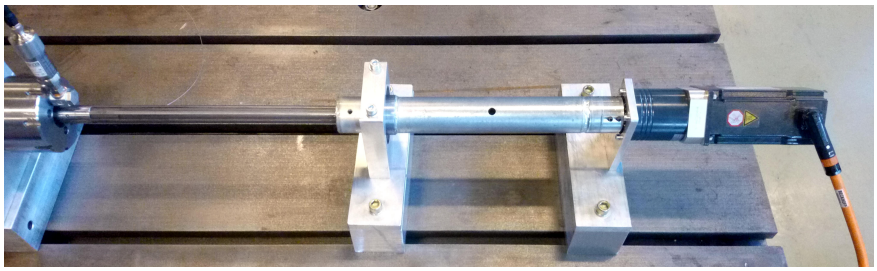

(a) General view of the servo motor with a spline coupling.

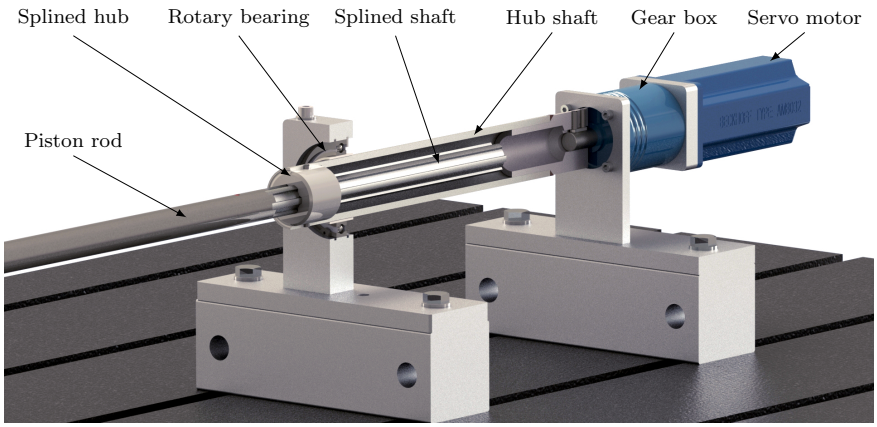

(b) Cut view of the spline coupling.

Figure 3.6: Servo motor with a gearbox and a spline coupling.

3.4 Expander

In order to control the inlet port with sufficient accuracy, the maximal piston length is chosen for the available test bench with the length of 3 m, taking into account the estimated lengths of the linear alternator and the servo motor. The maximum stroke length for the current setup is 340 mm and it can be reduced if necessary (Table 3.2).

The piston diameter of 80 mm is chosen from a practical point of view: a smaller diameter would cause certain machining problems and significantly reduce the swept volume. The bore/stroke ratio of 0.267 is in line with similar devices designed by other FPLA-machine developers mentioned in Section 1.5.

3.4.1 First generation expander.

As basis for the expander, a standard double acting dual rod pneumatic cylinder is adjusted which is shown in Figure 3.7(a) and Figure 3.7(c).

The in- and outlet ports have been made as shown in Figure 3.7(b) by electrical discharge machining (EDM) technology. In order to prevent deformations of the housing due to too large openings, the discharge port is composed of four separated openings. The "bridges" between the openings are not affecting the discharge flow significantly as they never cover the piston opening entirely.

The original cylinder housing is an extruded aluminum pipe with two guiding assemblies bolted together with four rods. The guiding assemblies are modified: the ports are sealed, the dampers are removed, two openings per flange are made in order to connect pressure and temperature sensors.

The inner surface of the cylinder is made with the H8 tolerance which means a deviation of 0–54 µm upwards. The original piston is replaced by a sleeve with a steel separating partition welded in the middle. The sleeve piston is made in accordance with the cylinder inner diameter in order to minimize the clearance. The first version of the piston is shown in Figure 3.8.

The maximum static force acting on the piston rod is estimated using the piston diameter and the maximum allowed pressure of 16 bar which is set by the manufacturer:

$$F_{p,\,st} = (p_{su} - p_{dis})\, S_{ps} = (p_{su} - p_{dis}) \frac{\pi}{4} \left(D_{ps}^2 - D_{rod}^2\right) , \qquad (3.8)$$

where S_{ps} is the piston surface area, D_{ps} is the piston diameter, D_{rod} is the piston rod diameter. The maximum static force is estimated to be 6.8 kN.

The pressure regulating valve has the limitation of 16 bar. The discharge pressure p_{dis} is set to atmospheric, so the maximum pressure ratio which can be achieved on the test setup is 16.

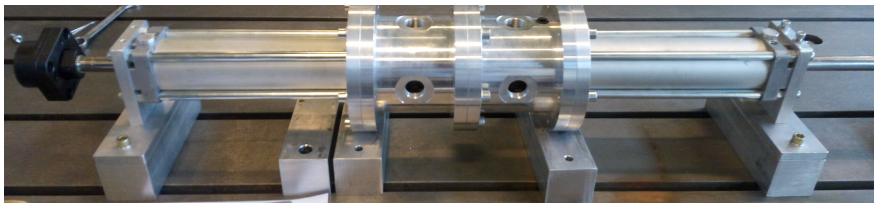

(a) Adjusted pneumatic cylinder with the distribution manifold installed.

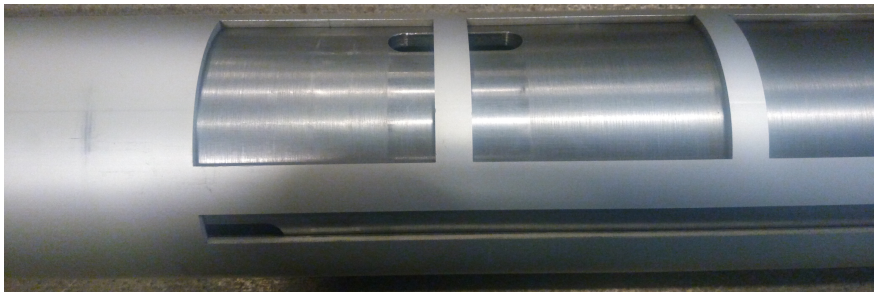

(b) Openings made in the cylinder wall, the distribution manifold is not installed.

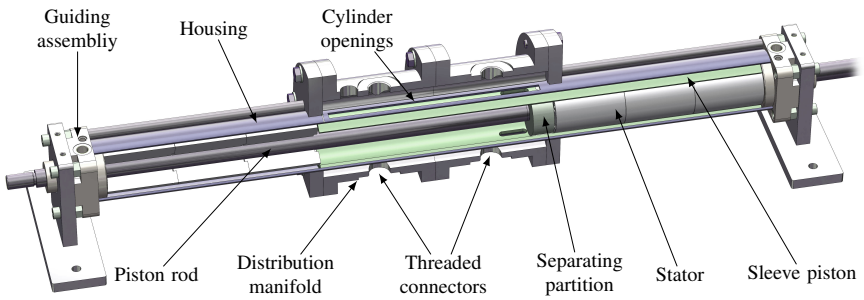

(c) Cut view of the first generation expander.

Figure 3.7: Schematic view of the first generation expander.

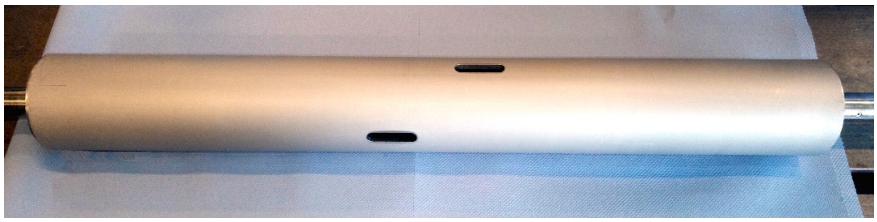

(a) Sleeve type piston with the port openings of both working chambers.

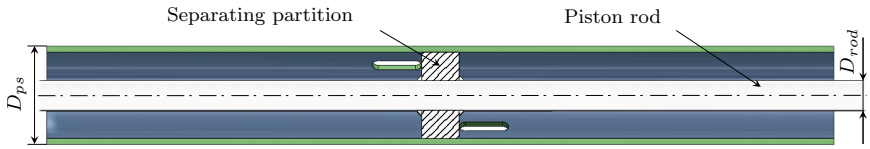

(b) Cut view of the sleeve piston.

Figure 3.8: General view and cut view of the sleeve piston.

Bore diameter, m	**Cylinder length,** m	**Stroke length,** m	**Port length,** m	**Opening length,** m	**Moving mass** kg
0.08	0.9	0.3	0.3	0.04	12.9

Table 3.4: Expander main parameters.

Since the discharge flow rate remains constant during the piston reciprocation, it can be calculated as follows:

$$V = \frac{\pi}{4}\left(D_{ps}^2 - D_{rod}^2\right) 2 L_{str} f \,, \tag{3.9}$$

where L_{str} is the stroke length and f is the reciprocation frequency. The expander is double-acting, which is accounted for by the coefficient 2 before L_{str}. The expansion process is simulated in Section 2.1 in order to obtain the in- and outlet gas thermodynamic parameters and the mass flow rate. These values are used for the setup sizing. The main expander design parameters are listed in Table 3.4.

Mechanical operations with the cylinder housing can easily damage it, especially operations associated with high temperatures, such as welding. Therefore, the port openings are connected to the gas supply and discharge system through a separate assembly which is made to be attached tight around the cylinder housing. The high and low pressure chambers of this distribution manifold are separated by means of ethylene propylene diene monomer (EPDM) seals. The piping of the gas supply system is connected to the manifold by means of threaded couplings which

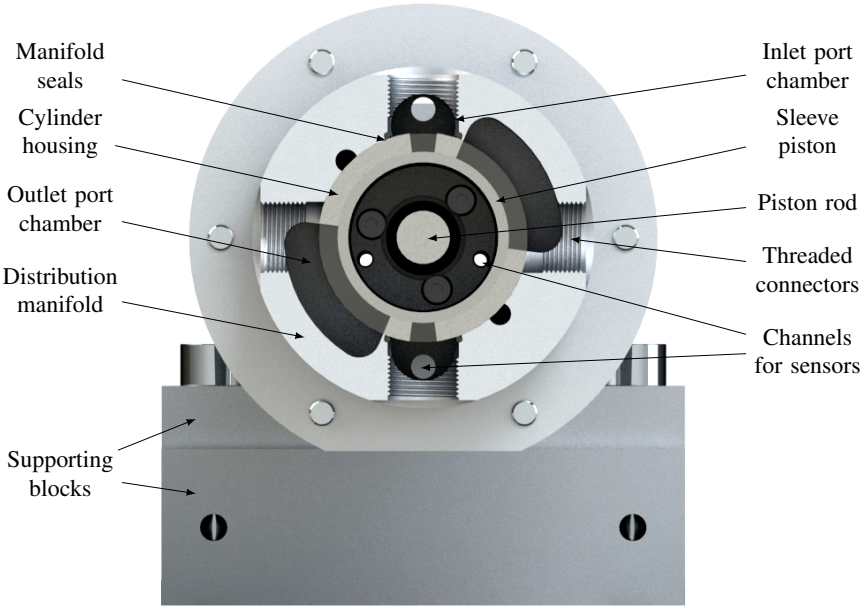

Figure 3.9: Axial cross-section view of the distribution manifold.

are shown in Figure3.9. The coils of the embedded generator are substituted by aluminum cylinders, further called "dummies" which are shown in Figure 3.7(c) as *Stator*. Dummies are attached to the cylinder guiding assemblies and are meant to preserve the functionality of the working chambers. Since the manufacturing of such a part in its full length using the available machining park was impossible, the dummies are assembled from three shorter centered pieces and bolted together. The piston rod and two sensor channels per chamber pass through the assembly. One channel is connected to the pressure sensor, the second one is used to draw the thermocouple to the working chamber.

After the expander was assembled, the setup was aligned and tested without applying pressure, then disassembled back and inspected. Both, the piston and the cylinder diameters have been measured with a micrometer. The measurement revealed an unacceptable deformation of the cylinder in the middle around the port openings. Regardless of all precautions, the inner diameter had increased, which led to a larger clearance of about 200 µm. This clearance would cause a too high leakage flow from the inlet to the outlet port and could make the validation of the model very difficult.

The second issue has been figured out during the assemblage of the expander. It was impossible to perfectly align the flanges highly likely because of the cylinder deformation. Regardless the relatively large gap between the dummies and the

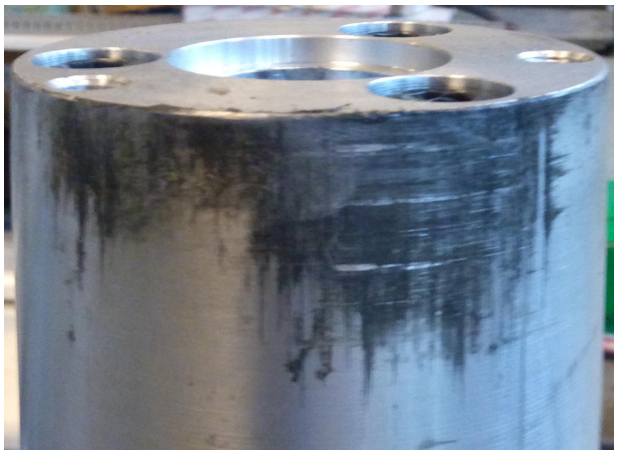

Figure 3.10: Wear of the dummies.

piston of 0.5mm, the dummies contacted with the inner wall of the sleeve piston resulting in additional friction and wear as it can be seen in Figure 3.10.

It was decided to use the current design temporarily, only for testing the linear generator in motor modus, in order to introduce a certain moving mass and a friction force so that the kinematic model can be further developed and validated. Two linear bearings have been installed into the dummies helping to align them with the rods during the assembly. In the mean time, a new design, based on the obtained experience has been developed.

3.4.2 Second generation expander.

The new cylinder is manufactured using a honed cold drawn seamless (CDS) 1026 steel tube with the surface roughness of maximum 0.4 µm which is shown in Figure 3.11. Such a prefabricated material provides uniform tolerances and a very high precision. The internal diameter tolerance (H8) is the same as the one of the pneumatic cylinder used before, but the mechanical strength is much higher not only because of the material properties but also because of the wall thickness. Which is chosen to be 10 mm. In contrast with the previous design, a steel thick-walled housing would promise a better form stability and size accuracy.

Also, the guiding flanges have been redesigned: the supporting function was dedicated to the housing itself, the flanges were unloaded and provided with a fine thread for connection to the housing. A flexible connection between the housing and the flanges of the first generation expander has been replaced by a rigid one and carefully centered to provide a better alignment of the dummy assemblies inside the housing. The achieved average clearance is about 15 µm. The cut view

(a) General view.

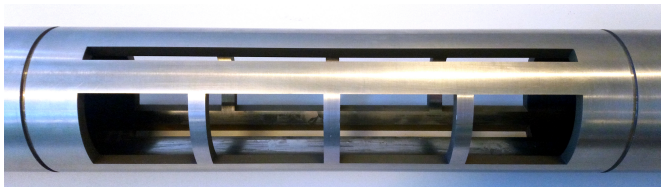

(b) Ports close up.

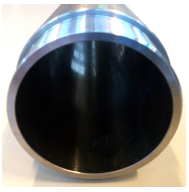

(c) Honed inner surface.

Figure 3.11: Second generation cylinder design.

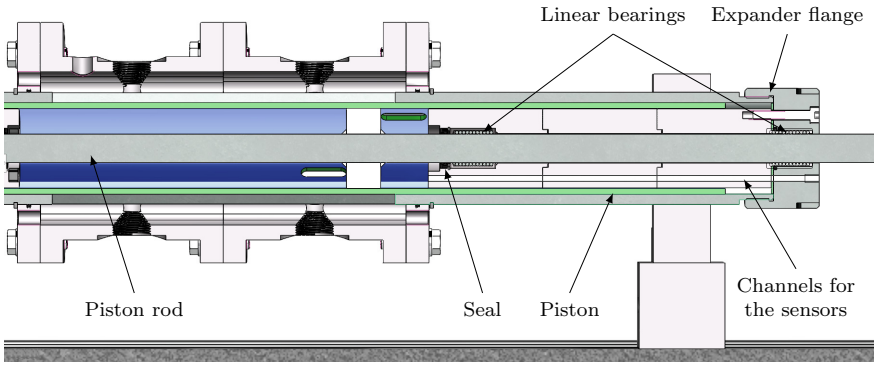

Figure 3.12: Second generation expander.

of the improved expander can be seen in Figure 3.12. The linear bearings holding the piston shaft are installed in the inner flange and the shaft is sealed at this place. Two bores per dummy connecting the working chambers with the outside are made to install the pressure and temperature sensors. A thermocouple type K with the diameter of 1 mm is inserted through one of these bores. The flanges of the improved dummies are shown in Figure 3.13.

As before, the adjusted port assembly is installed in the middle of the cylinder around the ports area, sealed and fixed by cir-clips. Welding or brazing is avoided in order to prevent the cylinder from thermal deformation.

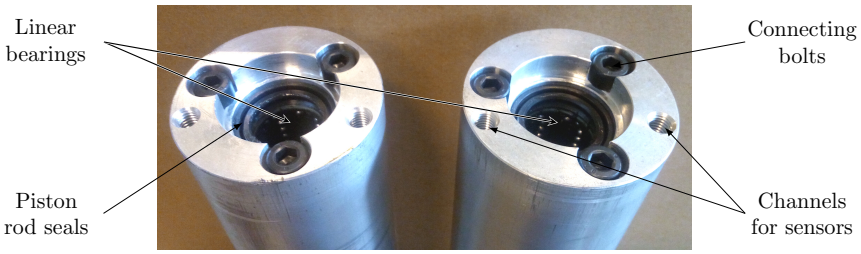

Figure 3.13: The inner dummy flanges with linear bearings ans shaft seals installed.

3.4.3 Commissioning

The cylinder/piston group has been produced with all precautions, however, several problems raised during the commissioning:

- Piston rod axial misalignment caused by the welding induced tension;
- Cylinder and piston walls deformation due to ports cutting;

3.4.3.1 Piston

The piston consists of a pipe divided into two parts by a round central partition wherein the piston rod is welded. First, the central element is welded together with the rod, then both are centered inside the piston and welded to the piston walls in several points. Finally, the outer surface of the piston was machined until the diameter of 80 mm with a tolerance of 30 µm.

In order to guarantee the concentricity of the piston and the rod, two cylindric accessories have been made. These elements center and fix the piston rod during the welding preventing it from deformation. Regardless of this, the tension caused by the welding led to the misalignment of the piston rod. Therefore, during the operation, the piston was pushed to the cylinder wall which caused its damage even in the presence of lubricating oil. The result of several hundreds of reciprocation cycles can be seen in Figure 3.14(a). The mechanism of wear is explained in [2] and helps to identify its cause. If the lubricating film is broken, two metal surfaces come in close contact under load which leads to a local temperature rise, a consequent adhesion and fracture as is shown in Figure 3.14(d) on the left. This phenomenon is also known as galling.

3.4.3.2 Cylinder

The inner wall of the cylinder has a higher hardness than the piston outer surface. Beside galling, sharp edges of the ports could initiate the wear by abrasion and fracture similar to Figure 3.14(d) on the right. Two light areas to the left and to the

right of the opening in Figure 3.14(c) indicate the starting point of the process. The damage appears first on the piston and gradually propagates to the cylinder's inner wall as the detached debris increase in size by being ploughed or rolled between two surfaces and attracting more material due to adhesion. Stopped debris of a large size can be clearly seen in Figure 3.14(b).

3.4.4 Possible improvements

The analysis of the obtained results is useful for the next steps, since even if there will be no guiding rods in the integrated design, the attracting forces of the magnets can cause similar problems. In order to repair the piston and the cylinder, both were partially disassembled and honed with an abrasive compound with a particle size of 44.5 µm, typically used for the finishing of motor valves. The piston was rotating and reciprocating for about several thousands of cycles. After that, the result was visually controlled. This procedure revealed noticeable variations in size of the cylinder inner walls, especially in the vicinity of the openings as it can be seen in Figure 3.15. The honed surface has become dull while some zones remained originally bright. This means that within these areas the clearance is larger than the grind size. This in turn will cause a higher than expected leakage flow rate. For further calculations, the clearance is assumed to be equal to 50 µm. By means of this operation, the piston eccentricity has been partially reduced at a cost of a larger clearance, so the setup become operational.

For the manufacturing of a next generation prototype, it can be recommended to apply a finishing procedure after the ports are made and the port manifold is attached. After these operations, no further deformations of cylinder walls can be expected. Depending on the value of the cylinder bore obtained after the finishing, the piston can be machined accordingly. To improve the sealing between the piston and the cylinder, a molybdenum oxide dry lubricant can be applied. During the experiments, Molycote® D-321R spray[1] was tested. This coating does not require high curing temperatures and it is characterized by a short curing time of 5 minutes at 20 °C.

3.5 Gas supply system

The pneumatic scheme of the setup is depicted in Figure 3.16. The source of the working medium is the gas cylinder filled with nitrogen with a maximum pressure of 200 bar. A manually adjustable gas regulator is installed to reduce the pressure down to 17 bar which is the maximum inlet pressure for the electronic pressure regulator. A normally closed cut-off valve provides the possibility to stop the gas

[1] Molycote® is the registered trademark of Dow Corning Corporation

(a) The piston surface contacted with the cylinder wall, real frame size: 175 mm × 80 mm.

(b) Close-up of galling wear debris, real frame size: 42 mm × 18 mm.

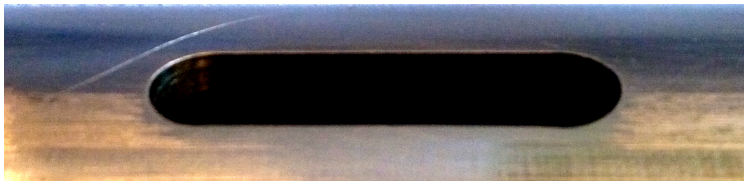

(c) Damage start point, real frame size: 63 mm × 18 mm.

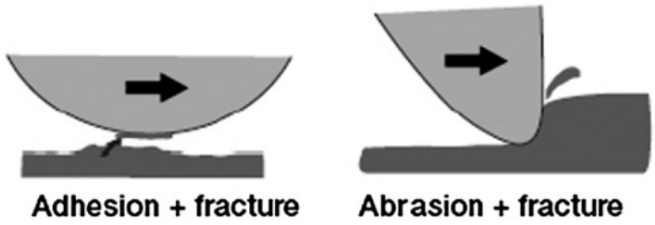

(d) Main mechanisms of the piston wear. Source: [2].

Figure 3.14: Piston wear.

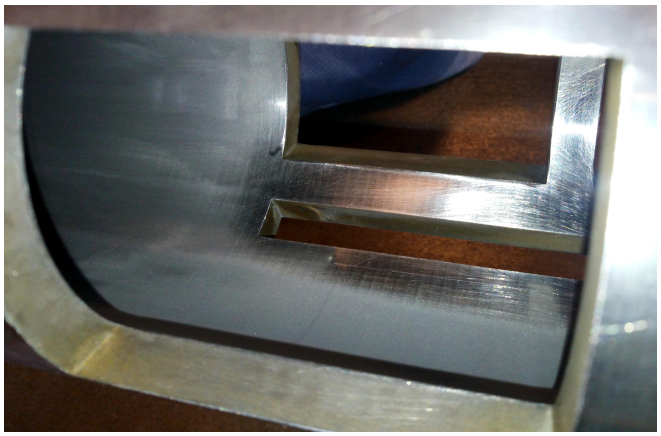

(a) Dull surface after honing.

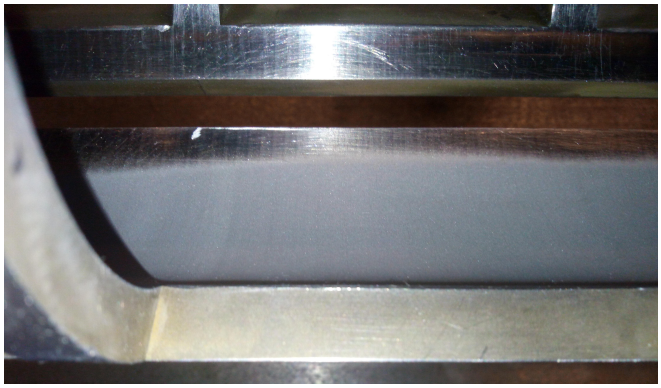

(b) The cylinder has expanded in the vicinity of the port openings.

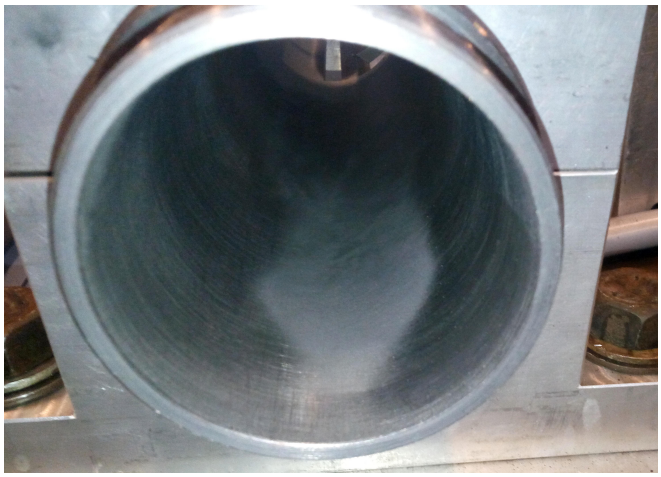

(c) Piston /cylinder contact spot.

Figure 3.15: The inner surface of the cylinder after lapping.

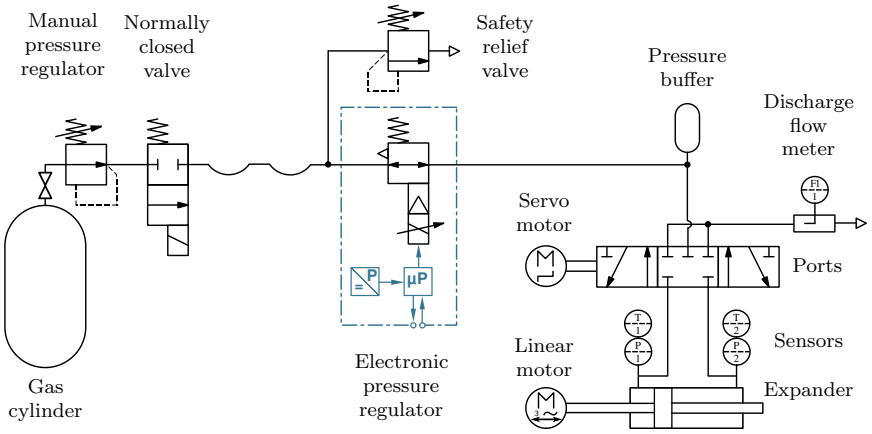

Figure 3.16: Pneumatic scheme of the setup.

flow in the case of any malfunction downstream or a power shut down. The pressure relief valve prevents the pressure before the electronic regulator from rising above 24 bar in order to avoid its damage in the case of faulty manual adjustment.

The electronic regulator is controlled by 4–20 mA current signal. The outlet pressure can be proportionally adjusted from 0 bar to 16 bar. A built-in microprocessor (μP) compares the pressure at the inlet port of the expander with the set point and adjusts the valve accordingly. If the pressure rises above the set point, the valve drains the excessive gas to the ambient. This functionality is useful if the setup operates in compressor mode. The data sheet for the regulator is attached in Appendix B.5.

After the electronic pressure regulator, a buffer with a volume of 20 l is installed to reduce pressure pulsations during the expander operation. The pressure buffer is equipped with an electric heater: the gas entering the expander is preheated up to 90 °C in order to prevent the gas temperature from dropping down to 0 °C during the expansion to avoid ice forming.

The in- and the outlet ports are schematically shown as a 3-position valve which is controlled by a servo motor. The linear motor is connected to another side of the piston. The pressure and the temperature sensors are installed at both inlet ports of the expander. The flow rate is measured at the outlet by means of the Pitot flow meter connected to a pressure difference meter. The temperature is also measured at the same position.

The general view of the gas supply system is depicted in Figure 3.17.

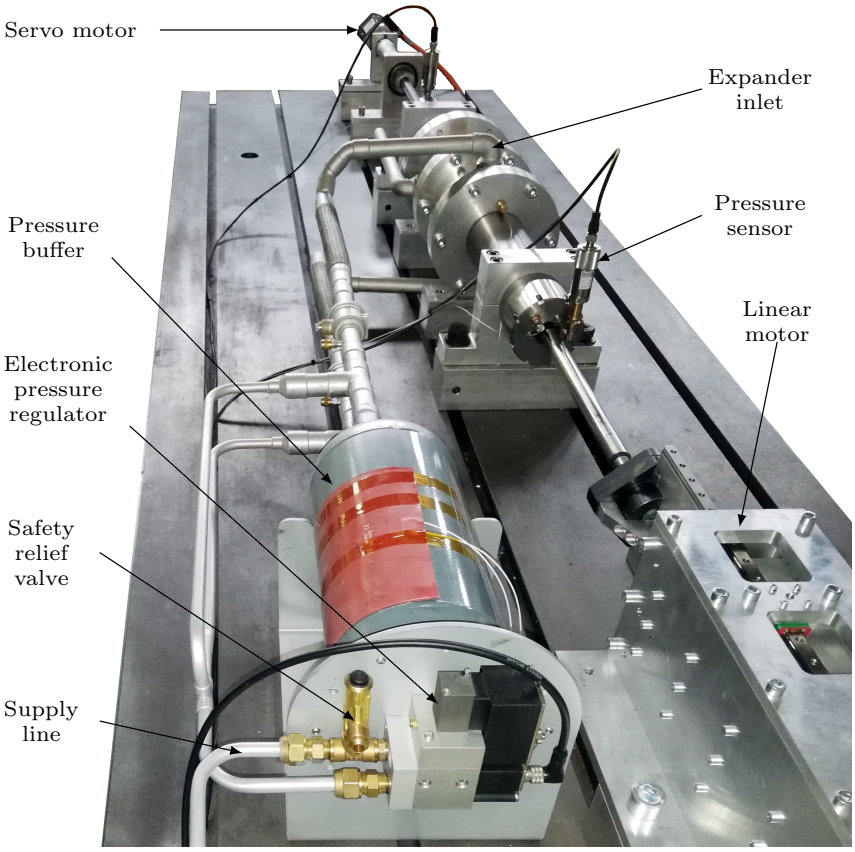

Figure 3.17: Gas supply system.

3.6 Data acquisition and control system

A high speed and deterministic data transfer within a control system for dynamic applications is of a great importance in order to realize a high positioning accuracy. The control and data acquisition system of the test setup is based on an industrial personal computer (IPC) with attachable input/output (I/O) modules. The programming environment is TwinCAT®[2]. The system is able to maintain a communication with up to 1000 distributed I/Os with an update time of 30 µs. As many as 100 servo axes can be controlled with the cycle time of 100 µs. Publisher/Subscriber approach instead of Master/Slave one. In this case, there is no central master for processing and controlling the communication. This allows to establish an unacknowledged data exchange, increasing its rate [3].

The motor drives are connected to the IPC through EtherCAT® interface, which is a field bus standardized under International Electrotechnical Commission (IEC)[3]. More detailed information is summarized in Appendix B.3.

The setup contains only three servo drives and five I/O modules, therefore, a cycle time of 50 µs has been set. The aforementioned allows to speak about real-time deterministic data acquisition, which means a guaranteed response within a required time frame. The main difference between conventional user mode programming and real-time programming in TwinCAT® is explained in the manual of this package [4]. Python is used for non-real time applications, such as preliminary model development and validation, data post-processing.

3.6.1 Sensors discrepancies

The general view of the test setup is shown in Figure 3.19. The applied force and torque are acquired from the motor drives. Both the linear and angular position of the piston are measured with the built-in incremental encoders.

- The linear magnetic encoder has an uncertainty of 0.1 mm.
- The temperature is measured with K-type thermocouples, isolated, with the diameter of 1 mm. The transducer accuracy is 0.3 % (relative to full scale value), conversion time 40 ms.
- The pressure is measured by fast response pressure transducers with a measuring range of 0–25 bar and 4–20 mA output. The standard accuracy is 0.1 % full scale without additional temperature error in a range of 10–60 °C. The measuring rates are up to 1 kHz.

[2] TwinCAT®, EtherCAT® are registered trademarks of and licensed by Beckhoff Automation GmbH.

[3] `http://www.iec.ch/`

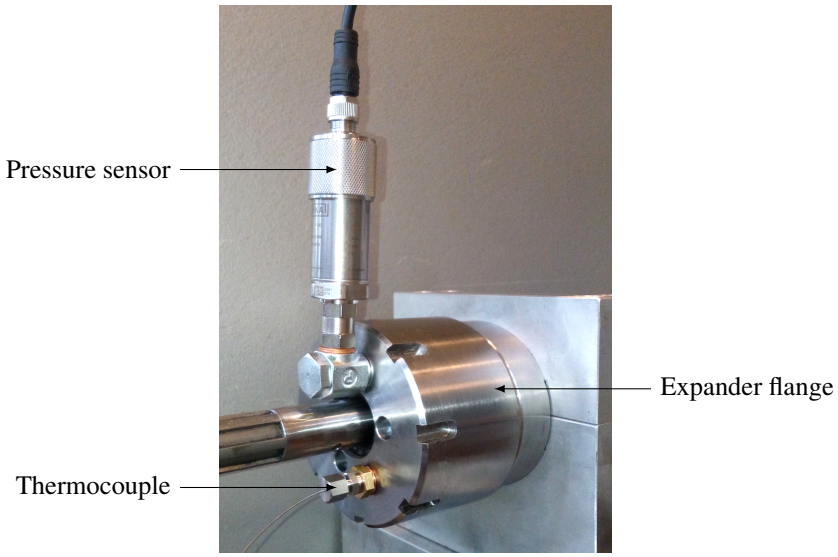

Figure 3.18: Pressure sensor and thermocouple connected with a working chamber.

- The pressure at the inlet ports of the expander is measured by a standard industrial pressure transducer integrated into the pressure regulator.

- The system updates the status each 0.25 ms which results in the acquisition frequency of 40 kHz.

In order to control the fluid parameters inside the working chambers, temperature and pressure sensors are installed on the cylinder flanges as shown in Figure 3.18. The sensors are connected with the working chambers through bores with a diameter of 6 mm. The total length of the bores is 425 mm. The major caveat of this measurement system is that Helmholtz-type gas oscillations in the bore can lead to a phase-shifted pressure profile and a higher peak pressure in respect to the true one. This phenomenon is reported by [5, 6]. The authors proposed a model based algorithm for the reconstruction of the in-cylinder pressure from the measured one. Being assumed a mass-spring system, the gas behavior in the channel can be modeled by means of the frequency response analysis. The working pressure and the frequency of the current setup are much lower than for the ICEs mentioned in these studies. Therefore, the influence of the oscillations in the measuring bore are neglected. However, this must be taken into account in a real design.

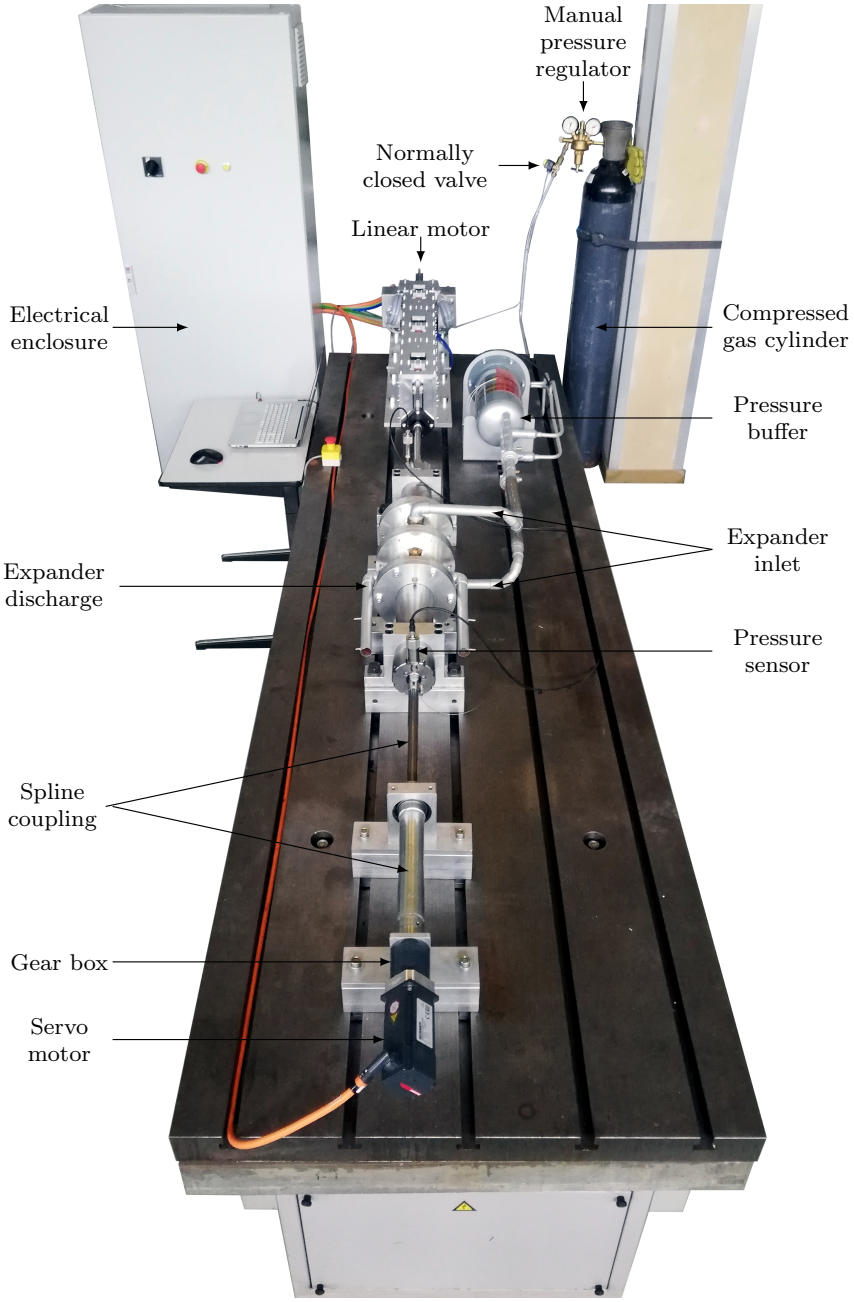

Figure 3.19: General view of the test setup.

3.6.2 Data Reduction and Uncertainty Analysis

The main goal of the planned experiments is the validation of the model obtained in Chapter 2 which involves a comparison of simulated pressures as function of the piston position. Piston position as function of time defines the piston speed and acceleration which are needed to simulate the piston dynamics. Also, the volume of the working chamber is used as input for the model. It is important to trace the propagation of the error of the position and pressure measurements in order to evaluate the influence of these errors on the results of the comparison. The method is explained in [7, 8].

The error sources can be divided in two groups: the sensors themselves and the data acquisition system (DAQ). While the temperature and position sensors are calibrated being connected to DAQ, the pressure sensors are calibrated by the manufacturer, so the sensor error shown in Appendix B.4 does not include the error introduced by DAQ.

In the case of error propagation, the most probable error can be expressed as follows:

$$\epsilon_{mp} = \sqrt{\sum_{i=1}^{n} \epsilon_i^2}\,, \tag{3.10}$$

where ϵ_i is the error of the i^{th} therm and n is the number of terms involved. Therefore, the most probable error of the logged value in respect to the true one is the sum of squares of the sensors' and the DAQ's errors when applicable.

When the measured values are used in equations, they can be multiplied, divided or been raised to a power.

For multiplication or division, the following equation can be used:

$$\frac{\epsilon_{mp}}{|Y|} = \sqrt{\sum_{i=1}^{n} \left(\frac{\epsilon_i}{X_i}\right)^2}\,, \tag{3.11}$$

where Y is a function of n X factors.

Raising X to a power j produces an uncertainty ϵ_{mp} of a function Y which can be calculated as follows:

$$\frac{\epsilon_{mp}}{|Y|} = |j|\frac{\epsilon}{|X|}\,. \tag{3.12}$$

More complicated formulas can be simplified by combining these cases.

3.6.2.1 Pressure error

For capturing the pressure sensors' signals, analog input modules are used. Each has an uncertainty of 0.3 % of the full scale. The most probable error of a calibrated

sensor is 0.01 % of a full scale as reported in Appendix B.4. By using Equation 3.10, the total error of 0.075 bar is obtained. The error propagation in the simulated pressure is shown in Figure 3.20.

3.6.2.2 Temperature error

The temperature measurements are included in Equation 2.22 which is substituted into Equation 2.21. This equation in turn is used to obtain the pressure inside the working chamber by means of Equation 2.37.

3.6.2.3 Position error

The position error of 0.1 mm declared in the datasheet includes the acquisition error. The position measurement is used in Equation 2.16 to calculate the volume of the working chamber which is further used in Equation 2.36.

Assuming there is no error in time measurements, Equation 3.10 can be used for the velocity and acceleration calculations. The error of a velocity value is 1.41×10^{-4} m/s and the error of an acceleration value is 2×10^{-4} m/s^2.

3.6.2.4 Piston mass error

The masses of the piston and of the LMA slider are measured with an accuracy of $\pm$ 0.1 kg.

3.6.2.5 Piston surface error

The piston and the cylinder diameters are measured with a micrometer. The error in the diameter measurement is $\pm$ 5 µm which is 0.00625 % in respect to the piston diameter of 0.08 m. This error can be neglected in further calculations.

3.6.2.6 Working chamber volume error

As aforementioned, the error in the surface measurement can be neglected. The error in the volume calculations is then a product of the positioning error of 0.1 mm and the surface area of the piston and it is equal to 5.03×10^{-7} m^3.

3.6.2.7 Gas force error

The gas force is a product of the pressure difference across the piston and the piston diameter as expressed in Equation 2.3.

$$\frac{\epsilon_{mp,gas}(t)}{|F_{gas}(t)|} = \frac{0.075}{|p_{cyl}(t)|} \tag{3.13}$$

3.6.2.8 Inertia force error

The inertia force is a product of the piston acceleration a_{ps} and the total mass of the moving components. This force is defined by Equation 2.2. The most probable error is varying in time and it can be calculated using Equation 3.11:

$$\frac{\epsilon_{mp,iner}(t)}{|F_{iner}(t)|} = \sqrt{7.72 \times 10^{-6} + \left(\frac{2 \times 10^{-4}}{a_{ps}(t)}\right)^2} \tag{3.14}$$

3.6.2.9 Frictional force error

The frictional force is a function of the piston speed and it is defined by Equation 2.7.

$$\frac{\epsilon_{mp,fr}(t)}{|F_{fr}(t)|} = f_\nu \frac{1.41 \times 10^{-4}}{|v(t)|} \tag{3.15}$$

3.7 Concluding remarks

The experimental setup has been designed and built using standard industrial linear motor components. The control of the motors and the data acquisition are realized TwinCAT®. This program allows sufficient flexibility of the configuration, data logging and visualization.

The setup commissioning revealed several mechanical problems caused by mistakes made during the design and manufacturing of the expander. In particular, the piston misalignment and the cylinder deformation.

The piston-rod system is only relevant for the setup and not for the final design. The first generation piston has been made with a semi-rigid threaded connection. This design has been abandoned because of a significant backlash which would increase due to a reciprocating movement. A more advanced ball joint system was considered but abandoned since welding, performed with all precautions, had been guaranteed to deliver an acceptable final result.

If the same piston would be manufactured again, the sequence of the machining operations must be changed:

- Milling or cutting of the openings.
- Welding of the manifold to the cylinder.
- Stress relieving by thermal treatment.
- Surface machining: eccentricity and misalignment removal and honing until the required tolerance is achieved.

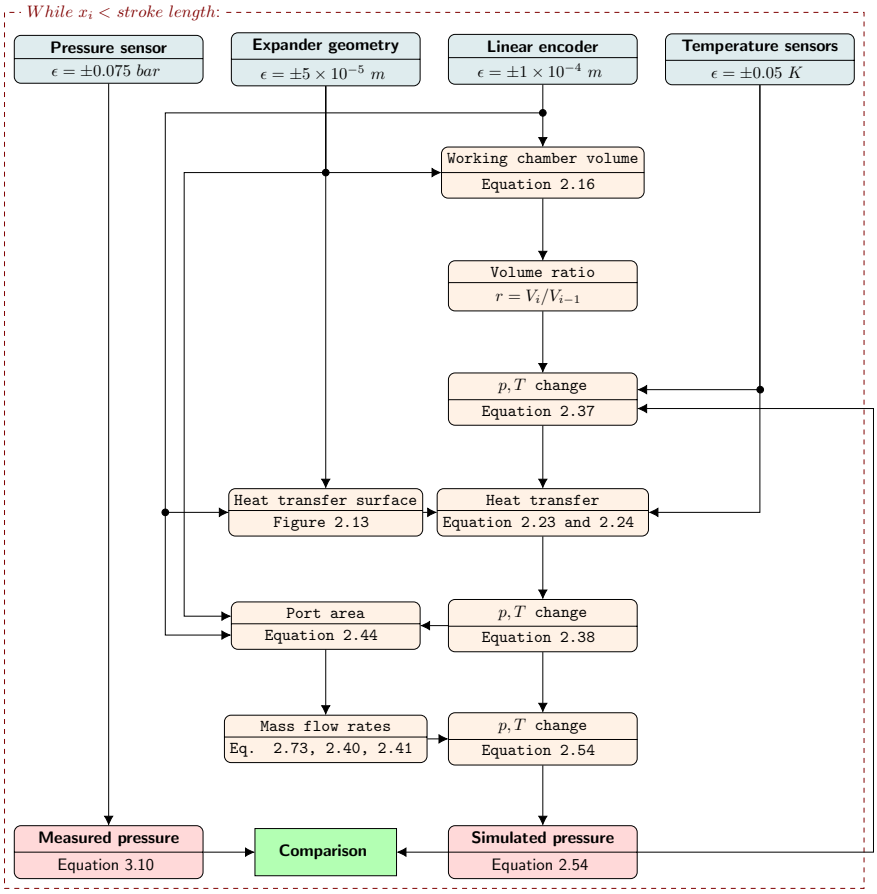

Figure 3.20: Error propagation chart.

The setup has been built within limited financial and time constraints. However, after all adjustments, the general condition and the functionality was found to be satisfactory and allowing to perform the experimental campaign.

References

[1] Franklin D Jones, Henry H Ryffel, Erik Oberg, Christopher J McCauley, and Ricardo M Heald. *Machinery's Handbook (Machinery's Handbook (Large Print))*. Industrial Press, Inc., 2004.

[2] Kenneth Holmberg, Helena Ronkainen, Anssi Laukkanen, and Kim Wallin. *Friction and wear of coated surfaces – scales, modelling and simulation of tribomechanisms*. Surface and Coatings Technology, 202(4):1034–1049, 2007. ICMCTF 2007.

[3] *Real-time Ethernet with TwinCAT network variables*.

[4] *From conventional user mode programming to real-time programming in TwinCAT*. Page 12.

[5] Raimo Turunen, Ossi Kaario, and Gösta Liljenfeldt. *Cylinder Pressure Measurement via Indicating Cock*. In Cimac Conference, Vienna, Austria, 2007. Cimac, 2007.

[6] E. Oezatay, P. Voegelin, P. Obrecht, Christopher H. Onder, P. Fuchs, and W. Fuchs. *Malfunction diagnosis at marine diesel engines based on indicator cock pressure data. Model based sensor reconstruction of in-cylinder pressure trace using indicator cock pressure information & Fundamental investigations on malfunction diagnosis at marine diesel engines based on reconstructed in-cylinder pressure information*. 2010. Cimac Congress 2010, Bergen, Norway, June 14-17.

[7] Richard S. Figliola and Donald E. Beasley. *Theory and Design for Mechanical Measurements*. John Wiley and Sons, 2010.

[8] J.R. Taylor. *Introduction To Error Analysis: The Study of Uncertainties in Physical Measurements*. A series of books in physics. University Science Books, 1997.

4

Experimental Characterization of the System

In this chapter, the experimental campaign is described. The linear motor / alternator (LMA) is tested with and without being connected to the expander. Friction losses have been measured in order to include these into the theoretical model. Also the speed and the force limits are defined. The control strategy is verified and tested. Main issues concerning the mechanical design appeared during the experiments were analyzed and fixed. The embedded design feasibility is proven.

4.1 Experimental setup commissioning.

During the preparation phase, the LMA was tested without being connected to the expander and operated in a motor mode. The goal of the first set of experiments was to define the velocity limit without load and to measure the friction forces in function of the translator velocity. Also, it was necessary to assess the positioning accuracy provided by the standard control algorithm implemented in the manufacturer's software. These preparations were necessary in order to avoid expander damage in future experiments if positioning overshoot occurs at the dead points.

4.1.1 Assessment of the operation of LMA without expander.

A movement profile, similar to one mentioned in Section 3.2.1 was used to control LMA. During the acceleration, the nominal thrust force has been applied until a certain target speed was reached. A constant speed part of the trajectory was needed to estimate the frictional force in the way which will be later explained in Section 4.3.1. At the end of the stroke, LMA was decelerated until it stopped at a set point position. The position deviation at this point gives the idea about the performance of the control algorithm.

This set of measurements has been performed starting from the target speed of 1 m/s, gradually increasing it with a step of 0.5 m/s until the alternator drive reported an unacceptable positioning error. As it can be seen on Figure 4.1, the maximum speed obtained during the experiment was 4.5 m/s. The speed stability decreases at higher values with the default motor settings resulting in "waves" clearly visible starting from 3 m/s. The absolute positioning error also increases with the speed as is depicted on Figure 4.2. If the piston is connected to LMA at this point, a certain deviation of the real piston speed from the desired one is not critical after the inlet port is closed and the piston is far enough from the dead points. However, when the piston approaches dead points, any divergence may cause the piston punching the cylinder flange. The central part of Figure 4.2 shows the discrepancy of the virtual piston speed close to the dead points. A mispositioning of 2–5 mm is clearly unacceptable but it can be mapped in function of the speed and anticipated in further experiments.

In the next set of experiments, LMA was programmed to follow the position profile obtained from the simulations. Figure 4.3 represents one more important result of this preliminary test campaign. The linear velocity profile acquired from the LMA drive remarkably differs from the desired one. More specifically, the readings from the drive are delayed in respect to the setpoint profile. Moreover, the velocity is not equal to zero at the dead points, which is obviously not possible. This issue is further investigated in Section 4.2.3 with the expander connected to LMA. At this point it was decided to keep the safety distance from the dead points of at least 10 mm.

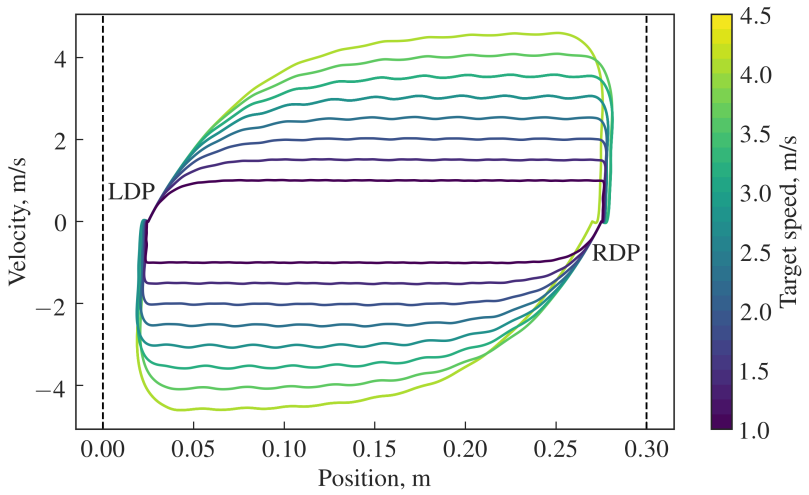

Figure 4.1: Slider velocity change in function of the position.

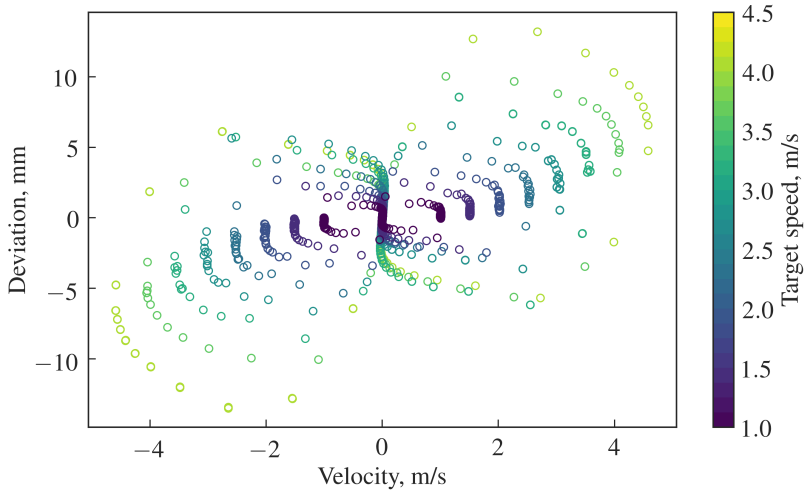

Figure 4.2: Absolute positioning error.

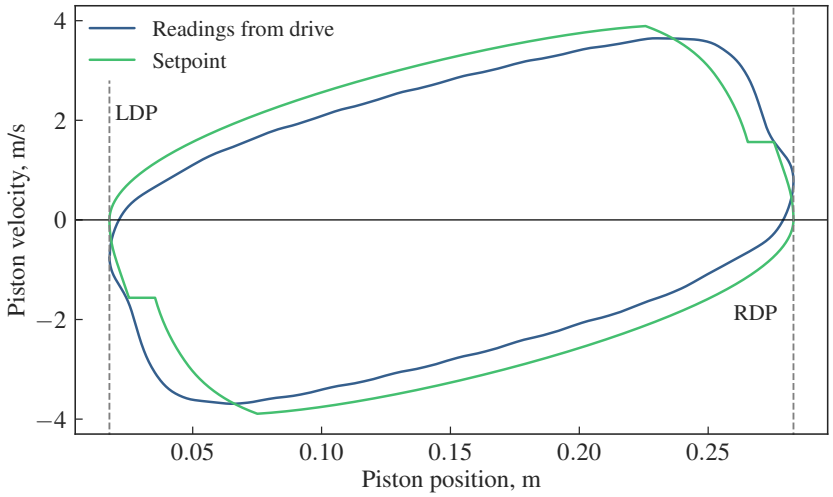

Figure 4.3: Velocity profile comparison.

4.1.2 Single-stroke run with the expander in compressor mode.

A first test campaign with the expander connected to the LMA was focused on the system identification and model validation. The stroke length was reduced in order to avoid possible piston collision with the expander housing at the dead points. The experiments have been performed with the ports closed. The piston was set to an angular position where the openings were pointed to the cylinder walls, equidistant from the cylinder openings, therefore the working medium was isolated inside the working chamber.

During the first run the piston stroke length has been set to 0.27 m and later to 0.28 m with equivalent distances from virtual to hardware dead points in order to study the pressure build-up. The rotation was disabled and the servo motor was used only to hold the angular position of the piston. The set-point of the maximum piston velocity was varied from 0.5 m/s to 5 m/s according to a trapezium profile, in the same way as in Section 3.2.1. After the piston reached its desired position, it was held until the pressure equalized with the ambient. The results of one of the experiments with the target piston speed of 4 m/s is shown in Figure 4.4 and Figure 4.5. By analyzing the pressure decrease after the piston is stopped, the leakage flow rate can be calculated.

The clearance size has been verified by means of an aluminum tape which has been attached to the piston surface as shown in Figure 4.6. The foil thickness is measured with a standard digital caliper. In order to increase the accuracy, 16 layers of the foil is measured, which gave the result of 0.88 mm, so the foil

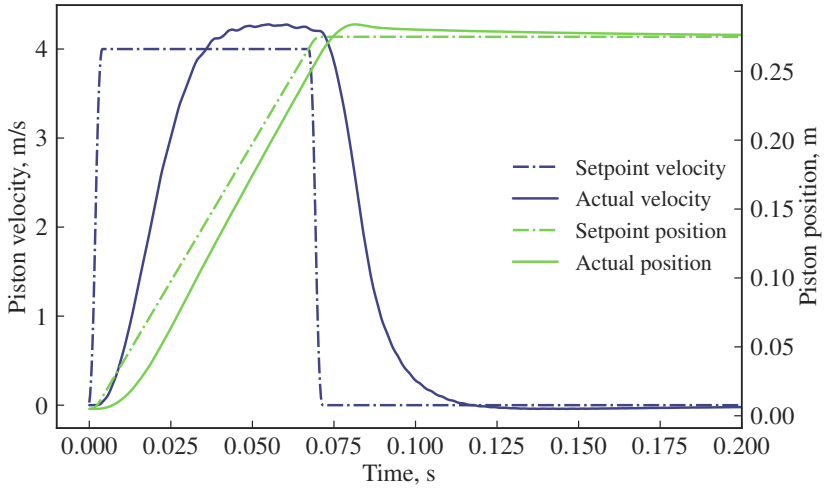

Figure 4.4: Setpoints and actual values of piston movement.

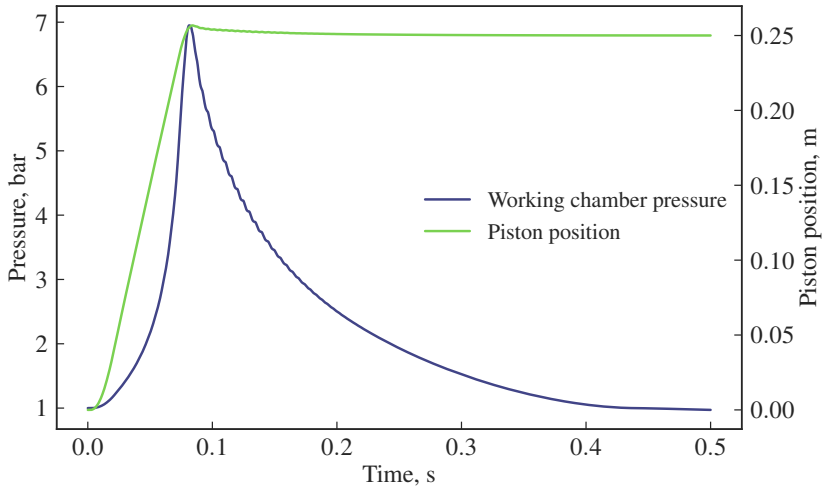

Figure 4.5: Working chamber pressure change.

Figure 4.6: Aluminum tape attached to the piston surface.

thickness is estimated to be about 50–55 µm. This is quite close to the clearance size estimated in Section 3.4.4. After this, the piston has been rotated and moved manually to ensure the undisturbed operation. Some resistance was detected, also scratches on the tape appeared, meaning a very close contact between the piston and the cylinder surfaces. In later experiments, Molykote D-321 R dry lubricant, mentioned in Section 3.4.4 will be applied in order to reduce the clearance size.

4.1.3 Continuous run in compressor mode

The second round of experiments has been performed using the same velocity profile but in continuous mode and with the piston rotating. The piping was not connected, so the discharge occurred to the ambient. The piston has been accelerated until a certain speed was reached and braked by the gas force and by the alternator. After the piston stopped at a safe distance from the left or right dead point, it was reversed and accelerated again. The rotation of the piston was synchronized with the linear motion in order to open the outlet at a certain piston position. By extending the end positions closer to the dead points, various compression rates can be obtained as shown in Figure 4.7. Only the right working chamber was pressurized during the experiments. The left working chamber remained in contact with the ambient. This allows to see the influence of a varying gas force on the alternator control operation. The experiments in continuous regime were focused on the piston positioning accuracy and repeatability.

A relatively low pressure build-up can be explained by the leakages, which are more significant at relatively low piston speeds. The major difficulty of the evaluation of the compressor/expander unit in the current setup is a limited robustness of the machine. This was never meant to operate in steady state for a long period

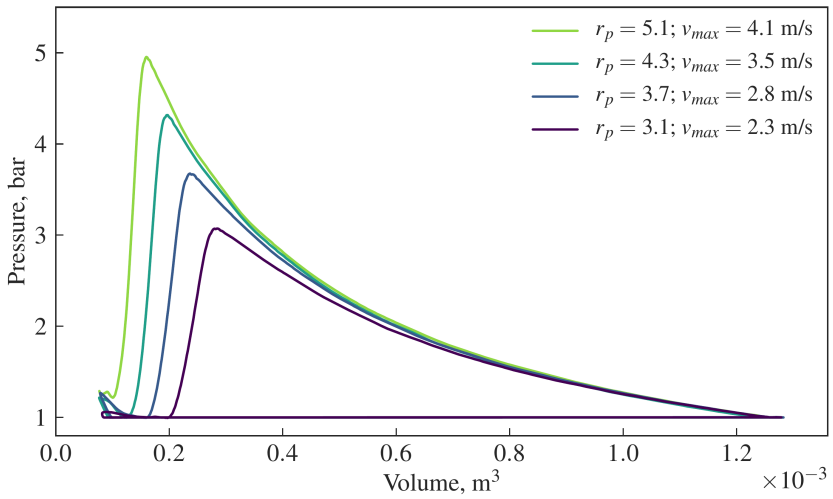

Figure 4.7: pV-diagram of continuous compression for several stroke lengths.

of time. Furthermore, the control of the piston motion was not optimized at the moment of this experimental campaign.

First test setup runs during the commissioning revealed several problems with the positioning accuracy at high linear speeds. All efforts to improve the positioning accuracy by means of the controller settings (PI-controller) led to a self-excitation of the control loop manifesting in a vibration and sound even when the slider was not moving. The frequency of the sound was measured. The value of about 400 Hz was quite stable with or without expander connected, which possibly means a solely software origin of this issue. This frequency corresponds with a cycle time of 0.25 ms and probably indicates a delay in signal processing.

4.1.4 Model validation

In order to validate the model developed in Chapter 2, the logged piston position profile in function of time from Section 4.1.2 was used in the simulation as input. The pressure change was simulated and compared with the measurements as shown in Figure 4.8. The deviation of the logged and simulated pressure change, which is depicted in Figure 4.9(a) and the deviation of the piston position, visible in Figure 4.9(b), are in a range of ± 10 % except a relatively larger deviations around small pressure ratios. However, this is not a major issue for the movement control since the piston speed at this point is close to zero. The piston position is simulated without taking into account residual forces but the deviation from the reference position does not exceed 10 %, which is acceptable and it can be

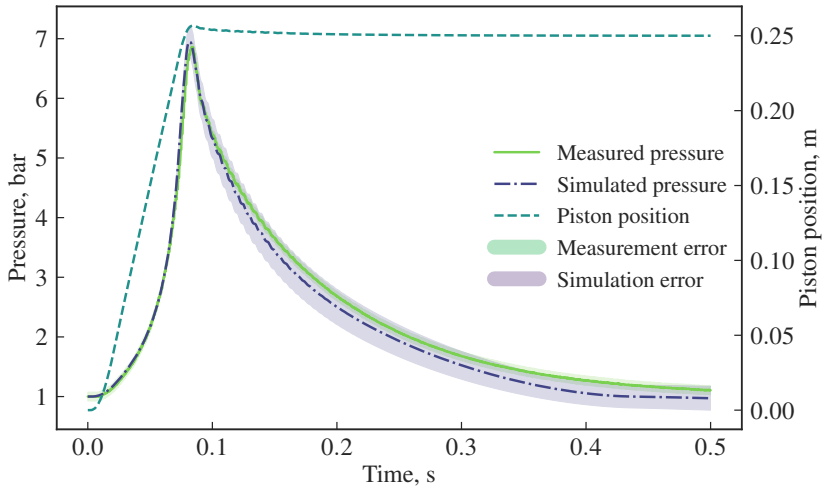

Figure 4.8: Pressure build-up and equalization as a function of piston displacement.

improved by the motor control system.

4.2 Sources of uncertainties

The design of LMA was described in detail in Section 3.2. A two-coil design was chosen in order to increase the power density of the machine and to compensate the attracting forces of each coil. The control software is configured according to Master/Slave synchronous approach. This means that only one motor is controlled using an encoder feedback and, therefore is set as master. The slave motor controller simply receives the output torque signal of the master motor controller as input and follows it without any feedback. The signal processing requires a certain time, therefore, the reaction of the slave motor is delayed which potentially can be an issue for high-dynamic systems such as the current one.

Such a configuration is still widely used in applications with moderate requirements to the positioning accuracy, settlement time and overshoots. This approach, being relatively easy to configure and to use, was for the first time used for dual arm robots, portal cranes and mills. The major drawback of such a closed loop configuration is that two motors are rigidly connected through an object being moved or a common beam. Since in real systems a certain difference between the operation of the two motors is unavoidable, the difference in thrust forces leads to undesired or even potentially dangerous tensions in construction elements of the machine. The efficiency and the positioning accuracy of the whole system is also

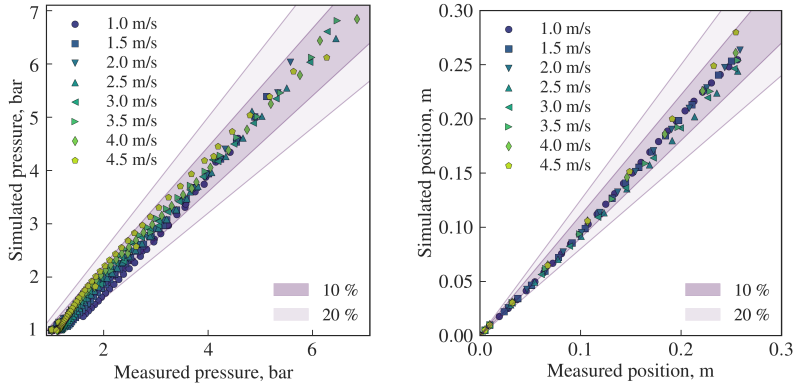

(a) Logged and simulated pressure change.

(b) Logged and simulated piston position.

Figure 4.9: Validation of the pressure and position simulation based on the logged motor force.

affected due to a higher power consumption of the motors working under a heavier load.

An overview of algorithms improving the control performance and synchronization of multi-motor systems is provided by [1] and [2]. In general, there are three major control techniques for multi-motor systems, namely parallel independent control, master-slave parallel control, and cross-coupling control. The last technique is reported to be the most appropriate one.

4.2.1 Analysis of the current setup

In the current experimental setup, the primary sections are rigidly connected with each other through the common housing and the secondary sections through the common moving frame. Therefore, no asynchronism of one motor in respect to the other is possible, however, the time lag of the slave thrust force leads to a non optimal system operation, especially when the thrust force alters. Practically, a difference between attraction forces leads to a higher frictional force acting on the guiding system which decreases the system efficiency and the life time.

In order to detect and to quantify this lag, the position signals from both encoders can be compared by means of an algorithm involving the fast Fourier transformation (FFT)[1] in the following four steps:

- By means of zero-crossing detection, one full period of both signals to be extracted from a log file;

[1] `https://stackoverflow.com/questions/4688715/find-time-shift-between-two-similar-waveforms`

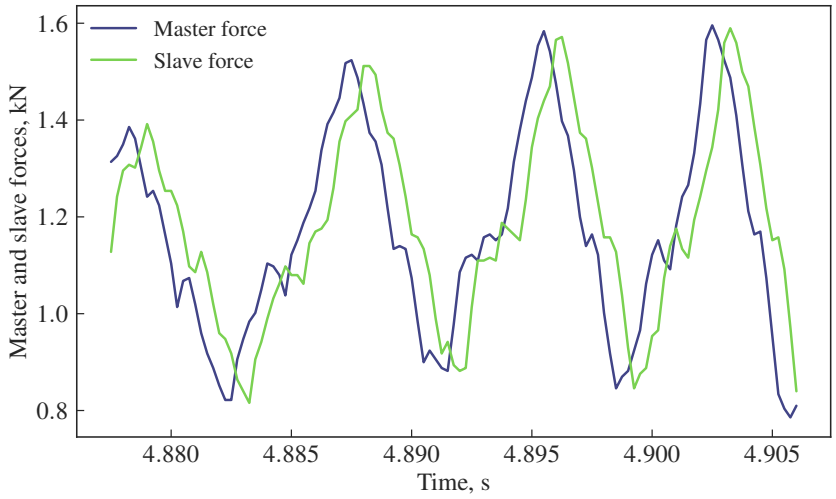

Figure 4.10: Time delay of the slave thrust force.

- Both signals must be Fourier-transformed using the *fft* function from *scipy.fftpack*[2];
- The slave signal must be inverted and conjugated;
- The product of both resulting transformed signals must undergo the reversed Fourier transformation.

As result, the number of time steps in the log file can be obtained indicating the delay of the slave signal relatively to the master one. This value, multiplied by the time step gives the time value of the delay. For this particular case, a delay of 0.75 ms was detected. As aforementioned, this time is needed for the slave controller to process the input and to send the control signal to the power electronics. This phenomenon is depicted in Figure 4.10.

Ideally, the thrust forces of the master and the slave motor must be equal since both motors are designed and manufactured identically. However, the comparison revealed a significant difference between these forces. This difference is larger for faster increasing forces. The maximum detected is about ± 0.7 kN which is about 12 % of the total nominal force of the LMA. This phenomenon is depicted in Figure 4.11. As can be seen, the difference reaches its maximum close to the dead points where a high positioning accuracy is especially important.

In the future, the current control structure will be replaced by more advanced model predictive control algorithm. By sending a feed-forward thrust force signal

[2] `https://docs.scipy.org/doc/scipy/reference/fftpack.html`

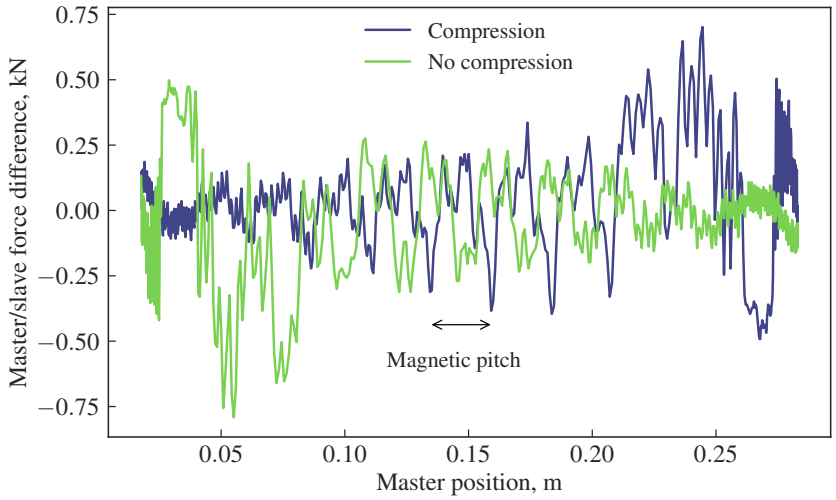

Figure 4.11: Master and slave force difference as a function of position.

to both controllers simultaneously should eliminate the described problem almost completely.

4.2.2 Correction of systematic errors

When the aforementioned problem is solved, the next issue is the hardware imperfections such as difference in magnet placement or their strength which can cause some difference in the reaction of the motors on the same control signal. This issue is known as Sine error which can be calculated as follows:

$$F_{dif} = F_{em} \sin\left(2\pi \frac{D_{dif}}{MP_{n-n}}\right), \tag{4.1}$$

where F_{dif} is the force difference between the two motors, F_{em} is the total force produced by both motors, D_{dif} the length of misalignment and MP_{n-n} the north-to-north magnetic pitch. By means of experiments, this force can be mapped and the correction can be integrated into the control algorithm.

The next potential source of systematic errors is the position acquisition circuit. First of all, the operation of the position sensors have been evaluated. The readings of both sensors have been compared after removing offsets. The results of the comparison are presented in Figure 4.12. As it can be seen, the measured position difference has a very clear pattern, which step corresponds with the magnetic pitch. Also the difference between the readings is larger while the piston moves to the right. However, no significant influence of the gas force was established.

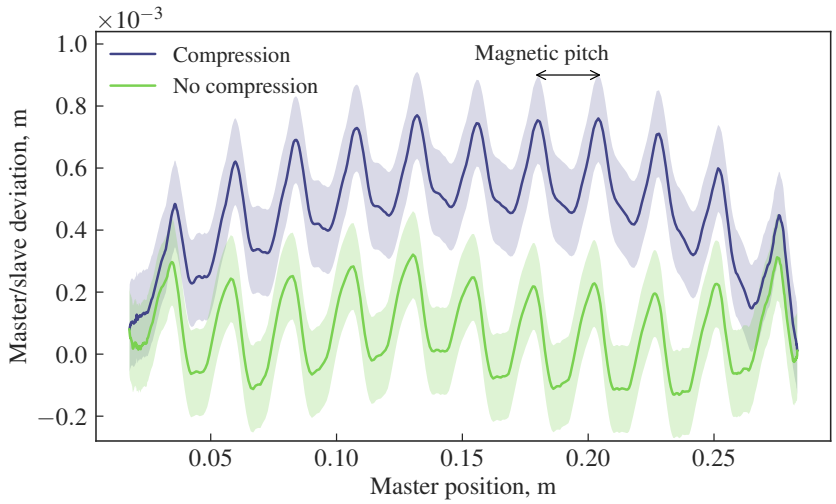

Figure 4.12: Master and slave encoders incoherence.

By mapping the linear dependency of the measured difference in function of the piston position and by applying a correction coefficient for the velocity, a first step to a better position acquisition can be made.

The pressure sensors, used to calculate the gas force for the model, are provided with calibration tables, therefore, a systematic error is eliminated.

4.2.3 Random noise filtering

Beside systematic errors and the alternator settings, a random noise, which is always present in a sensors signal, can be the reason for an uncertain positioning. Several interpolation and filtering methods can be used [3]. The right choice of a filtering method is crucial because too intensive smoothing can not only remove the noise but also distort the useful information. Furthermore, averaging over a wide sample window leads to a phase shift of the filtered signal [4]. This is a quite unwanted side effect for high dynamic applications where a system modeling is involved.

Not only the piston position but also its velocity and acceleration are used in a control algorithm. However, sufficiently accurate real time velocity and acceleration calculations, based on the position signal, is not a trivial task. Typically, these calculations are performed in the following way: by using two position measurements at time i and $i+1$, the average velocity between these points is calculated:

$$v = \frac{x_{i+1} - x_i}{t_{i+1} - t_i} \,. \tag{4.2}$$

Since the acquisition period $(t_{i+1} - t_i)$ is constant, it can be expressed as Δt. Assuming the uncertainty in time measurement is negligible, the error in piston velocity δv arises from the encoder uncertainty $\delta x = f(v, x)$.

$$(\delta v)^2 = \frac{(\delta x_{i+1})^2 + (\delta x_i)^2}{(\Delta t)^2}\,. \tag{4.3}$$

It can be seen in Equation 4.3 that the error in velocity is larger at smaller Δt but, on the other hand, a larger sampling interval leads to a larger phase difference, which means that the calculated signal is delayed relatively to the true one.

The acceleration is the second derivative of the position signal and the calculation method suffers from the same reason. Random noise in the position readings leads to even higher deviations of the calculated signal from the true values in respect to the velocity signal. An accelerometer installed on a moving part could provide the necessary input for the model, however, for the current design it is barely possible due to too high target temperatures of the machine parts for the electronic circuits. Therefore, the only viable solution to obtain the velocity and acceleration profiles is to use the position signal with the right filtering technique.

The most accurate filtering is the so called Zero-phase filtering, included in popular scientific software[3, 4]. This technique implies a signal smoothing in straight and reverse directions, averaging the results afterwards. The phase shift of the filtered signal in respect to the original one is therefore zero. This method can be recommended for the data post-processing but not for real time calculations since the information from the future is not available. Alternatively, a Savitzkiy-Golay filter [5] can be applied, which is reported to be more accurate than a standard polynomial filtering [6]. Both approaches are further combined according to the purpose of the data processing.

The velocity feedback signal from the drive was compared with an externally calculated one in order to quantify the delay and to figure out whether a deviation persists. The velocity was calculated by using Equation 4.2 based on a position signal filtered by the Savitzky-Golay filter. The obtained velocity signal itself was not filtered. The reference points are the piston extreme positions where the velocity becomes equal to zero. The results of this comparison are shown in Figure 4.13

Regardless of a good smoothing provided by the default control algorithm, the velocity signal is 8.5 ms delayed relatively to the calculated signal, which leads to a miscalculation of the instantaneous velocity from $\pm$0.5 m/s to $\pm$1.5 m/s as it can be seen in Figure 4.14. Also, it is clearly visible that the velocity value obtained from the motor controller alters while the piston keeps moving in the same direction which is obviously physically impossible.

[3] https://nl.mathworks.com/help/signal/ref/filtfilt.html

[4] https://docs.scipy.org/doc/scipy-0.14.0/reference/generated/scipy.signal.filtfilt.html

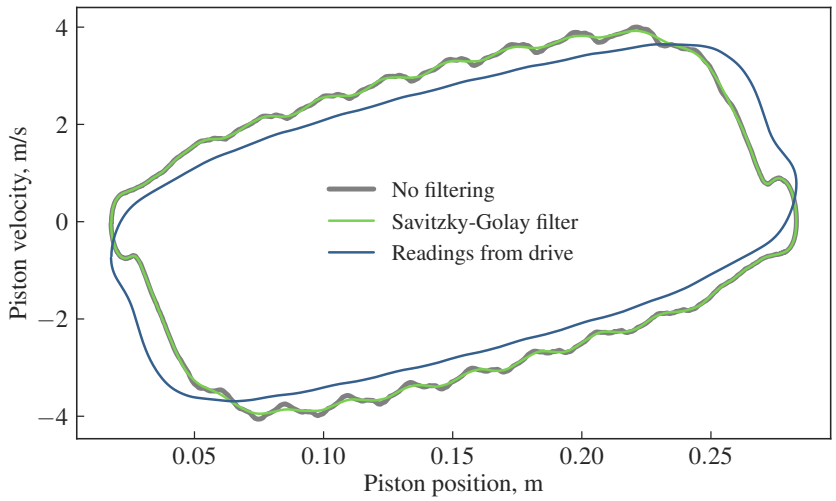

Figure 4.13: Illustration of various velocity calculation and filtering algorithms.

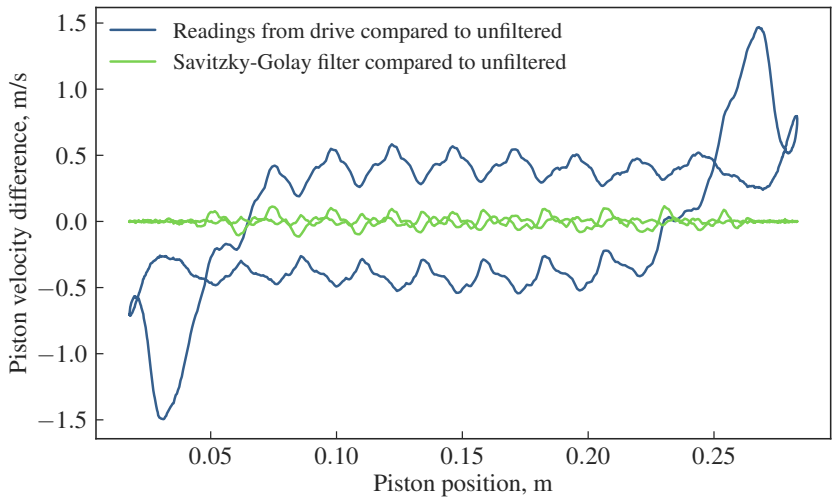

Figure 4.14: Comparison of filtering techniques.

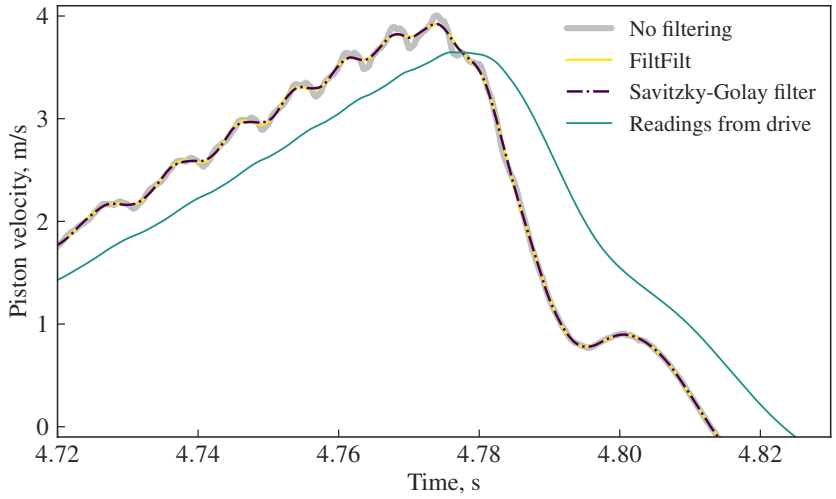

Figure 4.15: Comparison of filtering techniques.

Figure 4.15 illustrates the implementation of Savitzky-Golay and Zero-phase filter on the position signal. As a result, the calculated velocity signal is smoothed but not delayed significantly. Both filters provide almost the same results. The plotted data has been also verified by means of a high speed camera. The buckling on the descending part of the plot, almost completely filtered out by the default filter has been clearly observed on the video.

In order to configure the filter in the right way, the acceleration signals, as well unfiltered as obtained by means of several filtering methods, must be compared with the true signal. The latter, however, can not be known without additional measurements i.a. by means of an accelerometer but there is a possibility to estimate the accuracy of the calculated acceleration by comparing it with the force signal measured by the drive as it can be seen in Figure 4.16. The acceleration is related to the inertia force through the mass of the components being moved, which can be accurately measured. When the friction force is identified and the gas force is measured, both can be subtracted from the motor's thrust force. The obtained acceleration is compared with the calculated and filtered one, so the filtering settings can be adjusted accordingly and the inertia force can be estimated.

4.3 System identification

In order to identify the system forces, such as frictional force, which can not be measured directly by means of the available resources, the piston acceleration must

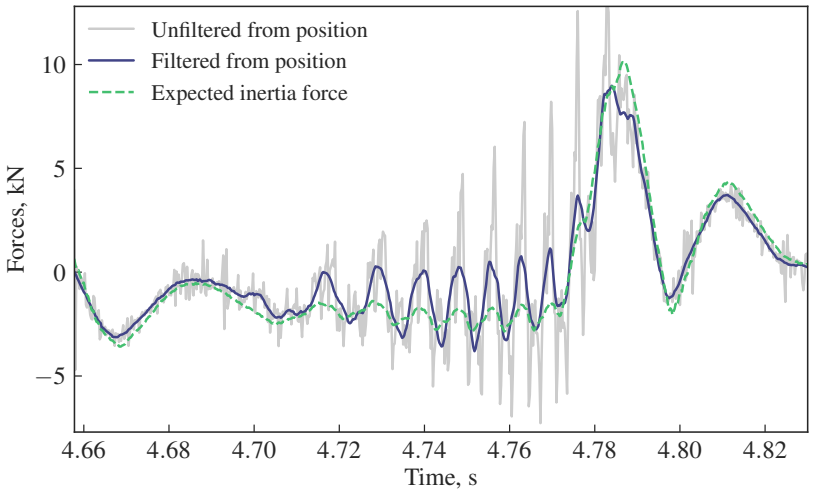

Figure 4.16: Force estimation from position signal.

be calculated. The inertia force can be estimated knowing the value of the moving mass and the acceleration as shown in Figure 4.16. It is important to match the inertia force and the thrust force profiles, otherwise, the residual force will be estimated incorrectly in real time measurements. By comparing the amplitudes of the filtered signal with the expected one and by minimizing the phase shift, a set of the filter settings can be obtained. Also a reversed approach can be useful: by knowing the mass of the moving parts and the maximum of the forces acting on the piston, the maximum acceleration can be estimated. The excessive values can be filtered out.

4.3.1 Frictional forces identification

As already mentioned in Section 2.2.1.2, friction is a complex phenomenon, so the choice of the right model for a specific design and its accurate identification is quite important. The major difference between the patented concept and the test setup is the placement of the LMA. In the setup, the LMA is placed outside the expander and is made of standard industrial components. The servo motor is connected to the expander by a spline shaft. The piston is supported by the rod and has a very limited contact with the housing. Any lubricants are avoided in the expander, but not on the spline shaft, guiding rails, the piston supporting shaft, and the shaft seals. These components will be unnecessary for the final design, which is not formulated in detail at this point.

The identification of the Coulomb and the viscous forces is performed in a

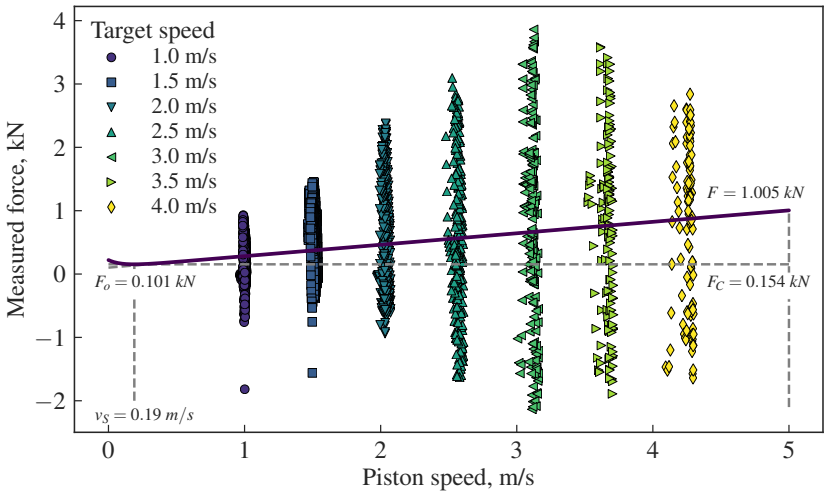

Figure 4.17: Measured force after pressure force subtraction as a function of piston speed.

similar way as is described in [7]. However, in contrast with the author's setup, the current one does not allow to obtain a long lasting constant piston speed. Because of the limited piston stroke length, the target speed can be maintained only for a very short period of time. The maximum speed is reached at the very end of the stroke. This is why the acquired data are filtered in order to extract nearly steady states as is shown in Figure 4.17. The gas force is subtracted from the force provided by the linear motor and set on the y-axis against the piston speed. The speed and the force fluctuations are caused by the drive settings which are kept standard with some minority adjustments. It can be assumed that at optimal drive settings, the maximum of the data density would be located in the middle of the data frames of each speed along the solid line on the plot which is obtained by means of the linear regression method. The slope of this line dF/dv of 180.7 N/(m · s) defines the viscous force. The offset value F_o of 101.5 N is obtained where the line crosses the y-axis.

By using the aforementioned coefficients, Equation 2.7 can be defined as is visualized by the dark blue line. The force of 153.8 N at Stribeck speed v_S of 0.19 m/s is the value of the Coulomb force, F_C. As explained in Section 2.2.1.2, the stick-slip effect, which is visible at a velocity below 0.19 m/s, can be neglected since the piston is accelerated with a force much larger than the stiction force. Furthermore, in a real operation, the piston rotates continuously, so stiction can only occur at the start up. The lowest velocity is expected to be around 1 m/s. The frictional force can be identified for the velocity range of 1–4.5 m/s and it

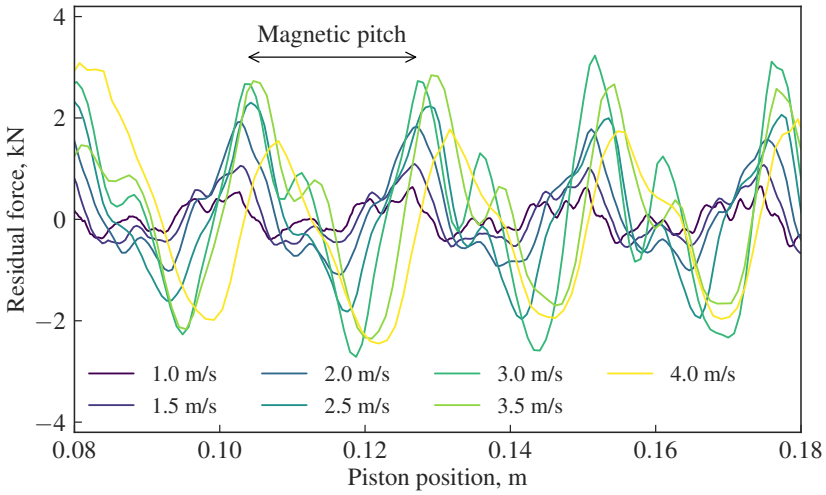

Figure 4.18: Residual forces as a function of the piston position.

can be fitted with linearly. Summarizing all mentioned above, Equation 2.7 can be simplified as follows:

$$F_{fr} = 101.5 + 180.7 v_{ps} \tag{4.4}$$

This model is used solely for the current setup. The choice of the friction model for the prototype with an embedded LMA must be made in accordance with other decisions concerning the final design.

4.3.2 Residual forces analysis

After the frictional and the pressure forces are subtracted from the electromagnetic one, the residual forces are analyzed in regimes with a relatively constant piston speed, so the inertia force can be neglected. The resulting forces are assumed to be a combination of the cogging and the reluctance forces as described in Section 2.2.1.4. From Figure 4.18 it can be seen that these forces are mainly position-dependent, namely have a step equal to the magnetic pitch of 0.024 m, which is the distance between two coils of the linear motor. There are some deviations between the periods caused by irregularities in the mechanical system. Also, the amplitude is speed-dependent as a result of a higher magnetization current at higher speeds. Either way, these results can be mapped and used for the motor fine-tuning as described in [8].

4.4 Efficiency assessment

The experimental campaign has been performed in a compressor mode assuming the machine is fully reversible. Therefore the most results obtained are also valid for an expander mode. The main difference which must be taken into account is that the direction of the pressure change across the machine is opposite to the flow direction in a compressor mode. Also, the heat transfer to the ambient affects the efficiency of both modes in different ways: while the cooling of the compressor increases its efficiency, the expander cooling is not beneficial.

4.4.1 Volumetric efficiency

The volumetric efficiency of a compressor or an expander is an important parameter influencing the machine performance. This can be defined as the ratio of the actual volume flow V_{act} to the theoretical one V_{theor}, which is calculated from the displacement volume V_d, and the frequency f as follows:

$$\eta_{vol} = \frac{\dot{V}_{act}}{\dot{V}_{theor}} = \frac{\dot{V}_{act}}{V_d f} \,. \tag{4.5}$$

There are two main factors having an effect on the volume flow rate. The first one is the leakage bypassing the machine, which increases the flow rate of an expander and decreases it of a compressor. Throttling during the intake process leads to a lower flow rate for both cases. In the case of dominating leakage losses, the volumetric efficiency of an expander may exceed the unity.

During the experiments, the pressure in the working chambers before the start of the compression process was equalized with the ambient one. At the end of the compression process, the ports remained closed. Hence, the throttling losses have been neglected.

Without leakages, the following relationship is valid:

$$\frac{\rho_{su}}{\rho_{dis}} = \frac{V_{dis}}{V_{su}} \,. \tag{4.6}$$

By combining Equation 4.5 and Equation 4.6, the volumetric efficiency can be approximately calculated from the experimental data as follows:

$$\eta_{vol} \approx \frac{\dot{m}_{act}}{\rho_{theor} V_d / f} \approx \frac{\rho(T,p)_{act}}{\rho_{theor}} \,, \tag{4.7}$$

where V_d is the displacement volume, f is the frequency, ρ_{theor} is the density of the working fluid calculated for ideal compression or expansion and $\rho(T,p)_{act}$ is the actual density calculated from the measured or simulated temperature and pressure. The results of the volumetric efficiency measurements are summarized in Figure 4.19.

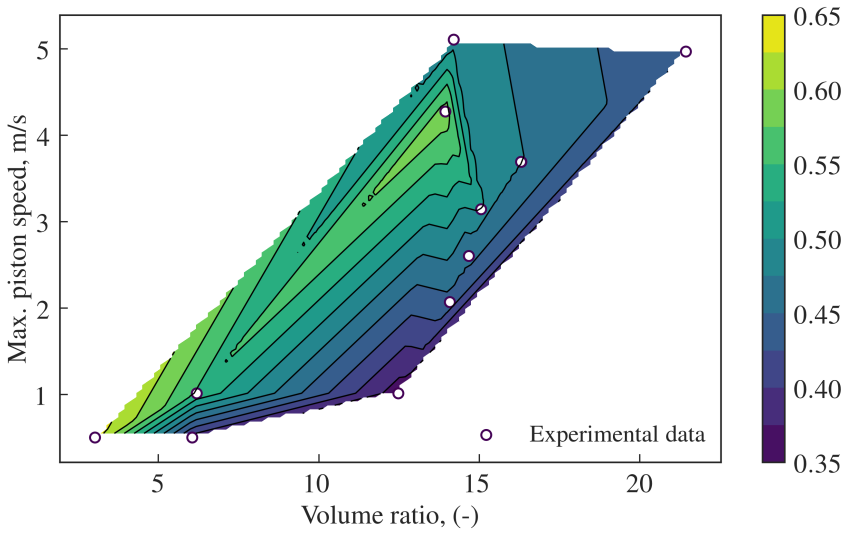

Figure 4.19: Compressor volumetric efficiency.

4.4.2 Isentropic efficiency

According to the First Law of thermodynamics, the power supplied to perform isentropic compression is equal to:

$$\dot{W}_s = \dot{m}\,(h_{2s} - h_1) \tag{4.8}$$

The Second Law states that:

$$\begin{cases} s_2 > s_1 \\ s_{2s} = s_1 \end{cases} \tag{4.9}$$

The isentropic efficiency of a compressor is therefore defined as follows:

$$\eta_{is} = \frac{h_{2s} - h_1}{h_2 - h_1} \tag{4.10}$$

Assumptions:

- Steady state.
- Constant in- and outlet pressures and temperatures.
- The compressor is adiabatic.

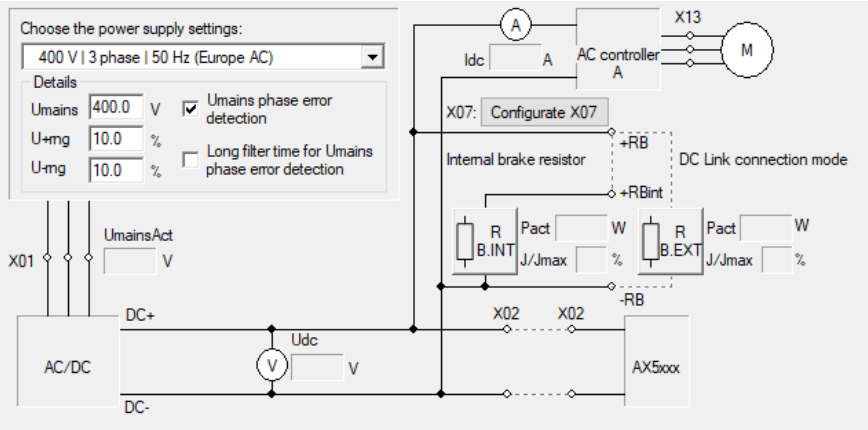

Figure 4.20: DC current and voltage measurement points configured in TwinCAT.

The power generated or consumed by the LMA can be measured with a power meter. However, the power dissipated by the drives is unknown. Therefore, it was decided to use the data from the drive itself, more specific, the current and the voltage of the DC-line as depicted in Figure 4.20.

The overall isentropic efficiency of one compression cycle can be calculated as follows:

$$\eta_{is,\,overall} = \frac{\dot{W}_{comp}}{\dot{W}_{el}} = \frac{\dot{m}_{comp}(h_{su,is} - h_{dis,is})}{\dot{W}_{el}}\,, \tag{4.11}$$

where $\dot{W}_{el}$ is the electric power measured by the inverter and $\dot{W}_{comp}$ is the power needed to perform the compression of the working fluid, which is equal to the mass flow rate multiplied by the isentropic enthalpy change $(h_{su,is} - h_{dis,is})$ across the compressor.

The overall isentropic efficiency of one expansion cycle can be defined in a similar way:

$$\eta_{is,\,overall} = \frac{\dot{W}_{el}}{\dot{W}_{exp}} = \frac{\dot{W}_{el}}{\dot{m}_{exp}(h_{su,is} - h_{dis,is})}\,, \tag{4.12}$$

where $\dot{W}_{exp}$ is the power extracted from the working fluid.

4.4.3 Alternator efficiency

The fact that the LMA is built from two independent motors sharing the same moving magnetic section provides a natural possibility to investigate the efficiency of the motors without any additional equipment as illustrated in Figure 3.4. The motor being tested must be configured to follow a reciprocating profile with a

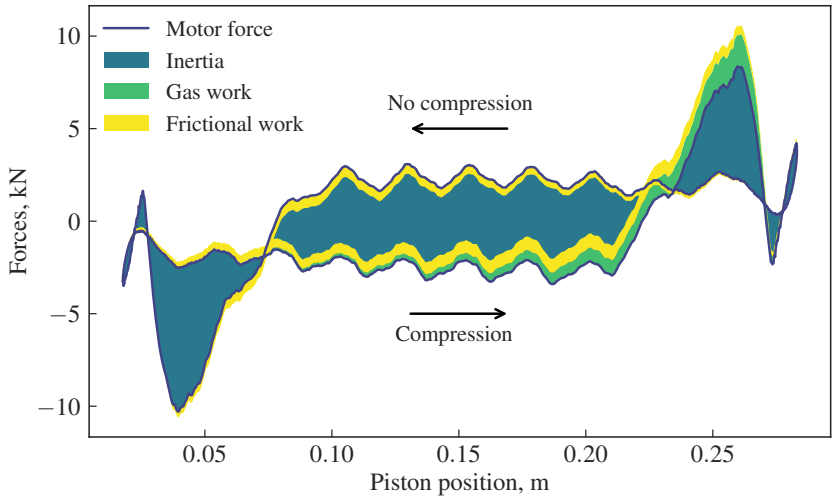

Figure 4.21: Energy transformation during one stroke.

certain constant speed during a part of the trajectory. The second one must provide a constant force independently of the first motor behavior. The unit being tested must overcome the load if the braking force is oriented against the movement direction, acting as a motor. During the returning part of the stroke, this unit acts as an alternator dissipating the produced electricity as heat in brake resistors. Therefore, one motor can be tested as well in motor as in alternator mode during one reciprocation cycle.

By varying the load and the speed values from zero to a maximum value, the efficiency map for the operation range can be obtained. Since both motors are connected and configured in the same way, both can be tested just by altering the configuration in the software of the setup.

4.4.4 Optimization possibilities

Forces acting on the piston and the energy accumulation and release are shown in Figure 4.21. A relatively low pressure build-up can be explained by the leakages, which are more significant at relatively low piston speeds. Furthermore, the control of the piston motion was not optimized at the moment of this experimental campaign.

The work provided by the motor is used to overcome the friction losses and the gas force. The excess is accumulated as the inertia energy and released back during the piston deceleration. Ideally, the energy provided to the acceleration phase is recovered during deceleration phase of the piston. The only question

still unanswered is how to quantify the losses which are unavoidable during this process. Unfortunately, it is difficult to estimate the influence of this phenomenon on the system efficiency since data about LMA efficiency as a function of speed and load was not available.

The piston movement profile optimization results in equalizing of the green zones close to the dead points, which means that all work of the motor except the frictional losses is transferred to the compression process by using the inertia of the moving piston. Furthermore, equal accelerating and decelerating forces are favorable for the LMA sizing.

If the mass of the piston would be reduced, the thrust force which is needed to accelerate the piston would be also lower. This, in turn, would decrease the motor/alternator losses associated with the acceleration part of the piston trajectory. The contribution of the gas force to the overall energy balance will be more significant, especially, if the leakage flow rate can be minimized.

Alternatively, the the LMA can be optimized in order to realize the maximum working frequency. This means a higher piston speed and a higher friction loss as the result. On the other hand, the time when the frictional force becomes significant will be shorter and the constant speed part of the piston trajectory will disappear. When the efficiencies of all processes are known, such a simulation can be performed in order to maximize the mass flow rate and to minimize the power consumption of the linear compressor.

4.5 Improvement of the control algorithm

The standard control algorithm implemented in the current setup shows adequate performance, however, the positioning accuracy must be improved in order to measure the motor efficiency or to realize the right port timing. Overshoots must be avoided as these lead to a mechanical damage in a real installation. The mechanistic model developed in Chapter 2 can be used to generate a force feedforward action for the controller as shown in Figure 4.22.

In the following experiments, a triangular piston movement profile was used as input. The goal was to achieve a constant speed during a relatively long period of time. Based on this profile and the expected forces acting on the piston, the thrust force which must be delivered by the LMA was simulated. Further, this force profile was linked to the LMA controller as feedforward action.

The piston speed and the thrust force depicted in Figure 4.23 and Figure 4.24 respectively have become more stable which is important for the efficiency assessment. The implementation of the new control algorithm results in more constant and predictable force profiles. This allows to map the cogging force and to compensate it by adding this force to the feedforward action.

The cogging force was estimated as shown in Figure 4.25. The obtained array

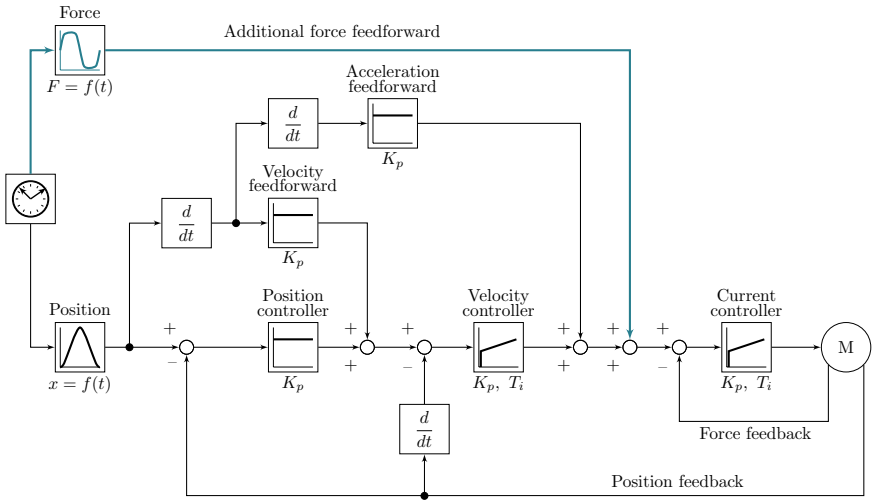

Figure 4.22: Positioning error with and without feedforward.

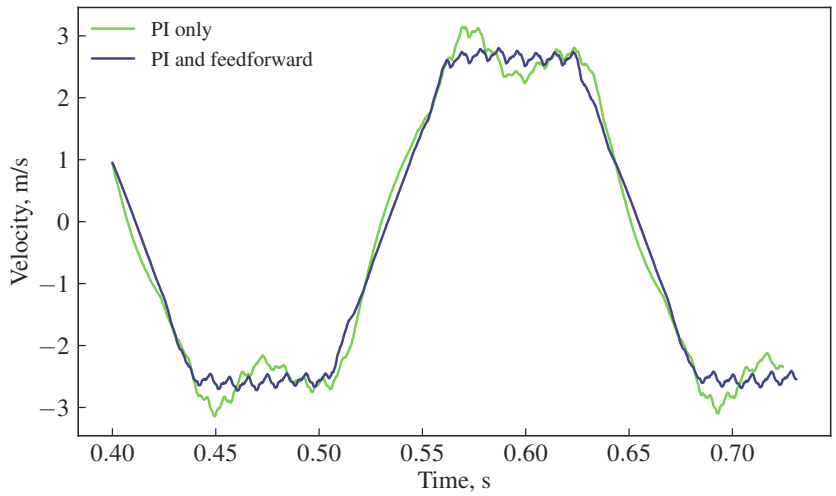

Figure 4.23: Speed profile with and without feedforward.

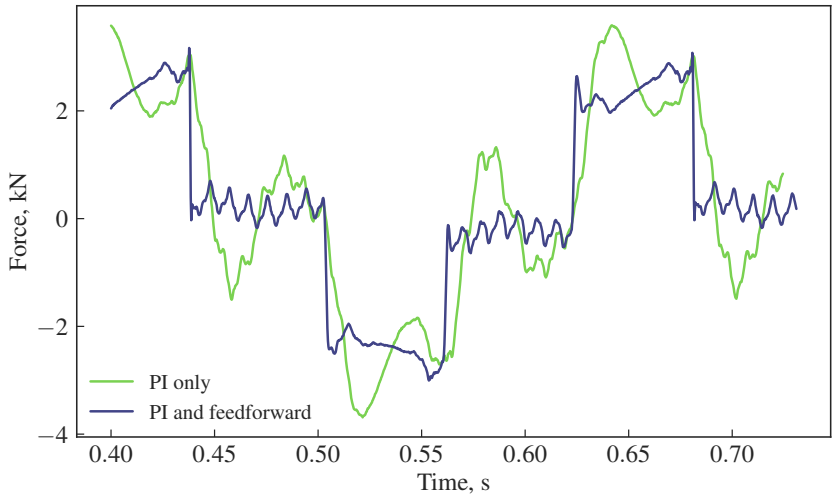

Figure 4.24: Thrust force profile with and without feedforward.

of values, linked to a piston position, was included into the model and applied in only one direction in order to visualize the impact of the cogging force on the piston dynamics.

Figure 4.26 shows the result of four runs with PI controller only, with the injection of the feedforward (FF) action, and both with a compensation of the cogging force during the piston backward motion. As it can be seen, the positioning in the vicinity of the dead points is significantly improved from about 4 mm in the reference case to less than 1mm with feedforward. Ripples from uncompensated cogging force are still present, however, an improvement in respect to the case without cogging compensation can be clearly seen.

By analysing the aforementioned figures, the following can be determined:

- The cogging force profile has a good repeatability from one magnetic pole to another.
- The measured force pitch is shifted in time and its amplitude changes depending on the piston speed.
- The cogging force is different for different movement directions.

Therefore, the cogging force must be mapped as well as a function of the position as the speed separately for the movement directions.

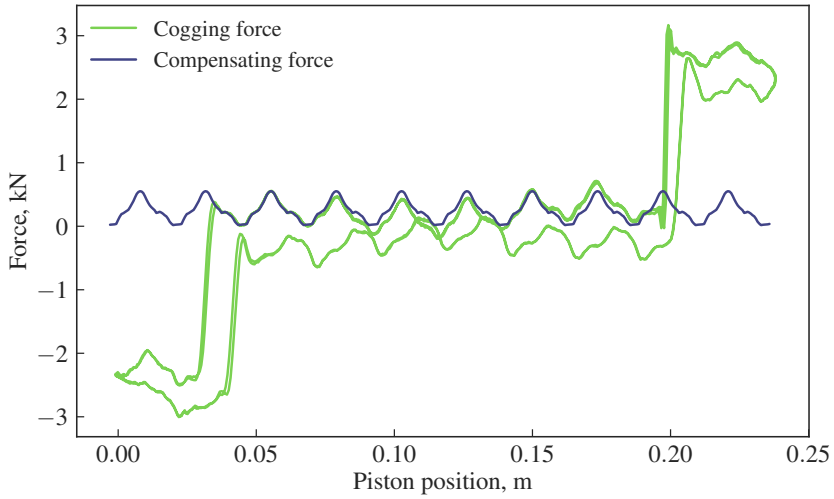

Figure 4.25: Captured cogging force.

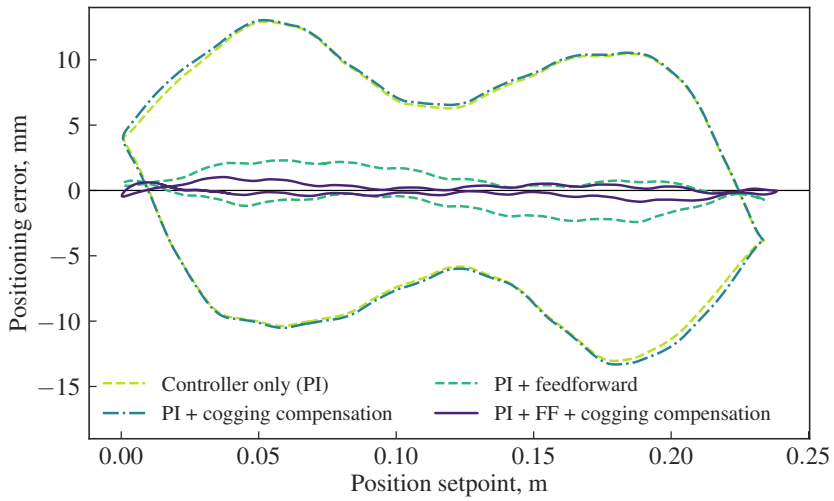

Figure 4.26: Positioning error with and without feedforward.

Design type	**Magnets surface,** m^2	**Magnets volume,** m^3	**Magnets weight,** kg	**Moving mass,** kg	**Coils volume,** m^3
External	0.296	1.24×10^{-3}	9.3	30.4	10.4×10^{-3}
Embedded	0.151	0.79×10^{-3}	6.0	14.5	3.0×10^{-3}

Table 4.1: Comparison of an external and embedded placement of electromagnetic components.

4.6 Integrated alternator design

The goal of the current study was to develop a device to proof the concept and the feasibility of an integrated design with a linear alternator and a servo motor embedded into the expander. The performance of a realistic prototype must be at least the same as the performance of the proof-of-concept device. The power density must allow the magnets and the coils to fit the inner space of the expander, so the volume and the weight of the major components must be lower or equal to the current ones. The comparison of both designs with the same swept volume is shown in Table 4.1. The row "Embedded" introduces the parameters of an imaginary embedded generator for the same piston diameter and the stroke length as these of the test setup.

4.6.1 Primary section

The volume of coils used for the setup is also three times larger than the volume available if these are integrated into the expander. However, the coils used in the current setup contain a water cooler besides the housing and some free space filled with a resin compound. It is difficult to estimate the exact volume of the coils since the information about its design is proprietary, but based on the available drawings it is estimated to be around 50 % of the total volume which is very close to the desired value. Furthermore, a smaller moving mass will not require a motor/alternator with such characteristics.

The expected alternator frequency will increase due to a smaller moving mass, which means a higher volume flow rate and therefore a higher gross power produced by the expander.

4.6.2 Secondary section

It is clear that the current design with external power units is characterized by an excessively large moving mass, mostly because of the use of standard industrial

components and auxiliary parts, such as the magnet frame with rails, coupling and the spline shaft. All these components are not needed in an embedded unit, so the expected moving mass will be much smaller and it is estimated to be around 14.5 kilogram. This is the sum of the piston mass and the mass of the magnets attached to it. The piston walls will serve as the back iron for the magnets.

4.7 Concluding remarks

The experimental campaign was performed in order to validate the obtained model and to test its applicability for the control of the piston movement. The most important is the gas force model since this force defines the piston dynamics the most.

The gas force, in turn, is defined by the inlet and leakage flows. The inlet flow is simulated as an adiabatic nozzle. In the current setup this flow can not be isolated from the others without a modification of the expander. The discharge coefficient is calculated using experimental data from the literature obtained on setups with similar parameters.

The leakage flow model was validated with the in- and outlet ports closed. The deviations of the simulated pressure and position from the measured ones were in the range of 10 % as is shown in Figure 4.9.

The frictional force is identified experimentally. The general model is further used in its simplified form since there will be no stick-slip effect during a normal operation.

The cogging force is also identified experimentally and its model is tested. A visible improvement of the piston positioning is observed in Figure 4.26. This force is also dependent on the piston speed. Therefore in the future, the mapping must be performed for the whole range of the piston speed. This will help to improve the positioning accuracy.

The original Master/Slave configuration of the motors is not optimal. A cross-coupling control is mentioned as a possible solution. If implemented, each motor can operate independently receiving a feedforward signal from the model. In this case, both motors must be tuned separately. This configuration can be tested in the future.

References

[1] Perez-Pinal, C. Nunez, R. Alvarez, and I. Cervantes. *Comparison of multimotor synchronization techniques*. In 30th Annual Conference of IEEE Industrial Electronics Society, 2004. IECON 2004, volume 2, pages 1670–1675, Nov 2004.

[2] F. He and C. Wang. *Cross-coupling synchronous control of dual-motor networked motion control system*. In 2017 36th Chinese Control Conference (CCC), pages 7628–7633, July 2017.

[3] S. T. Jenkins and J. M. Hilkert. *Sin/cosine encoder interpolation methods: encoder to digital tracking converters for rate and position loop controllers*. In Proceedings of SPIE - the International Society for Optical Engineering, Bellingham, Wash., 2008 2008. Society of Photo-optical Instrumentation Engineers.

[4] Steven W. Smith. *The Scientist and Engineer's Guide to Digital Signal Processing*. California Technical Publishing, San Diego, CA, USA, 1997.

[5] Abraham. Savitzky and M. J. E. Golay. *Smoothing and Differentiation of Data by Simplified Least Squares Procedures.* Analytical Chemistry, 36(8):1627–1639, 1964.

[6] William H. Press, Saul A. Teukolsky, William T. Vetterling, and Brian P. Flannery. *Numerical Recipes in C: The Art of Scientific Computing*, chapter 14, pages 650–655. Cambridge University Press, New York, NY, USA, 2nd edition, 1992.

[7] Magnus Gäfvert. *Comparison of two Friction Models*, 1996. Student Paper.

[8] Hai-Hua Mu, Yun-Fei Zhou, Xin Wen, and Yan-Hong Zhou. *Calibration and compensation of cogging effect in a permanent magnet linear motor*. Mechatronics, 19(4):577–585, 2009. Robotics and Factory of the Future, New Trends and Challenges in Mechatronics.

[9] J. Lemmens, K. Mulier, J. Driesen, K. Vanvlasselaer, S. Goossens, and W. Symens. *Efficiency improvement of a high dynamic BLDC linear motor by multiphase control*. In 2013 IEEE Energy Conversion Congress and Exposition, pages 1191–1196, Sept 2013.

5

Expander analysis, optimization and application perspectives

In this chapter, a sensitivity analysis of the expander is presented. A real operation of an ORC with a variable-BVR expander is simulated in order to define the expander boundaries. A fixed BVR expander derived from a standard reciprocating compressor and the BVR-one under variable load conditions are compared. Based on the results, adjustments to the inlet port are proposed.

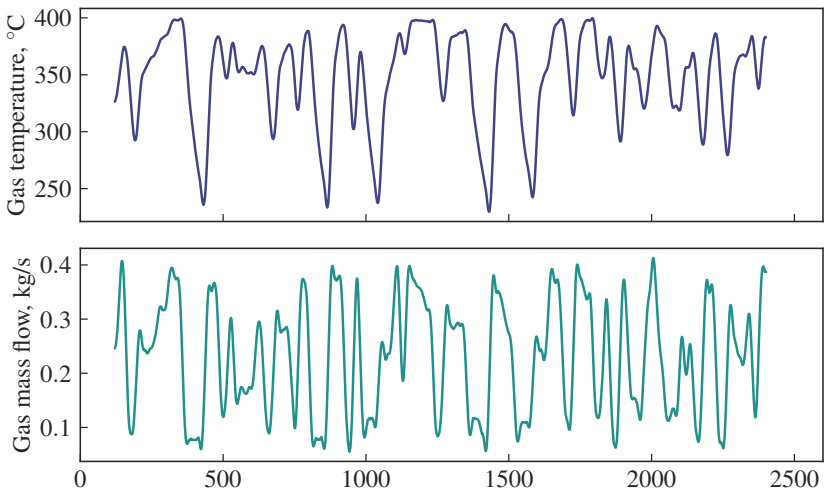

Figure 5.1: Waste heat parameters for Rolling Hills Road Cycle. Source: [1].

5.1 Expander design space in a real application

Since the current design is mainly focused on the waste heat recovery from ICE, an estimation of the gain of using a variable BVR expander in comparison with a fixed one, is useful. As a starting point, several long haul truck operation profiles can be used. These profiles are publicly available and can be found in several publications, for instance, [1]. The Rolling Hills Road Cycle which is shown in Figure 5.1 is used to explain the method. This cycle is characterized by the exhaust gas temperature fluctuations between 225 °C and 415 °C and the mass flow rate between 0.07 kg/s and 0.41 kg/s.

For the optimization of the inlet port geometry, an estimation of the inlet pressure range can be done by simulating a cycle with relevant working fluids. According to the results published in the literature [2, 3], a mixture of water and ethanol appears to be the best choice for automotive applications taking into account the temperature levels typical for combustion engines. In addition, ethanol prevents water from freezing in the winter time.

The cycle is simulated as described in Section C. Since ethanol is a wet working fluid, it leaves the expander slightly superheated as shown in Figure 5.2 and therefore, no internal heat exchanger (IHX) is needed.

If the exhaust gas temperature is higher than approximately 360 °C, the maximum achievable waste heat utilization can be reached since gas can be cooled down almost until the condenser temperature. The evaporation pressure in this case must be as high as possible in order to maximize the cycle efficiency, which

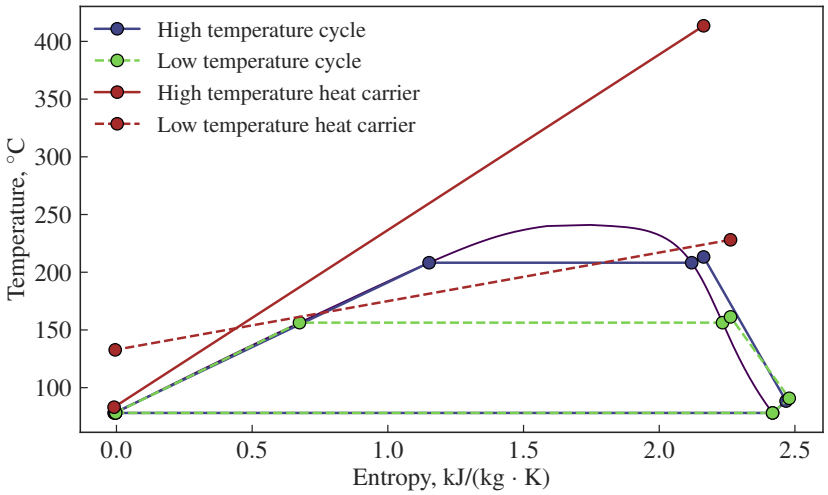

Figure 5.2: Optimized cycles for different waste heat temperatures.

is defined as follows:

$$\eta_{cycle} = \frac{\Delta h_{exp} - \Delta h_{pump}}{\Delta h_{evap}}\,, \tag{5.1}$$

where Δh_{exp}, Δh_{pump} and Δh_{evap} are the enthalpy change over the expander, the pump and the evaporator respectively.

The heat utilization rate is the amount of the waste heat utilized by the ORC in respect to the potentially recoverable heat:

$$\eta_{heat} = \frac{\Delta T_{wh}}{T_{wh,su} - T_{cond}}\,, \tag{5.2}$$

where ΔT_{wh} is the temperature change of the waste heat carrier, $T_{wh,su}$ is the initial temperature of the waste heat carrier and T_{cond} is the condenser temperature. If, in theory, the exhaust gas is cooled down until the condenser temperature, the heat utilization rate reaches the unity.

For lower temperatures, the cycle must be optimized for maximum power output. The higher the evaporation pressure, the higher the cycle efficiency, however, the heat utilization ratio tends to decrease at high values of the evaporation pressure. The power output, being the function of both, has a certain maximum which can be found by analyzing the results for the given evaporation pressure range and the waste heat temperature:

$$\eta_{power} = \frac{\Delta h_{exp} - \Delta h_{pump}}{max(\Delta h_{exp} - \Delta h_{pump})}\,. \tag{5.3}$$

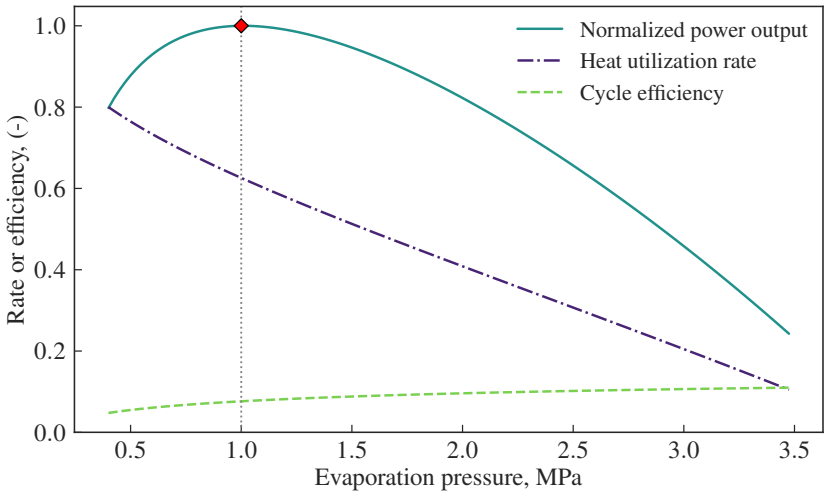

Figure 5.3: Optimal pressure for maximal power output at lowest waste heat temperature.

Figure 5.3 illustrates the method for the cycle optimization for the lowest exhaust gas temperature.

By simulating the cycle optimized for a maximum power output for both fluids, the following can be drawn:

- The lower limit of the evaporation pressures of water and ethanol are 6.22 and 11.13 bar respectively. The evaporation pressure of the mixture will be between these values depending on the ethanol percentage as depicted in Figure 5.4.

- The optimal upper evaporation pressure for water is 49.9 bar. A higher pressure will lead to a lower heat utilization and respectively, to a lower power output. For ethanol, there is no pinch point limit, therefore, the evaporation pressure can be chosen as high as possible. However, the highest evaporation pressure is defined by the specific design of an ORC installation and it is greatly affected by the clearance volume which must be kept as small as possible. Furthermore, the evaporation pressure is limited because of high temperatures of the working fluid. The working fluid at a temperature above 250 °C may damage the expander magnets and makes the choice of sealing and insulating materials more difficult.

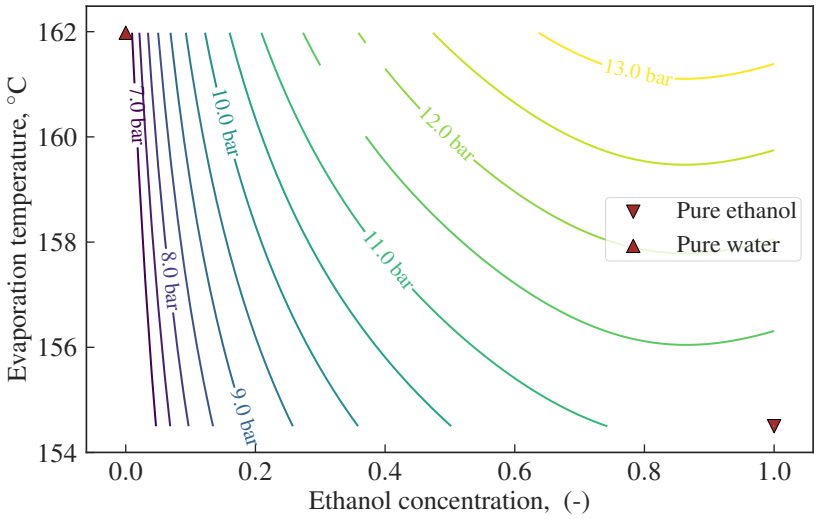

Figure 5.4: Evaporation pressure for optimized cycles.

5.1.1 Intake port optimization

The leakage from the inlet to the outlet port affects the machine volumetric efficiency, which is defined as a ratio of the actual mass flow rate to the theoretical one calculated from the displacement volume:

$$\eta_{vol} = \frac{\dot{m}_{act}}{\rho_{theor} V_d / f} = \frac{\rho(T,\ p)_{act}}{\rho_{theor}}\,, \tag{5.4}$$

where V_d is the displacement volume, f is the frequency, ρ_{theor} is the density of the working fluid calculated for ideal compression or expansion and $\rho(T,\ p)_{act}$ is the actual density calculated from the measured or simulated temperature and pressure.

The inlet port size in Figures 2.1 and 2.2 is shown equal to the stroke length, however, it can be reduced since only a fraction of its length is used within the range of target volume ratios.

For the inlet pressures from 8 bar and above, only 10 % of the total length on the left and on the right side is needed as shown in Figure 5.5. Therefore, the middle part of the port can be avoided. If the total port length is reduced, the leakage flow rate bypassing the expander (number 1 in Figure 2.26) becomes lower increasing the volumetric efficiency of the machine. The specific port size is defined as the ratio of the shortened port length, x_{adm}, and the full size port length, L_{port}. The influence of the piston clearance on the expander volumetric efficiency

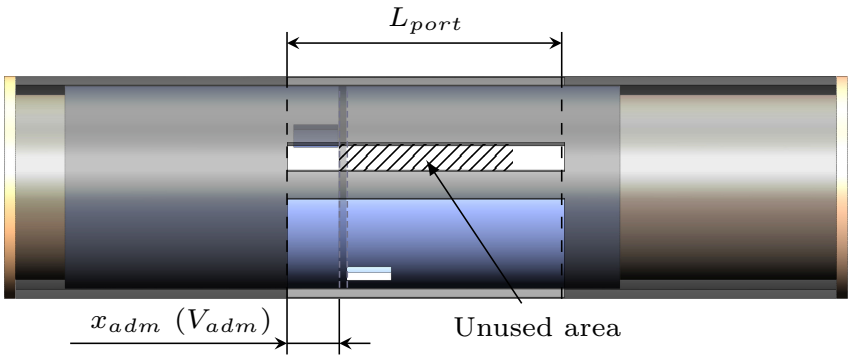

Figure 5.5: Unused port area is shown shaded.

is also depicted in Figure 5.6. Clearance values lower than 30 µm results in relevant expander volumetric efficiencies.

From the literature, the maximum of the volumetric efficiency, was found for the gap size in range of 5–10 µm [4], Sher [5] suggests the gap size to be around 20 µm. With a smaller gap size, the friction losses become dominant, while a larger gap leads to a drastic decrease of the volumetric efficiency.

The influence of the piston clearance on the expander volumetric efficiency is depicted in Figure 5.6. Clearance values lower than 30 µm results in relevant expander volumetric efficiencies. Also, the inlet port size can be reduced since only a fraction of its length is used within the range of target volume ratios, namely, about 10 % on the left and on the right side. Therefore, the middle part of the port can be avoided. If the total port length is reduced, the leakage flow rate bypassing the expander becomes lower increasing the volumetric efficiency of the machine. The port size in Figure 5.6 is defined as the ratio of the total modified port length and the simplified port length.

5.1.2 The gain of a variable-BVR expander in terms of the output power

An example of expansion profiles with different expander pressure ratios is depicted in Figure 5.7. Starting from the evaporation pressure of 10 bar and a superheating level of 5 K, the working fluid is expanded until the condenser pressure of 1 bar. If an expander with a smaller BVR is used, the working fluid leaves it underexpanded, so a part of useful work got lost due to throttling down to the condenser pressure. The only energy remaining can be expressed as follows:

$$\Delta h_{exp} = \Delta h_{und} \tag{5.5}$$

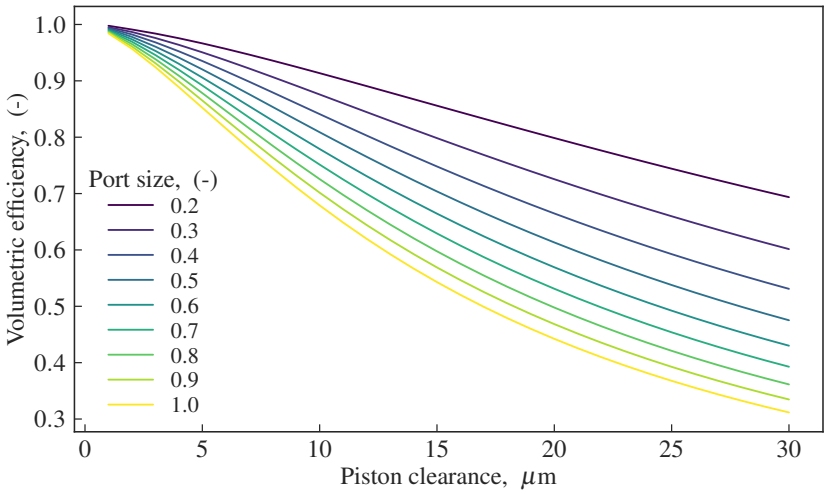

Figure 5.6: Expander volumetric efficiency in function of the piston clearance and port size.

If an expander with a BVR larger than optimal is used, the working fluid is expanded beyond the condenser pressure. Expansion lower than the condenser pressure requires additional work, therefore, this must be subtracted from the work done by the working fluid being expanded until the condenser pressure:

$$\Delta h_{exp} = \Delta h_{opt} - \Delta h_{over}. \tag{5.6}$$

Equations 5.5 and 5.6 are used to obtain the useful enthalpy difference, Δh_{exp} and to substitute it in Equation 5.3. In order to compare performances of a fixed- and a variable-BVR expanders a simulation has been performed with the following boundary conditions and assumptions:

- Isentropic efficiency of both expanders is assumed equal to 55 %.
- Circulation pump isentropic efficiency is assumed to be 50 %.
- The working fluid is pure ethanol.
- Condenser pressure is constant at 1 bar.
- Superheating at the inlet of the expander is 5 K.
- The cycle is optimized for maximum power output.

For the chosen driving profile, the gross power output of the variable-BVR expander was compared with the one of a several fixed-BVR expanders with VR

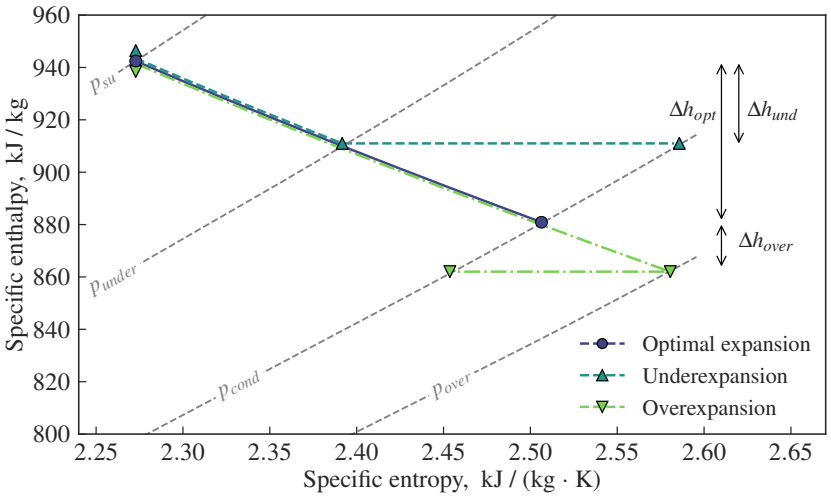

Figure 5.7: Over- and underexpansion in comparison with optimal expansion.

in the range from 4 to 35. Figure 5.8 demonstrates the results of the power output gain for a BVR-expanders in respect to a fixed one. The x-axis represents the volume ratio of a fixed-BVR expander. The following can be concluded:

- An expander with a fixed-BVR of about 18 will show almost the same performance as a variable one for the given driving profile. An expander with a lower BVR will operate with an underexpansion most of the time, while a higher BVR will lead to an overexpansion. The gain for a variable BVR-expander is therefore minimal at this point.
- An optimal fixed BVR for any particular driving cycle can be found. Indeed, the benefit of using a variable BVR expander is low at relative stable driving conditions. The problem of such cycles is their repeatability in a real life. A truck optimized for relatively flat roads can be sent to a mountainous region where its ORC will perform badly and vice versa. Therefore, a variable-BVR will perform better on an annual/lifetime base.
- By knowing the general operation regime of an ICE, the range of required volume ratios can be simulated. Thereafter, the expander can be optimized for these ratios, namely, the intake port can be made shorter as is discussed in Section 2.5 which will increase the volumetric efficiency of the machine.
- This method provides also a possibility to find an optimal fixed-BVR for any waste heat flow profile.

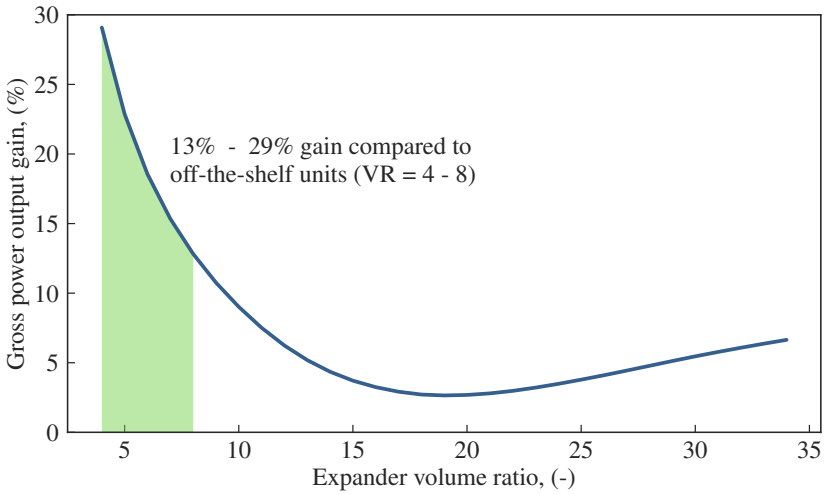

Figure 5.8: Power output gain.

5.2 Optimization criteria

The model developed in Chapter 2 contains several factors influencing the expander performance. This involves the mass flow rate through the machine and the heat transfer between the working fluid and the environment. Further, the most important parameters are listed.

5.2.1 Working frequency

The geometry of the machine was defined in Section 3.4 and is kept constant in all simulations. The first optimization criterion is the piston frequency which is dependent on the forces acting on the piston and the total mass of the moving parts. The higher the reciprocation frequency, the higher the mass flow rate through the expander and therefore the power delivered by the machine. Also, the volumetric efficiency is higher at higher frequencies since the leakage flow rate does not change significantly and mostly depends on the gap size. The characteristics of the linear alternator limit the maximum speed of the translator and the electromagnetic force.

In the realistic design, a more accurate sizing of the piston can be performed. The wall thickness of the piston and the mass of the magnets attached to it can be reduced. A lightweight metal alloy or a composite structure can be used if the magnets are arranged in Halbach array. In this case, no back iron would be needed. A more accurate sizing of the piston and an adjustment of the coil design can also

help to increase the frequency.

5.2.2 Intake area

The drawback of the higher frequency are the higher friction losses. In addition, it becomes difficult to maximize the amount of working medium entering the cylinder due to a higher speed of the piston during the intake. Two different inlet pressures have been simulated, namely 10 and 6 bar as shown in Figure 5.10(a). The piston movement profile was adjusted in order to reach the same pressure of 1 bar at the end of the expansion process. As it can be seen, the maximum available port area for 10 bar is about two times smaller than for 6 bar. In order to maximize the mass flow rate during the intake, not only the trajectory of the piston must be optimized but also the port shape.

The so called filling factor, introduced by [6], means the measured flow rate divided by the working chamber volume change.

$$\Phi_{ff} = \frac{\rho_{cyl}}{\rho_{su}}\,, \tag{5.7}$$

where ρ_{cyl} is the actual working fluid density in the cylinder and ρ_{su} is the gas density in the supply line. In absence of throttling losses, the density of the working fluid in the working chamber is the same as the one at the inlet port after it is closed. The ratio between the actual density in the cylinder and the ideal one gives the indication of the intake efficiency. However, as it was already mentioned above, the working medium is cooled down in the working chamber during the intake which causes a higher density in the cylinder than in the supply line after the pressure equalization. The filling factor can rise above the unity in this case, which does not mean automatically a better intake efficiency.

A possible way to increase the filling factor could be by decreasing the piston linear speed during the angular positioning as depicted in Figure 5.10(b) and optimizing the opening trajectory in order to maximize the port surface area over a time as described in [7]. This approach demonstrates again the advantage of a free-piston technology. The piston control algorithm is depicted in Figure 5.9. The optimization coefficients $k1$ and $k2$ are used to maximize the power output of the system.

5.2.3 Throttling and friction losses

Based on the comprehensive mechanical model, several piston movement profiles have been analyzed in the simulation. For each profile, the accelerating force was kept constant in the range of zero and the nominal one as shown in Figure 5.11. When the maximum speed or a critical stroke length has been reached, the piston has been decelerated by the same motor acting as an alternator. The gas force and

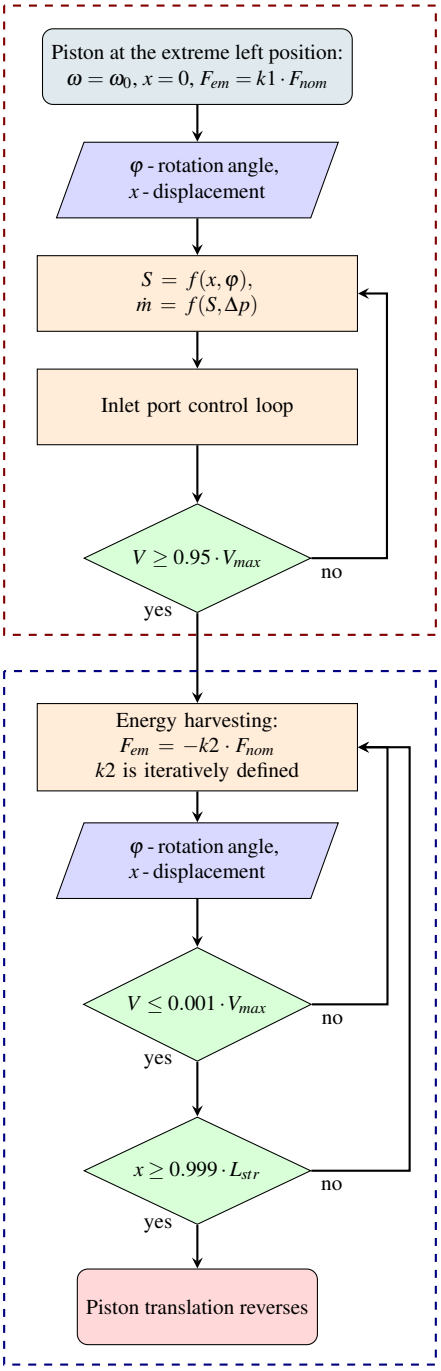

Figure 5.9: Piston rotation algorithm.

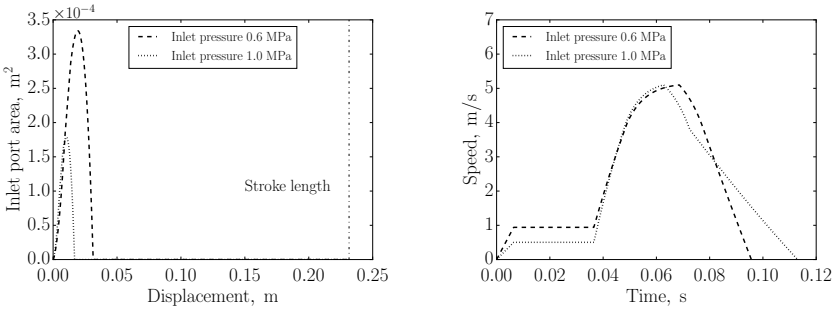

Figure 5.10: Inlet port area (a) and the piston speed (b).

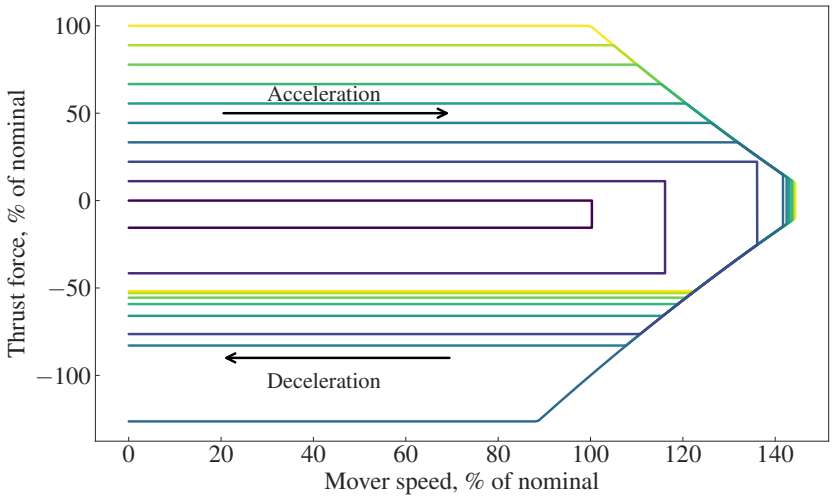

Figure 5.11: Thrust force profiles.

the frictional force are included into the model basing on the experimental setup parameters. The considered inlet pressure is 16 bar and the discharge one is 1 bar. The required brake force was found iteratively in order to stop the piston at its dead points.

The distribution of the gas work and friction losses for the acceleration force equal to the nominal one is shown in Figure 5.12. The work which can be potentially produced by the expanding working fluid, is considered as 100 %. Due to the throttling losses, this work is reduced by 13.1 %. The friction losses are estimated to be around 51.5 %. This obviously high value is obtained because the

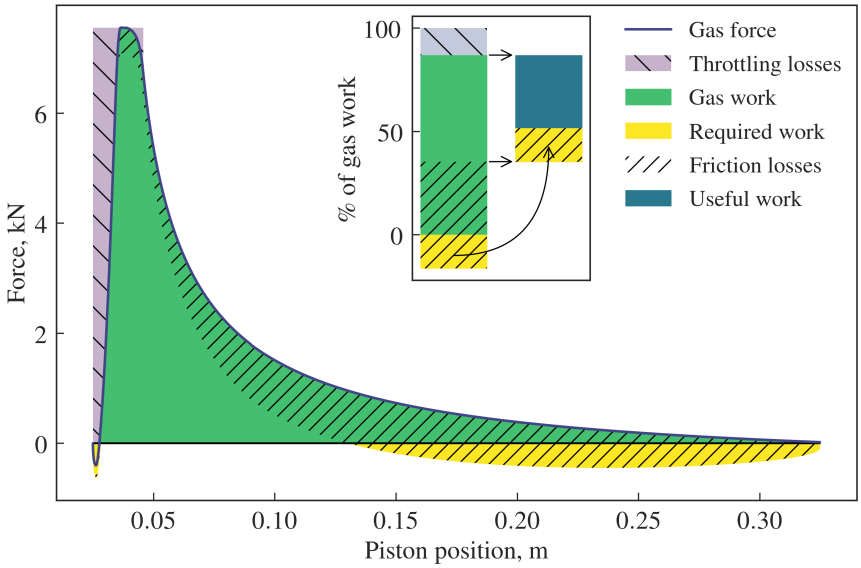

Figure 5.12: Gas work distribution.

piston movement profile was not optimized. The piston control is focused on the maximization of the piston oscillation frequency only. In this case, the useful work is expected to be approximately 35.4 %.

Similarly, a net mean power is calculated for each value of the accelerating thrust force. The maximum is found at 38 % of the nominal force as depicted in Figure 5.13. The reason of low power output at low acceleration force values is a relatively low obtained speed, and therefore a high influence of the leakage losses. The maximum power output is reached at moderate speed values while the friction losses are not significant yet. This method does not take LMA efficiency into account, therefore the obtained movement profile is only optimal from the thermodynamical point of view.

5.2.4 Leakage paths

The average pressure in the vicinity of the ports manifold is closer to the supply pressure p_{su}, which causes a high leakage flow rate at the piston's left and right extreme positions. A square port shape is chosen in order to simplify the preliminary analysis of the system but it is definitely not optimal. More specific: only a part of the intake port length is used, so the middle part can be sealed. This will reflect in a smaller leakage area S_{leak} used in Equation 2.70.

Since the leakage flow rate is dependent on the path length, the latter must be extended in the vicinity of the LDP and RDP by making each side of the sleeve

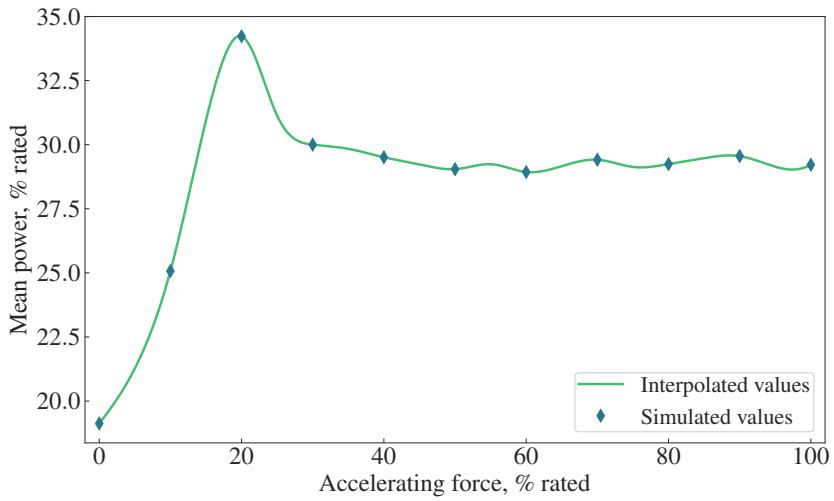

Figure 5.13: Mean net power produced at different accelerating forces.

10–15 % longer so it can sufficiently overlap the port length.

5.2.5 Alternator performance

The copper losses of a linear alternator play a more significant role than ones in rotating machines. The disadvantage of the reciprocating movement is the fact that during acceleration and deceleration, the velocity is very small so the copper losses are dominant in these areas. This means that the acceleration and deceleration of the moving mass must be optimized from this point of view. By reducing these losses, the heat generated by the windings and, therefore, the power losses of the alternator can be minimized.

The main challenge of this study is to optimize the compression/expansion profile with the maximum efficiency profile of the motor/alternator which can be found by means of an adjusted method described in [8] and [9] for rotating machines.

5.3 Concluding remarks

The applicability of the proposed expander is investigated under the realistic conditions. The influence of the the main parameters, such as the piston clearance, the inlet port shape and the working frequency, is highlighted. The potential advantages of the proposed expander have been shown. In the future, the design and

the manufacturing technology can be improved and a prototype with an integrated LMA can be built. It would be then useful to integrate an ORC system, based on the variable-BVR expander, into the power train of a vehicle and to test the whole system in a real operation.

References

[1] D. Luong. *Modeling, Estimation, and Control of Waste Heat Recovery Systems.* PhD thesis, UCLA, 2013.

[2] Dieter Seher, Thomas Lengenfelder, Jürgen Gerhardt, Nadja Eisenmenger, Michael Hackner, and Ilona Krinn. *Waste Heat Recovery for Commercial Vehicles with a Rankine Process*. 21st Aachen Colloquium Automobile and Engine Technology 2012, 2012.

[3] V. Grelet, V. Lemort, T. Reiche, M. Nadri, and P. Dufour. *Waste heat recovery rankine cyclebased system modeling for heavy duty trucks fuel saving assessment.* In 3rd International Seminar on ORC Power Systems (ORC15), 2015.

[4] Craig Bradshaw, Eckhard A. Grol, and Suresh Garimella. *A Sensitivity Analysis of a Miniature-Scale Linear Compressor for Electronics Cooling using a Comprehensive Model*. International Compressor Engineering Conference, 2012.

[5] I. Sher, D. Levinzon-Sher, and E. Sher. *Miniaturization limitations of HCCI internal combustion engines*. Applied Thermal Engineering, 29(2-3):400–411, 2009.

[6] V. Lemort, S. Quoilin, C. Cuevas, and J. Lebrun. *Testing and Modeling a Scroll Expander Integrated into an Organic Rankine Cycle*. Applied Thermal Engineering, 29:3094–3102, 2009.

[7] Sergei Gusev, Andres Hernandez, Davide Ziviani, and Martijn van den Broek. *Modeling of a Variable-BVR Rotary Valve Free Piston Expander/Compressor*. In Latin American conference on Automatic Control, pages 42–48, Medellin, Colombia, 2016.

[8] W. Deprez, J. Lemmens, D. Vanhooydonck, W. Symens, K. Stockman, S. Dereyne, and J. Driesen. *Iso efficiency contours as a concept to characterize variable speed drive efficiency*. In The XIX International Conference on Electrical Machines - ICEM 2010, pages 1–6, Sept 2010.

[9] D. Vanhooydonck, W. Symens, W. Deprez, J. Lemmens, K. Stockman, and S. Dereyne. *Calculating energy consumption of motor systems with varying load using iso efficiency contours*. In The XIX International Conference on Electrical Machines - ICEM 2010, pages 1–6, Sept 2010.

6
Conclusions

In this chapter, the general conclusions are provided.

Waste heat recovery by means of organic Rankine cycles is a proven technology. Numerous references of stable and reliable operating installations are available worldwide. The ORC was deeply studied last two decenia what introduced various small-scale and even mobile installations to be manufactured. Advanced cycle architectures and expander designs increased the system efficiency and allowed to reduce the payback time.

In this study, the potential advantages of a positive displacement expander with an integrated alternator have been shown. In particular, a simple design with only one moving part is potentially inexpensive in production and therefore attractive for small-scale ORC systems. Summarizing the performed study, the following can be highlighted:

- The design and the mechanistic model of a BVR-expander is developed, a test setup is built and the model is experimentally validated.
- The control strategy is formulated and formalized for controller programming.
- The feasibility of an embedded design is proven. The volume of magnets and coils used in the proof-of-concept setup is larger than the volume available for the same diameter. However, this difference is not drastic and by some adjustments it can be equalized.
- Further improvement can be the use of magnets with a higher density of magnetic energy. By placing the magnets in Halbach array allows to reduce the thickness of the piston acting as a back-iron.
- The moving mass of an integrated unit is expected to be much lower, which provides a possibility to increase the working frequency and therefore the mass flow rate and the power output of the unit.
- The inlet port shape needs to be optimized in order to decrease throttling losses during the intake and to reduce the leakage flow bypassing the expander.
- The leakage flow model is not sufficiently accurate because of the geometry complexity and needs to be further improved eventually using CFD-methods.
- The gas-wall heat transfer model is accurate for reciprocating machines with a direct contact between a working medium and the cylinder walls. For the proposed design, this model must be adjusted or redesigned since there is a piston sleeve in between.

- Tribological aspects are not covered in the current study. In the future, the influence of the clearance size on the expander volumetric efficiency and on the frictional force must be studied more in detail.
- Finally, the model obtained in Chapter 2 can be used to simulate the behavior of the expander in reversed mode, working as a compressor. The proposed design is reversible on-the-fly by altering the rotational direction, no check valves are needed for the compressor mode. Therefore, the unit can be potentially interesting for hybrid ORC/HP installations.

Despite the performed study and the obtained results, there is still much work to be done in order to bring this concept to the market. Based on the lessons learned, a realistic prototype needs to be built and tested under conditions typical for the target application.

A Publications

Patent application

S. Gusev. *Free piston device*, 2016. WO2016198554A1 Patent App. PCT/EP2016/063223.

Publications as first-author in peer-reviewed international journals

S. Gusev, D. Ziviani, J. Vierendeels, and M. De Paepe. *Variable volume ratio free-piston expander: Prototyping and experimental campaign*. International Journal of Refrigeration, 98:70 – 79, 2019.

Publications as co-author in peer-reviewed international journals

Adriano Desideri, Bertrand Dechesne, Jorrit Wronski, Martijn van den Broek, Sergei Gusev, Vincent Lemort, and Sylvain Quoilin. *Comparison of moving boundary and finite-volume heat exchanger models in the modelica language*. Energies, 9(5):339:1–339:18, 2016.

Adriano Desideri, Sergei Gusev, Martijn van den Broek, Vincent Lemort, and Sylvain Quoilin. *Experimental comparison of organic fluids for low tempera-*

ture ORC (organic Rankine cycle) systems for waste heat recovery applications. Energy, 97:460–469, 2016.

Adriano Desideri, Jairo Andres Hernandez Naranjo, Sergei Gusev, Martijn van den Broek, Vincent Lemort, and Sylvain Quoilin. *Steady-state and dynamic validation of a small-scale waste heat recovery system using the ThermoCycle Modelica library*. Energy, 115(1):684–696, 2016.

Jairo Andres Hernandez Naranjo, Adriano Desideri, Sergei Gusev, Clara-Mihaela Ionescu, Martijn van den Broek, Sylvain Quoilin, Vincent Lemort, and Robain De Keyser. *Design and experimental validation of an adaptive control law to maximize the power generation of a small-scale waste heat recovery system*. Applied Energy, 203:549–559, 2017.

Davide Ziviani, Sergei Gusev, Steven Lecompte, EA Groll, JE Braun, WT Horton, Martijn van den Broek, and Michel De Paepe. *Optimizing the performance of small-scale organic Rankine cycle that utilizes a single-screw expander*. Applied Energy, 189:416–432, 2017.

Davide Ziviani, Sergei Gusev, Steven Lecompte, Eckhard Groll, James Braun, W Travis Horton, Martijn van den Broek, and Michel De Paepe. *Characterizing the performance of a single-screw expander in a small-scale organic Rankine cycle for waste heat recovery*. Applied Energy, 181:155–170, 2016.

Related publications as first-author in international conferences

Sergei Gusev and Martijn van den Broek. *Analysis and comparison between fixed and variable volume ratio expander for micro-scale ORC*. In Proceedings of the Asme Power Conference, 2015, page 9. ASME, 2016.

Sergei Gusev, Heinz Vervaeke, Davide Ziviani, and Michel De Paepe. *Free Piston Compressor with a Variable Volume Ratio: Insights on Modeling Approach and Control Strategy*. In 24th International Compressor Engineering Conference at Purdue, 2018.

Sergei Gusev, Davide Ziviani, Ian Bell, Michel De Paepe, and Martijn van den Broek. *Experimental comparison of working fluids for organic rankine cycle with single-screw expander*. In 15th International Refrigeration and Air Conditioning Conference at Purdue, Proceedings, pages 1–10. Purdue Univerisity, 2014.

Sergei Gusev, Davide Ziviani, and Martijn van den Broek. *Solar heat driven water circulation and aeration system for aquaculture*. 2017.

Sergei Gusev, Davide Ziviani, and Martijn van den Broek. *Experimental characterization of single screw expander performance under different testing conditions and working fluids*. In Proceedings of the 3rd International Seminar on ORC Power Systems, page 9, 2015.

Sergei Gusev, Davide Ziviani, Jasper De Viaene, Stijn Derammelaere, and Martijn van den Broek. *Modelling and preliminary design of a variable-BVR rotary valve expander with an integrated linear generator*. In 23rd International Compressor Engineering Conference, page 10, 2016.

Related publications as co-author in international conferences

Adriano Desideri, Martijn van den Broek, Sergei Gusev, Steven Lecompte, Vincent Lemort, and Sylvain Qouilin. *Experimental study and dynamic modeling of a WHR ORC power system with screw expander*. In 2nd International Seminar on ORC Power Systems, Proceedings, page 4, 2013.

Adriano Desideri, Martijn van den Broek, Sergei Gusev, Vincent Lemort, and Sylvain Quoilin. *Experimental campaign and modeling of a low-capacity waste heat recovery system based on a single screw expander*. In 22nd International Compressor Engineering Conference at Purdue, Proceedings, pages 1451:1–1451:10. Purdue University, 2014.

Adriano Desideri, Jorrit Wronski, Bertrand Dechesne, Martijn van den Broek, Sergei Gusev, Sylvain Quoilin, and Vincent Lemort. *Comparison of moving boundary and finite-volume heat exchangers models in the Modelica language*. In Proceedings of the 3rd International Seminar on ORC Power Systems, page 10, 2015.

Jairo Andres Hernandez Naranjo, Clara-Mihaela Ionescu, Sergei Gusev, Adriano Desideri, Martijn van den Broek, Vincent Lemort, and Robain De Keyser. *Performance evaluation of MPC for waste heat recovery applications using organic rankine cycle systems*. In Latin American conference on AUtomatic Control, pages 280–285, 2016.

I Vankeirsbilck, B Vanslambrouck, S Gusev, and Michel De Paepe. *Organic rankine cycle as efficient alternative to steam cycle for small scale power generation*. In 8th international conference on heat transfer, fluid mechanics and thermodynamics, Proceedings, pages 785–792. Ghent University, Department of Flow, heat and combustion mechanics, 2011.

Ignace Vankeirsbilck, Bruno Vanslambrouck, Sergei Gusev, and Michel De Paepe. *Efficiency comparison between the steam cycle and the organic Rankine cycle for small scale power generation*. In Polygeneration, 2nd European conference, Proceedings, page 11, 2011.

Ignace Vankeirsbilck, Bruno Vanslambrouck, Sergei Gusev, and Michel De Paepe. *Energetical, technical and economical considerations by choosing between a steam and an organic rankine cycle for small scale power generation*. In 1st international seminar on ORC power systems, Abstracts, pages 68–68, 2011.

Bruno Vanslambrouck, Sergei Gusev, Tobias Erhart, Michel De Paepe, and Martijn van den Broek. *Waste heat recovery via organic rankine cycle: results of a era-SME technology transfer project*. In 2nd International Seminar on ORC Power Systems, Proceedings, page 4, 2013.

Bruno Vanslambrouck, Ignace Vankeirsbilck, Martijn van den Broek, Sergei Gusev, and Michel De Paepe. *Efficiency comparison between the steam cycle and the organic rankine cycle for small scale power generation*. In Renewable Energy World Conference and Expo North America, Proceedings, page 13. Geothermal Energy Association, 2012.

Bruno Vanslambrouck, Ignace Vankeirsbilck, Sergei Gusev, and Michel De Paepe. *Turn waste heat into electricity by using an Organic Rankine Cycle*. In Polygeneration, 2nd European conference, Proceedings, page 14, 2011.

Bruno Vanslambrouck, Ignace Vankeirsbilck, Sergei Gusev, and Michel De Paepe. *Electricity from waste heat by using an organic rankine cycle*. In 1st international seminar on ORC power systems, Abstracts, pages 44–44, 2011.

B

Hardware specifications

B.1 Linear motor/alternator

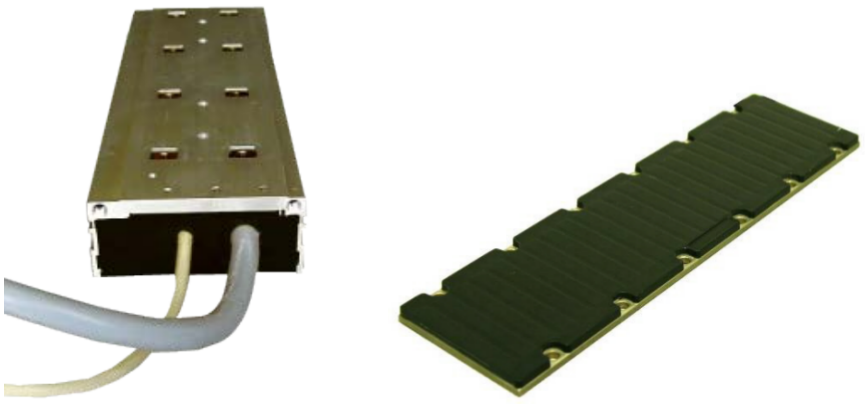

(a) Primary section (b) Secondary section

Figure B.1: Type AL2845-100 motor, water cooled.

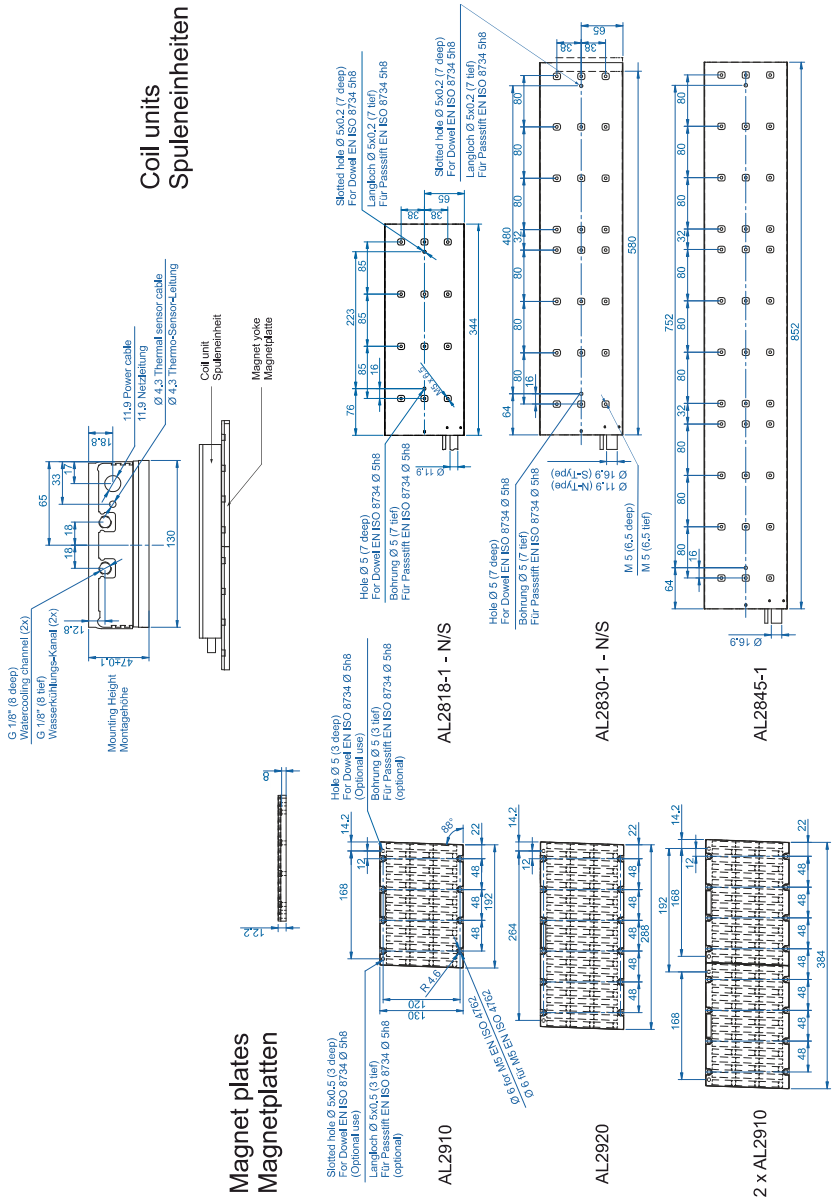

Figure B.2: Primary and secondary section drawings.

Technical data	AL2818-100x	AL2830-100x	AL2845-100x
Winding type	N / S	N / S	N / S
Motor configuration	3-phase synchronous linear motors (400 – 480 V AC)		
Peak force 3 s (F_P)	2700 N	4500 N	6750 N
Peak current (I_{Pa})	19,6 A (N) 41 A (S)	26 A (N), 66 A (S)	41 A (N), 98 A (S)
Continuous force with water cooling (F_{cw})	1200 N	2000 N	3000 N
Continuous force with air cooling (F_{ca})	1140 N	1900 N	2850 N
Continuous current with water cooling (I_{cw})	6.5 A (N) 13.4 A (S)	8.9 A (N), 21.5 A (S)	13.4 A (N), 32.3 A (S)
Continuous current with air cooling (I_{ca})	6.1 A (N) 12.7 A (S)	8.5 A (N), 20 A (S)	12.5 A (N), 31 A (S)
Continuous power loss (P_{ca})	726 W	1209 W	1650 W
Power constant (K_f)	186 N/A (N) 90 N/A (S)	225 N/A (N), 93 N/A (S)	225 N/A (N), 93 N/A (S)
Motor constant (K_m)	2580 N²/W	4300 N²/W	6450 N²/W
Magnetic pitch	24 mm		
Winding resistance - phase (R_f)	8.8 Ω (N) 2.0 Ω (S)	3.8 Ω (N), 0.65 Ω (S)	2.6 Ω (N), 0.44 Ω (S)
Winding inductance - phase (L_f)	70 mH (N) 16 mH (S)	30 mH (N), 5 mH (S)	21 mH (N), 3 mH (S)
Thermal resistance (R_{th})	0,10 °C/W	0.065 °C/W	0.04 °C/W
Magnetic attractive force (F_a)	4900 N	8300 N	12450 N
Weight of the coil unit (M_p)	7.3 kg	12 kg	18 kg
Weight of the magnetic plate (M_s)	10.5 kg/m		
Air gap	0.5 mm		
Temperature sensor	PTC 1 kΩ & KTY26-1		
Cable length unassembled	1m		
Cable length with connector	-		
Suitable servo drive	AX5x06 AX5112	AX5112 (N), AX5125 (S)	AX5118 (N), AX5118 (S)
Cable diameter power	11.9 mm (N) 11.9 mm (S)	11.9 mm (N) 16.9 mm (S)	16.9 mm (N) 16.9 mm (S)
Cable diameter temperature sensor	4,3 mm		
Minimum static bending radius	4 x cable diameter		
Motor cable cross section	4 x 2,5 mm² (N) 4 x 6 mm² (S)		4 x 6 mm² (N)
Temperature sensor cable external diameter	6,3 mm (N) 7,3 mm (S)		8,3 mm (N) 9,3 mm (S)
Temperature sensor cross section	4 x 0,14 mm²		

Figure B.3: Single motor specifications (S winding type).

B.2 Servo motor

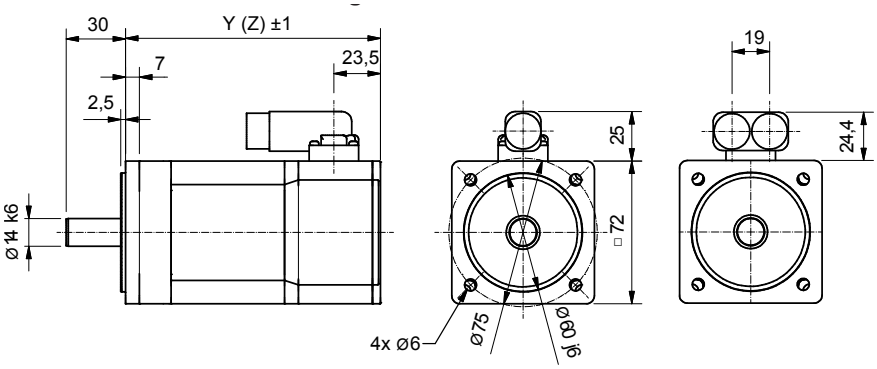

Motor type	Y	Z (brake)
AM8031	129	168
AM8032	154	194
AM8033	180	229
AM8531	168	194
AM8532	194	229
AM8533	229	---

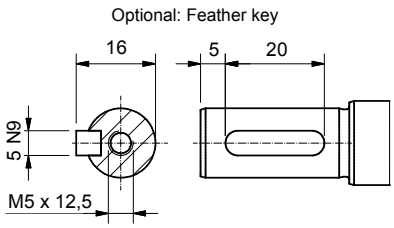

Figure B.4: Servo motor type AM8032-0D20

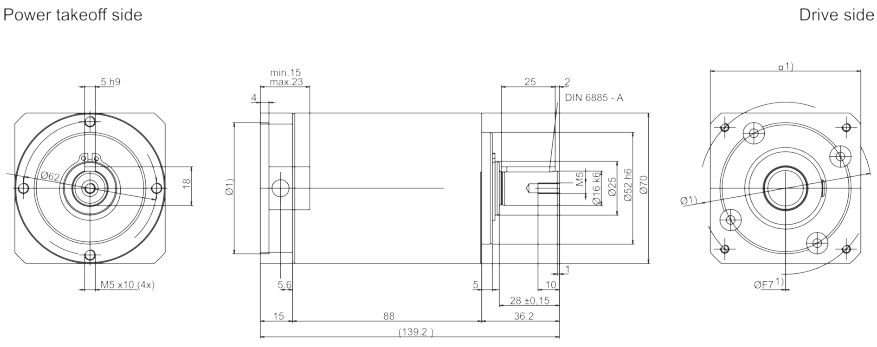

Figure B.5: Gear box type AG2210-LP070S-MF1-7-1D1.

Technical data		Symbol	AM80xx / AM85xx								
		[Unit]	31C	31D	31F	32D	32E	32H	33E	33F	33J
Electrical data											
	Standstill torque*	M_0 [Nm]	1,37	1,38	1,40	2,38	2,37	2,37	3,20	3,22	3,22
	Standstill current	I_{orms} [A]	1,00	1,95	3,20	1,70	2,95	5,10	2,10	4,10	6,80
	Max. mechanical speed	N_{max} [min^{-1}]	10000								
	Max. rated mains voltage	U_N [VAC]	480								
U_N = 115V	**Rated speed**	**Nn [min-1]**	**400**	**1400**	**2700**	**600**	**1400**	**2700**	**600**	**1400**	**2700**
	Rated torque*	M_n [Nm]	1,36	1,38	1,37	2,37	2,34	2,29	3,15	3,10	3,05
	Rated output	P_n [kW]	0,06	0,20	0,39	0,15	0,34	0,65	0,20	0,45	0,86
U_N = 230V	**Rated speed**	**Nn [min-1]**	**1400**	**3300**	**6000**	**1500**	**3000**	**6000**	**1500**	**3000**	**5900**
	Rated torque*	M_n [Nm]	1,35	1,36	1,34	2,34	2,23	2,10	3,10	3,00	2,70
	Rated output	P_n [kW]	0,20	0,47	0,84	0,37	0,76	1,32	0,49	1,00	1,67
U_N = 400V	**Rated speed**	**Nn [min-1]**	**3000**	**6000**	**9000**	**3000**	**6000**	**9000**	**3000**	**6000**	**9000**
	Rated torque*	M_n [Nm]	1,34	1,33	1,30	2,30	2,20	1,85	2,98	2,70	2,30
	Rated output	P_n [kW]	0,42	0,84	1,23	0,72	1,38	1,74	0,94	1,70	2,17
U_N = 480V	**Rated speed**	**Nn [min-1]**	**3400**	**6800**	**9000**	**3400**	**6800**	**9000**	**3400**	**6800**	**9000**
	Rated torque*	M_n [Nm]	1,33	1,32	1,30	2,26	2,10	1,85	2,95	2,60	2,30
	Rated output	P_n [kW]	0,47	0,94	1,23	0,80	1,50	1,74	1,05	1,85	2,17
	Peak current	I_{0max} [A]	5,50	10,70	17,60	9,60	17,20	29,50	12,90	24,60	39,80
	Peak torque	M_{0max} [Nm]	6,10	6,07	6,07	11,66	11,66	11,65	17,19	17,71	17,22
	Torque constant	K_{Trms} [Nm/A]	1,37	0,71	0,44	1,40	0,80	0,46	1,52	0,78	0,47
	Voltage constant	K_{Erms} [mVmin]	99	50	30	100	56	32	106	57	34
	Winding resistance Ph-Ph	R_{20} [Ω]	51,00	12,60	5,0	21,00	6,50	2,20	13,20	3,90	1,35
	Winding inductance Ph-Ph**	L [mH]	134	36,0	13,3	71,9	22,6	7,7	46,3	14,0	4,9

*reference flange aluminium 230 mm x 130 mm x 10 mm.
**measured at 1kHz.
The installation of a shaft seal ring leads to a reduction of the rated values.

Mechanical data		AM8031	AM8531	AM8032	AM8532	AM8033	AM8533
Rotor moment of inertia (without brake)	J [kgcm^2]	0,467	1,67	0,847	2,05	1,23	2,44
Rotor moment of inertia **(with brake)**	J [kgcm^2]	0,546	1,76	0,926	2,15	1,46	---
Pole number		8	8	8	8	8	8
Static friction torque	M_R [Nm]	0,009	0,009	0,015	0,015	0,020	0,020
Thermal time constant	t_{TH} [min]	24	24	26	26	28	28
Weight (without brake)	G [kg]	1,80	2,40	2,40	3,00	3,00	3,60
Weight (with brake)	G [kg]	2,20	2,60	2,80	3,30	3,60	---
Permitted radial force at shaft end	F_R [N]	siehe 10.3.2					
Permitted axial force	F_A [N]						

Figure B.6: Servo motor specifications.

LP70		2-stage											
Ratio		9	12	15	16	20	25	30	35	40	50	70	100
Maximum acceleration torque (max. 1000 cycles per hour) [T_{2B}]	Nm	55	55	55	42	42	40	55	40	42	40	40	37
Nominal output torque (at n_{1N}) [T_{2N}]	Nm	29	29	29	22	21	21	22	21	22	21	21	19
Emergency stop torque[1)] [T_{2NOT}]	Nm	75	75	75	75	75	75	75	75	75	75	75	75
Nominal input speed [n_{1N}]	min^{-1}	3700											
Max. continius speed [n_{1Max}]	min^{-1}	6000											
Average no-load running torque[2)] [T_{012}]	Nm	0,15	0,15	0,15	0,15	0,15	0,15	0,15	0,15	0,15	0,15	0,15	0,10
Torsional backlash [j_T] (arcmin)		Standard ≤ 10											
Torsional rigidity [C_{t12}] (arcmin)		4,0	4,0	4,0	4,0	4,0	3,3	4,0	3,3	4,0	3,3	3,3	2,8
Max. axial force [F_{2A}]	N	1550											
Max. radial force [F_{2R}]	N	1450											
Efficiency at full load	%	97											
Service Life [L_h]	h	> 20.000											
Weight incl. adapter plate [m]	kg	2											
Noise level (At n1=3000 rpm without load) [L_{PA}]	dB	< 64											
Max. permissible housing temperature	°C	+ 90											
Ambient temperature	°C	- 15 to + 40											
Lubrication		Lubricated for life											
Paint		Blue RAL 5002											
Direction of rotation		Motor and gearhead same direction											
Type of protection		IP 65											

Figure B.7: Gear box specifications.

B.3 Control and data acquisition system

The test setup is controlled by an industrial PC CX2030-0120 with Windows Embedded Standard 7 operating system.

Technical data	CX2020	CX2030	CX2040
Processor	Intel® Celeron® 1.4 GHz, single-core	Intel® Core™ i7 1,5 GHz, dual-core	Intel® Core™ i7 2,1 GHz, quad-core
Internal Flash memory	4 or 8 GB CFast Flash card (optionally expandable)	4 or 8 GB CFast Flash card (optionally expandable)	4 or 8 GB CFast Flash card (optionally expandable)
Internal main memory	2 GB DDR3-RAM	2 GB DDR3-RAM	4 GB DDR3-RAM
Persistent memory	128 kB NOVRAM integrated	128 kB NOVRAM integrated	128 kB NOVRAM integrated
Interfaces	2 x RJ 45, 10/100/1000 MBit/s, DVI-I, 4 x USB 2.0, 1x option interface	2 x RJ 45, 10/100/1000 MBit/s, DVI-I, 4 x USB 2.0, 1x option interface	2 x RJ 45, 10/100/1000 MBit/s, DVI-I, 4 x USB 2.0, 1x option interface
Diagnostics LED	1 x power, 1 x TC status, 1 x flash access, 2 x bus status	1 x power, 1 x TC status, 1 x flash access, 2 x bus status	1 x power, 1 x TC status, 1 x flash access, 2 x bus status
Clock	Internal clock with battery backup for time and date (battery replaceable)	Internal clock with battery backup for time and date (battery replaceable)	Internal clock with battery backup for time and date (battery replaceable)
Operating system	Microsoft Windows Embedded Standard 7 P	Microsoft Windows Embedded Standard 7 P	Microsoft Windows Embedded Standard 7 P
Control software	TwinCAT 2 PLC Runtime, NC PTP Runtime, NC I Runtime | TwinCAT 3. See TwinCAT 3 price list	TwinCAT 2 PLC Runtime, NC PTP Runtime, NC I Runtime | TwinCAT 3. See TwinCAT 3 price list	TwinCAT 2 PLC Runtime, NC PTP Runtime, NC I Runtime | TwinCAT 3. See TwinCAT 3 price list
Power supply	24 V DC (-15 %/+20 %)	24 V DC (-15 %/+20 %)	24 V DC (-15 %/+20 %)
Max. power loss	15 W (including system interfaces)	20 W (including system interfaces)	42 W (including system interfaces)
Dielectric strength	500 V (supply / internal electronics)	500 V (supply / internal electronics)	500 V (supply / internal electronics)
Dimensions (W x H x D)	144 mm x 100 mm x 91 mm	144 mm x 100 mm x 91 mm	144 mm x 100 mm x 91 mm
Weight	approx. 1,160 g	approx. 1,165 g	approx. 1,230 g
Operating/storage temperature	-25° C ... +60° C / -40° C ... +85° C	-25° C ... +60° C / -40° C ... +85° C	-25° C ... +60° C / -40° C ... +85° C
Relative humidity	95 % no condensation	95 % no condensation	95 % no condensation
Vibration/shock resistant	conforms to EN 60068-2-6 / EN 60068-2-27	conforms to EN 60068-2-6 / EN 60068-2-27	conforms to EN 60068-2-6 / EN 60068-2-27
EMC immunity/emission	conforms to EN 61000-6-2 / EN 61000-6-4	conforms to EN 61000-6-2 / EN 61000-6-4	conforms to EN 61000-6-2 / EN 61000-6-4
Protection class	IP 20	IP 20	IP 20

Figure B.8: CX2030-0120

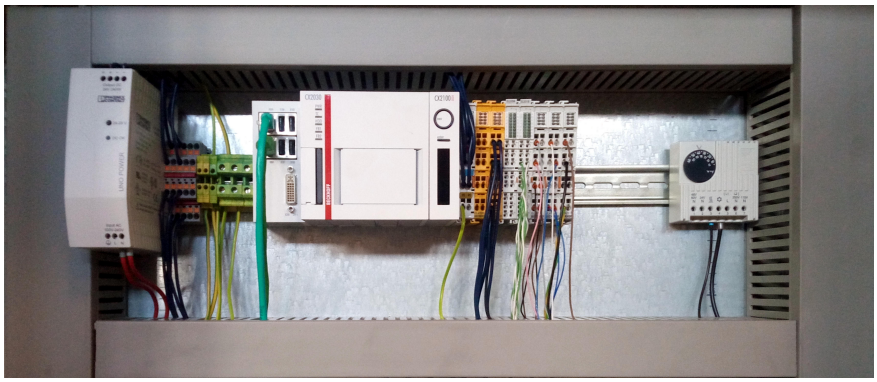

Figure B.9: IPC CX2030-0120, safety and acquisition modules

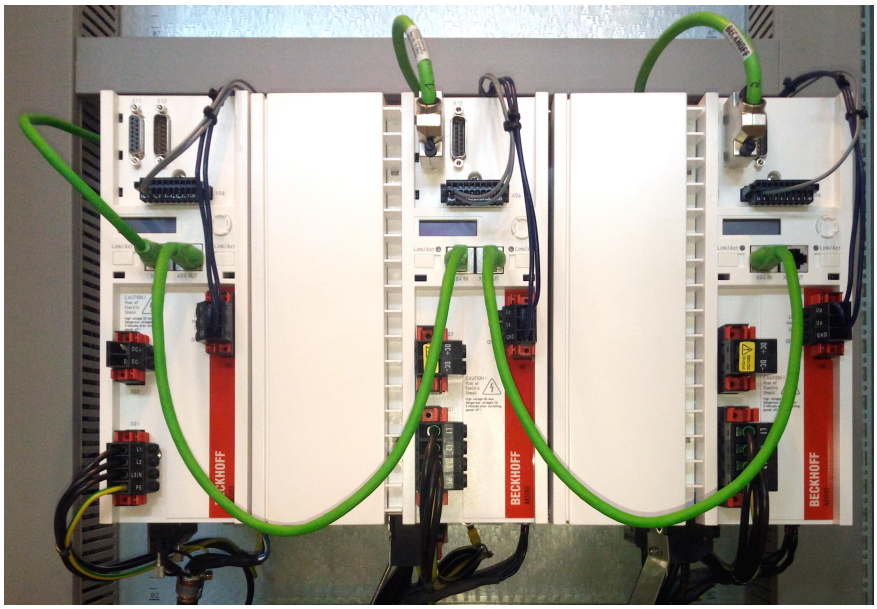

Figure B.10: From left to right: servo drive, drive coil 1, drive coil 2

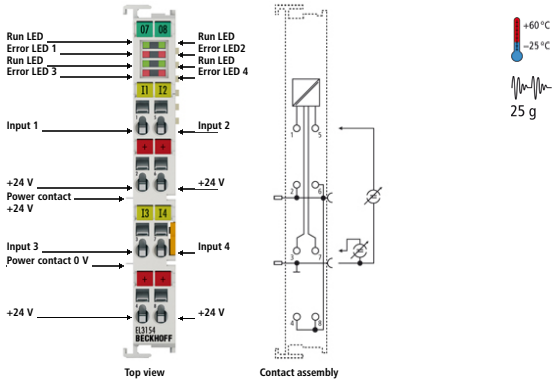

EL3154 | 4-channel analog input terminal 4…20 mA, single-ended, 16 bit

The EL3154 analog input terminal processes signals in the range between 4 and 20 mA. The current is digitised to a resolution of 16 bits and is transmitted (electrically isolated) to the higher-level automation device. The input electronics are independent of the supply voltage of the power contacts. In the EL3154 with four inputs, the 24 V power contact is connected to the terminal in order to enable connection of 2-wire sensors without external supply. The power contacts are connected through. The signal state of the EtherCAT Terminal is indicated by light emitting diodes. The error LEDs indicate an overload condition and a broken wire.

Technical data	EL3154 | ES3154
Number of inputs	4 (single-ended)
Technology	single-ended
Signal current	4…20 mA
Distributed clocks	yes
Internal resistance	85 Ω typ. + diode voltage
Input filter limit frequency	5 kHz
Dielectric strength	max. 30 V
Conversion time	~ 100 µs
Resolution	16 bit (incl. sign)
Measuring error	< ±0.3 % (relative to full scale value)
Electrical isolation	500 V (E-bus/signal voltage)
Current consumption power contacts	–
Current consumption E-bus	typ. 130 mA
Bit width in the process image	inputs: 16 byte
Configuration	no address or configuration setting required
Special features	standard and compact process image, activatable FIR/IIR filters, limit value monitoring
Weight	approx. 60 g
Operating/storage temperature	-25…+60 °C/-40…+85 °C
Relative humidity	95 %, no condensation
Vibration/shock resistance	conforms to EN 60068-2-6/EN 60068-2-27
EMC immunity/emission	conforms to EN 61000-6-2/EN 61000-6-4
Protect. class/installation pos.	IP 20/variable
Pluggable wiring	for all ESxxxx terminals

Figure B.11: EL3154 analog input module

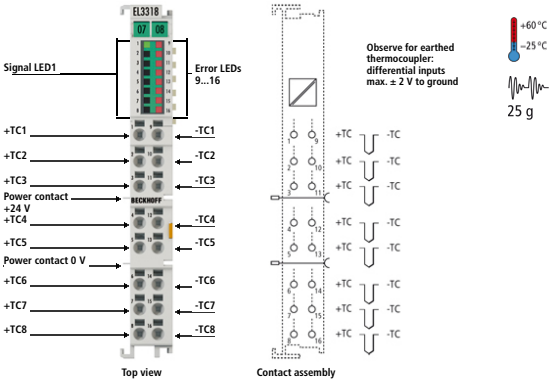

EL3318 | HD EtherCAT Terminal, 8-channel thermocouple input with open-circuit recognition

The EL3318 analog input terminal allows eight thermocouples to be connected directly and is thus particularly suitable for space-saving use in control cabinets. The EtherCAT Terminal circuit can operate thermocouple sensors using the 2-wire technique. A microprocessor handles linearisation across the whole temperature range, which is freely selectable. The error LEDs indicate a broken wire. Compensation for the cold junction is made through an internal temperature measurement at the terminal. The EL3318 can also be used for mV measurement.

The HD EtherCAT Terminals (High Density) with increased packing density feature 16 connection points in the housing of a 12 mm terminal block.

Technical data	EL3318
Number of inputs	8
Power supply	via the E-bus
Thermocouple sensor types	types K, J, L, E, T, N, U, B, R, S, C (default setting type K), mV measurement
Distributed clocks	–
Input filter limit frequency	typ. 1 kHz; dependent on sensor length, conversion time, sensor type
Connection method	2-wire
Wiring fail indication	yes
Conversion time	approx. 5 s up to 40 ms, depending on configuration and filter setting, default: approx. 500 ms
Temperature range	in the range defined in each case for the sensor (default setting: type K; -200…+1370 °C); voltage measurement: ±30 mV…±75 mV
Resolution	0.1 °C per digit
Measuring error	< ±0.3 % (relative to full scale value)
Electrical isolation	500 V (E-bus/signal voltage)
Current consumption power contacts	–
Current consumption E-bus	typ. 210 mA
Bit width in the process image	8 x 32 bit TC input, 8 x 16 bit TC output
Configuration	no address setting, configuration via the controller
Conductor types	solid wire, stranded wire and ferrule
Conductor connection	solid wire conductors: direct plug-in technique; stranded wire conductors and ferrules: spring actuation by screwdriver
Rated cross-section	solid wire: 0.08…1.5 mm²; stranded wire: 0.25…1.5 mm²; ferrule: 0.14…0.75 mm²
Special features	open-circuit recognition
Weight	approx. 70 g
Operating/storage temperature	-25…+60 °C/-40…+85 °C
Relative humidity	95 %, no condensation
Vibration/shock resistance	conforms to EN 60068-2-6/EN 60068-2-27
EMC immunity/emission	conforms to EN 61000-6-2/EN 61000-6-4
Protect. class/installation pos.	IP 20/variable
Approvals	CE, UL, Ex

Figure B.12: EL3318 thermocouple module

B.4 Sensors

Name	Value / property
Signal period	Pole pair spacing 24 mm
Output signal	Analog signal 1 Vss, sine-cosine
Termination resistor	R = 120 Ω
Accuracy	< 100 µm The prerequisite is the precise installation of the magnetic plates with an accuracy of ± 20 µm and offset, phase and amplitude compensation.
Repeatability	< 50 µm
Resolution	5 – 10 µm
Power supply	5 V_{DC}
Connection cable	• 8-core • with twisted pairs • material PUR • UL-certified • diameter 3.2 mm • length 3 m

Assignment (color code)	
green	SIN +
yellow	SIN -
blue	COS +
red	COS -
brown	+ 5 V_{DC}
white	GND
pink	+ 5 V sense
grey	GND sense
Shield	PE / GND

Pin assignment for AX2000 / AX2500 and AX5000

MES	MES – without connector	MES D-Sub (15-pin)	AX2000 / AX2500	AX5000 (X11 / X21)
Signal	**Color**	**Pin**	**Pin**	**Pin**
SIN +	green	8	11	1
SIN -	yellow	15	3	9
COS +	blue	6	9	3
COS -	red	13	1	11
+ 5 V_{DC}	brown	5	4*1	4*1
+ 5 V sense	pink	12	12*1	12*1
GND	white	7	2*1	2*1
GND sense	grey	14	10*1	10*1

Figure B.13: Magnetic Encoder System (MES)

Pressure transmitter for precision measurements
Model P-30, standard version
Model P-31, flush version

WIKA data sheet PE 81.54

for further approvals
see page 5

CANopen certified
CiA201106-301V402/20-0136

Applications

- Measurement and test benches
- Calibration technology
- Laboratories
- Plant construction and machine building

Special features

- Accuracy 0.1 %, without additional temperature error in a range of 10 ... 60 °C
- Optional accuracy of 0.05 % (full scale) available
- Fast measuring rates up to 1 kHz
- Analogue, USB and CANopen® output signals available
- On-site calibration possible using product software

Fig. left: Pressure transmitter model P-30
Fig. right: Pressure transmitter model P-31

Description

Precise
The model P-30 and P-31 pressure transmitters have been developed for precision measurements. Through the use of special WIKA pressure sensors, precision measurements with a maximum measuring deviation of as low as 0.05 % of span are guaranteed. As a result of their active temperature compensation, these pressure transmitters have no additional temperature error in the range of 10 ... 60 ° C.

Fast
The high measuring and output rates of up to 1 kHz make the measured value available as quickly as possible.

Compact
The compact design makes the pressure transmitter ideal for mounting into test benches, such as 19" racks.

Versatile
The models P-30 and P-31 offer a wide selection of electrical connections, process connections and measuring ranges, as well as a large number of different output signals. In addition to the standard analogue signals, USB and CANopen® versions are also available.

Via a USB service interface and the WIKA configuration software "EasyCom", the models P-30 and P-31 can quickly and easily be adjusted on site.

Thanks to the simple-to-use software "Wika data logger", the USB version can also be used to save measured values and create customised reports.

Figure B.14: Pressure transmitter P-30, general description.

Output signal

Signal type	Signal
Current (2-wire)	4 ... 20 mA
Current (3-wire)	4 ... 20 mA 0 ... 20 mA
Voltage (3-wire)	DC 0 ... 10 V DC 0 ... 5 V
USB	per P-30/P-31 interface protocol
CANopen®	per CiA DS404

Voltage supply

Power supply
The permissible power supply depends on the corresponding output signal.

- 4 ... 20 mA (2-wire): DC 9 ...30 V
- 4 ... 20 mA (3-wire): DC 9 ...30 V
- 0 ... 20 mA (3-wire): DC 9 ...30 V
- DC 0 ... 5 V: DC 9 ...30 V
- DC 0 ... 10 V: DC 14 ... 30 V
- USB: DC 4,5 ... 5,5 V
- CANopen®: DC 9 ...30 V

Total current consumption
The total current consumption is dependent on the respective signal type.

- Current (2-wire): max. 25 mA
- Current (3-wire): max. 45 mA
- Voltage (3-wire): max. 10 mA
- USB: 40 mA
- CANopen®: 60 mA

Load

- Current (2-wire): ≤ (power supply - 9 V) / 0,02 A
- Current (3-wire): ≤ (power supply - 9 V) / 0,02 A
- Voltage (3-wire): > max. output signal / 1 mA

Accuracy data

Accuracy at reference conditions

Accuracy	
Standard	≤ ±0,1 % of span
Option	≤ ±0,05 % of span [1]

1) For +/- measuring ranges and measuring range ≤ 0.4 bar on request

Including non-linearity, hysteresis, non-repeatability, zero offset and end value deviation (corresponds to measured error per IEC 61298-2). Calibrated in vertical mounting position with process connection facing downwards.

Non-linearity (per IEC 61298-2)
≤ ±0.04 % of span BFSL

Temperature error
In the range of -20 ... +80 °C the instrument is actively compensated.

- -20 ... +10 °C: ≤ ±0,2 % of span/10 K
- 10 ... 60 °C: no additional error [1]
- 60 ... 80 °C: ≤ ±0,2 % of span/10 K

1) For the optional accuracy at reference conditions of ≤ ±0.05 % of span there is an additional temperature error of ≤ ±0.05 % of span.

Total error band (10 ... 60 °C)
≤ ±0.1 % of span

Long-term stability
≤ ±0.1 % of span/year

Adjustability
Adjustment via the "EasyCom 2011" or "EasyCom CANopen®" software

Zero point: -5 ... +10 % of span
Span: -50 ... +5 % of span

Measuring rate
The measuring rate is dependent on the respective signal type.

- 2-wire: 2 ms
- 3-wire 1 ms
- USB 3 ms
- CANopen®: 1 ms

Figure B.15: Pressure transmitter P-30, detailed information.

Inspection certificate according to EN 10204 - 3.1
Abnahmeprüfzeugnis nach EN 10204 - 3.1

Page / *Seite* 1 / 2

Customer: / *Kunde:*
Universiteit Gent, Campus Coupure
Vakgroep Mechanica van str.
Graaf Karel de Goedelaan 5
BE 8500 Kortrijk

Certificate No. / *Zeugnis-Nr.* **03080591**

Date / *Datum* **22.06.2017**

Customer Order No. / *Kundenbestellnummer*	**4204638469**	Customer Part. No. / *Kunden Artikel-Nr.*		Order Date / *Bestelldatum*	**07.06.2017**
Order No. / Item / *Auftrags-Nr. / Pos.*	**SO00318650/0**	Part No. / *Artikel-Nr.*	**47431280**	Output signal / *Ausgangssignal*	**4 ... 20 mA**
Model / *Typ*	**P-30**			Scale range / *Anzeigebereich*	**0 ... 25 bar rel.**
Serial number / *Seriennummer*	**2261978**			Class / *Klasse*	**0,1 %**
Tag No. / *Messstellen-Nr.*					

Reference / *Referenzgerät*
25 bar 0,01 %

Calibration No. / *Kalibriernummer*
02561662 D-K 16-07

Result / *Ergebnis*

Temperature / *Temperatur* **20°C +/- 1 K**

Standard Referenz bar	Test Item Prüfling mA ↑	Test Item Prüfling mA ↓	Test Item Prüfling bar ↑	Test Item Prüfling bar ↓	rel. Deviation rel. Abweichung % ↑	rel. Deviation rel. Abweichung % ↓
0,0000	3,9996	3,9991	-0,0007	-0,0014	-0,003	-0,006
2,5000	5,5986	5,6000	2,4978	2,5000	-0,009	0,000
5,0000	7,1993	7,2015	4,9989	5,0023	-0,005	0,009
7,5000	8,7995	8,8014	7,4992	7,5022	-0,003	0,009
10,0000	10,3981	10,4004	9,9970	10,0006	-0,012	0,002
12,5000	11,9979	12,0001	12,4967	12,5002	-0,013	0,001
15,0000	13,5997	13,6012	14,9996	15,0019	-0,002	0,007
17,5000	15,1995	15,2016	17,4992	17,5026	-0,003	0,010
20,0000	16,7974	16,7997	19,9959	19,9996	-0,016	-0,002
22,5000	18,3971	18,3999	22,4955	22,4998	-0,018	-0,001
25,0000	19,9990	20,0000	24,9984	25,0000	-0,006	0,000

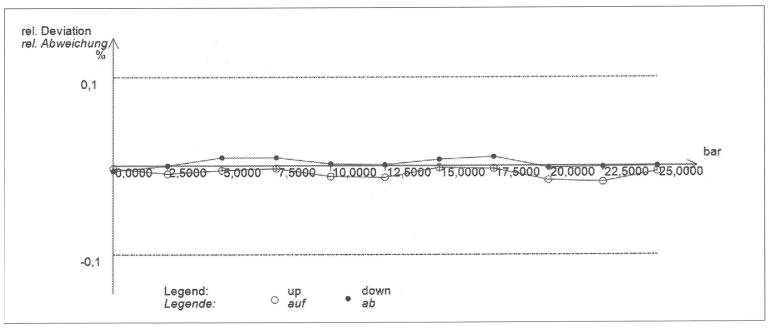

WIKA Alexander Wiegand SE & Co. KG
Alexander-Wiegand-Str. 30
63911 Klingenberg

Phone: +49 9372 132/0
Fax Inland: +49 9372 132/406
E-Mail: info@wika.de

Figure B.16: Pressure transmitter P-30, inspection certificate.

B.5 Pressure regulating valve

Proportional pressure control valve

VP23

G 1/4 ... G 3/4

Step-response diagram

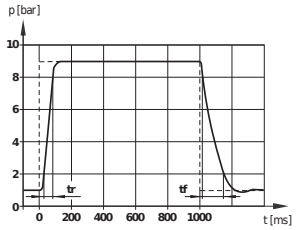

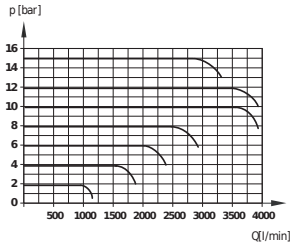

All-digital control electronics

Variable pressure control, external pressure control upon request

Optional: serial interfacing with VP-Tool program

Optional actuation via fieldbus

Valve conforms to CE

Free of lacquer affecting substances

TECHNICAL DATA

Medium:
Filtered 50 µm, unlubricated or lubricated condensate-free compressed air or neutral gases
Due to the lubricants and their additives, use of lubricated compressed air can affect the dynamics and service life

Operation:
Directly-controlled seat valve with µP-driven pressure control

Orifice (nominal):
8, 16 mm

Operating pressure p1 (nominal):
7 bar, 12 bar, 17 bar max

Pressure setting p2:
0 (0,02) to 2 bar/0 (0,1) to 10 bar/0 (0,16) to 16 bar

Flow direction:
1 > 2, 2 > 3

Fluid temperature:
-5 to +50°C (no condensation permitted)

Ambient
Valve series is designed for indoor use at normal industrial ambient

Ambient temperature:
-5 to +60 °C
Contact our technical service for use below +2°C

Degree of protection:
IP65 (M12-variant with connected plug)

Service life:
> 10 Million operations, max. stroke

Tolerance:
Linearity < ±1,0 (% p2 max.)

Control accuracy:
< ±1,0 (% p2 max.)

Response accuracy:
< ±0,2 (% p2 max.)

Hysteresis:
< ±0,5 (% p2 max.)

Repeat accuracy:
< ±0,5 (% p2 max.)
values related to 20°C and 24 V d.c. power supply

Materials:
Valve housing: aluminium
Electronic housing: PAA
Seals: NBR, HNBR on request
Internal parts: PBT
Springs : steel

Actuation	Orifice (mm)	Output pressure (bar)	Set point	Actual value	MODEL
	8	0 ... 16	4 ... 20 mA	0 ... 10 V/4 ... 20 mA	VP2316BD1461Mxxxx

Pneumatic parameters

Recommended application area by nominal value:
NG8: Volume (closed) from 100 to 1500 cm³
NG16: Volume (closed) from 1000 to 8000 cm³

Residual ripple max.	[%]	10
Input pressure p1 max.	[bar]	17 / 12 / 7
Output pressure p2 max.	[bar]	0-16 / 0-10 / 0-2
Flow quantity NG 8	[l/min]	see diagram
Flow quantity NG16	[l/min]	see diagram
Switching times (10%-90%) nominal size 8 at volume 400 cm³		
Typical values for P1=12 bar		
Pressure build-up (tr) 1 bar _ 9 bar	100 [ms]	
Pressure build-up (tf) 4 bar _ 5 bar	50 [ms]	
Pressure drop (tr) 9 bar _ 1 bar	250 [ms]	
Pressure drop (tf) 5 bar _ 4 bar	50 [ms]	
Switching times (10%-90%), nominal size 16 at volume 1000 cm³		
Typical values for P1=12 bar		
Pressure build-up (tr) 1 bar _ 9 bar	100 [ms]	
Pressure build-up (tf) 4 bar _ 5 bar	50 [ms]	
Pressure drop (tr) 9 bar _ 1 bar	100 [ms]	
Pressure drop (tf) 5 bar _ 4 bar	50 [ms]	

Dynamic value stated relates to 24 V d.c. power supply

Figure B.17: Pressure regulating valve VP23

C

ORC working principle

The operation of an ORC installation can be illustrated and described by considering an experimental setup built within the frame of the ORCNext project[1] and shown in Figure C.1. Such installation is a good example of a small-scale ORC using a dry or isentropic working fluid such as R245fa in this case. A buffer tank (6) contains a necessary amount of the working fluid which is needed to fill the piping and the heat exchangers when the ORC starts.

A 14-stage 2.2 kW centrifugal pump (7) builds up the required pressure in the evaporator (1). After evaporation and slight superheating, the working fluid enters the expander (2), producing a certain mechanical work. This unit is in fact a reversed single-screw compressor, connected to a standard asynchronous 11 kWe motor acting as generator (3).

At the expander outlet, the working fluid remains superheated. The remaining sensible heat is recovered by means of an internal heat exchanger (IHX) (4). After that, the fluid is condensed in the same type heat exchanger acting as a condenser (5) which is cooled with a circulating ethylene glycol / water mixture. The condenser heat is dissipated to the ambient.

The cycle is shown in Figure C.2. $T_{hc,\ su}$ and $T_{hc,\ dis}$ are the in- and the outlet temperatures of a heat carrier, $T_{cool,\ su}$ and $T_{cool,\ dis}$ are the in- and the outlet temperatures of a coolant respectively.

[1] http://www.orcnext.be/

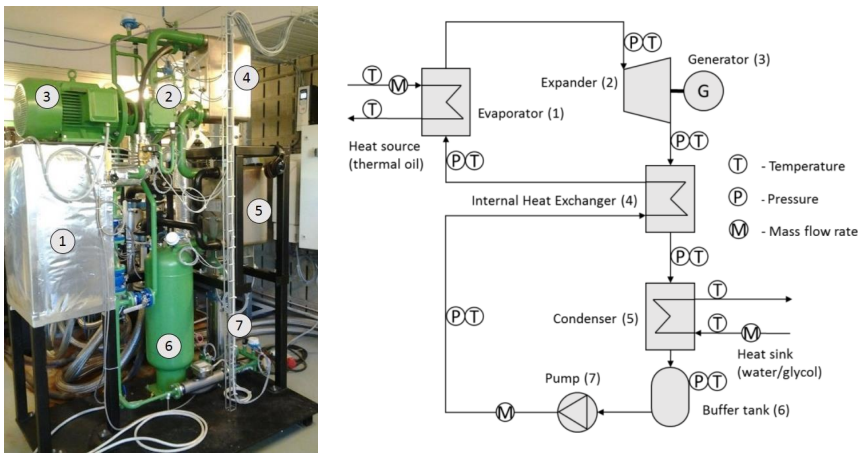

(a) Lab test setup (b) ORC schematics

Figure C.1: Reference test setup

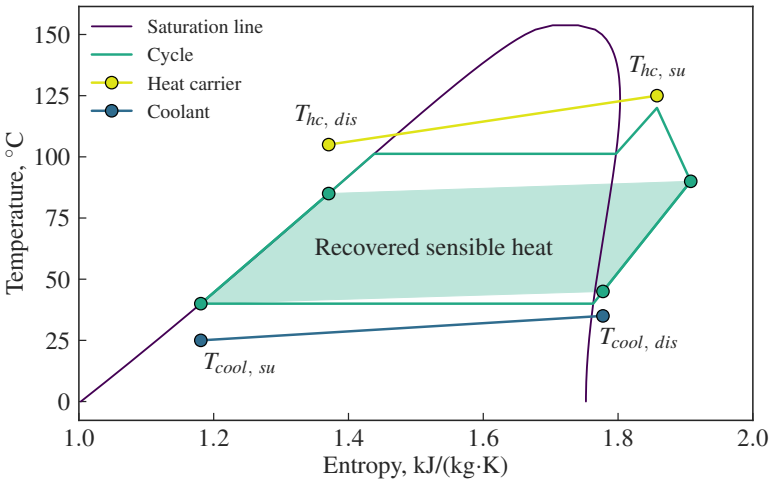

Figure C.2: Organic Rankine Cycle

C.1 ORC working fluids

In most cases, dry or isentropic fluids like R245fa, SES36, R152a, R600a, R1234yf and R1234ze(Z) are used for waste heat recovery [2–5]. The benefit of using these working fluids is that during the expansion process they remain superheated, preventing the droplet formation, which causes turbine blades erosion. For volumetric machines, this is not an issue. However, the fact that the working fluid remains superheated after being expanded makes the use of an internal heat exchanger (IHX) necessary in order to recover the sensible heat and to increase the cycle efficiency. For small-scale automotive targeted ORC installations, the compactness is the key aspect. Depending on the superheating level at the inlet of the expander, the heat to be recovered in IHX varies from 20% to 30% of the heat input as shown in Figure C.3 [6]. This helps to roughly estimate the size and the weight of an IHX, including piping, and the amount of working fluid, which is necessary to fill the additional volume. The only way to avoid the use of an IHX without significant overall efficiency losses is a cycle configuration, where the expansion finishes at the saturation line. Trilateral cycle or partial evaporation cycle provide such a possibility [7]. These solutions imply the use of expanders with a high BVR due to evaporation continuing during the expansion. Reciprocating expanders are the type of volumetric machines, which are easily adjustable to almost any expansion ratio and, therefore, are more attractive than scroll or screw expanders [8]. The use of wet fluids becomes interesting as well. According to the results published in the literature [9–11], a mixture of water and ethanol due to its high evaporation enthalpy appears to be the best choice for automotive applications taking into account the temperature levels typical for combustion engines. In addition, ethanol prevents water from freezing in the winter time. However, [12] warns readers about potential danger of alcohols or hydrocarbons in automotive applications. Since the target group of this study is commercial vehicles, this issue is considered as a minor one.

The right choice of the working fluid for a certain application involves, first of all, the knowledge of the heat source temperature.

So, for low temperature applications such as geothermal, thermal solar [13] or some industrial sources like flash steam or originating from cooling of mechanical equipment, temperature levels are usually in the range from 90 °C to 180 °C. Only large installations can be profitable in this case because of a very low cycle efficiency and a quite large specific price of the equipment needed to recover and to transform the waste heat into electricity. The defining criteria and the choice of the working fluid is very well covered in the literature [14–16].

Waste heat sources with a moderate temperature level [17] are typical for biomass plants. Biomass consists of wood with a very high moisture content beside the fact that the structure of its main components such as cellulose and lignin

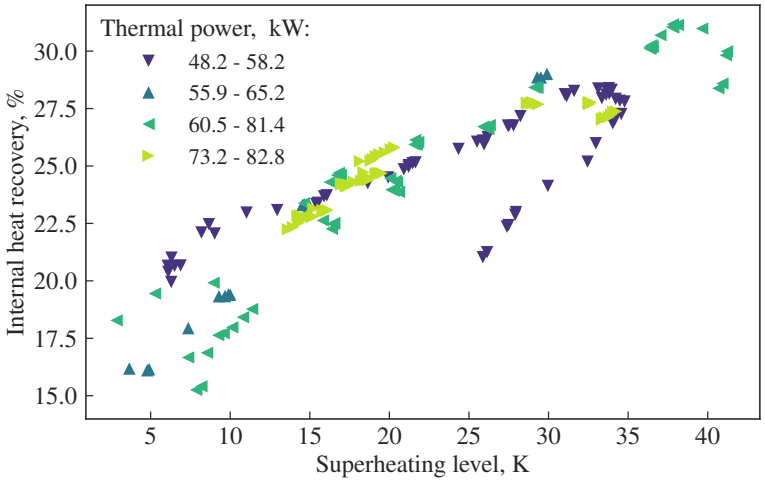

Figure C.3: Trilateral cycle with reheating.

contains about 30% of oxygen which results in an amount of heat produced from combustion of wood twice as low in comparison with fossil fuels.

The same problem is typical for domestic solid waste incinerators. Low caloric value of the fuel leads to a lower temperature of flue gas.

Another issue which usually arises is the acid dew point. Flue gases with a high amount of sulfur oxides can not be cooled down lower than 160 °C because of acid formation and corrosion in heat exchangers.

Also, cement, expanded clay pebbles and brick plants can be mentioned as a source of moderate temperature waste heat [18–20]. The economical feasibility of steam cycle below 350 °C is questionable because of its low efficiency combined with a high plant complexity and therefore, the need for high investments for a relatively low power output. ORC closes the gap where the implementation of steam cycle is economically unattractive.

If the condenser pressure is lower than the ambient, any small leakage will cause accumulation of air inside the installation and, as a consequence, a lower cycle efficiency due to a lower pressure ratio and a higher subcooling of the working fluid. This phenomenon has been detected in the installation mentioned in Section C operating with Solkatherm® (SES36) which boiling point is 36.7 °C.

The same issue is typical for siloxanes [21]. The working fluids like MM (hexamethyldisiloxane) and MDM (octamethyltrisiloxane) show a good performance, however the boiling point is quite high: 101 °C and 153 °C respectively. Furthermore, these working media are extremely superheated after being expanded which

means a need for large regenerators to recover the sensible heat.

There are several competitors for siloxanes, which are listed in [22]. According to these authors, butylbenzene, propylbenzene, ethylbenzene and toluene have a better cycle efficiency, here mentioned in the decreasing order.

Another difficulty for using fluids with a relatively low condensing pressure is the pump priming and cavitation.

Ammonia as a working medium is used in Kalina cycle. Its performance was compared with OMTS-based ORC by [23] for the waste heat recovery from two diesel engines. The exhaust gas temperature was 34 °C, both working media demonstrated almost the same performance. However, the pressure level of the Kalina cycle was about 100 bar, which means a more expensive and heavy equipment in comparison with ORC. The corrosivity of ammonia is also a well-known issue. Not all materials are compatible with it. Detailed description of a Kalina power plant in Húsavík, Iceland with a special attention to corrosion problematic can be found in [24].

Concluding the above analysis, the following criteria can be formulated for the choice of the working fluid for the ORC:

- Thermodynamic parameters: critical temperature, condensing pressure, saturated vapor temperature/entropy slope.
- Material compatibility: corrosivity, ability to solve polymers.
- Compatibility with electrical equipment: flammability and explosivity.
- Chemical stability at high temperatures.
- Health impact: toxicity, cancerogenicity.
- Environmental impact: GWP and ODP.

C.2 Advanced cycle architectures

Heat recovery from internal combustion engines is not a trivial task when the unit operates at a variable load. Both the mass flow rate of the exhaust gas and its temperature are strongly fluctuating in this case. In order to follow the changes in thermal input, the cycle with an adjustable evaporation pressure must be designed. Considering a stable condenser heat rejection, this means a variable pressure ratio over the expander.

This study focuses on heat recovery from combustion engines used in vehicles of a medium power range such as heavy trucks, buses, tugboats or locomotives.

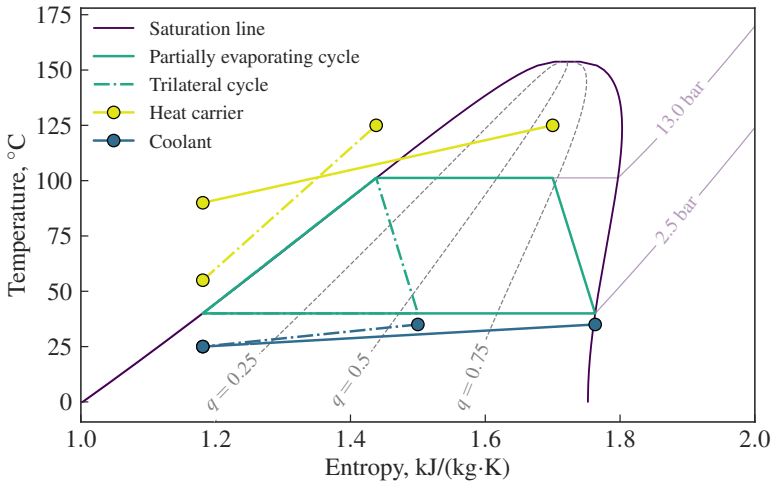

Figure C.4: Partially evaporating cycle.

C.2.1 Trilateral cycle

For such applications, a trilateral cycle (TLC) depicted in Figure C.4 becomes interesting [7]. The main difference with a classical organic Rankine cycle is that the working fluid evaporation is completely avoided.

The cycle efficiency is lower in comparison with standard ORC, also a much higher working fluid mass flow rate is required, but the waste heat utilization reaches its maximum by cooling of the heat carrier almost until the ambient temperature. The power output is higher in this case. To implement a trilateral cycle, an expander with a very high pressure ratio (up to 100) has to be used. Among existing positive displacement machines, only piston expanders can handle pressure ratios above 10 in one stage.

C.2.2 Partially evaporating cycle

The main issue preventing the wide use of TLC architecture is the fact that after the expansion, a part of the working working medium remains in the liquid phase. An excessive liquid circulation produces no work passing the expander, requires a higher power pump and transfers the thermal power from the heat source to the heat sink, creating a thermal "short circuit" between them.

In order to avoid liquid phase at the outlet of the expander, the working fluid must be partially evaporated (Figure C.4). The ratio between the vapor flow rate

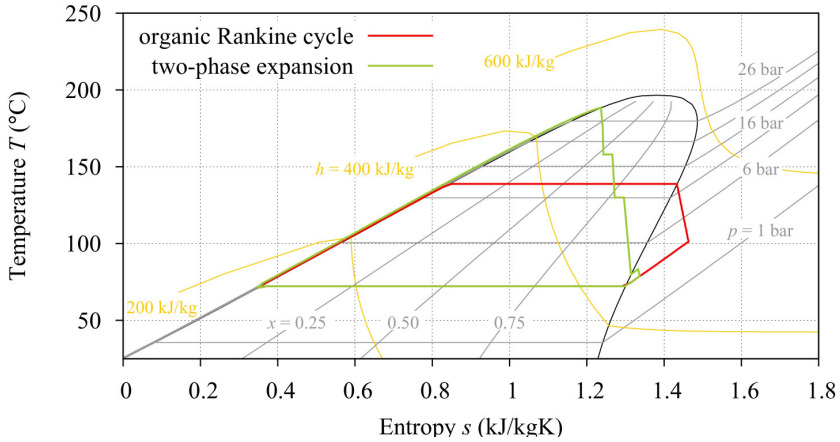

Figure C.5: Trilateral cycle with reheating. Source: [25].

and the total mass flow rate of the working fluid is defined as vapor quality:

$$q = \frac{\dot{m}_{vap}}{\dot{m}_{vap} + \dot{m}_{liq}}, \tag{C.1}$$

where $\dot{m}_{vap}$ and $\dot{m}_{liq}$ are the mass flow rates of the vapor and the liquid phases respectively.

Another way to finish the expansion process at the saturation line is to provide an additional heat input during the expansion (Figure C.5) as it is proposed by [25].

By adjusting the vapor quality at the inlet of the expander, a saturation state at the outlet can be achieved. This gives an additional benefit: the use of an IHX can be avoided. The experimental results shows that the power transferred through such an IHX can vary from 15% to 30% of the thermal input as it is illustrated in Figure C.3. This gives an idea about the weight of the piping, the heat exchanger and the amount of working fluid needed to fill the additional volume.

C.2.3 Liquid injected cycle

In order to define an optimal cycle architecture to be applied at a finite waste heat source, a low order cycle model was developed and validated using the experimental data obtained during ORCNext project. The goal was to propose a method to define the vapor quality at the inlet of the expander, so that after the expansion, the working fluid is at saturation conditions and the heat carrier is cooled down as low as it possible. This will give a possibility to avoid the use of IHX and to maximize the power output.

The experiments have been performed with R245fa as a working fluid, the heat source temperature was kept constant at 125 °C. The flow rate was adjusted

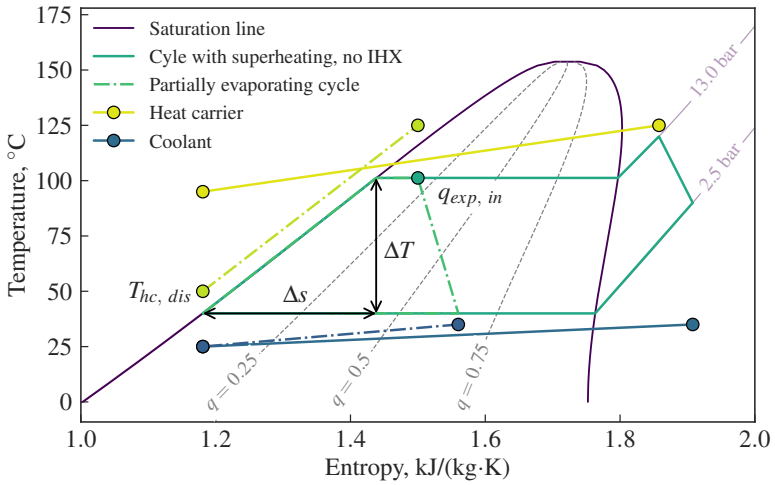

Figure C.6: Required vapor quality ant the expander inlet.

in order to introduce different available levels of thermal power.

The obtained model is further extended to provide a variable volume ratio for the expander in order to find the optimal one for each case. A two-phase working medium is simulated as two independent flows: a saturated vapor and a saturated liquid which is injected into the flow. An optimized cycle is shown in Figure C.6.

In order to minimize the exergy loss, the heat carrier temperature profile has to match the working fluid preheating profile. The temperature/entropy slope of the working fluid in the expected operation region is calculated as follows:

$$\frac{\Delta s}{\Delta T} = \frac{s(p_{evap}; q = 0) - s(p_{cond}; q = 0)}{T(p_{evap}; q = 0) - T(p_{cond}; q = 0)}\,, \tag{C.2}$$

where $s(p_{evap}; q = 0)$ and $s(p_{cond}; q = 0)$ are the entropy values corresponding with q = 0 at the condensing and evaporating pressure. The evaporation pressure is typically limited by the used mechanical components such as expanders, pumps or pipes. The condenser pressure is dictated by the heat sink. Assuming the heat source will be cooled down to the temperature equal to one of the working fluid entering the evaporator plus ΔT_{lo} = 2 – 5 °C (the lowest temperature difference depending on the evaporator sizing), the corresponding entropy value $s_{hc,\ su}$ for the expander inlet can be found:

$$s_{exp,\ su} = s(p_{cond}; q = 0) + (T_{hc,\ dis} - T_{hc,\ su})\frac{\Delta s}{\Delta T}\,, \tag{C.3}$$

where $T_{hc,\ dis} = T(p_{cond}; q = 0) + \Delta T_{lo}$. Using the CoolProp library [26] and

the evaporating pressure together with the entropy obtained in the previous step as parameters, a corresponding vapor quality $q_{exp,\ su}$ can be calculated.

As it can be seen, saturated vapor at the outlet of the expander is only possible to obtain for one certain heat carrier temperature. In case of a fluctuating heat source, the cycle can be optimized for the highest one and the working fluid can be reheated during the expansion process as it was mentioned in Section C.2.2. This requires additional heat which can be only partially obtained from the heat source.

The use of cycles with liquid evaporation during the expansion requires expanders with a high and variable volume ratio because of a very large difference in densities of the liquid and the gas phase. A variable volume ratio expander provides an additional power output in comparison with a fixed one since there is no over- or under-expansion and therefore there are no throttle losses during the discharge.

References

[1] Joost J. Brasz. *Assessment of C6F as Working Fluid for Organic Rankine Cycle Applications*. In International Refrigeration and Air Conditioning Conference. Paper 941, 2008.

[2] Sylvain Quoilin, Martijn van den Broek, Sébastien Declaye, Pierre Dewallef, and Vincent Lemort. *Techno-economic survey of Organic Rankine Cycle (ORC) systems*. Renewable and Sustainable Energy Reviews, 22:168–186, 2013.

[3] S. Quoilin, S. Declaye, A. Legros, L. Guillaume, and V. Lemort. *Working fluid selection and operating maps for Organic Rankine Cycle expansion machines*. International Compressor Engineering Conference at Purdue, 2012.

[4] Junjiang Bao and Li Zhao. *A review of working fluid and expander selections for organic Rankine cycle*. Renewable and Sustainable Energy Reviews, 24:325–342, 2013.

[5] E.H. Wang, H.G. Zhang, B.Y. Fan, M.G. Ouyang, Y. Zhao, and Q.H. Mu. *Study of working fluid selection of organic Rankine cycle (ORC) for engine waste heat recovery*. Energy, 36(5):3406–3418, 2011.

[6] Sergei Gusev and Martijn van den Broek. *Analysis and comparison between fixed and variable volume ratio expander for micro-scale ORC*. In Proceedings of the ASME Power Conference, 2015, page 9. ASME, 2016.

[7] Steven Lecompte, Martijn van den Broek, and Michel De Paepe. *Thermodynamic analysis of the partially evaporating trilateral cycle*. In 2nd International Seminar on ORC Power Systems, Proceedings, page 4, 2013.

[8] V. Lemort, L. Guillaume, A. Legros, S. Declaye, and S. Quoilin. *A comparison of piston, screw and scroll expanders for small scale Rankine cycle systems*. 3rd International Conference on Microgeneration and Related Technologies, 2013.

[9] Dieter Seher, Thomas Lengenfelder, Jürgen Gerhardt, Nadja Eisenmenger, Michael Hackner, and Ilona Krinn. *Waste Heat Recovery for Commercial Vehicles with a Rankine Process*. 21st Aachen Colloquium Automobile and Engine Technology 2012, 2012.

[10] V. Grelet, V. Lemort, T. Reiche, M. Nadri, and P. Dufour. *Waste heat recovery rankine cyclebased system modeling for heavy duty trucks fuel saving assessment.* In 3rd International Seminaron ORC Power Systems (ORC15), 2015.

[11] J. Ringler, M. Seifert, V. Guyotot, and W. Hübner. *Rankine Cycle for Waste Heat Recovery of IC Engines*. SAE 2009-01-0174, 2009.

[12] Feng Zhou, Shailesh N. Joshi, Raphael Rhote-Vaney, and Ercan M. Dede. *A review and future application of Rankine Cycle to passenger vehicles for waste heat recovery*. Renewable and Sustainable Energy Reviews, 2016.

[13] R. Rayegan and Y.X. Tao. *A procedure to select working fluids for Solar Organic Rankine Cycles (ORCs)*. Renewable Energy, 36(2):659–670, 2011.

[14] Dongxiang Wang, Xiang Ling, Hao Peng, Lin Liu, and LanLan Tao. *Efficiency and optimal performance evaluation of organic Rankine cycle for low grade waste heat power generation*. Energy, 50:343–352, 2013.

[15] Henrik Öhman and Per Lundqvist. *Comparison and analysis of performance using Low Temperature Power Cycles*. Applied Thermal Engineering, 52(1):160–169, 2013.

[16] Bertrand F. Tchanche, Gr. Lambrinos, A. Frangoudakis, and G. Papadakis. *Low-grade heat conversion into power using organic Rankine cycles – A review of various applications*. Renewable and Sustainable Energy Reviews, 15(8):3963 – 3979, 2011.

[17] Jim Swithenbank, Karen N. Finney, Qun Chen, Yao Bin Yang, Andy Nolan, and Vida N. Sharifi. *Waste heat usage*. Applied Thermal Engineering, 60(1 - 2):430–440, 2013.

[18] Sanne Lemmens and Steven Lecompte. *Case study of an organic Rankine cycle applied for excess heat recovery: Technical, economic and policy matters*. Energy Conversion and Management, 138:670–685, 2017.

[19] Abid Ustaoglu, Mustafa Alptekin, and Mehmet Emin Akay. *Thermal and exergetic approach to wet type rotary kiln process and evaluation of waste heat powered ORC (Organic Rankine Cycle)*. Applied Thermal Engineering, 112:281–295, 2017.

[20] C. Casci, G. Angelino, P. Ferrari, M. Gaia, G. Giglioli, and E. Macchi. *Heat recovery in a ceramic kiln with an organic rankine cycle engine*. Journal of Heat Recovery Systems, 1(2):125–131, 1981.

[21] F.J. Fernández, M.M. Prieto, and I. Suárez. *Thermodynamic analysis of high-temperature regenerative organic Rankine cycles using siloxanes as working fluids*. Energy, 36(8):5239–5249, 2011.

[22] Ulli Drescher and Dieter Brüggemann. *Fluid selection for the Organic Rankine Cycle (ORC) in biomass power and heat plants*. Applied Thermal Engineering, 27(1):223–228, 2007.

[23] Paola Bombarda, Costante M. Invernizzi, and Claudio Pietra. *Heat recovery from Diesel engines: A thermodynamic comparison between Kalina and ORC cycles*. Applied Thermal Engineering, 30(2-3):212–219, 2010.

[24] Peter Whittaker. *Corrosion in the Kalina cycle. An investigation into corrosion problems at the Kalina cycle geothermal power plant in Húsavík, Iceland*. Master's thesis, The School for Renewable Energy Science, 2009.

[25] J. Wronski, M. J. Skovrup, B. Elmegaard, H. N. Rislå, and F. Haglind. *Design and Modelling of a Novel Compact Power Cycle for Low Temperature Heat Sources*. In The 25th International Conference on Efficiency, Cost, Optimization, Simulation and Environmental Impact of Energy Systems., 2012.

[26] Ian H Bell, Jorrit Wronski, Sylvain Quoilin, and Vincent Lemort. *Pure and pseudo-pure fluid thermophysical property evaluation and the open-source thermophysical property library Coolprop*. Industrial & engineering chemistry research, 53(6):2498–2508, 2014.